Hyperspectral drill-core scanning in geometallurgy

Der Fakultät für Geowissenschaften, Geotechnik und Bergbau
der Technischen Universität Bergakademie Freiberg

genehmigte

Dissertation

zur Erlangung des akademischen Grades

Doctor rerum naturalium
(Dr. rer. nat.)

Vorgelegt

von **M.Sc. Laura Tusa**
geboren am 23. Juli 1991 in Turda, Rumänien

Gutachter: **Dr. Jens Gutzmer**
(Helmholtz Institute Freiberg for Resource Technology – Helmholtz-
Zentrum Dresden-Rossendorf, Technische Universität Bergakademie
Freiberg, Germany)
Dr. Regina Baumgartner Bendezu Juarez
(Pontificia Universidad Catolica del Peru, Teck Resources Limited,
Canada)

Tag der Verleihung: 12 May 2022

Hyperspectral drill-core scanning in geometallurgy

By the Faculty of Geosciences, Geoengineering and Mining
of the Technische Universität Bergakademie Freiberg

is approved this

Thesis

to attain the academic degree of

Doctor rerum naturalium
(Dr. rer. nat.)

submitted

by **M.Sc. Laura Tusa**
born on the 23rd of July 1991 in Turda, Romania

Reviewers: **Dr. Jens Gutzmer**
(Helmholtz Institute Freiberg for Resource Technology – Helmholtz-Zentrum Dresden-Rossendorf, Technische Universität Bergakademie Freiberg, Germany)
Dr. Regina Baumgartner Bendezu Juarez
(Pontificia Universidad Catolica del Peru, Teck Resources Limited, Canada)

Date of the award: 12 May 2022

Plagiarism declaration

I hereby declare that I completed this work without any improper help from a third party and without using any aids other than those cited. All ideas derived directly or indirectly from other sources are identified as such.

In the selection and use of materials and in the writing of the manuscript I received support from the following persons:

- Jens Gutzmer (supervisor, co-author of articles 1, 2, 3 and 4)
- Richard Gloaguen (supervisor, co-author of articles 1, 2, 3 and 4)
- Mahdi Khodadadzadeh (co-author of articles 1, 2, 3 and 4)
- Cecilia Contreras (co-author of articles 1 and 2)
- Margret Fuchs (co-author of articles 3 and 4)
- Paul Ivascanu (co-author of articles 1 and 4)
- Louis Andreani (co-author of article 1)
- Kasra Rafiezadeh-Shahi (co-author of article 2)
- Marius Kern (co-author of article 3)
- Rosie Blannin (co-author of article 3)
- Robert Zimmermann (co-author of article 4)

Persons other than those above did not contribute to writing of the thesis. I did not seek advice from a professional doctorate consultant. No persons received payment for assistance rendered to me in the writing of this thesis.

This thesis has not previously been submitted to another examination authority in the same or similar form in Germany or abroad.

Acknowledgements

Preface

This thesis comprises of seven chapters: A general introduction (Chapter 1) presenting the motivation of the thesis, followed by an overview of the state of the art in the use of hyperspectral imaging in the mining industry and additional information on the case study used in this work (Chapter 2). These are providing a framework for Chapter 3, Chapter 4, Chapter 5 and Chapter 6 which have been published (Chapter 3, Chapter 4 and Chapter 5) or in preparation (Chapter 6) for internationally peer reviewed journals. The articles are presented as they were published or submitted to the journals with the exception of minor formatting changes and the reference sections being merged at the end of the manuscript.

Chapter 3: Tusa, L., Andreani, L., Khodadadzadeh, M., Contreras, C., Ivascanu, P., Gloaguen, R., Gutzmer, J., 2019. Mineral Mapping and Vein Detection in Hyperspectral Drill-Core Scans: Application to Porphyry-Type Mineralization. Minerals 9, 122. https://doi.org/10.3390/min9020122

Chapter 4: Tusa, L., Khodadadzadeh, M., Contreras, C., Rafiezadeh Shahi, K., Fuchs, M., Gloaguen, R., Gutzmer, J., 2020. Drill-core mineral abundance estimation using hyperspectral and high-resolution mineralogical data, Remote Sensing *12*(7), 1218; https://doi.org/10.3390/rs12071218

Chapter 5: Tusa, L., Kern, M., Khodadadzadeh, M., Blannin, R., Gloaguen, R., Gutzmer, J., 2019. Evaluating the performance of hyperspectral short-wave infrared sensors for the pre-sorting of complex ores using machine learning methods. Minerals Engineering 146. https://doi.org/10.1016/j.mineng.2019.106150

Chapter 6: Tusa L., Khodadadzadeh M., Fuchs M., Zimmermann R., Gilbricht S., Ivascanu P., Gloaguen R., Gutzmer J., 2021. Hyperspectral drill core scanning in geometallurgy: a case study *(In preparation)*.

As part of the research performed on the Bolcana porphyry copper-gold deposit, 54 thin sections and 188 drill-core samples (Chapter 6) were analysed for the current work. These results have also contributed to the publication of manuscripts in collaboration with other authors:

Blannin R., Frenzel M., **Tuşa L.,** Birtel S., Ivăşcanu P., Baker T., Gutzmer J., 2021. Uncertainties in quantitative mineralogical studies using scanning electron microscope-based image analysis, Minerals Engineering, Volume 167, https://doi.org/10.1016/j.mineng.2021.106836.

Contreras, I.C., Khodadadzadeh, M., **Tusa, L.**, Ghamisi, P., Gloaguen, R., 2019. A Machine Learning Framework for Drill-Core Mineral Mapping Using Hyperspectral and High-Resolution Mineralogical Data Fusion. Institute of Electrical and Electronics Engineers (IEEE) Journal of Selected Topics in Applied Earth Observations and Remote Sensing. 1–14. https://doi.org/10.1109/jstars.2019.2924292

Lorenz, S., Seidel, P., Ghamisi, P., Zimmermann, R., **Tusa, L.,** Khodadadzadeh, M., Contreras, I.C., Gloaguen, R., 2019. Multi-sensor spectral imaging of geological samples: A data fusion approach using spatio-spectral feature extraction. Sensors (Switzerland) 19, https://doi.org/10.3390/s19122787.

Rafiezadeh Shahi, K.; Khodadadzadeh, M.; **Tusa, L**.; Ghamisi, P.; Tolosana-Delgado, R.; Gloaguen, R. Hierarchical Sparse Subspace Clustering (HESSC): An Automatic Approach for Hyperspectral Image Analysis. Remote Sensing. 2020, 12, 2421, https://doi.org/10.3390/rs12152421

Additionally, the methodologies developed during the current PhD work were tested on hyperspectral datasets acquired from different platforms, proving the potential of adapting these tools at different scales. This led to the publication of articles in collaboration with other authors:

De La Rosa, R., Khodadadzadeh, M., **Tusa, L.,** Kirsch, M., Gisbert, G., Tornos, F., Tolosana-Delgado, R., Gloaguen, R., Mineral quantification at deposit scale using drill-core hyperspectral data: A case study in the Iberian Pyrite Belt, Ore Geology Reviews, Volume 139, Part B, 2021, 104514, ISSN 0169-1368, https://doi.org/10.1016/j.oregeorev.2021.104514.

Flores, H., Lorenz, S., Jackisch, R.; **Tusa, L.,** Contreras, I.C., Zimmermann, R., Gloaguen, R. UAS-Based Hyperspectral Environmental Monitoring of Acid Mine Drainage Affected Waters. Minerals 2021, 11, 182. https://doi.org/10.3390/min11020182

Jackisch R, Lorenz S, Kirsch M, Zimmermann R, **Tusa L**, Pirttijärvi M, Saartenoja A, Ugalde H, Madriz Y, Savolainen M, Gloaguen R., 2020. Integrated Geological and Geophysical Mapping of a Carbonatite-Hosting Outcrop in Siilinjärvi, Finland, Using Unmanned Aerial Systems. Remote Sensing. 12(18):2998, https://doi.org/10.3390/rs12182998

Kern, M., **Tusa, L**., Khodadadzadeh, M., Leißner, T., Gloaguen, R., van den Boogaart, K. G., Gutzmer, J., 2020, Rethinking ore sorting - The search for the optimal sensor, AT Minerals Processing 61(2020)3, 54-64

Kern, M., **Tusa, L**., Leißner, T., Gerald van den Boogaart, K., Gutzmer, J., 2019. Optimal sensor selection for sensor-based sorting based on automated mineralogy data. Journal of Cleaner Production 234, 1144–1152, https://doi.org/10.1016/j.jclepro.2019.06.259

Kirsch, M., Lorenz, S., Zimmermann, R., **Tusa, L.,** Möckel, R., Hödl, P., Booysen, R., Khodadadzadeh, M., Gloaguen, R., 2018. Integration of terrestrial and drone-borne hyperspectral and photogrammetric sensing methods for exploration mapping and mining monitoring. Remote Sensing 10, https://doi.org/10.3390/rs10091366

Kirsch, M.; Lorenz, S.; Zimmermann, R.; Andreani, L.; **Tusa, L.;** Pospiech, S.; Jackisch, R.; Unger, G.; Khodadadzadeh, M.; Ghamisi, P.; Middleton, M.; Ojala, A.; Mattila, J.; Nordbäck, N.; Palmu, J.-P.; Ruskeeniemi, T.; Sutinen, R.; Tiljander, M.; Heikkilä, P.; Gloaguen, R., 2019, Hyperspectral outcrop models for palaeoseismic studies, The Photogrammetric Record 34(2019)168, 385-407

Abstract

Raw materials from geogenic resources will be essential to enable the global shift to renewable energy sources. A steady supply of ores and metals requires mineral exploration that is both efficient and successful in discovering new ore deposits. Mineral exploration programs rely on the acquisition of a multitude of geological, geophysical, mineralogical and geochemical data. A significant amount of geological data comes from drill-cores targeted to test subsurface areas for their mineralisation potential. Exploration drilling is, however, time-consuming and expensive, whilst quantitative data extracted from these cores is commonly limited to whole-rock geochemistry. Quantitative data on mineralogy and microfabric become steadily more important in the process of ore deposit characterisation and evaluation, in order to develop so-called geometallurgical models that are required for deposit valuation. Hyperspectral drill-core scanning has the potential to be an excellent tool for providing quantitative data on mineralogy and microfabric at high spatial resolution in a fast, non-destructive and reproducible manner. However, there has been a distinct lack of data processing tools as well as integrated methodologies to make use of quantitative data on mineralogy and microfabric from early exploration through to the development of robust geometallurgical models.

The main aim of this thesis was thus to develop a framework for the use of hyperspectral drill-core scanning as a pillar in geometallurgical programmes through its use from early exploration and targeting to resource definition and eventual mining. This is achieved in three distinct stages of method development. As a case study the Bolcana porphyry copper-gold deposit in Romania is used as it shows variable and complex mineralogy and mineralization styles, representing therefore a challenge for most established methods for ore characterisation and geometallurgical modelling.

In the first stage, a methodology was developed to identify alteration assemblages and extract structural features from exploration drill core for the preliminary characterisation of the architecture of the Bolcana deposit. This methodology is combining algorithms previously applied in different fields of hyperspectral image processing. The methodology does not only allow the identification of main alteration minerals but also the mapping of their relative abundances. From the relative abundance maps, veins are delineated and their geometric parameters extracted allowing therefore to discriminate between pervasive alteration and that related to vein selvages. These types of data are key to the understanding of alteration zonation in a porphyry system. Together with the assay data obtained from geochemical analyses, the alteration data can be used to define the drilling strategy for further exploration targeting and resource evaluation.

In the second stage, a methodology is proposed to fuse quantitative high resolution mineralogical data from thin section with hyperspectral data obtained for entire exploration cores. This upscaling of quantitative mineralogical data becomes key for the definition of various mineralogical and engineering parameters in the context of resource evaluation. Quantitative mineralogical estimates for spectrally diagnostic minerals in the short-wave infrared spectrum in the Bolcana porphyry system is the most important outcome of this study. In addition, quasi-quantitative estimates of non-diagnostic minerals and mineral groups based on their subtle association with the spectrally diagnostic phases was achieved together with the estimation of further

mineralogical parameters such as an adapted mineral association calculation at the coarse resolution of the hyperspectral data.

Following the application of hyperspectral drill-core scanning in resource characterisation the potential use of hyperspectral sensors in the beneficiation stage was evaluated in the third and final stage. Hyperspectral sensors are usually not suited for the direct detection and identification of ore minerals. Yet, they can prove suitable for identifying proxies for mineralization. Due to the complexity of the Bolcana porphyry system and the lack of a direct mineral proxy for copper or gold grades, a machine learning approach was developed for the estimation of commodity grade. The methodology relies again on the resampling and coregistration of quantitative high resolution mineralogical data obtained by scanning electron microscope-based image analysis with hyperspectral imaging data. This final stage proves that subtle proxies for porphyry mineralization can be identified which are not clear by direct spectral and mineralogical analysis.

The individual methodologies are finally combined into a workflow suitable for the development of a geometallurgical model already at the exploration stage. This model can be further populated with various engineering, environmental and economical parameters allowing for reduced risk of operations and improved decision-making through the entire raw materials value chain.

Table of Contents

List of Figures

List of Tables

Chapter 1 Introduction

1.1   Motivation of the thesis

Mineral resources are essential to the energy transition. The transition is driven by sustainability concerns, a key factor being the ambition to combat climate change (Markard, 2018). One of the main steps taken into this direction is the decarbonisation of the energy sector through the replacement of fossil or nuclear fuels by renewable energy sources such as wind or solar (Mitchell, 2016). The transition towards a low-carbon economy has however increased the demand for raw materials to supply the new technological developments. In an ideal circular economy, recycling of end-of-life goods would account for the demand of raw materials. In the current environment however, recycling cannot supply the increased demand for metals needed for the technologies supporting the energy transition. Copper for instance is one of the key metals supporting the industrialisation as well as the energy transition, being widely used due to its high electrical conductivity, in conjunction with its excellent corrosion resistance, formability, and joinability (Schlesinger et al., 2011). Even though it has one of the highest recycling rates, exceeding 50% (Graedel et al., 2011), in 2020, only around 16 % of the copper production came from recycling while the remaining 84% (20.6 million tons) came from primary ore production (Copper International Study Group, 2021). Copper supply and demand is currently considered to be in deficit, meaning there is more market demand than available product. The copper demand is expected to grow from 1-5.3 % yearly depending on the sector (Sutton, 2021). With the transition towards electromobility the demand for copper will additionally increase as electric cars require 3 to 4 times the copper amount needed for traditional vehicles. The increase in copper demand is also supported by the development of renewable energy systems (Herrington, 2021), and therefore the discovery and mining of new primary deposits is needed. In many cases, resources are increasingly complex in terms of mineralogy (Mudd and Jowitt, 2018), hidden under cover or may be deeper than previously known mineralization (Thompson, 2020).

There are numerous ore deposits discovered worldwide which have not been mined due to various reasons, including low grades, tonnages, high mineralogical complexity or environmental impact rendering them uneconomical. To reduce the related technical and financial risks associated to these projects, the use of a geometallurgical programme can support the resource characterisation and mining process. Through integrated, multidisciplinary approaches, geometallurgical programmes are designed to ensure the resource optimization and increased energy efficiency in exploration and mining operations (Michaux and O'Connor, 2020).

A successful geometallurgical programme relies on the strategic integration of geological, mining, metallurgical, economical and geoenvironmental parameters to maximize the project value through responsible resource management (Dominy et al., 2018b). One of the pillars in the development of a geometallurgical model is the acquisition of compositional data through systematic sampling and analysis. This sampling is usually achieved during exploration campaigns in which thousands of kilometres of diamond drill-cores are extracted to test subsurface regions with high mineral resource potential. The extracted cylindrical core samples are traditionally analysed visually by geologists and subjected to geochemical analyses (Kruse, 1996; R. Wang et al., 2017). Bulk geochemical analysis is a standard routine applied to drill-core, but the turnaround time is

long and the analysis is performed on crushed large drill-core intervals, presenting limitations in terms of spatial resolution and making the conversion to mineralogy difficult, if not impossible. Quantitative mineralogical information is usually restricted to selected regions of interest assumed as representative in terms or mineralization style and grade for the respective sampled interval. Standard quantitative analyses include X-Ray diffraction (XRD) applied on powder samples (Lindholm, 1987) or Scanning Electron Microscopy (SEM) based image analytical techniques (Fandrich et al., 2007) applied on polished thin sections prepared from the selected samples. Qualitative mineralogical and petrographic (e.g. textural) analyses are performed through optical microscopy on (polished) thin sections. These laboratory techniques provide valuable mineralogical information and derived mineralogical and metallurgical parameters, but they are only local in scale, require a very high level of expertise, are marred by a subjective bias and are rather expensive and time-consuming to obtain. As spatial variability in terms of grade, mineralogy and microfabric attributes is key for the understanding of a deposit as well as the definition of geometallurgical domains, hyperspectral drill-core scanning is becoming an emerging technique for this purpose as it provides a rapid, spatially continuous, automated and non-invasive tool for mineralogical and possibly textural data acquisition. While the use of hyperspectral drill-core scanning in the context of geometallurgy continues to be researched and achievements have been made particularly in the context of grade control (Johnson et al., 2019) and selective mining using tripod-based system for mine face mapping (Barton et al., 2021), there is a need for an integrated approach for the analysis and use of hyperspectral data from early exploration through mining.

To address the remaining challenges the Bolcana porphyry system (Apuseni Mountains, Romania) is used in this work as a case study. Its variable and complex mineralogy and mineralization styles represent a challenge for most established methods for ore characterisation and geometallurgical models, making therefore the Bolcana porphyry system ideal for testing new technologies and methodologies

1.2   Objective and structure of the thesis

The purpose of this thesis is to assess the opportunities of the use of hyperspectral imaging for alteration mapping and semi-quantitative mineralogical analyses of cores during exploration and mining. In this regard, four methodological approaches are proposed, each relying on a different degree of understanding of the mineralogy, structure and texture of a porphyry system. This way, the current thesis provides guidelines on the use of hyperspectral drill-core scanning in a geometallurgical framework, through its implementation from early exploration to resource characterisation, and finally mining and beneficiation. The development of a geometallurgical model using the developed workflows will have profound impact on planning of the stage of active exploitation and post-mining environmental impact. During mining, adopting a geometallurgical approach will optimize resource and energy efficiency, decrease environmental impact, decrease technical and financial risk and broadly improve sustainability.

The following chapter will lay the theoretical foundations for the proposed methodological approaches in Chapters 3-6. Chapter 2 will therefore provide a summarized description of the Bolcana porphyry deposit, an introduction to the reflectance spectroscopy of minerals, its potential applications in the characterization of ore deposits and a brief overview on the state of the art in hyperspectral imaging for exploration and mining.

In the third chapter a new methodology for the analysis of drill-core hyperspectral data in early exploration projects, where no pre-existing mineralogical information is available, is presented. The proposed methods allow for a rapid mapping of the main alteration assemblages, both pervasive and related to veins and link them to different vein types and alteration zones. The obtained results consist of mineral and vein distribution maps with quantified vein abundances and azimuths. This approach is validated using mineral maps obtained through the analysis of thin sections prepared from regions of interest of the drill-core samples and analysed by Scanning Electron Microscopy-based Mineral Liberation Analysis. The proposed approach is therefore ideal for early exploration stages, enabling the characterization of the main alteration assemblages associated to different vein types within the porphyry system. The approach helps to demonstrate that the use of hyperspectral scanning allows for faster, non-invasive and more efficient drill-core mapping, providing a useful tool for complementing core-logging performed by on-site geologists.

With the availability of quantitative mineralogical information usually obtained on selected samples in advanced exploration stages, the need for upscaling arises in order to obtain results on mineral abundances and associated mineralogical parameters over entire boreholes. To address this need, the fourth chapter presents a new methodology for upscaling high resolution mineralogical data (i.e., SEM-MLA) to entire drill-cores as well as for the estimation of the mineral association of sulphides, considered here, the main ore-bearing minerals over the drill-cores. The methodology relies on the fusion of hyperspectral data and SEM-MLA mineral maps. Within the chapter, three multivariate regression algorithms are presented and evaluated in order to identify their suitability.

The fifth chapter illustrates a methodology to assess the potential to extend the impact of hyperspectral imaging beyond the exploration stage. While direct sensing of the ore using hyperspectral imaging can be performed for minerals with diagnostic absorption features in the VNIR-SWIR regions of the electromagnetic spectrum, in the case of porphyry copper deposits, where the target commodities (i.e., copper, gold) are hosted in the sulphides, mineralogical and spectral proxies are required to estimate their abundance and association. In the case of the Bolcana porphyry mineralization, the ore minerals show different mineralogical associations depending on the location in the system, and therefore the use of direct proxies, such as the abundance of a selected alteration mineral or mineral assemblage is not possible. In order to tackle this issue, the use of machine learning (ML) algorithms is proposed to classify the samples as either ore or waste based on a selected cut-off (minimum equivalent copper grade). Like in Chapter 4, this methodology relies on the fusion of hyperspectral and SEM-MLA data to train an ML classifier to predict the ore grade on new samples.

Following the investigation of the use of hyperspectral sensors in distinct stages of an exploration or mining project, in the sixth chapter, the use of hyperspectral data in the broad geometallurgical context is explored. This research is motivated by the strong need for continuous data over large drill-core intervals that can be used to define mineralogical and textural (geometallurgical) domains. Hyperspectral imaging of drill-cores is identified in this study as a key technology to deliver such data, provided that suitable processing tools are made available. In this regard, a processing and analysis methodology is developed for the available hyperspectral data, allowing for a broad domain definition based on spectral point analysis which can be further used for strategic sampling for higher resolution analyses (for example by SEM-based image analysis at

micrometer-scale). These high-resolution data on a local scale can be co-registered to the hyperspectral data. The mineralogical and textural information is further upscaled to entire drill-core samples for mineral abundance estimation, using random forest, the algorithm identified in Chapter 4 as best suited for the dataset. The mineral abundances obtained can in a next step be used for extraction of structural or morphological features as well as for defining domains of known average mineralogical composition. This mineralogical knowledge can further support decision making for metallurgical testing and can be incorporated into a 3D model for predicted metallurgical performance in the subsequent mining stages.

Based on the experience gained in the developed individual methodologies on a small number of samples, in the concluding chapter (Chapter 7) a methodological framework is proposed for the use of hyperspectral drill-core scanning in the geometallurgical context, from early exploration drilling to mining, as well as for the continuous updating of the geological, resource and mining models.

Chapter 2   Materials and methods

2.1   The Bolcana mineralized system

Bolcana is a porphyry copper-gold mineralized system located in the "Gold Quadrilateral" epithermal Au-Ag-Te and porphyry Cu-Au province in South Apuseni Mountains, Romania (Berbeleac et al., 2014). This region is considered one of Europe's most significant porphyry Cu-Au and epithermal provinces (Figure 2-1) (Berbeleac et al., 2014; Cioacă et al., 2014). The district has been historically mined for gold with an estimated production of c.a.100 tonnes of gold since pre-Roman times (Ghitulescu and Socolescu, 1941; Udubaşa et al., 2001). Porphyry Cu systems are major global sources of metals, supplying >80% of the world's Cu (Sun et al., 2013) ~50% of the Mo, and 20% of the Au (Sillitoe, 2010). To meet future demands of metal resources, the discovery and exploitation of new porphyry deposits is essential. Being located in a metallogenic province with a long history of exploration and mining, Bolcana is surrounded by multiple epithermal and porphyry-type deposits on which the developed methodologies could be tested in the future. As it shows variable and complex mineralogy and mineralization styles, Bolcana represents a challenge for most established methods of characterisation. Furthermore, the variable copper grades represent a strong motivation for the understanding of the different ore types and their composition for the pre-concentration of the ore after crushing, prior to further beneficiation stages.

2.1.1   Regional geology

At regional scale, the Bolcana porphyry system is located in the Western Tethyan magmatic belt which is distributed in Slovakia, Hungary, Romania, Serbia, Bulgaria, Kosovo, Macedonia, Greece and Turkey (Baker, 2019). Here, the tectonic setting and geodynamic evolution along the 3,500-km strike broadly developed from Cretaceous subduction-related arc magmatism, transitioning from convergence and collision to post-orogenic extension from the late Eocene to early Oligocene, and widespread post-collisional extension-related magmatism during the Miocene (Baker, 2019; Richards, 2005).

In the South Apuseni Mountains, the metallogenic endowment is related to a Miocene post-collision extension-related magmatic event, mainly between 14.9 and 9 Ma (Pécskay et al., 2006; Roşu et al., 1997) The significant metallogenic activity leading to the emplacement of porphyry systems (Cu-Au ± Mo) and epithermal veins (Neubauer et al., 2005; Pécskay et al., 2006; Roşu et al., 1997). Three main mineralization styles can be defined based on age, geological setting and geochemistry (Marcoux et al., 2002):

1.   Mid Miocene Au-Ag epithermal deposits hosted in acidic rocks (Rosia Montana);

2.   Mid to late Miocene Au–Ag–(Te) epithermal deposits (Săcărâmb, Baia de Aries), Pb–Zn–Cu–(Au, Ag) mineralisation and porphyry Cu–Au±Mo deposits (Bolcana, Rosia Poieni, Valea Morii)

3.   Mid to late Miocene quartz andesite-hosted Cu–As–(Au) mineralisation
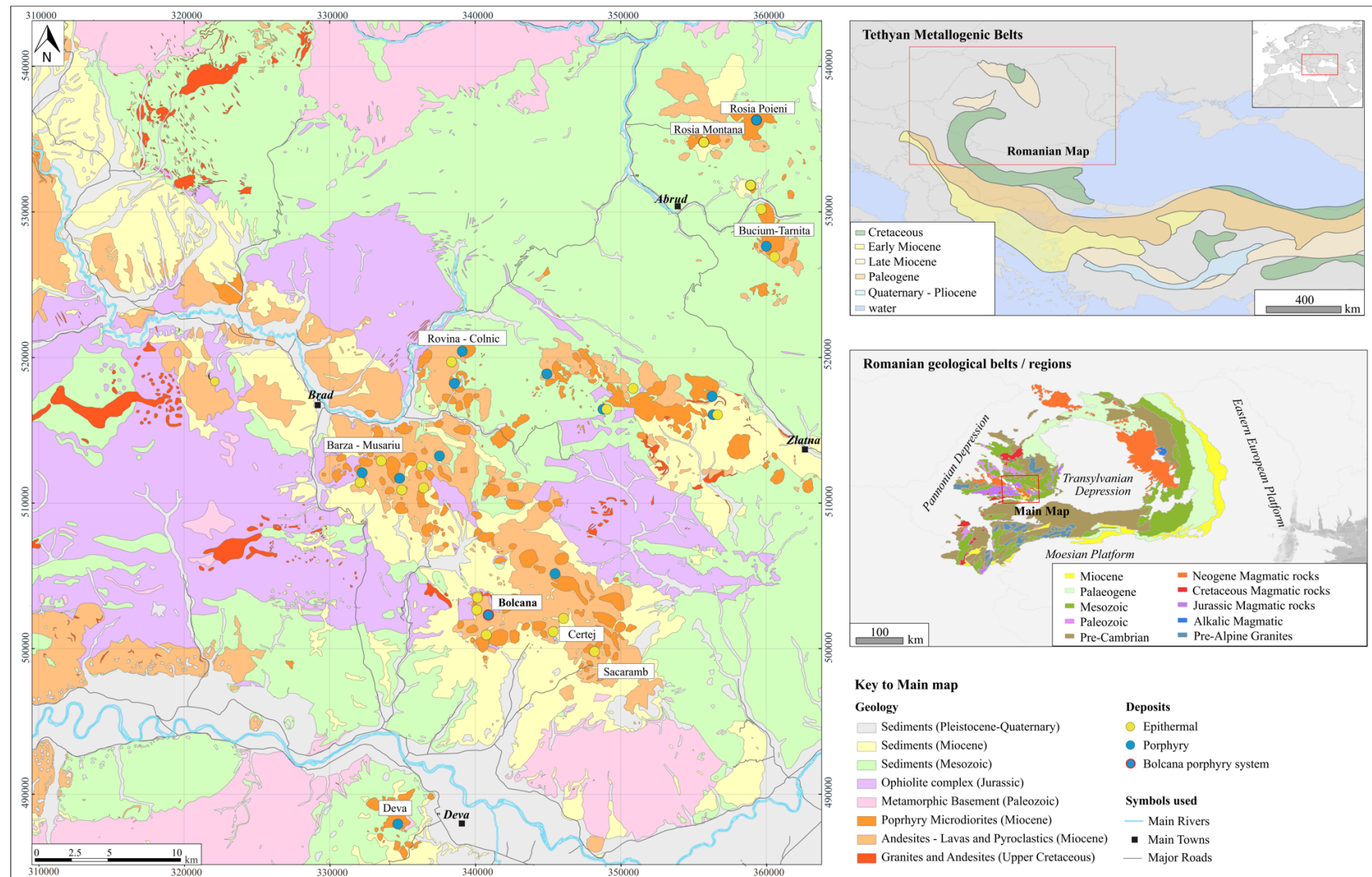
Figure 2-1. Regional and local geological setting for the Bolcana Porphyry system.

Porphyry-style mineralisation occurs in the core of subvolcanic bodies, associated with peripheral base metal (Pb–Zn–Cu ± Au, Ag) and Au–Ag epithermal veins (Cardon et al., 2008; Cioacă et al., 2014). Bolcana falls within the belt of NW trending Miocene age andesitic subvolcanic intrusive rocks and local volcanic rocks within the South Apuseni Mountains and more precisely in the south-eastern part of the Brad-Săcărâmb metallogenic district (Figure 2-1) (Apopei et al., 2014). Here the main direction of the distribution of the ore deposits follows an ESE-trending dextral, strike-slip fault system (Neubauer et al., 2005). The basement in the area consists of Middle Jurassic-Lower Cretaceous basaltic andesites, lava flows and pyroclastics, as well as Lower Cretaceous rhyolites, overlain by Palaeocene and Miocene sedimentary series. Neogene subvolcanic bodies, of dioritic composition, intrude the basement and the older sedimentary units (Rhys, 2014).

2.1.2   *Local geology and mineralogy*

Bolcana is a porphyry-type Cu-Au ore deposit with associated epithermal veins hosted by a microdioritic subvolcanic body. At the surface, the system has a broad 2 by 1 km N-S elongated argillic footprint, controlled by faults that host late epithermal veins flanking the deposit (Ivascanu et al., 2019). The Bolcana system has a known depth extent of approximately 1.5 km. The main alteration types encountered are phyllic-argillic alteration on the flanks of the system and near-surface. The latter transitions to a magnetite-chlorite dominant assemblage and further to a potassic alteration style towards the centre of the system (Figure 2-2) (Blannin et al., 2019; Ivascanu et al., 2019). Additionally, a sodic-calcic core was described by Ivascanu et. al (2019). The ore minerals are represented by chalcopyrite, bornite, chalcocite, covellite and native gold and occur mainly as stockworks, hydrothermal breccias and subordinately as disseminations. Vein types and vein densities are variable, and linked to the lithology and depth of occurrence. Quartz-magnetite veins are prevalent in the carapace of the system. Vuggy quartz and quartz-magnetite veins are typically associated with early and intermineral porphyries. Quartz or anhydrite veins with sulphide centreline are dominant in intermineral porphyries and commonly occur with magnetite veins and locally with quartz-carbonate sulphide veins. The latter two become dominant in late intermineral and late porphyries. The associations of vein types with the breccias are more variable, but dominated by sulphide, quartz with sulphide centreline veins and magnetite stringers.

Chalcopyrite is the main copper-bearing mineral, with minor contributions to the copper grade from bornite, chalcocite, covellite, tetrahedrite and freibergite (Blannin et al., 2019). Chalcopyrite is generally found in veins, and frequently as disseminations in the groundmass or alteration haloes of veins. At shallow depths, bornite, chalcocite and covellite occur as rims around chalcopyrite grains, as a result of supergene processes and/or alteration related to late epithermal events. At greater depths, primary bornite occurs, and both chalcopyrite and primary bornite grains commonly present rims of chalcocite and covellite. The gold association varies with its location in the deposit. At shallow levels, in the phyllic and argillic zones, gold is mostly present as fine inclusions in pyrite, while at depth it is dominantly associated with copper sulphides (Blannin et al., 2019).
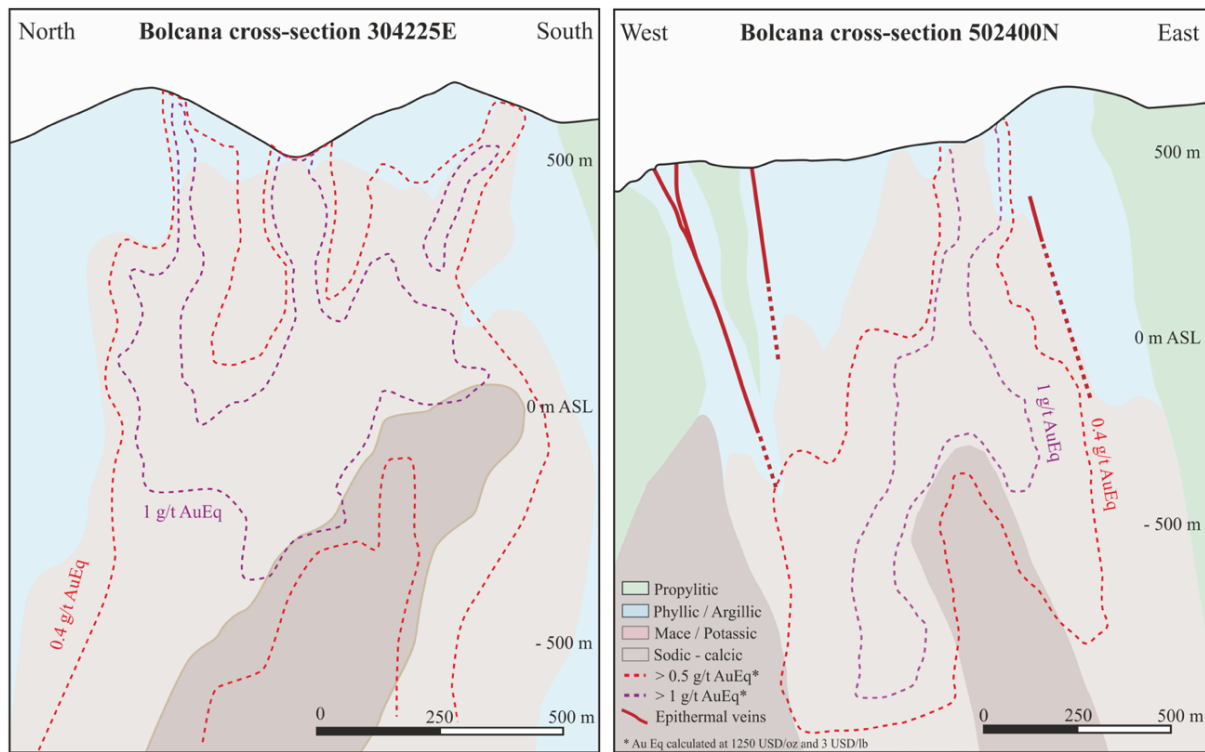
Figure 2-2. North-South and West-East simplified cross sections over the Bolcana system, illustrating the main mapped alteration assemblages and grade domains (Ivascanu et al., 2019).

2.1.3   *History of exploration*

Ore deposits of the Bolcana-Certej district have been exploited for gold since Austro-Hungarian times (Ghitulescu and Socolescu, 1941) and continued until 1990. Originally, the mining was focused on epithermal veins outcropping on the western flank of the system and only later transitioned to underground mining. The presence of the copper mineralization was only discovered late in the 19th century but mining was not attempted then. In more recent times, the main focus for industrial mining in the Bolcana-Certej district has been the Coranda-Hondol open pit where base metals and gold were mined between 1983 and 2006. The first exploration performed on the Bolcana system started in the mid 1980s, performed by the Romanian state as part of the program targeting porphyry-copper mineralisation in the South Apuseni Mountains (Bostinescu, 1984). The main target commodity being copper, the samples were never assayed for gold until the exploration licence was taken over by European Goldfields in 2002 when near-surface drilling was conducted. In 2006, Minvest SA conducted a concentration experiment of the ore by mining the top part of the system and subjecting it to flotation. The preliminary results not being promising and the time of the experiment coinciding with the closing of all mines that depended on state subsidies, no further work was performed in Bolcana until 2016 (Ivascanu et al., 2019). In 2016, Eldorado Gold acquired the license and conducted extensive near-surface exploration which has revealed a 1x2 km phyllic alteration footprint with distal stockwork veins. The drilling campaign conducted between 2017 and 2018 defined a mineralized system of 1200 m and 900 m lateral lengths and around 1200 m depth. This led to an inferred resource of 381mt at 0.53 g/t gold and 0.18 % copper, resulting in an inferred resource of 6.5 Moz gold and 686 000 tons of copper (Ivascanu et al., 2019).

2.1.4 *Project and sampling strategy*

Following the start of exploration drilling in 2017, in the context of the current study, a total of 188 drill-core samples from three boreholes were collected during two sampling campaigns. These samples were selected to ensure the representation of the main alteration and mineralization styles encountered in the Bolcana deposit as known from exploration drill core. The first borehole (BH1) from the early drilling campaigns crosses the mineralized system from ENE to WSW, with a length of around 2 km and vertical extent of 1.5 km. From this borehole, 43 samples were selected based on visual analysis and they were considered representative of the mineralization and alteration styles identified in the system until that point. Further drilling and investigation have led to the delineation of the mineralized body, identifying an additional prospective porphyry body near the surface. Two boreholes crossing this area of the system and capturing varying mineralization stages continued to be studied for a better mineralogical understanding and economic potential. In the second sampling campaign 83 samples were collected from BH2 and 62 samples from BH3. These samples were transferred to Freiberg for further studies.

2.2 Hyperspectral imaging in the minerals industry

This section provides an introduction into the reflectance spectroscopy of minerals, including the main trends particularly focused on drill-core scanning, a description of the main principles and processes causing absorption features diagnostic of minerals and mineral groups, followed by an overview of the motivation of the use of reflectance spectroscopy in mineral exploration and mining.

2.2.1 Reflectance spectroscopy – principles

Reflectance spectroscopy is the study of light as a function of the reflected wavelength from a solid, liquid or gas (Clark, 1999). In the case of minerals, as photons enter a mineral grain, some are reflected, some pass through the mineral grain while others are absorbed. The photons that are reflected from the surface of the mineral sample and those which are refracted through the mineral grain are referred to as scattered (Clark, 1999). The photons can be absorbed in mineral samples by several processes and the specific wavelengths at which photons are absorbed by a mineral can be used as a proxy for its presence and composition (Laukamp et al., 2021). For the specific case of reflectance spectroscopy applied to minerals there is a small range of the electromagnetic spectrum that is being used, characterized by the highest atmospheric transmittance of light (Figure 2-3) (Clark, 1999). These regions range from visible to near infrared (VNIR = 380-1300 nm), short-wave infrared (SWIR = 1300–2600 nm), mid-wave infrared (MWIR = 2600–5500 nm) and long-wave infrared (LWIR = 5500–15000 nm). In these regions of the electromagnetic spectrum, minerals produce diagnostic features. The obtained reflectance spectra from geological materials contain the spectral signature of their constituting minerals, signatures which can be used for identification of mineral species, their relative abundance. In some cases, additional information can be retrieved on chemistry and crystallinity of the minerals in question (Laukamp et al., 2021).
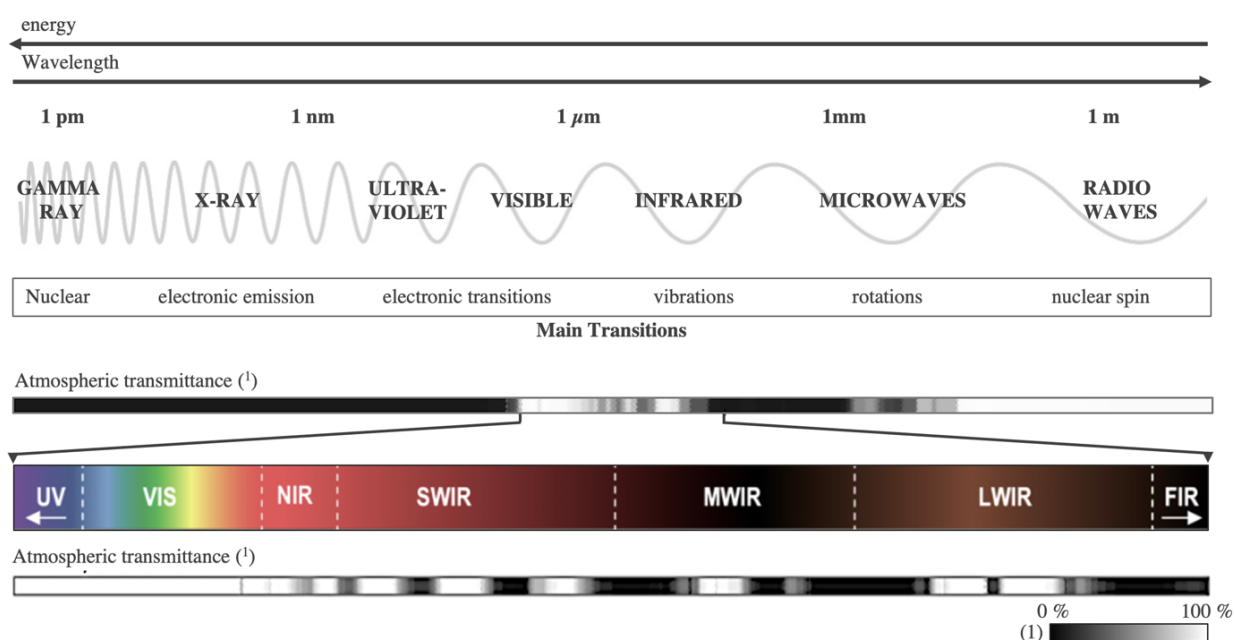
Figure 2-3 The ranges of the electromagnetic spectrum with highlighted areas of highest atmospheric transmittance where reflectance spectroscopy is most commonly used (Modified after Lorenz, 2019).

2.2.2 *Reflectance spectroscopy of minerals*

In the current study, the focus will be assigned to the VNIR-SWIR range of the electromagnetic spectrum and more specifically to the 380-2500 nm range used by most commercially available VNIR-SWIR spectrometers. The absorption of photons in minerals is caused by several processes. The main processes encountered in the visible to near-infrared (VNIR) relate to electronic processes. The lower wavelengths of the SWIR (1300-1850 nm) are dominated by the first overtones of the OH-stretching related fundamental vibrations (Laukamp et al., 2021). In the higher wavelength range of the SWIR the absorption features are dominated by the OH combination bands of fundamental stretching and bending vibrations as well as other overtones such as those related to the CO_3 group (Clark, 1999; Hunt, 1977). In the MWIR, the main spectral signatures are caused by OH-related fundamentals and overtones. Overtones and combinations of many fundamental vibrational modes of C-O, B-O, S-O, P-O and Si-O are characteristic for the LWIR (Laukamp et al., 2021).

In the VNIR, absorption features in minerals most commonly result from the **crystal field effects.** These are encountered in the case of transition elements such as Ni, Cr, Co or Fe. This effect occurs when an atom is located in a crystal field, leading to the splitting of the d orbital energy states. As a result, an electron can be moved from a lower to a higher level through the absorption of a photon having a matching energy to the difference between the states. The energy levels are given by the atom valence state, the coordination number as well as by the symmetry of the site it occupies within the mineral. As the crystal field effects are controlled by the crystal structure of the mineral, the same ion can produce different absorption features. A common case where this effect is observed is that of Fe^{2+} (Hunt, 1977). Fe^{2+} presents a different spectral response depending on the host mineral, such as amphibole or chlorite (Figure 2-4). **Charge transfer** is another electronic process causing absorption features in the VNIR. In this case, the absorption of a photon causes the electron to move between ions or ions and ligands. The transition between different valence states of the same metal is also common, particularly in the case of iron. Charge-transfer related absorption is the main cause of the red colour of iron oxides and hydroxides (Clark, 1999). Some minerals present band gaps, caused by the difference between two energy levels, a higher one, called the **conduction band** and the lower called the valence band. In the conduction band the electrons are moving freely throughout the lattice while in the valence band they are attached to individual atoms. This band gap can cause the specific colour of minerals such as native sulphur and show distinct features in the visible region of the electromagnetic spectrum. Another cause for colour in minerals can be the absorption of **colour centres** caused by the irradiation of an imperfect crystal. The defects in the crystal lattice tend to produce energy levels and therefore electrons can be bound to them (Clark et al., 2006; Hunt, 1977).

In the SWIR, the main mineral absorption features are caused by **vibrational processes**. Within the bonds of a molecule, the frequency of vibration depends on the strength of each bond in a molecule and elemental masses of the atoms in the respective molecule. The normal modes of vibration are called fundamentals and overtones occurring at roughly multiples of the fundamental frequency. Absorption features caused by vibrational processes only occur in the infrared spectrum if the respective molecule shows a dipole

moment – called infrared-active (Hollas, 2004). The wavelength at which absorption features occur depends on the energy that is associated with the change in dipole moment. Minerals for which vibrating molecule bonds do not change the dipole moment will not absorb electromagnetic radiation (Clark, 1999; Clark et al., 2006).

The lower wavelengths of the SWIR range (1300-1950nm) are dominated by the first overtones of fundamental stretching vibrations of the hydroxyl groups. The OH-related absorption features in this range are characteristic for hydroxylated mineral groups, such as hydroxylated silicates and sulphates. The location and intensity of these features are controlled by the type of cation bonded to the OH group. In this regard, Al and Mg sheet silicates present absorption at lower wavelengths compared to Fe silicates (The same observation can be made for hydroxylates sulphates. In this spectral range the composition of alunite can be evaluated based on the location of the 1470 nm feature. The lower wavelengths indicate a sodic composition while the longer wavelengths are characteristic of a potassic composition (Bishop and Murad, 2005). Additional mineral diagnostic features which can be identified in this range are overtones of H_2O-related bending vibrations, such as in the case of gypsum and montmorillonite (Figure 2-4), and combinations of NH_4-related fundamental stretching vibrations, such in the case of buddingtonite (Krohn and Altaner, 1987).

In the higher wavelength range of the SWIR (1950-2500 nm) the main mineral-related absorption features are caused by OH-related fundamental stretching and bending vibrations, combinations or overtones of CO_3-related fundamental stretching vibrations as well as overtones of NH_4-related fundamental vibrations located in the LWIR. The OH-related absorption features are controlled by the crystal structure and the cation the OH group is bonded to. Kaolinite group minerals such as kaolinite (Figure 2-4) show an absorption doublet, with the deepest feature located at 2209 nm caused by the stretching vibration of the inner OH group and a shallower feature at around 2160 nm caused by the stretching vibrations of the outer OH layer. The changes in this second absorption feature are sensitive to the changes in the crystal structure and crystallinity of the kandite-group minerals (Laukamp et al., 2021; Murray and Lyons, 1955).

White micas, exemplified by muscovite in Figure 2-4, present the main diagnostic absorption feature around 2200 nm, given by the Al-OH bond. The location of this feature is sensitive to the replacement of Al in octahedral configuration by Fe^{2+} or Mg, and the resulting replacement of Al by Si in tetrahedral configuration to compensate for the charge. The replacement of the OH group by F for some micas such as lepidolite also leads to the decrease and shift of the 2200 nm feature to longer wavelengths. Additionally, the increase in Fe2+ and Mg leads to more prominent features around 2350 and 2450 nm for micas which are absent in the case of smectites such as montmorillonite. Similar to white micas, smectites show a shift in the location of the Al-OH absorption features, from 2183 nm for beidellite (Al-rich) to 2215 nm for montmorillonite (Post and Noble, 1993; Scott and Yang, 1997; Yang et al., 2011).

Biotites and chlorites present diagnostic absorption features around 2250 nm caused by the OH groups bound to the octahedral layers (Figure 2-4). The Mg:Fe ratio in this layer influences the location of the position of this absorption feature. High molar Mg# leads to minima of the absorption at lower wavelengths (Lypaczewski and Rivard, 2018). Both minerals present a second absorption feature around 2350 nm, variations in composition leading to the change in the location of the minima between 2330 nm and 2390 nm.

As this absorption presents overlaps with those of other SWIR diagnostic minerals such as amphiboles or carbonates, the interpretation of chlorite or biotite composition, unless dealing with pure samples is not recommended (Laukamp et al., 2021). In the case of amphiboles, the absorption feature around 2320 nm is assigned to combinations of overtones OH stretching fundamentals related to Fe^{2+} and Mg bonds in the MWIR. The second diagnostic absorption feature around 2380 nm is believed to be related to the OH stretching fundamentals. Actinolite is used as an example in Figure 2-4. Epidote presents similar absorption features to those of chlorites and biotites in the SWIR. However, a deeper feature at 2250 nm can be observed and sometimes a shift to higher wavelengths as a result of Fe3+ and Al bonded to the OH group. In chlorites and biotites, Mg and Fe2+ are usually the main cations bonded to OH (Laukamp et al., 2021).
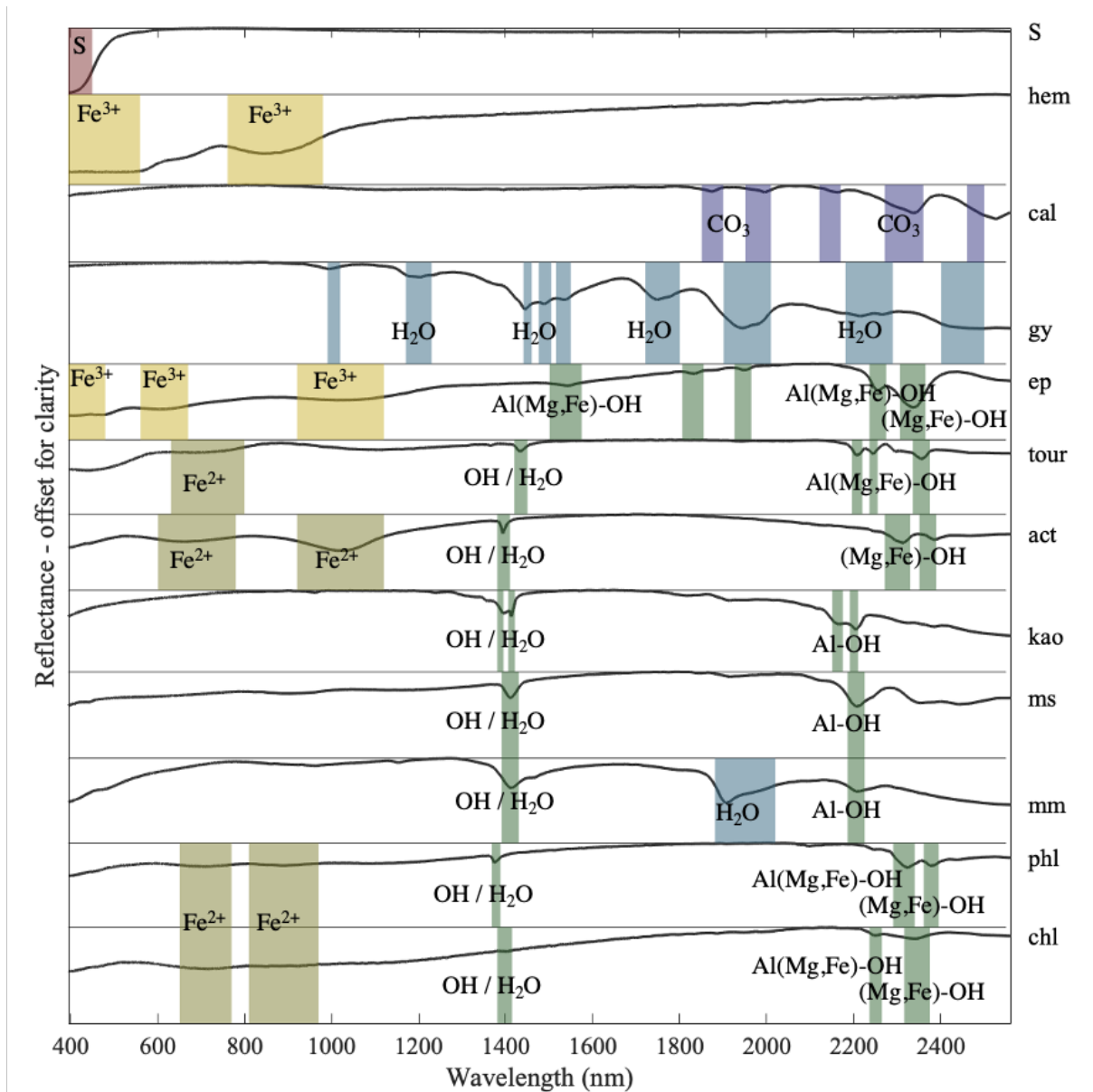
Figure 2-4 Examples of common minerals having diagnostic absorption features in the VNIR and SWIR regions of the electromagnetic spectrum (S = sulphur, hem = hematite, cal = calcite, gy = gypsum, ep = epidote, tour = tourmaline, act = actinolite, kao = kaolinite, ms = muscovite, mm = montmorillonite, phl = phlogopite, chl = chlorite). Compiled based on Clark, 1999; Hunt, 1977; Laukamp et al., 2021, spectra from the USGS spectral library (Kokaly et al., 2017).

Tourmaline presents diagnostic absorption features in the higher wavelength of the SWIR at 2174, 2204, 2256, 2302 and 2290 nm (Laukamp et al., 2021). The origin of these features is assigned by many authors to overtones of OH group fundamental stretching and bending combinations. The subject is however still controversial, other authors suggesting that some of the features can be assigned to the B-O bond (Bierwirth, 2008; Clark, 1999; Hunt, 1977).

Besides hydroxylated silicates, also carbonates and hydroxyl-bearing sulphates present absorption features in the higher wavelength range of the SWIR. Carbonates have a diagnostic absorption feature in the 2300-2340 nm range as a result of C-O stretching vibrations. Calcite is used as an example in Figure 2-4 (Laukamp et al., 2021).

2.2.3 *Hyperspectral imaging and ore deposits*

Hyperspectral analyses have become increasingly attractive tools within the exploration industry in the last decades (Laukamp et al., 2021; van der Meer et al., 2012). Mapping of alteration patterns used as proxies for mineralization in early exploration stages remains the main driver for the use of hyperspectral imaging in exploration, particularly for the use of VNIR-SWIR sensors. These sensors allow for the mapping of key minerals and assemblages for exploration of various deposit types. Figure 2-5 showcases examples of deposit types and the key spectrally diagnostic minerals for the exploration and characterisation of each of these deposits. The figure illustrates that specific mineral assemblages serve as a proxy for the location within an epithermal or hydrothermal system.

In the case of epithermal deposits, alteration minerals used as proxies for their discovery and characterisation are clays of the kaolinite group for the advanced argillic, transitioning towards a kaolinite-smectite assemblage in the argillic and intermediate argillic zones. White micas, such as muscovite and illite are key components of the phyllic alteration assemblage. The clay crystallinity can be used as an indicator for the forming process of the minerals as well as a proxy towards mineralization. It is defined as the degree of hydration based on the ratio of the water feature around 1900 nm and the Al-OH feature located around 2200 nm. The same applies to the composition of these micas, evaluated based on the shift in the location of the minimum of the Al-OH feature located around 2184 nm for paragonitic compositions to 2228 for phengitic compositions. Chlorite can also serve as a proxy for mineralization in several systems, either based on its presence in the phyllic and propylitic alteration zones or based on its composition. The Mg:Fe ratio can be calculated based on the shift of the Al(Mg,Fe)-OH absorption feature around 2250 nm. Lower wavelengths indicate a magnesian composition while higher wavelengths an increase in iron content. These changes in chlorite composition are related to formation temperature and can be used as proxies for mineralization in skarn (Markowski et al., 2006) and VMS deposits (Gisbert et al., 2021).

With regards to porphyry systems, used as a case study in this work (Section 1.2), a characteristic alteration-mineralization zoning pattern is exhibited. From the centre of the system and upwards, alteration comprises sodic-calcic, potassic, chlorite-sericite, phyllic and argillic domains. Distal alteration consists of propylitic and sometimes shallow chloritic alteration (Lowell and Guilbert, 1970; Sillitoe, 2010).
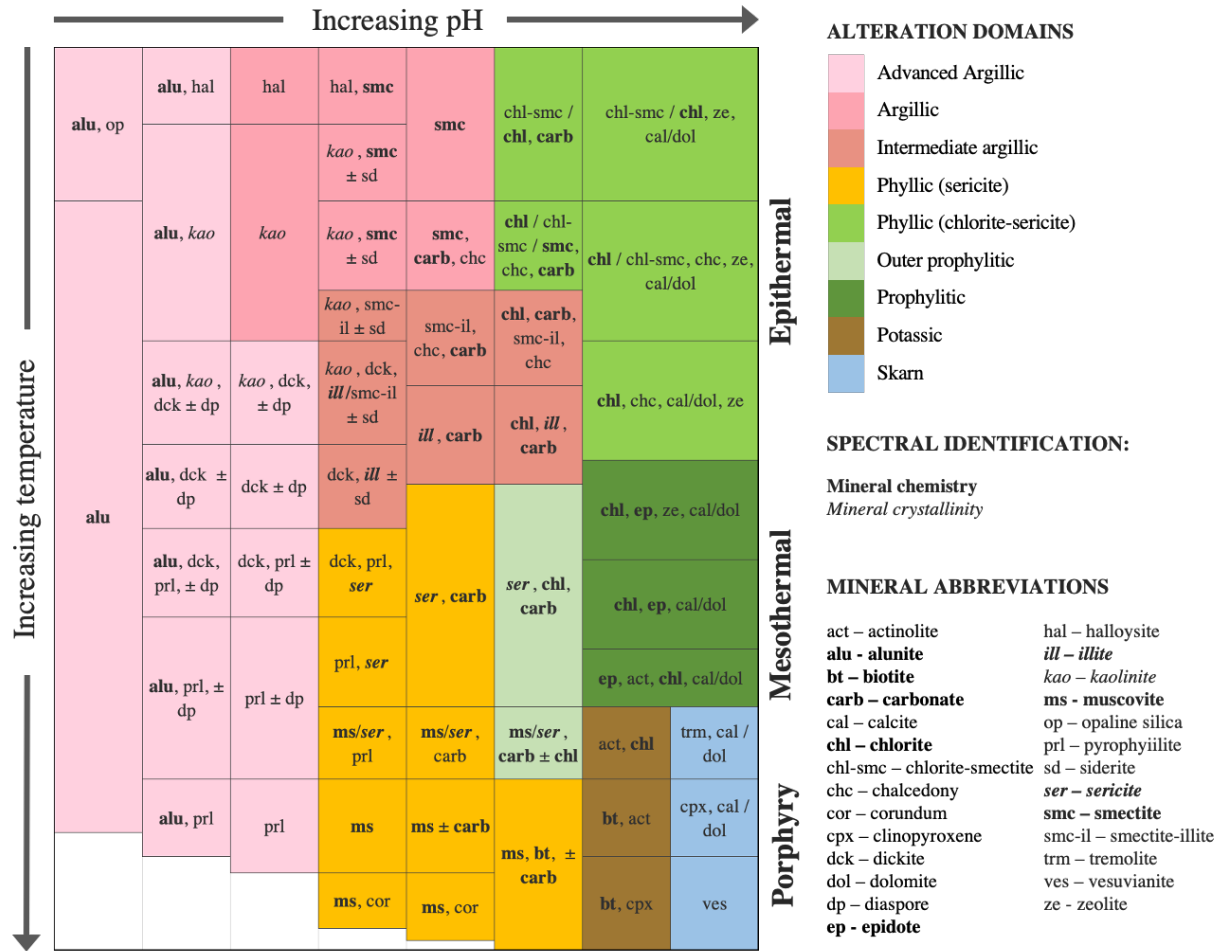
Figure 2-5. Common SWIR diagnostic alteration mineralogy in hydrothermal systems (modified after (Corbett and Leach, 1998)*. For minerals in bold the mineral chemistry can be identified through spectral analysis, while for minerals in italic their crystallinity can be estimated.*

2.2.4 *Towards hyperspectral drill-core scanning in the mining industry*

In the context of mineral exploration, several well-established platforms for hyperspectral data acquisition are currently available for use. Within regional exploration satellite or airborne hyperspectral imaging for mapping alteration minerals has become increasingly used since the launch of the Advanced Spaceborne Thermal Emission and Reflectance Radiometer (ASTER) and, more recently, higher resolution sensors such as Worldview and Hyperion (Booysen et al., 2020). Such spectral information has been used for mapping alteration patterns characteristic of various mineral deposits such as epithermal gold or porphyry-copper (Crósta et al., 2003; Di Tommaso and Rubinstein, 2007; Pour and Hashim, 2011) or for lithological mapping (Mars and Rowan, 2011).

In the context of advanced exploration projects, with drill-core intersections providing a first three-dimensional access to the orebody explored, higher spatial and spectral resolution are possible and are required for ore characterisation. The increased spatial resolution allows for distinguishing more subtle mixtures while the increased spectral resolution for the differentiation of fine variations in mineral composition. Point

spectrometers such PIMA-II were the first to provide high spectral information on geological materials. These spectrometers are used for either point measurements on field samples (Herrmann et al., 2001), cores or on crushed core pulps over meter intervals (Yang et al., 2000). Whilst both of these approaches provide mineralogical information, they are unsuitable to obtain spatial and textural information needed for geometallurgical modelling. Kruse (1996) was the first to identify and tackle this limitation. He used a PIMA II spectrometer for spectral sampling in a grid to create a dataset similar to an HS datacube. Since then, the use of spatial hyperspectral sensors for drill-core analysis became increasingly attractive with new systems being developed. The most widely used spectral point sampling systems are geoLOGr and the HyLogger (Mason, 2012; Schodlok et al., 2016), which integrate a point spectrum over several measurements and can cover VNIR, SWIR and LWIR. It is widely used for drill-core logging in mineral exploration (Arne et al., 2016; Ayling et al., 2016; Gordon et al., 2016; Tappert et al., 2011). Further need for increased speed, spatial resolution and coverage extent have led to the development of so-called push broom sensors (Lorenz, 2019). To achieve a high spectral quality at a sufficient throughput, the spatial resolution is relatively low (around 1–2 mm). Examples for such cameras are the Specim AisaFENIX (VNIR-SWIR) and AisaOWL (LWIR). The acquisition and processing of the data is often provided by external companies specialized in HS drill-core scanning (e.g., TerraCore Geospectral Imaging, Corescan Pty Ltd), therefore not all technical developments in hyperspectral data processing are published (Lorenz, 2019).

2.2.5 *Application of hyperspectral imaging – tools and workflows*

For exploration purposes, traditional hyperspectral mapping methods include band ratios, or mapping of wavelength parameters such as position, depth and width of the absorption features. These tools provide good results for exploration targeting when the composition of the mineralogical proxies for mineralisation are known. In such cases, band ratios and wavelength parameters are used to map the distribution and relative abundance of specific minerals (Asadzadeh and De Souza Filho, 2016; Kopăcková and Koucká, 2017; Laukamp et al., 2021; Mathieu et al., 2017; Roache et al., 2011; Tappert et al., 2011; Turner et al., 2014; Van Ruitenbeek et al., 2014). In order to investigate the variation in mineralogy and extract distinct endmembers from a dataset, one of the most common procedures makes use of some of available tools in the Environment for Visualizing Images software (ENVI, Exelis Visual Information Solutions, Boulder, Colorado). Such tools comprise endmember extraction (Farooq and Qurat-ul-ain, 2012), identification of the minerals using the Spectral Analysis or Material Identification by comparison to a specific library in the software (e.g., in ENVI) or online reference (e.g., USGS - Kokaly et al., 2017), and finally the mineral mapping task using similarity measure algorithms or determination of partial abundances using unmixing algorithms (Calvin and Pace, 2016; Kratt et al., 2010; Littlefield et al., 2012). These methods have, however, been difficult to automate on large datasets in order to provide real-time results. Further advances in mineral mapping using supervised machine learning algorithms have shown great improvements in the automation of the mapping process. An example is the contribution of Contreras et al. (2019) proposing the fusion of hyperspectral and high-resolution mineralogical data for accurate mineral identification.

In the context of mining and mineral beneficiation, hyperspectral sensors have not been widely used due to the lack of diagnostic absorption features of the ore minerals in the spectral ranges of most commercially available sensors. Successful use of SWIR sensors for pre-sorting of ores has been achieved mostly on industrial minerals because they are spectrally active in the SWIR (Robben and Wotruba, 2019). There are underlying cogenetic relationships in most metalliferous ores between alteration (i.e. gangue) and ore minerals (Kern et al., 2018a). These relationships are widely applied within the context of mineral exploration. Such intimate cogenetic relations may, however, also be exploited during eventual mining through the evaluation of the preferential association of ore and gangue minerals using statistical methods - as shown in some previous studies (Dalm et al., 2018, 2014; Kern et al., 2019). Additionally, Johnson et al. (2019) were among the first to present the use of HSI of blast hole cuttings to predict metal recovery and throughput in a processing plant. These previous studies also illustrate that the relationship between ore mineralogy and grade, and spectral response of alteration minerals is not always linear or simple. While for some ores a specific gangue mineral can be used to predict the grade, for some others a combination of minerals and even variation in their composition would be needed. Further method developments to identify all these features are needed.

While hyperspectral data has been increasingly used in the last decade for exploration targeting, and less for ore characterization and pre-concentration, little has been done to for the development of a geometallurgical model already during the exploration stage. Studies were conducted in the use of either hyperspectral drill-core scanning system on blast hole chips (Johnson et al., 2019) or mounted on tripods for the scanning of mine faces (Barton et al., 2021), however, these approaches are implemented once mining has already started. Integrating the information from spectral analysis gained during the exploration stage into the definition of geometallurgical domains is an obvious opportunity. Such an integrated approach can lead to a better understanding of the ore types and thus allow for improved decision making on material handling, processing routes and waste disposal.

Chapter 3 Assessment of alteration mineralogy and vein types using hyperspectral data

Preface

The mapping of alteration assemblages, both pervasive and related to veins are key in the understanding the architecture of mineral deposits. Hyperspectral drill-core scanning has the potential to be an excellent tool for providing this type of information in a fast, non-destructive and reproducible manner. However, there is a distinct lack of data processing tools for the automated discrimination of vein-related and pervasive alteration. For this purpose, a methodology was set in place combining algorithms previously applied in different fields of hyperspectral image processing. The developed methodology allows for endmember extraction and unmixing and further subjecting the mineral abundance maps obtained from the unmixing process to morphological analyses leading to vein extraction. This approach therefore allows for:

(1) Identifying the main alteration minerals in the core and mapping their abundance

(2) Discriminating mineral abundances related to both veins and pervasive alteration

(3) Estimation of vein abundance and orientation (azimuth).

The early-stage results of this research were presented at the *2018, IEEE International Geoscience and Remote Sensing Symposium (IGARSS) [1]* in Valencia. Later, the full paper presented in this thesis was published in the *MDPI Minerals [2]* journal in 2019 under the title "Mineral Mapping and Vein Detection in Hyperspectral Drill-Core Scans: Application to Porphyry-Type Mineralization". This contribution was later awarded the MDPI Minerals best paper award in 2020. This achievement highlighted the need for automated methods for hyperspectrald data analysis in the field of mineral exploration and mining, motivating further developments such as those presented in the later chapters.

Authors and contributions

Laura Tusa [1], Louis Andreani [1], Mahdi Khodadadzadeh [1], Cecilia Contreras [1], Paul Ivascanu [2], Richard Gloaguen [1] and Jens Gutzmer [1]

[1] *Helmholtz-Zentrum Dresden-Rossendorf, Helmholtz Institute Freiberg for Resource Technology*

[2] *Eldorado Gold Corporation*

Conceptualization, L.T., L.A., R.G. and J.G.; *methodology*, L.T. and L.A.; *software*, L.T., L.A., M.K. and C.C.; *validation*, L.T. and R.G.; *formal analysis*, L.T., L.A., M.K. and C.C.; *investigation*, L.T. and L.A.; *resources*, P.I.; *data curation*, L.T. and L.A.; *writing—original draft preparation*, L.T. and L.A.; *writing—review and editing*, all authors.; *visualization*, L.T. and L.A.; *supervision*, R.G. and J.G.; *project administration*, L.T., L.A., R.G. and J.G.

[1] Tusa, L.; Andreani, L.; Pohl, E.; Contreras, I. C.; Khodadadzadeh, M.; Gloaguen, R.; Gutzmer, J., 2018, Extraction of structural and mineralogical features from hyperspectral drill-core scans, IGARSS 2018 - 2018 IEEE International Geoscience and Remote Sensing Symposium, 23.-27.07.2018, Valencia, Spain

[2] Tusa, L., Andreani, L., Khodadadzadeh, M., Contreras, C., Ivascanu, P., Gloaguen, R., Gutzmer, J., 2019. Mineral Mapping and Vein Detection in Hyperspectral Drill-Core Scans: Application to Porphyry-Type Mineralization. Minerals 9, 122. https://doi.org/10.3390/min9020122

Abstract

The rapid mapping and characterization of specific porphyry vein types in geological samples represent a challenge for the mineral exploration and mining industry. In this paper, a methodology to integrate mineralogical and structural data extracted from hyperspectral drill-core scans is proposed. The workflow allows for the identification of vein types based on minerals having significant absorption features in the short-wave infrared. The method not only targets alteration halos of known compositions but also allows for the identification of any vein-like structure. The results consist of vein distribution maps, quantified vein abundances, and their azimuths. Three drill-cores from the Bolcana porphyry system hosting veins of variable density, composition, orientation, and thickness are analysed for this purpose. The results are validated using high-resolution scanning electron microscopy-based mineral mapping techniques. We demonstrate that the use of hyperspectral scanning allows for faster, non-invasive and more efficient drill-core mapping, providing a useful tool for complementing core-logging performed by on-site geologists.

Graphical abstract
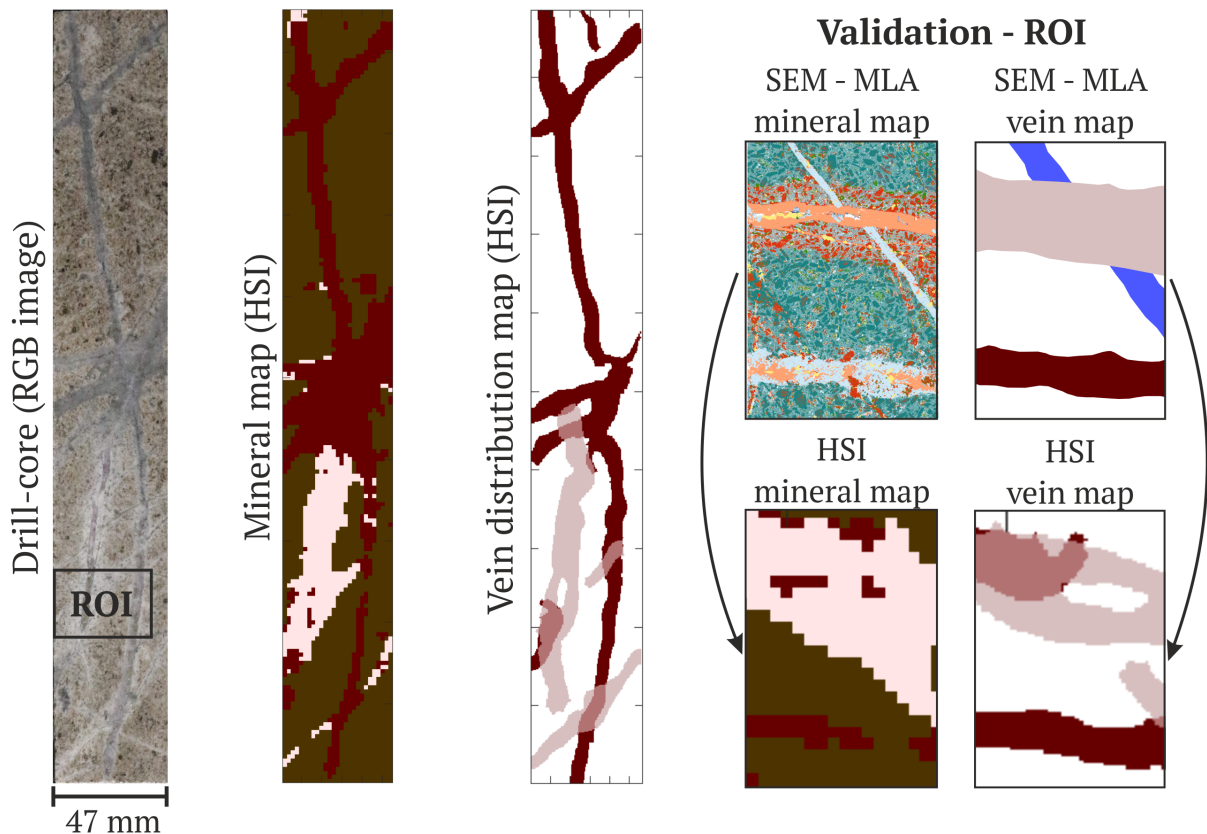
Keywords: hyperspectral imaging; drill-core; mineral mapping; short-wave infrared; porphyry-type veins

3.1 Introduction

With global demand for raw materials steadily increasing, large exploration investments are required to discover the ore deposits needed to satisfy the demand. Exploration includes thousands of kilometres of diamond drill-cores that are obtained to test subsurface regions with high mineral resource potential. The

drilling consists of the extraction of cylindrical core samples, which are traditionally analysed visually by on-site geologists and subjected to geochemical analyses (Kruse, 1996; D. Wang et al., 2017). These methods are slow, and the mineralogical information extracted from the cores is limited and usually influenced by the subjectivity of the observer. During the last decade, hyperspectral imaging techniques have been increasingly used to complement traditional logging methods and provide fast, efficient, and unbiased means of extracting valuable compositional information (Clark et al., 2006; Kruse et al., 2010, 2012; Tappert et al., 2011). However, most existing hyperspectral data processing tools only target the compositional mineralogical information and not the spatial distribution and geometry of minerals comprising the ore. For this purpose, a workflow integrating the analysis of mineral abundance with mineral spatial distribution is proposed in this paper.

Common hyperspectral sensors cover the visible to near-infrared (VNIR) and short-wave infrared (SWIR) regions of the electromagnetic spectrum. In these ranges, specific absorption features allow the identification of common mineral groups such as phyllosilicates, amphiboles, iron oxides and hydroxides, carbonates and hydrated sulphates, phosphates and arsenates (Pontual et al., 1997). Several of these mineral groups are associated with hydrothermal alteration and are known to occur in different mineral systems (Schwartz, 1959). They are commonly used as proxies for mineralization vectoring (Pour and Hashim, 2011; Roache et al., 2011; Wilkinson et al., 2015) making their identification key to the discovery and mapping of mineral exploration targets.

Several techniques have been proposed in the literature for the analysis of hyperspectral drill-core data and mineral mapping (Asadzadeh and De Souza Filho, 2016; Huntington et al., 2006; Kruse, 1996; Kruse et al., 2012; Mathieu et al., 2017; Mauger et al., 2007; Tappert et al., 2011; Taylor, 2000). Among these, band ratios and minimum wavelength maps are useful tools for the evaluation and visualisation of the relative abundance of chemical groups characteristic for specific minerals (Asadzadeh and De Souza Filho, 2016; Kopăcková and Koucká, 2017; Simpson, 2015; Turner et al., 2014; Van Ruitenbeek et al., 2014). Another approach for mineral mapping consists of the use of the spectral angle mapper (SAM), a classifier which works based on the similarity measure between an unknown spectrum and reference spectra. The reference spectra are acquired from either spectral libraries or from endmembers, for instance, obtained by the pixel purity index method followed by the n-Dimensional visualiser (Farooq and Qurat-ul-ain, 2012). This approach is widely used due to the availability of the algorithms in common software such as ENVI (Exelis Visual Information Solutions, Boulder, CO, USA). Although the aforementioned mineral mapping tools can provide good results, batch implementation is difficult, as it requires extensive human interaction.

While progress has been made on (semi-)automated mineral mapping, few studies have addressed the identification and extraction of structural features. Yet, this kind of analysis is particularly relevant for vein-type mineralization such as encountered in porphyry style deposits (Lowell and Guilbert, 1970; Sillitoe, 2010). The characterization of alteration halos, both in terms of width and composition, is critical for assessing the mineralization/alteration stage. The composition of the pervasive alteration and the vein halos also represents an indicator on the location of the sample within the mineralized system as well as on the expected vein composition in terms of ore mineralogy. Wang et al., (2016) used a seeded region growing method combining

a similarity and homogeneity analysis of optical data (unmixing of short-wave infrared spectra and RGB 3-band natural-colour imagery) with an edge map to extract quartz and carbonate veins. The results cover the extraction of predefined vein types and do not include their orientation, which for the mapping and modelling of a porphyry-style mineral system would be a key attribute.

In the last two decades, a broad variety of methods has been proposed to extract linear features from images. The most commonly used approaches are based on edge detection algorithms, which identify discontinuities in greyscale images (e.g., Papari and Petkov, 2011, and references therein). These methods have been widely used in Earth sciences to extract structural features such as faults scarps and lineaments, but are often difficult to apply to the extraction of structural entities such as veins. Edge detection methods perform poorly when the edges of the object are smooth (i.e., gradual transitions from vein alteration halo to matrix) and are very susceptible to noise. An alternative approach relies on ridge detection algorithms (e.g., Kirbas and Quek, 2004, and references therein). While the purpose of edge detectors is to extract the boundary of an object, ridge detection makes it possible to identify the major axis of symmetry of an elongated object using the curvature associated with the brighter or darker components in a greyscale image. These algorithms make it possible to specifically target the linear components of an image and have been broadly used in various fields such as medical sciences and geographic information sciences to extract curvilinear features such as blood vessels (Frangi et al., 1998; Jin et al., 2013)and road or drainage networks (Steger, 1998).

In this paper, a workflow that enables extraction of both the mineralogical and structural information from drill-core samples is developed and tested. The approach combines hyperspectral data analysis and image processing techniques. The workflow consists of three main steps: (1) endmember extraction and spectral unmixing, followed by (2) mineral mapping, and (3) vein extraction. The results provide mineral maps illustrating the distribution of the main mineral assemblages and vein distribution maps including the composition, calculated abundance and azimuth of different vein-types. This type of information can become a valuable tool for exploration. For vein-hosted mineralization, the identification of the vein composition and density and the assessment of the abundance of different vein types can represent key parameters to be used in ore body modelling and evaluation.

The workflow performance is assessed based on three selected samples from the Bolcana porphyry-copper gold project in Romania. The samples were collected from typical alteration zones at different depths in order to showcase different vein compositions and structures. The validation is achieved based on high resolution mineralogical analyses of thin sections using a Scanning Electron Microscopy (SEM) equipped with the Mineral Liberation Analyser (MLA) software (Gu, 2003).

3.2 Test Site

The Bolcana copper-gold mineralized system is located in the Brad-Sacaramb metallogenic district within the Golden Quadrilateral in South Apuseni Mountains, Romania (Figure 3-1). The Golden Quadrilateral hosts around 20 porphyry-type deposits and represents Europe's largest epithermal Au-Ag-Te province. The region is also one of Europe's most important porphyry Cu–Au provinces (Berbeleac et al., 2014; Cioacă et al., 2014; Milu et al., 2003). The mineralization in the Golden Quadrilateral is conditioned by the emplacement of Neogene volcanic rocks, mainly between 14.9 and 9 Ma (Cioacă et al., 2014; Neubauer et al., 2005; Pécskay

et al., 2006; Roșu et al., 2004, 1997). The main direction of the distribution of the ore deposits follows an ESE-trending, dextral, strike-slip fault system (Neubauer et al., 2005). Here, the basement consists of Middle Jurassic–Lower Cretaceous basaltic andesites, basaltic lava flows and pyroclastics, and Lower Cretaceous rhyolite overlain by Paleocene and Miocene sedimentary series. Neogene volcanic and subvolcanic bodies are intruding the basement and Paleocene sedimentary units.

Bolcana is a porphyry-type Cu–Au ore deposit with associated epithermal veins hosted by the Bolcana microdioritic subvolcanic body. The mineralization is represented by chalcopyrite, bornite, chalcocite, covellite, pyrite, magnetite, hematite, molybdenite. The gold is predominantly present as fine inclusions in the copper sulphides. The mineralized body shows a large extension at depth being characterized by a large potassic core with a wide transition to sodic-calcic alteration. The transition is characterized by the presence of chlorite as the main pervasive alteration phase (Blannin et al., 2019).
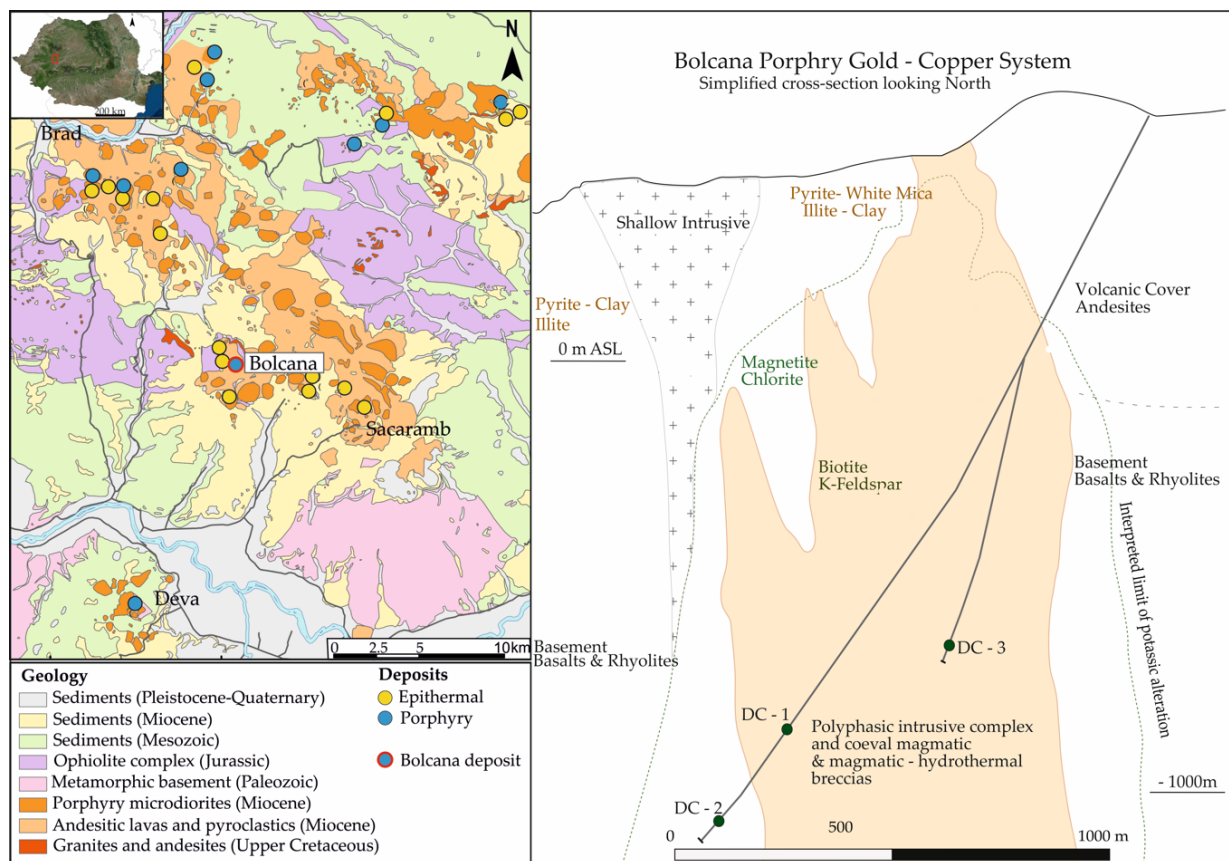
Figure 3-1. Geological map of the Brad-Sacaramb metallogenic district (left) and E–W cross section through the Bolcana porphyry system with shown location of the sampled drill-holes (right).

3.3   Data Acquisition

Three drill-core samples (here labelled DC-1, DC-2 and DC-3), which show variability in terms of pervasive alteration and vein types, were selected for testing of the proposed workflow. The drill-core samples were collected from the potassic, sodic-calcic and intermediate zones of the Bolcana porphyry copper-gold prospect. The samples are representative in terms of vein and alteration styles for a larger drill-core interval (Figure 3-2). The three samples described in the current work consist of half cores. The analysed surfaces have 47 mm width for all samples and lengths around 290 mm. The drill-cores were selected from intervals of

uniform appearance based on visual observations by a specialist. The presence of different vein types in terms of composition and thickness was also considered in the sampling.
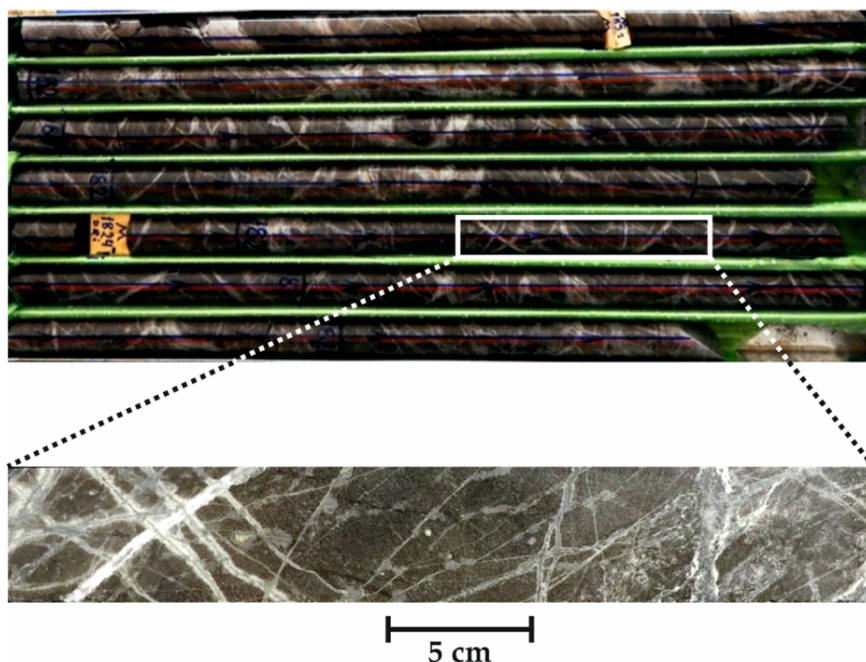
Figure 3-2. Representative sample selection from homogenous drill-core intervals.

3.3.1 *Hyperspectral Drill-Core Scanning*

The hyperspectral data was acquired using a SisuROCK drill-core scanner (Spectral Imaging Ltd., Oulu, Finland) equipped with an AisaFENIX VNIR-SWIR hyperspectral sensor (Spectral Imaging Ltd., Oulu, Finland). The sensor specification and chosen settings are listed in Table 3-1. The spatial resolution of the resulting hyperspectral scans is 1.5 mm/pixel.

Table 3-1. Specifications and setup parameters of the SisuROCK drill-core scanner and AisaFENIX VNIR-SWIR hyperspectral sensor.

Parameter	Value
Wavelength Range	VNIR 380–970 nm SWIR 970–2500 nm
Sampling Distance	VNIR 1.7 nm SWIR 5.7 nm
Number of Bands	450
Spectral Binning	VNIR 4 SWIR 1
Field of View (FOV)	32.3°
Samples	384
Frame Rate	15 Hz
Scanning Speed	25.06 mm/s
Integration Time	VNIR 15 ms SWIR 4 ms
Spatial Binning	VNIR 2 SWIR 1

The conversion to reflectance was performed with the acquisition software (LUMO Scanner version 2018-5, Spectral Imaging Ltd., Oulu, Finland) using PTFE reference panels (>99% VNIR and >95% SWIR).

For the pre-processing, the scans of the selected core samples were corrected and averaged using the MEPHySTo toolbox (Jakob et al., 2017). A correction was applied between the VNIR and SWIR sensors to compensate for the spatial shift and a geometric correction was used to neutralize the lens effect. The corrected hyperspectral data were smoothed using the Savitzky-Golay (SavGol) filter (Ruffin and King, 1999) in order to correct for the noise present particularly at the beginning of the spectrum in the VNIR. The smoothing was considered necessary, as noise in this region of the spectrum would otherwise strongly influence the performance of the endmember extraction algorithms. After testing different parameters, a radius of 5 and a 3rd degree polynomial were used for the SavGol filter.

3.3.2 SEM-MLA

Regions considered representative for the entire core samples were cut and prepared into 25 mm × 40 mm thin sections and further analysed with scanning electron microscopy. The sample preparation consisted of grinding and polishing of the sample surface. This leads to the removal of a small fraction of the material of a thickness up to 0.5 mm. The change in analysed surface causes a small shift in the location of the veins, but for the current purpose it is considered neglectable.

Quantitative mineralogical data were collected from each thin section using an automated approach (Fandrich et al., 2007; Gu, 2003). The analyses were performed using a Mineral Liberation Analyser (MLA) equipped with a FEI Quanta 650 F field emission SEM (FEI, Hillsboro, OR, USA) with two Bruker Quantax X-Flash 5030 energy-dispersive X-ray (EDX) detectors (Bruker, Billerica, MA, USA). Backscattered electron (BSE) images are used to define mineral grains. BSE images are greyscale images, in which the greyscale level ranges from 0–255 according to the average atomic number (AAN) of the elements comprising a mineral/phase. Lower AAN values correspond to darker grey appearance and indicate that minerals comprise of light elements (in this case, for example, quartz and silicates). Brighter grey shades, in contrast, reflect higher AAN values, and indicate minerals comprised of elements with high atomic weight (e.g., native gold). Mineral grains were discriminated based on their grayscale level in the BSE images and then identified by performing EDS X-ray measurements on a closely spaced grid. The operating conditions used for SEM and MLA are listed in Table 3-2.

Table 3-2. SEM-MLA data acquisition parameters.

SEM Settings		MLA Settings	
Acceleration voltage (kV)	25	Pixel size (µm)	3
Probe current (nA)	10	Resolution (pixels)	1000 × 1000
Spot size (µm)	5.6	Step size (pixels)	6 × 6
Frame width (pixels)	1500	Acquisition time (ms)	5
Brightness	96.2	BSE trigger	26–255
Contrast	18.5	Minimum particle size (pixels)	3
BSE calibration (Au)	254	Minimum grain size (pixels)	3

Data processing was carried out using the MLA Suite software package (version 3.1.4.686, FEI, Hillsboro, OR, USA) (MLA Image Processing, MLA Mineral Reference Editor and MLA Dataview). The mineral reference editor was used in online mode in order to complete the mineral list required for the classification of the tested samples. MLA Image Processing software was used for preliminary corrections of

data, such as frame edge removal, and for further processing steps. The first processing step consists of the spectral classification with a spectrum matching threshold of 90% and a low count threshold of 2000 counts. Two touch-up scripts were used in order to assign the glass spectrum from voids to the background and to assign minerals with a grain size lower than 4 μm to the host mineral.

3.4   Proposed methodology

The proposed methodology includes a parallel workflow consisting of mineral mapping on one side and extraction of linear features, here veins, on the other (Figure 3-3). Additional tools are used for endmember analysis, mineral chemistry and abundance mapping.
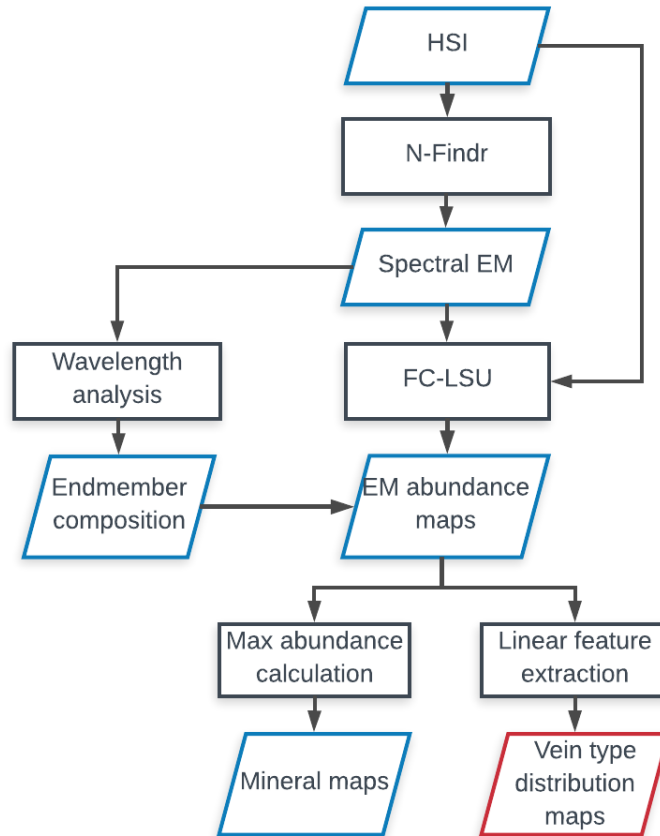
Figure 3-3 Schematic workflow of the proposed methodology (HSI = hyperspectral images, EM = endmembers, FC-LSU = fully constrained linear spectral unmixing).

3.4.1   Mineral Mapping

The first step of the proposed technique consists of endmember extraction. Several algorithms for endmember extraction were tested. Among all tested methods, the N-Findr algorithm proved to give the best results with the current dataset and is thus used in the current study. This method assumes that the N-volume contained by a simplex formed by the purest pixels in a dataset is larger than any other potential volume formed from other selected combinations (Plaza and Chang, 2005; Winter, 1999). Virtual dimensionality estimation techniques are known to be used for the estimation of the appropriate number of endmembers in hyperspectral data. An attempt to implement these techniques was made. However, results yielded a higher number of endmembers than minerals actually present according to the previous knowledge of the samples (petrographic

observations and validation data). The choice of three endmembers for each of the selected drill-cores proves to be appropriate considering the variability within the samples. The endmember spectra are then subjected to wavelength analyses in different ranges in order to identify the main occurring SWIR active minerals such as white mica, chlorite group minerals, gypsum, biotite, phlogopite, amphiboles and carbonates. SWIR inactive phases such as some rock-forming minerals (e.g., quartz, feldspars, pyroxenes) or sulphides cannot be identified with the spectral ranges used. For the purpose of defining veins with specific alteration halos, consisting dominantly of SWIR active minerals; however, the used sensors provide the necessary information. The selected minerals are identified based on the depth of their specific absorption features. The location of the minima in the selected spectral ranges indicates the presence or absence of a specific mineral as well as the relative chemical variation within specific mineral groups.

The obtained endmembers are used for unmixing to develop mineral abundance maps. The fully constrained linear spectral unmixing (FC-LSU) method is used for this purpose based on the consideration of a linear contribution of each mineral within the pixel. The method is based on the hypothesis that meaningful endmember fractions must respect two constraints: they must sum up to one and they must be nonnegative. The fractional contribution of each endmember is then calculated through an inversion of the linear model (Li and Chang, 2015; Silván-Cárdenas and Wang, 2010). Once the endmember abundance maps are obtained, each pixel is classified corresponding to the maximum abundance of the endmembers.

3.4.2 *Vein Extraction*

An approach based on Steger's detector of curvilinear structures (Steger, 1998) was developed. This method allows for the extraction of vein traces from mineral abundance maps together with their true shapes and extents (Figure 3-4).

The first step of the vein extraction process consists of the identification of the points of maximum curvature in an image. These correspond to the specific signature of a mineral or mineral association related to the vein composition or vein alteration halo. The analysis of the image curvature is based on the eigenvalues of the Hessian matrix (Frangi et al., 1998; Jin et al., 2013). The 2×2 Hessian matrix is composed of second-order partial derivatives of an input image. The second-order partial derivatives are defined as a convolution with derivatives of Gaussian filter at scale σ. The eigenvalue analysis allows for the extraction of the principal directions and the magnitude in which the local second order structure of the image can be decomposed. Each pixel is assigned a set of eigenvectors such as $|\lambda 1| \leq |\lambda 2|$. Linear features are characterised by a very small magnitude of $\lambda 1$ (ideally close to zero) and a large magnitude of $\lambda 2$. Point features will show similar magnitudes of $\lambda 1$ and $\lambda 2$ and features without preferential directions or random variation will have low magnitudes for both of the eigenvectors. The approach developed by Steger (Steger, 1998) is used, and this allows us to identify the points of maximum curvature within the image. These points are then connected into lines using a recursive approach. Each line is constructed by identifying the point with maximum second derivative and then by adding the appropriate neighbours to the current line. The choice regarding the appropriate neighbour is based on the distance as well as the angle difference between the points. The procedure is repeated until no more points with a curvature above a defined threshold are left. This threshold is introduced to avoid extracting "weak" features. Edges can be detected using the absolute gradient derived from the first-order partial derivatives. A Gaussian

filter is first applied in order to remove the noisy component of the image. However, the smallest possible scale ($\sigma = 3$) is used in order to obtain the most accurate localisation of the edge points. For each pair of points of an extracted line, the closest absolute gradient maxima along an orthogonal line with a defined length are located in order to extract the contours of the veins. In case no peak values are found in the vicinity of a pair of points, the position of the edge is interpolated based on valid edges for previous and following pairs.

This approach is highly sensitive to the scale of the Gaussian filter used to extract the axial traces of the veins in the first place. To tackle this problem, the procedure is repeated for a range of parameters and then the results are combined, ensuring the detection of both thin and thick veins.
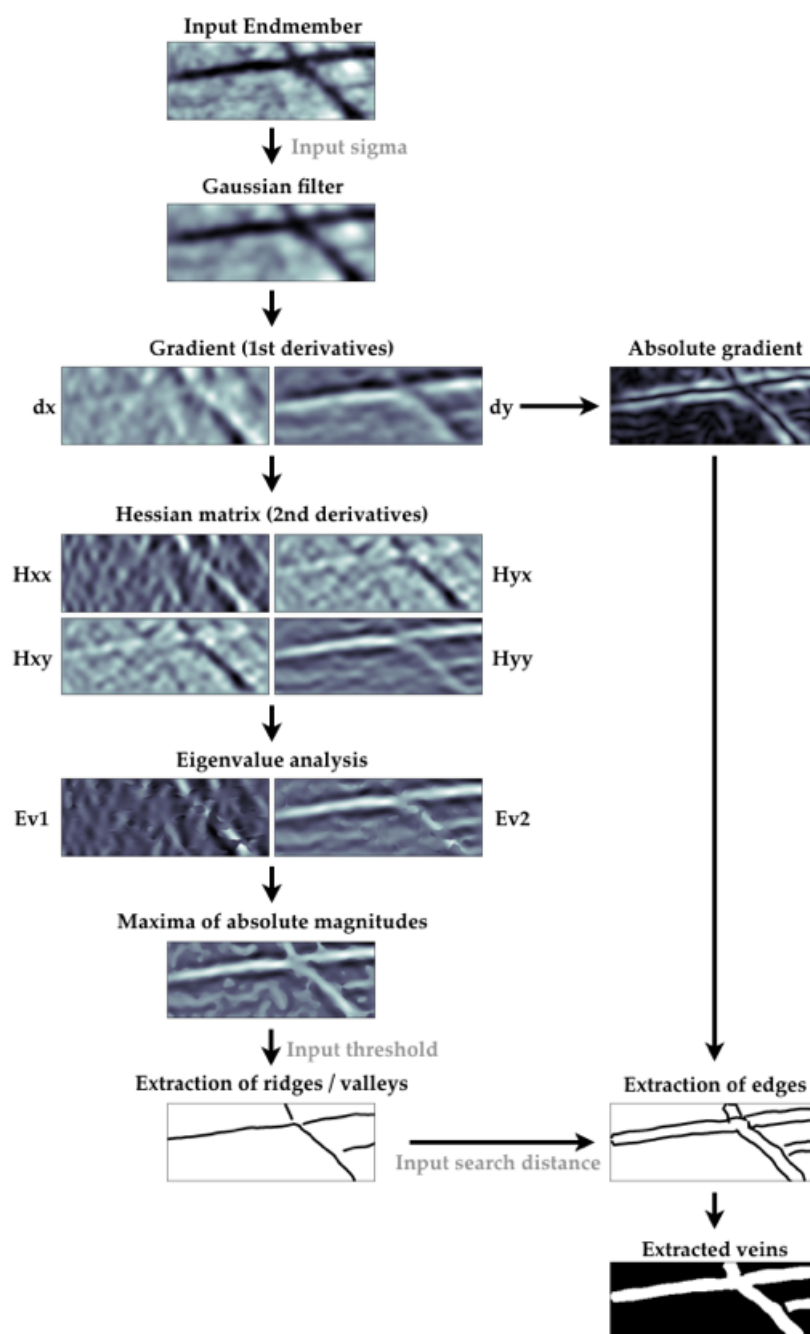
Figure 3-4. Proposed workflow for vein extraction.

3.5   Results

The potential and limitations of the proposed method are illustrated on three samples from the Bolcana porphyry system (DC-1, DC-2 and DC-3). The samples contain different vein types and styles of pervasive alteration. Macroscopic observations of the drill-core pieces and SEM-MLA data acquired on polished thin sections are used as ground truth for data validation.

3.5.1   Validation Data

Minerals that absorb parts of the incoming light between 1000 and 2500 nm are further called SWIR-active minerals. The SWIR active minerals identified in the samples are white micas, chlorites, biotite, epidotes, carbonates and amphiboles. Calcium sulphates are present as either gypsum (SWIR active) or anhydrite (SWIR inactive). MLA mineral maps are used for the identification and validation of the main alteration styles and mineral assemblages recognized in the samples (Figure 3-5).

The distribution of SWIR active and non-active minerals is illustrated in these results. The association of specific SWIR active and inactive minerals can help define a specific alteration zone. In this way, specific SWIR-active assemblages can be further linked to a defined location within the porphyry system. The main alteration styles encountered in the samples are phyllic (quartz–white mica–pyrite), potassic (k-feldspar–biotite) and calcic-sodic (plagioclase-chlorite/actinolite and subordinate white mica). Additionally, transitions between these alteration styles are noted. The main vein types present in the samples are B-type veins consisting of mainly quartz or calcium sulphate with a sulphide dominant centreline and D-type late veins consisting dominantly of sulphides and subordinately calcium sulphate. The nomenclature of the vein stage and morphology follows the description provided by Gustafson and Hunt, 1975.

Sample DC-1 is marked by pervasive potassic alteration characterized by the presence of K-feldspars, biotite and minor chlorite. Two main vein types are present in this sample. D-type veins consist of sulphides and show a strong phyllic alteration halo caused by the late reaction of mineralizing hydrothermal fluids with the host rock. B-veins consist dominantly of quartz with sulphide or sulphide and calcium sulphate (gypsum or anhydrite) centreline.

Sample DC-2 shows a less intense potassic alteration with a transition towards sodic-calcic alteration. The matrix is composed of feldspars, chlorite and minor amounts of biotite. Two main vein types are encountered. These are quartz B-veins with a centreline of sulphides and calcium sulphate, and calcium sulphate B-veins with a sulphide centreline and a transition towards D-veins. The complexity of the vein architecture can be explained by a late opening of a B-vein and a D-vein overprint. This overprint also explains the formation of an alteration halo of strong phyllic composition. A sodic-phyllic rock matrix hosting two main vein-types characterizes sample DC-3. The first vein type is a D-vein with a large white mica alteration halo. The second vein type consists predominantly of quartz, calcium sulphate and sulphides. The changing symmetry and mineral association in these latter veins indicate the reopening of an initially present quartz or B-vein.
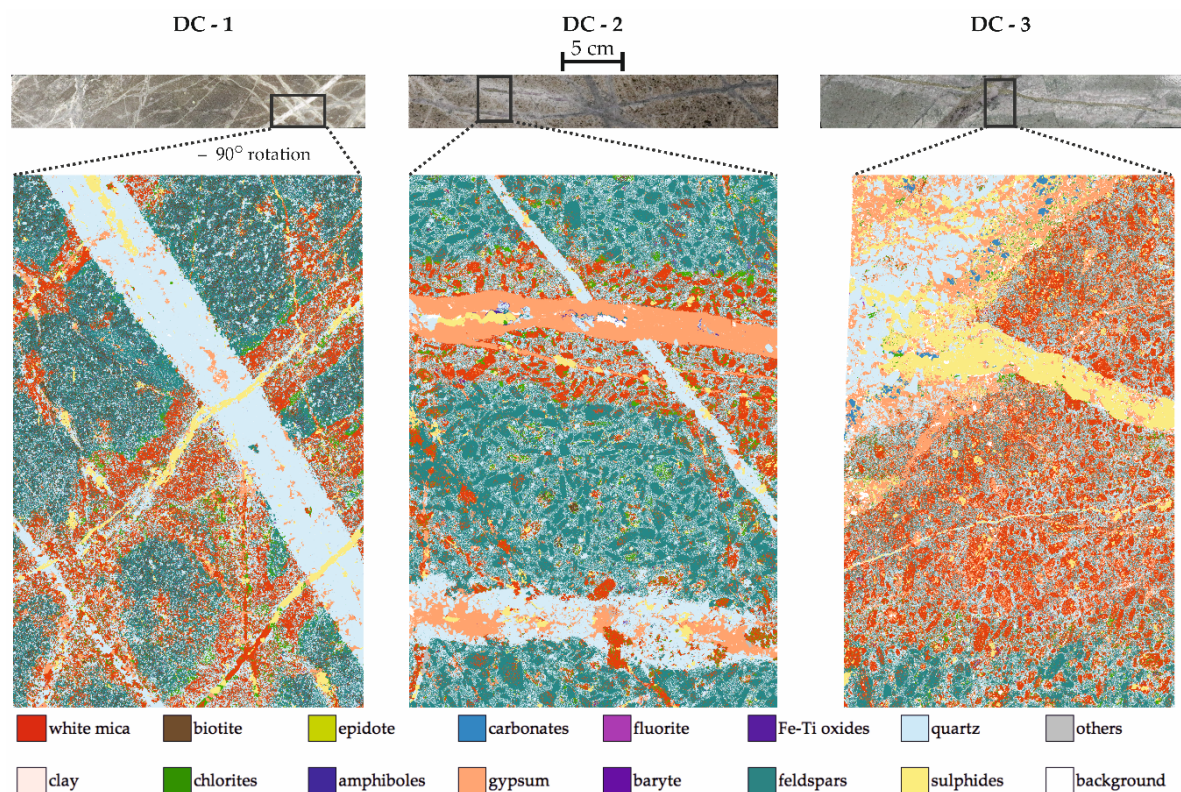
Figure 3-5. SEM-MLA mineral maps used for the validation and evaluation of the mineral mapping based on hyperspectral scans.

3.5.2 Mineral Mapping

As a first stage of the hyperspectral data processing, endmembers are extracted using the N-Findr algorithm. Three endmembers are considered in the present study, as they cover the strongest variability within the alteration mineralogy (Figure 3-6). The analysis of the endmembers is performed using a decision tree-based wavelength analysis tool for the identification of the main minerals present in the endmembers. For white mica, for instance, three types are identified based on the minimum wavelength position within the selected ranges: paragonitic (2180–2195 nm), intermediate (2195–2210 nm) and phengitic (2210–2228 nm).

After applying FC-LSU for estimation of the abundance, the final mineral maps are obtained by using the maximum abundance among the three endmembers in each pixel. Please note that in FC-LSU the endmember abundances sum to one (Figure 3-7). The main spectrally active assemblages observed in sample DC-1 are chlorite–white mica, white mica–chlorite and chlorite–biotite. The first two constitute alteration selvages around the main vein types, while the latter assemblage is dominant in the rock matrix. In sample DC-2, the main vein-related alteration assemblages are white mica and white mica–gypsum–chlorite. The matrix in sample DC-2, as in sample DC-1, is characterized by the dominance of chlorite and biotite among the SWIR active minerals. In sample DC-3, an aspectral endmember corresponding to the occurrence of sulphide and quartz is mapped. The alteration selvage of these veins is dominated by white mica whereas the pervasive alteration consists mostly of a white mica–chlorite assemblage.

Sample DC-1 hosts two endmembers containing white mica. In the white mica–chlorite endmember, white mica shows an intermediate composition while in the chlorite–white mica it has a phengitic composition. The low-intensity absorption white mica endmember (called low white mica) in Sample DC-2 has a paragonitic composition in comparison to the endmember white mica–gypsum–chlorite, where the white mica has an intermediate character. Sample DC-3 shows an inverse relationship between the composition of the micas in the veins and in the matrix compared to sample DC-1. The matrix-characteristic endmember here has a phengitic composition while the vein selvage has a paragonitic one. These results were confirmed and supported by minimum wavelength maps in the ranges of 2180–2228 nm for white mica and 2240–2263 for chlorite (Appendix 3A).
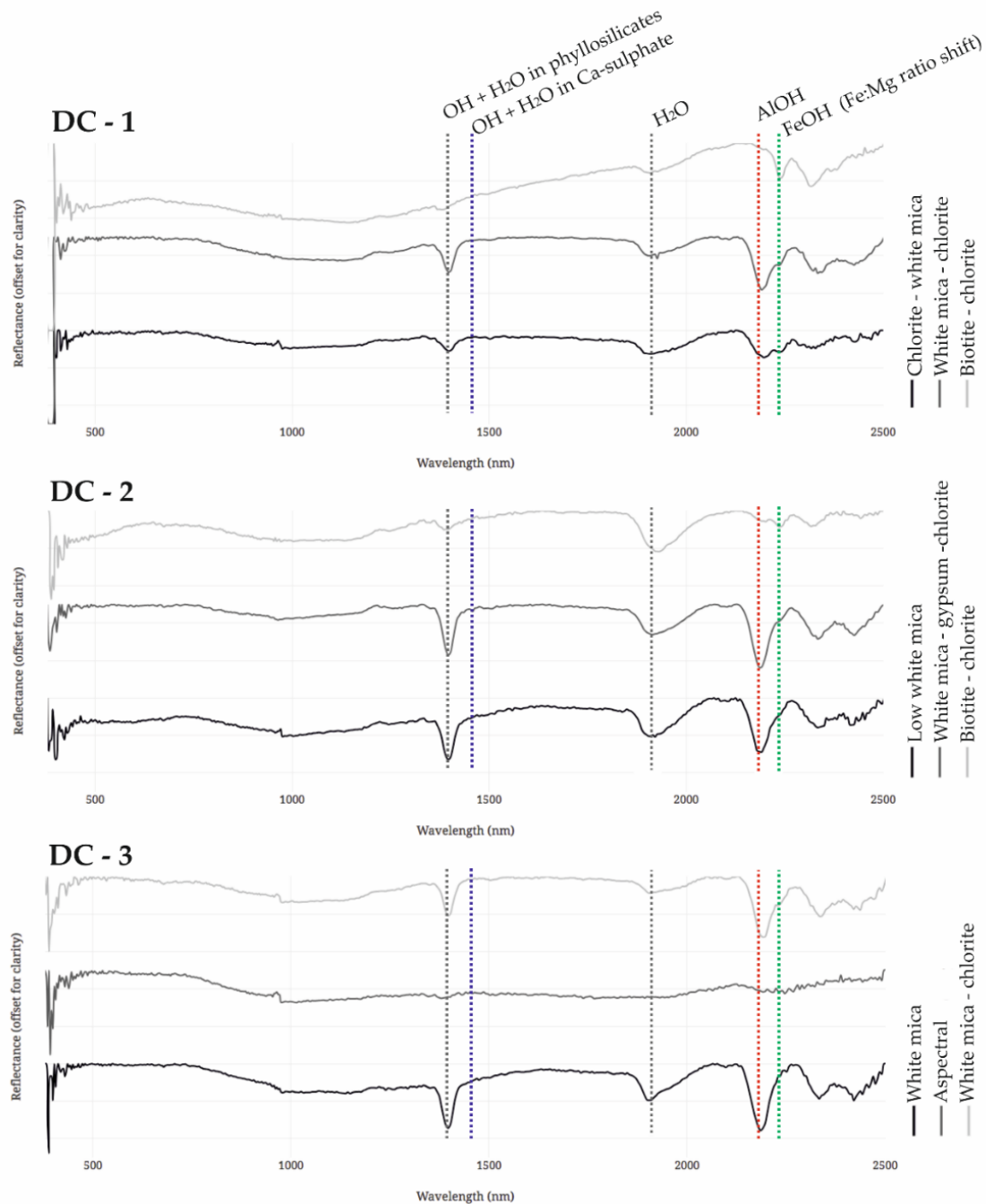
Figure 3-6. VNIR-SWIR spectra of the endmembers extracted from the three drill-core scans.
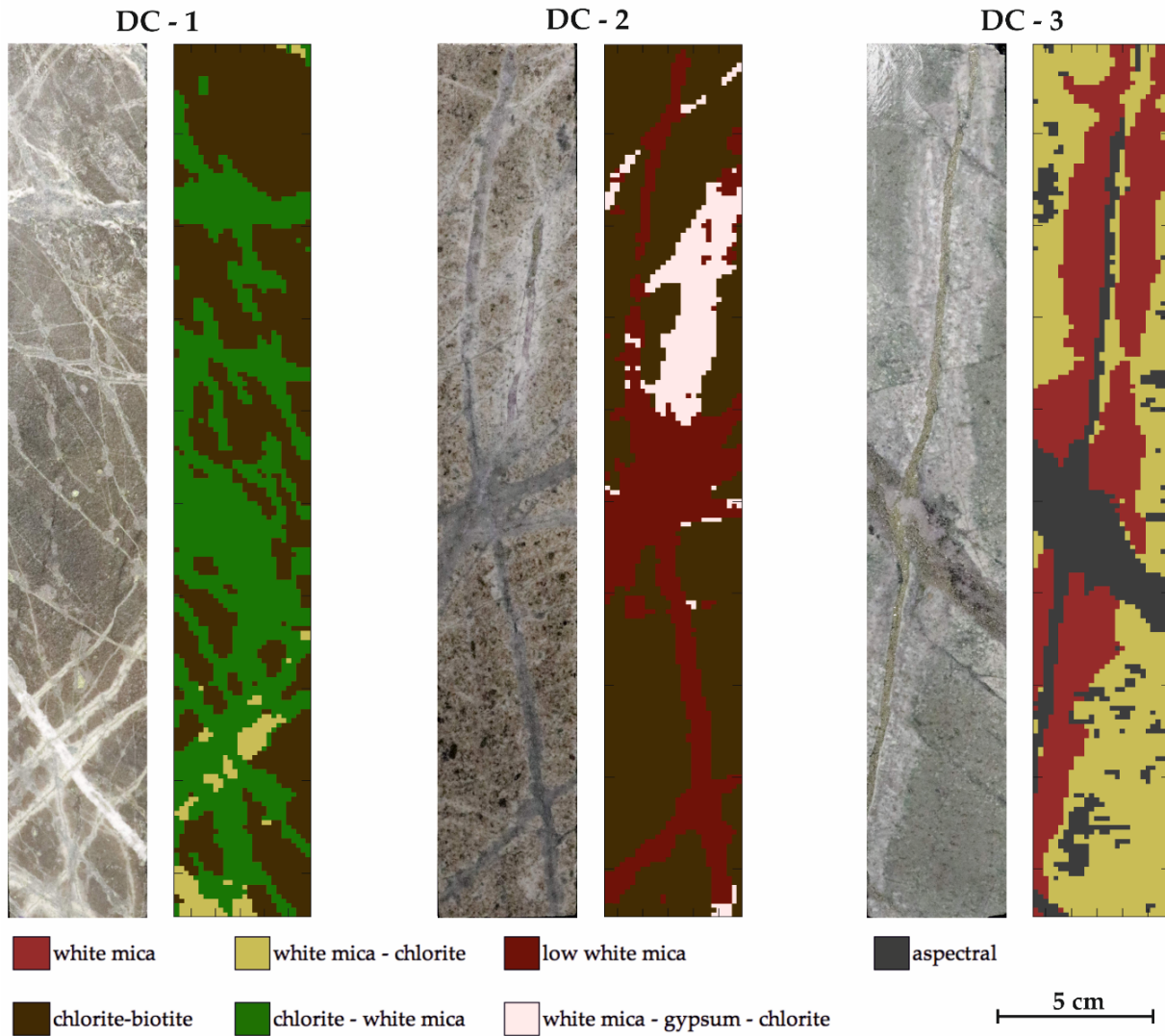
Figure 3-7. RGB image of the drill core samples and mineral maps obtained from N-Findr, FC-LSU and maximum abundance mapping using 3 endmembers.

3.5.3 Structural Feature Extraction

The extraction of structural features is performed on each of the endmember abundance maps obtained by FC-LSU (Figure 3-8). For each of the samples, endmembers 1 and 2 correspond to vein alteration selvage or vein internal composition, while endmember 3 reflects pervasive alteration.

For sample DC-1, a combination of two vein types is present. One of the endmembers shows a white mica-dominant alteration selvage, while the other a chlorite-dominant selvage. However, in places, due to vein reopening and compositional complexity, the endmember abundances as well as the extracted vectors show a partial overlap of the two vein-related endmembers. This can be observed particularly in the left-hand side of the sample.

For sample DC-2, the mineral mapping and vein extraction results show a good overlap in terms of vein mineralogy mapping. For endmember 1, a good performance of the extraction consistent with the macroscopic observations and the validation data is achieved. Moreover, the artefacts from mineral mapping observed in the vicinity of the second vein type are not present here. Additionally, a distinction between the thick, sub-

horizontal vein at the top of the image and the intersecting oblique vein is made, which was not possible in the mineral maps. For endmember 2, due to the low intensity in the endmember abundance map, the third vein present and mapped at the centre of the image is not extracted here with the selected parameters. Yet, with a decrease in the sigma value or in the threshold ranges it was possible to extract this vein. However, the drawback of decreasing the sigma value or the minimum threshold would be the risk to map noise as veins. We therefore refrained from pursuing this further.

Sample DC-3 was chosen as an example with exceptionally thick alteration selvages exceeding one centimetre in width. The D-vein present in this sample shows a particularly wide alteration halo of similar composition to the quartz–anhydrite–sulphide vein. Extending the ranges for the sigma parameter would still not allow for an accurate extraction of this vein. Here, the use of endmember 1 corresponding to the alteration halo of both veins leads to the extraction of two features parallel to the D-vein. The vein extraction from the abundance map of endmember 2, characterized as aspectral, leads to the detection of structural features characteristic to the intrinsic composition of both veins.

For all three samples, endmember 3 is characteristic of the pervasive alteration. The vein extraction should allow for the mapping of all veins based on the areas of minimum abundance of endmember 3. For samples DC-1 and DC-2, the results show an overlap of the vein types mapped from the first 2 endmembers. Exceptions occur particularly for sample DC-2, where some veins are very thin and the alteration halo has a low intensity in comparison to the matrix and in relation to the compositional variability of the pervasive alteration. The expected vein thickness to be extracted is estimated at 0.5 mm. This value, however, can vary, as the performance of the method is highly dependent on the abundance of the SWIR active phases in the veins or vein alteration halos. Depending on the location within the system, as well as the stage of mineralization, the contrast between the abundance of the SWIR active phases within and in proximity to veins compared to the matrix varies.

In addition to the use of the linear extraction tool for the extraction of veins from endmember abundance maps, the same approach can be used for other input files such as images resulting from band math calculation or minimum wavelength analysis. The band math (2170/2206 nm) characteristic of white mica's distribution for the studied samples is performed on continuum-removed spectra (Gomez et al., 2008). As only the intermediate composition white mica is considered here, the vein extraction results (Appendix 3B) will not be entirely consistent with the distribution of all white mica types illustrated in the endmember abundance maps.

By using the centreline of the extracted features, the azimuth of the different vein types can be evaluated in each of the endmembers (Figure 3-9). An E-W horizontal orientation of the drill-cores is considered as shown in Figure 3-8, for illustrative purposes. For the integration of the data into a 3D model, the orientation of the drill-hole should be considered. The orientation and abundance of the veins are highly variable within the three tested drill-core samples, particularly in samples DC-1 and DC-2, which were taken from the same drill-hole at different depths. Additionally, an overlap in the orientation of the veins identified in the two vein-related endmembers can also be observed. In sample DC-2, the overlap between the two orientations is mostly caused by the similar dominant azimuth between the two main vein types. In sample DC-3, however, the

overlap is due to the extraction of the inner composition of the vein from the first endmember and the extraction of the vein alteration halo from the second endmember.
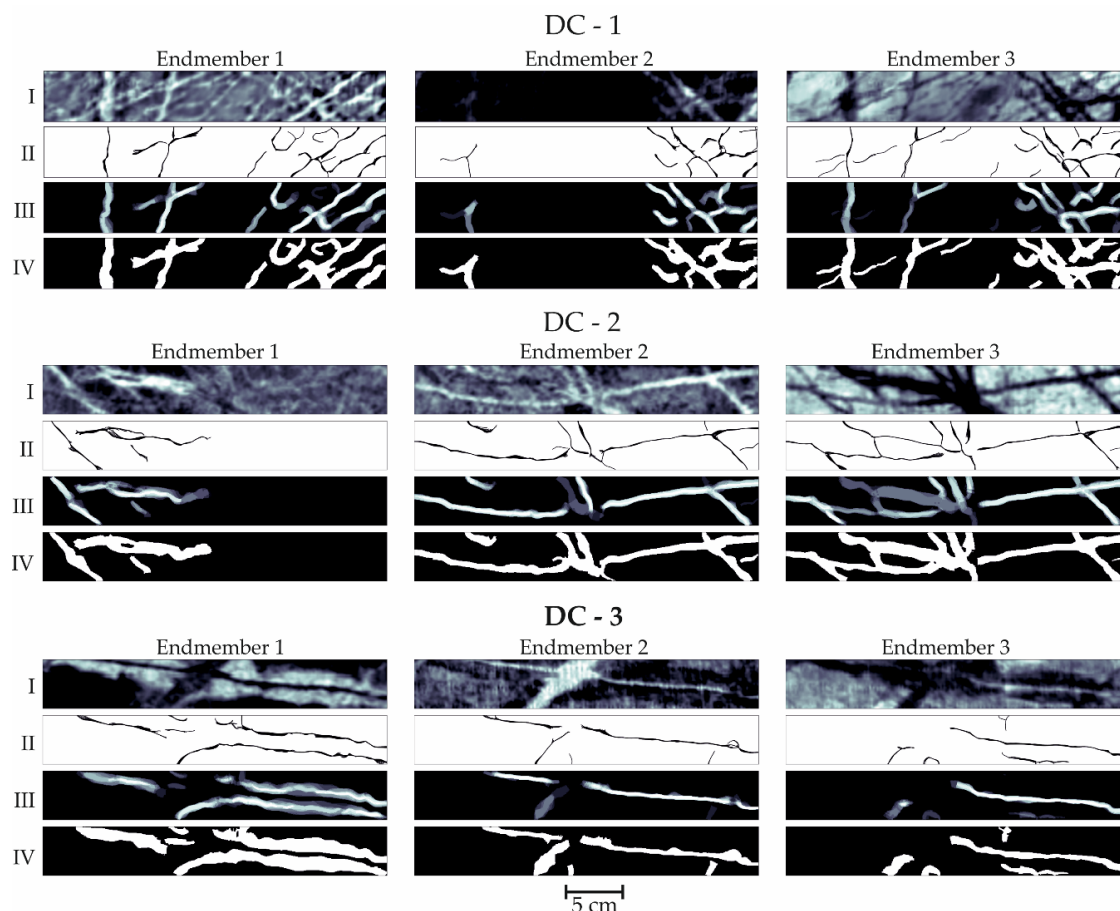
Figure 3-8. Results of the vein extraction performed on the endmember abundance maps obtained by FC-LSU. I = endmember abundance map, II = extracted ridges for sigma ranging from 3 to 10 and thresholds ranging from 98% to 92%, III = overlapping polygons after connecting extracted lines to their respective edges (features detected with wider range of sigma are brighter), IV = extracted veins after merging all polygons.
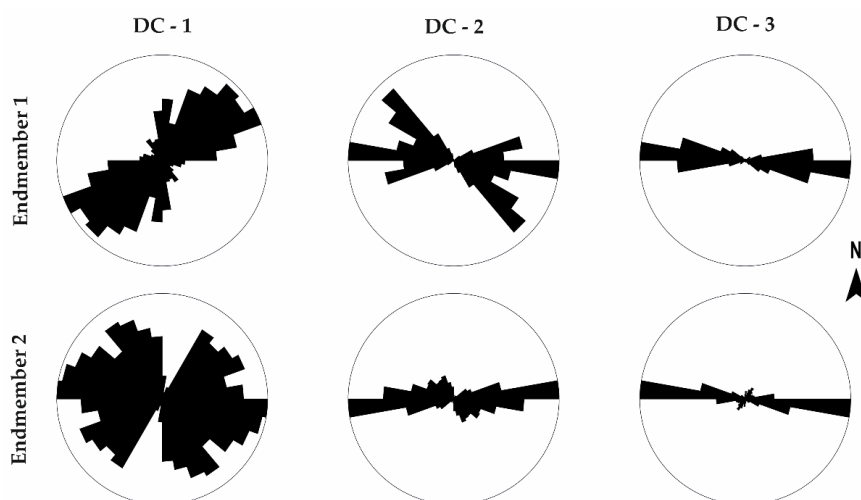
Figure 3-9. Rose diagrams illustrating the orientation of the veins in the first two endmembers of each sample. The azimuth is calculated here based on the horizontal (E–W) layout of the drill-cores as illustrated in Figure 3-7.

The abundance of each vein type is quantified based on the surface percent within the samples (Table 3-3).

Table 3-3. Summary of vein extraction results (EM = endmember, BR = band ratio). The estimated density is represented by the surface percent covered by a particular vein type extracted from the input image; for the extracted features, bright indicates high abundance, while dark indicates low abundance.

Sample	Input	Mineralogy	Distribution	Extracted Feature	Estimated Surface Abundance (%)
DC-1	EM 1	Chlorite–white mica	Vein halo	Bright	22
	EM 2	White mica–chlorite	Vein halo	Bright	14
	EM 3	Biotite–chlorite	Matrix	Dark	23
	BR	White mica	Vein halo	Bright	18
DC-2	EM 1	White mica–gypsum–chlorite	Vein halo	Bright	13
	EM 2	Low white mica	Vein halo	Bright	23
	EM 3	Chlorite–biotite	Matrix	Dark	30
	BR	White mica	Vein halo	Bright	26
DC-3	EM 1	White mica	Vein halo	Bright	33
	EM 2	Aspectral	Vein halo	Bright	13
	EM 3	White mica–chlorite	Matrix	Bright	11
	BR	White mica	Vein halo	Dark	145

For samples DC-1 and DC-2, endmembers 1 and 2 are representative of particular vein types. For sample DC-3, endmember 1 is representative of the alteration halo whereas endmember 2 is characteristic of the internal vein composition, which is aspectral, being composed predominantly of sulphides. Endmember 3, for samples DC-1 and DC-2, refers to the rock matrix, so by mapping the minimum abundance in the image (dark phase), the total amount of veins with a considerable thickness or distinct alteration halo are extracted. Due to the large thickness of the alteration halo of the D-vein in Sample DC-3, for endmember 3, mainly characteristic of pervasive alteration, the edges of the alteration halo and the small presence of chlorite with the sulphide in the vein are extracted as linear structures.

The structural features extracted from images obtained from band ratios are characteristic of white mica abundance. Due to the location of the samples in the potassic and sodic-calcic zones of the system, the phyllic alteration is be dominantly related to vein halos.

3.6   Validation of Results

MLA mineral maps can be used to locally validate hyperspectral data processing results. As a first step, the RGB images, HSI-based maximum abundance mineral maps and vein distribution maps are illustrated together with markings of the location of the thin sections analysed by MLA on the RGB images (Figure 3-10). For further analysis, the MLA mineral maps, digitised simplified MLA maps, HSI-based maximum abundance maps, and the vein distribution maps are presented together at the field of view of the thin section (Figure 3-11). A slight but consistent shift between the MLA maps and HSI vein maps can be observed for most of the samples. This shift is caused by the orientation (dip) of the vein, as around 0.5 mm of material is lost during sample preparation between the analysed surface of the drill-core and the surface of the thin section. As most vein types are vertical and subvertical in relation to the surface of the sample, the presence of the small shift in the location of the vein is generally 1 mm or smaller, and it does not strongly impact the hyperspectral data classification validation procedure.
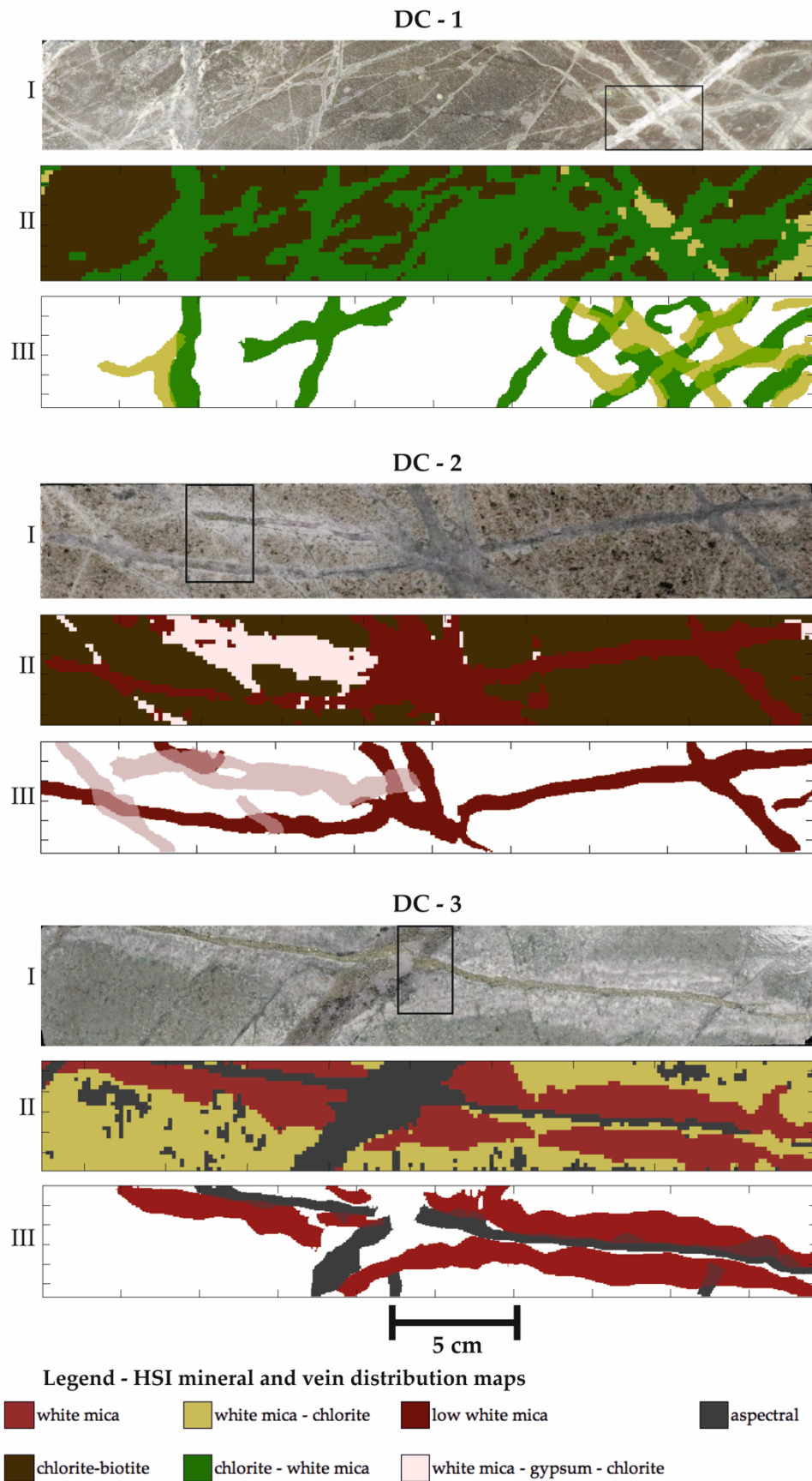
Figure 3-10. Illustrative diagram of data validation for each of the three samples. I = RGB image of the drill cores with marked area of the location of the SEM-MLA mineral map, II = HSI-based maximum abundance mineral map, III = vein distribution maps.

Figure 3-11. Comparison of SEM-MLA and HSI-based analyses: I—SEM-MLA mineral map at full resolution, II—HSI-based maximum abundance mineral map, III—digitised SEM-MLA map emphasizing the main vein types, IV—HSI-based vein distribution map.

For the three studied samples, the evaluation of the SWIR-active mineralogy is consistent with the main minerals identified by MLA, including white mica, chlorites, biotite and calcium sulphate, here described as gypsum. The presence of calcium sulphate in some of the MLA maps and the absence of gypsum in the mineral maps suggests the occurrence of SWIR inactive anhydrite rather than SWIR-active gypsum.

Based on the abundance of the different veins in each sample, several features were selected and marked on the simplified MLA vein maps, for the evaluation of the vein extraction performance (Figure 3-12). Five veins were selected in sample DC-1, three in sample DC-2, and three features characteristic of either vein, or vein halos in sample DC-3.

Most of the marked features in sample DC-1 show a good correspondence between the data obtained from MLA and the extracted structural features. The areas where 2 veins crosscut each other cause, however, overlaps and shifts between the extracted features. This is similar in sample DC-2, where features 1 and 2 are well extracted. Yet, one of the veins described in the MLA map (in purple) is not identified in the HSI-based vein distribution map as distinct but rather as a mixture or overlap between two vein types. The reason for this is the small width of the vein in relation to the spatial resolution of the hyperspectral camera (1.5 mm/pixel), as well as its composition, intermediate between the two main veins, which were extracted. In sample DC-3, a relatively good extraction of feature 1, representative of the sulphide vein, is observed, as well as a good overlap of its alteration halo extent (feature 3). The thicker aspectral vein (feature 2), on the other hand, was not well extracted from the HSI data.
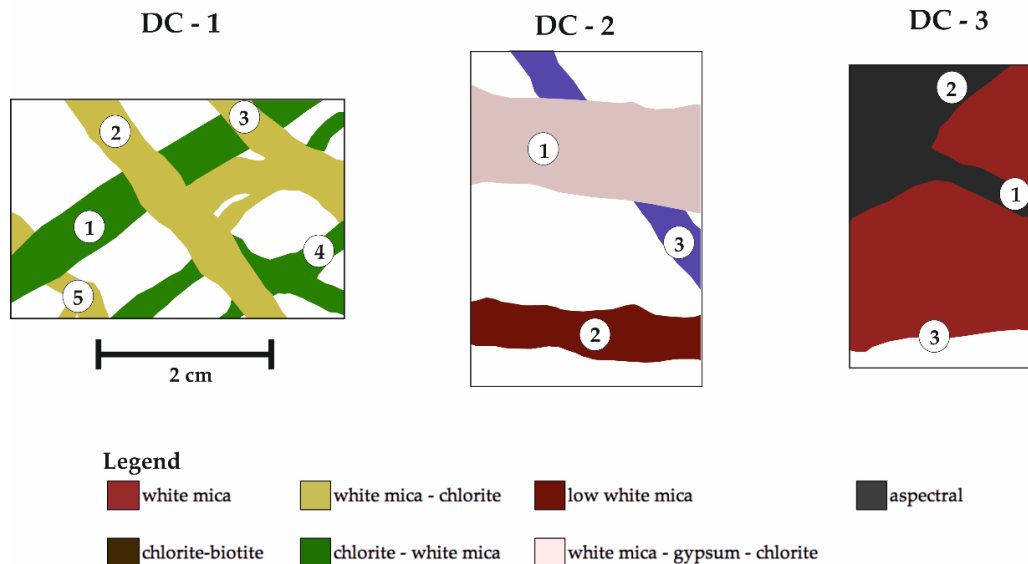
Figure 3-12. Simplified MLA mineral maps with markers on selected features for the vein width and azimuth validation.

For numerical evaluation of the performance of the vein extraction tool, vein distribution maps and digitised simplified MLA maps are used. For this purpose, the orientation and thickness accuracy of each selected feature is analysed where possible (). Features 2 and 3 in sample DC-3 could not be evaluated in terms of thickness and orientation due to their incomplete capture in the MLA mineral map.

The orientation is analysed using the average angle of the veins on different centre segments. The average thickness calculated on the intersection of the overlap is used for the vein thickness evaluation. Up to 4.5° azimuth deviation was observed for the vein orientation between the HSI and MLA-based vein analysis. Regarding the extracted thickness, the accuracy ranged between 65% and 95%, with a mean value of 81%, by considering all the veins and of 85% by considering only veins of thickness higher than the spatial resolution of the used hyperspectral sensor.

Table 3-4. Results of vein extraction validation for selected features.

Feature	DC-1		DC-2		DC-3	
	Azimuth Deviation (°)	Width Accuracy (%)	Azimuth Deviation (°)	Width Accuracy (%)	Azimuth Deviation (°)	Width Accuracy (%)
F1	1.3	91	4	82	4.5	75
F2	4	95	0.5	90	-	-
F3	3.7	93	0.5	92	-	-
F4	0.2	67	-	-	-	-
F5	2.5	65	-	-	-	-

3.7   Discussion

The suggested workflow for processing of the VNIR-SWIR hyperspectral drill-core scans consists of a sequence of endmember extraction, spectral unmixing, mineral mapping and vein extraction techniques. The workflow is used for development of mineral maps; a suite of geomorphological analysis tools can then be used to extract the vein distribution and architecture from endmember abundance and band ratio images.

The mapping of veins, quantification of their distribution and understanding of the dependency between the alteration assemblage surrounding different vein-types is essential to the mapping and evaluation of stockwork-type deposits, such as Cu porphyry type deposits. The proposed methodology is shown to provide insight into the vein type variability, distribution and quantification within the selected samples. This methodology has the potential to provide fast and unbiased compositional and quantitative vein information which can become a valuable tool for a running exploration project, allowing for fast evaluation of the distribution and abundance of vein-related and pervasive alteration assemblages.

Visual analysis of drill-core trays from the studied porphyry has shown that in the core of the system, the degree of mineralogical variation in one drill-core tray is similar to what is observed and analysed at drill-core sample scale. As a result, implementation of the proposed method at the scale of the drill-core tray (Figure 3-2) would be appropriate for providing a fast evaluation of the main vein and alteration styles. Even though the three endmembers provide sharp abundance maps for both mineral mapping and vein extraction, a necessity for more information on the composition of the alteration minerals arises. It is common that a general zonality of the white mica and chlorite compositions is observed at deposit scale (Maydagán et al., 2018); however, in the case of porphyry deposits, this zonation can also be observed at drill-core scale. Both white mica and chlorite tend to be present in variable amounts within the sample, but their composition is highly dependent on the proximity to the different vein types. In samples DC-1 and DC-2, the mica shows a more phengitic composition, and the chlorites a rather high Fe: Mg ratio in the proximity of the veins, while in sample DC-3, an inverse relationship is observed. Although the location of the absorption minima for white mica is likely to be shifted to higher wavelengths when chlorite is abundant, a strong heterogeneity in white mica chemistry was observed in SEM spectra. The dependency of the white mica and chlorite chemistry to the stage of the mineralization or to the composition of the pervasive alteration is still to be researched.

For vein extraction, the results appear promising, in terms of both vein thickness and orientation estimation, considering the high degree of automation of the method. By using different values of the sigma filter for each sample a more controlled extraction of the veins could be achieved. However, using thresholds

for vein thickness is difficult when the alteration halo around veins shows a diffuse character and gradual transition into the (less altered) host rock. In such cases, the choice in threshold remains rather subjective. Furthermore, features which do not represent veins but rather clusters in the matrix may also be included.

Due to the difficulty in the selection of the number of endmembers in an industry-scale operation, the extraction of veins could also be achieved from minimum wavelength maps or band ratio images characteristic of a specific mineral or mineral assemblages such as hydrated calcium sulphate in any pervasive alteration zone, white mica in the potassic and sodic-calcic alteration zones, or chlorite in the phyllic zone. The high abundance-based extraction of these features could lead to the mapping of selected veins. A positive performance for this purpose was obvious for sample DC-1 where some of the thinner veins, which are not extracted from endmember abundance maps, were recognized in the band ratio image illustrative of white mica abundance. Another approach could be the mapping of the low abundance of hydrated phases using the abundance of the water feature around either 1400 nm or 1900 nm. In this manner, wide sulphide veins presenting an alteration halo would be extracted. Such an example can be seen also for the band ratio for sample DC-3 where the sulphide and sulphide-quartz veins are extracted.

3.8   Conclusions

In this contribution, a novel methodology for extracting and complementing mineralogical and structural features from hyperspectral drill-core scans is introduced. The workflow consists of three main steps: (1) endmember extraction and spectral unmixing, followed by (2) mineral mapping, and (3) vein extraction. The N-Findr algorithm is used on hyperspectral scans to extract potential endmembers. Fully constrained linear spectral unmixing is then performed in order to obtain mineral abundance maps. These maps are further used for mineral mapping by the analysis of the maximum abundance in each pixel. Finally, potential veins are identified in abundance maps using an approach based on Steger's detector of curvilinear features, which combines ridge and edge detection. This approach allows for the extraction of veins as vectorised lines or polygons. The proposed methodology shows very good performance with regard to:

- Distinguishing between pervasive and vein-related alteration mineralogy through mineral maps and vein distribution maps;
- Mapping different vein types based on their alteration halo or intrinsic composition when minerals such as gypsum or carbonates are part of the vein;
- Vein density estimation based on their surface abundance;
- Evaluation of the orientation (azimuth) of different vein types;
- The degree of automation in comparison with existent techniques;
- High potential for the compositional and numerical data to be integrated in a 3D model in ongoing exploration campaigns;

There is a strong link between the performance of the vein extraction tool, the chosen number of endmembers, and the performance of the endmember extraction algorithm. With an increase in the selected number of endmembers, a higher resolution is added to the mineralogical variation within the samples. However, this will lead to abundance maps of reduced sharpness, and therefore will negatively influence the

performance of the vein extraction algorithm. Further work is necessary for the development of algorithms for the estimation of the virtual dimensionality of the data and therefore a consistent number of endmembers.

Appendix 3A

The analysis of the white mica composition and abundance is performed in the wavelength range of 2175 and 2235 nm and for chlorites between 2235 and 2273 nm on continuum removed spectral subsamples in the mentioned ranges. However, only the ranges with a minimum representative of mica (2180–2228 nm) and chlorite (2240–2263 nm) are illustrated (Figure 3-13), lower and higher wavelengths of minima being masked. A variation in the maximum feature depth between the samples is present for both chlorite and white mica and therefore the different depths are shown for each drill-core. For the first two samples it can be observed that an intermediate phengitic (higher wavelength) composition of the white mica and an intermediate to iron-rich composition of the chlorites are dominant surrounding the veins, while the pervasive alteration is characterized by a low abundance of the mica of paragonitic composition and a high abundance of chlorites and biotite of magnesian composition. These properties are inversed in the third sample. For the thinner sulphide vein where the white mica has a paragonitic composition next to the vein and an intermediate composition in the halo with phengitic spots. The chlorite composition for this vein halo is intermediate towards magnesian. In the matrix the chlorite shows a strong ferric composition. The second vein, however, exhibits a dominance of the intermediate mica and intermediate to ferric chlorites. The spectral analyses results obtained from minimum wavelength are overall consistent with the analyses of the endmembers spectral features.
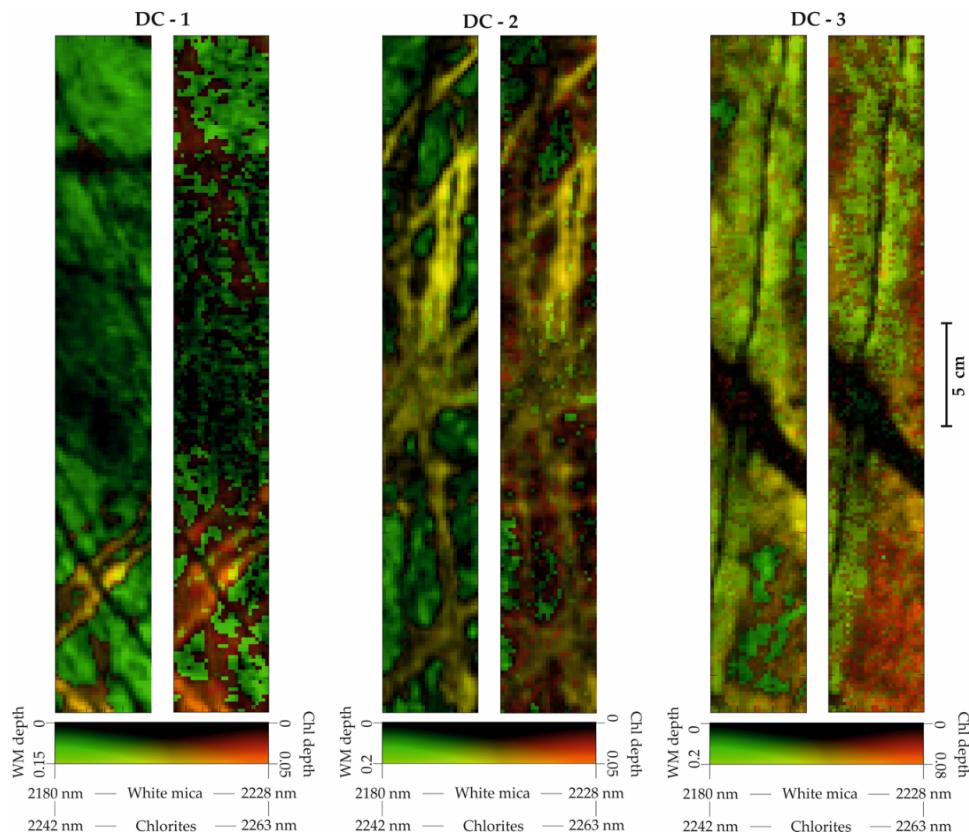
Figure 3-13. Minimum wavelength maps for white mica (left) and chlorites (right) for the three analysed samples (WM = white micas, Chl = chlorites).

Appendix 3B
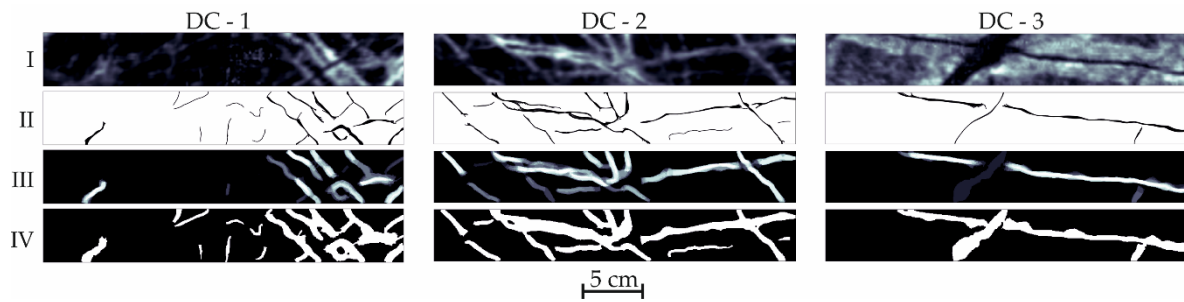
Figure 3-14. Results of the vein extraction performed on binary images resulting from a band math calculation representative of the abundance of white mica: 2170/2206. I = endmember abundance map, II = extracted ridges for sigma ranging from 3 to 10 and thresholds ranging from 98% to 92%, III = overlapping polygons after connecting extracted lines to their respective edges (features detected with wider range of

Chapter 4 Hyperspectral imaging for quasi-quantitative mineralogical studies

Preface

Quantitative mineralogical data becomes essential with the evolution of an exploration process. Most of the available techniques are either applied on small samples only (such as thin sections or hand specimens) or on homogenized and granulated bulk samples that lack textural and spatial information. Hyperspectral imaging can serve as a tool to provide extensive imaging data over entire boreholes, however, most standard spectral analysis routines cannot deliver a quantitative mineralogical assessment. To overcome the limitations related to both analytical approaches, within this chapter a methodology for fusing high resolution mineralogical and hyperspectral data is proposed for upscaling the quantitative mineralogical information from thin section to drill-core scale. In addition, several machine learning regression algorithms are evaluated both visually and numerically for their performance for mineralogical applications. Mineral abundance maps and modal mineralogy estimates for spectrally diagnostic minerals in the short-wave infrared spectrum is the one important outcome of this study, complemented by quasi-quantitative estimates of non-diagnostic minerals and mineral groups based on their subtle association with the spectrally diagnostic phases. Further mineralogical parameters can be defined from these datasets such as an adapted mineral association calculation at the coarse resolution of the hyperspectral data. While only presented here for a limited number of samples, the methodology can be applied at deposit scale. They will contribute to exploration and mining projects through:

(1) Understanding of the modal mineralogy related to different domains within an ore deposit

(2) Support in metallurgical design based on modal mineralogy and mineral association

(3) Definition of geometallurgical domains.

Preliminary results of this work were firstly presented at the EGU General Assembly [1] in 2019 and the complete content of this chapter was published in the journal Remote Sensing [2] under the title "Drill-Core Mineral Abundance Estimation Using Hyperspectral and High-Resolution Mineralogical Data".

Authors and contributions

Laura Tuşa[1], Mahdi Khodadadzadeh[1], Cecilia Contreras[1], Kasra Rafiezadeh Shahi[1], Margret Fuchs[1], Richard Gloaguen[1] and Jens Gutzmer[1]

1   Helmholtz-Zentrum Dresden-Rossendorf, Helmholtz Institute Freiberg for Resource Technology

Conceptualization, L.T.; *methodology*, L.T. and M.K.; *software*, L.T., M.K. and C.C.; *validation*, L.T.; *formal analysis*, L.T.; *investigation*, L.T.; writing - *original draft*, L.T., M.K., C.C. and K.R.S.; *review—all authors; visualization*, L.T.; *supervision*, M.K., M.F., R.G. and J.G.; *project administration*, R.G. and J.G.;

---

[1] Tusa, L.; Khodadadzadeh, M.; Contreras Acosta, I. C.; Fuchs, M.; Gloaguen, R., Gutzmer, J., 2019, Supervised machine learning for the quantification of mineral phases in drill-core hyperspectral data, EGU General Assembly, 07.-12.04.2019, Vienna, Austria

[2] Tusa, L., Khodadadzadeh, M.; Contreras, C.; Rafiezadeh Shahi, K.; Fuchs, M.; Gloaguen, R.; Gutzmer, J. Drill-Core Mineral Abundance Estimation Using Hyperspectral and High-Resolution Mineralogical Data. Remote Sens. 2020, 12, 1218. https://doi.org/10.3390/rs12071218

Abstract

Due to the extensive drilling performed every year in exploration campaigns for the discovery and evaluation of ore deposits, drill-core mapping is becoming an essential step. While valuable mineralogical information is extracted during core logging by on-site geologists, the process is time consuming and dependent on the observer and individual background. Hyperspectral short-wave infrared (SWIR) data is used in the mining industry as a tool to complement traditional logging techniques and to provide a rapid and non-invasive analytical method for mineralogical characterization. Additionally, Scanning Electron Microscopy-based image analyses using a Mineral Liberation Analyser (SEM-MLA) provide exhaustive high-resolution mineralogical maps, but can only be performed on small areas of the drill-cores. We propose to use machine learning algorithms to combine the two data types and upscale the quantitative SEM-MLA mineralogical data to drill-core scale. This way, quasi-quantitative maps over entire drill-core samples are obtained. Our upscaling approach increases result transparency and reproducibility by employing physical-based data acquisition (hyperspectral imaging) combined with mathematical models (machine learning). The procedure is tested on 5 drill-core samples with varying training data using random forests, support vector machines and neural network regression models. The obtained mineral abundance maps are further used for the extraction of mineralogical parameters such as mineral association.

Graphical abstract
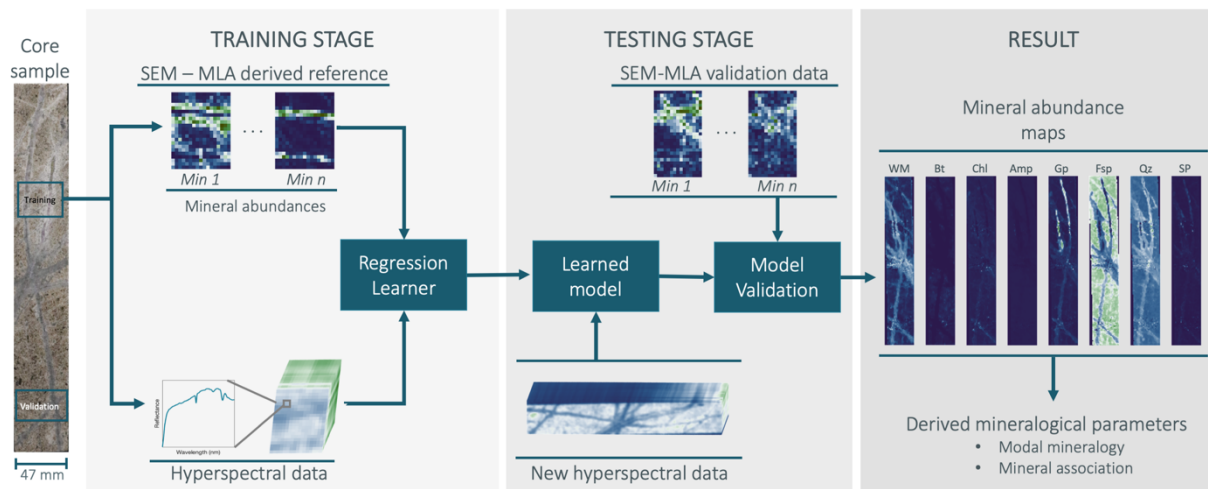
Keywords: hyperspectral imaging; drill-core; SWIR; mineral abundance mapping; mineral association; machine learning

4.1 Introduction

Exploration campaigns are fundamental steps towards the discovery and evaluation of mineral deposits required to fulfil the global demand of raw materials. Drilling is an essential part of exploration surveys and consists of the extraction of long cylindrical core samples from underground areas associated with relevant exploration potential. Traditionally, drill-cores are visually analysed by on-site geologists, who document characteristics such as mineralization type, lithology, structures and alteration types (Gandhi et al., 2016). Subsequently, core samples are used for laboratory-based geochemical and mineralogical measurements to

complement core logging results. While bulk geochemical analyses are often available for entire boreholes, quantitative mineralogical information is usually restricted to selected representative regions of interest. Standard quantitative analyses include X-Ray diffraction (XRD) applied on powder samples (Lindholm, 1987) or Scanning Electron Microscopy (SEM) based image analyses techniques (Fandrich et al., 2007) applied on polished thin sections prepared from areas of interest in the drill-cores. Additionally, qualitative mineralogical analyses are performed through optical microscopy on thin sections. These laboratory techniques provide valuable mineralogical information and derived mineralogical and metallurgical parameters, but they are of small scale, highly time-consuming, destructive, and rather expensive. This represents a challenge since thousands of meters of core are acquired during exploration campaigns.

Hyperspectral imaging is currently being used in the mining and exploration industries as an alternative tool to complement traditional logging techniques and to provide a rapid and non-invasive analytical method to obtain mineralogical information (Calvin and Pace, 2016; Contreras Acosta et al., 2019; Kirsch et al., 2018; Kruse, 1996). Typical hyperspectral core imaging systems can deliver data from a whole core tray (which holds approximately 5 m of core) in a matter of seconds. Available sensors cover a wide range of the electromagnetic spectrum and record data in several hundreds of contiguous spectral bands. Minerals have different spectral responses in specific portions of the electromagnetic spectrum. These responses are influenced by the vibrational and electronic absorption processes dependent on the bonds between atoms and electron orbitals (Clark, 1999). Sensors covering the visible to near-infrared (VNIR) and short-wave infrared (SWIR) are commonly used to identify and estimate the relative abundance of minerals such as phyllosilicates, amphiboles, carbonates, iron oxides and hydroxides as well as sulphates (Pontual et al., 1997).

Because of the increasing interest in hyperspectral data in the raw materials industry, with a wealth of hyperspectral data becoming available, the development of methods to effectively analyse these data is required. Traditional mapping methods include the use of spectral reference libraries (e.g., USGS spectral library) for mineral identification and mapping on hyperspectral imagery (Huntington et al., 2006; Mauger et al., 2007). Slightly more automatic approaches, such as band ratios, or wavelength parameters such as position, depth and width of the absorption features are also used to map the distribution and relative abundance of specific minerals (Mathieu et al., 2017; Roache et al., 2011; Tappert et al., 2011). One of the most common procedures makes use of some of available tools in a software called Environment for Visualizing Images (ENVI, Exelis Visual Information Solutions, Boulder, Colorado). Such tools comprise endmember extraction, identification of the minerals using the Spectral Analysis or Material Identification by comparison to a specific library in the software (e.g., in ENVI) or online reference (e.g., USGS), and finally the mineral mapping task using similarity measure algorithms or determination of partial abundances using unmixing algorithms (Calvin and Pace, 2016; Kratt et al., 2010; Littlefield et al., 2012).

Although these approaches may produce good results, they require continuous expert input and thus, they tend to be time-consuming and difficult to automate for large dataset analysis. More importantly, the performance of available unmixing algorithms highly relies on the determination of the number of end-members and the selection of their representative spectra. In drill-core hyperspectral data, highly mixed pixels of hardly pure mineral associations represent a challenge. Methods such as unmixing, band ratios and minimum wavelength analysis can only provide mineral abundances for spectrally diagnostic phases. Additionally, due

to the nature of the hyperspectral data and the spatial resolution allowed by commercially available sensors, the estimation of important mineralogical parameters in the characterization of complex ores (e.g., mineral association), is currently challenging.

We propose a novel machine learning approach to estimate mineral quantities in drill-core hyperspectral data. The procedure comprises four steps: 1) drill-core hyperspectral scanning (VNIR –SWIR), 2) computing mineral abundances in a small but representative area of a drill-core by using high-resolution mineralogical analyses (e.g., SEM-based image analyses using a Mineral Liberation Analyser), 3) linking the mineral abundances in this small area to their corresponding spectra by a multivariate regression model, and 4) estimating mineral abundances for the whole drill-core hyperspectral data by using the learned model. The multivariate regression problem in the proposed scheme is solved using three algorithms: random forest (RF), support vector machines (SVM) and feedforward artificial neural networks (FF-ANN). The proposed procedure allows the abundance estimation of the main mineral groups using their spectral characteristics (SWIR active) and using those SWIR active minerals additionally as proxies for the SWIR non-active minerals or mineral groups such as quartz, feldspar and sulphide. The obtained mineral abundance mapping results can be used for the calculation of additional mineralogical parameters, relevant to exploration and mining projects. As an example, the concept of mineral association at hyperspectral pixel scale based on relative abundances is introduced in the current study.

4.2 Data Acquisition

4.2.1 *Hyperspectral Data*

The hyperspectral data used in this study were acquired from unpolished halves of diamond drilling core samples with a SisuROCK drill-core scanner equipped with an AisaFENIX hyperspectral sensor (Spectral Imaging Ltd., Oulu, Finland). The scanner is a fully automatic hyperspectral imaging workstation which employs a tray table which carries the drill-core trays or samples under the field-of-view of the spectrometer. The AisaFENIX camera implements two sensors to cover the VNIR and SWIR regions of the electromagnetic spectrum. The sensor specifications and acquisition settings are presented in Table 4-1.

Table 4-1 AisaFENIX sensor specification and setup for hyperspectral data acquisition.

Wavelength Range	VNIR 380–970 nm SWIR 970–2500 nm	**Integration Time**	VNIR 15 ms SWIR 4 ms
Sampling Distance	VNIR 1.7 nm SWIR 5.7 nm	Spatial Binning	VNIR 2 SWIR 1
Number of Bands	450	Frame Rate	15 Hz
Samples	384	Scanning Speed	25.06 mm/s
Spatial Resolution	1.5 mm/pixel	Field of View (FOV)	32.3°
Detector	CMOS (VNIR) Stirling cooled MCT (SWIR)	Spectral Binning	VNIR 4 SWIR 1

The conversion from radiance to reflectance of the hyperspectral data was performed within the acquisition software (LUMO Scanner version 2018-5, Spectral Imaging Ltd., Oulu, Finland) using PTFE reference panels (>99% VNIR and >95% SWIR). To correct the sensor-specific optical distortions (i.e., fish-eye and slit-bending effects on the images) and the spatial shift between the VNIR and SWIR sensors, the toolbox MEPHySTo (Jakob et al., 2017) was used. To avoid bands with little or no coherent information, the

data were spectrally resampled to 480—2500 nm by removing the first 30 bands. The Savitzky–Golay filter was applied to decrease noise while preserving spectral features (Ruffin and King, 1999). Principal component analysis (PCA) (Rodarmel and Shan, 2002) was performed on the hyperspectral dataset for data dimensionality reduction and de-correlation while preserving 99.9% of the information.

4.2.2 *Scanning Electron Microscopy-Based Mineral Liberation Analysis.*

Regions considered representative based on visual observations for the mineralogical variation within the drill-core samples were cut and prepared into polished thin sections. The preparation process consisted of grinding and polishing the sample surface followed by coating with a thin carbon layer to avoid surface charging during data acquisition. The grinding and polishing led to the removal of around 300 μm of material between the surface analysed with the hyperspectral sensor and the surface subjected to the high-resolution mineralogical analysis. Considering the sample morphology and orientation of structural features the mineralogical variation is considered negligible for the encountered shift.

The quantitative mineralogical data were acquired from the thin sections using an automated approach. The analyses were carried out using Scanning Electron Microscope (SEM)-based Mineral Liberation Analysis (MLA) (Fandrich et al., 2007; Kern et al., 2018b). For this, a FEI Quanta 650 F field emission SEM instrument (FEI, Hillsboro, OR, USA), equipped with two Bruker Quantax X-Flash 5030 energy dispersive X-ray (EDX) detectors (Bruker, Billerica, MA, USA) and the MLA Suite software package (version 3.1.4.686, FEI, Hillsboro, OR, USA) were used. The grain-based X-ray mapping (GXMAP) mode was used to collect the mineralogical information as follows: the MLA software collects the back-scattered electron images (BSE) and uses them to effectively distinguish individual mineral grain boundaries based on the grey scale variations. The grey scale values of the BSE images are proportional to the average atomic density of the mineral grains and are used to provide a first mineralogical segmentation. The identification of minerals is performed based on X-ray analysis by placing a closely-spaced grid on a particle in the BSE image and collecting the X-ray data at the defined points of the grid. When dealing with fine grained material of lower size than the placed grid, the GXMAP mode allows us to collect additional spectra where variations in the BSE image are observed in between the measured grid points. Finally, the mineral is determined by matching the resultant spectrum of energy peaks with a reference library of X-ray spectra provided by the instrument company (FEI, Hillsboro, OR, USA), or from sample extracted spectra analysed based on peak locations and intensities (Gu, 2003). Specifications of the operating conditions used in this study are shown in Table 4-2.

Table 4-2 Operating conditions and parameters used for the acquisition of high-resolution SEM-MLA mineralogical data.

SEM Settings		MLA Settings	
Acceleration voltage (kV)	25	Pixel size (μm)	3
Probe current (nA)	10	Step size (pixels)	6 × 6
Frame width (pixels)	1500	Acquisition time (ms)	5
BSE calibration (Au)	254	Minimum grain size (pixels)	4

For classification, a mineral list was developed using the mineral reference editor in online mode. The resulting mineral list contained a total of 59 entries. However, for the integration of the HSI with SEM-MLA, further grouping was performed in this paper, such as considering all feldspars in one class, all white micas in another or, all sulphides, sulphosalts and gold in another. Accessory minerals were included in the final grouping labelled as "others". As a result, ten main mineral groups are considered: white mica (WM), biotite (Bt), chlorite (Chl), amphibole (Amp), carbonate (Cb), gypsum (Gp), feldspar (Fsp), quartz (Qz), sulphide (Sp) and other.

4.3   Data Description

For testing the proposed methodology, 5 samples, labelled DC-1 to DC-5, from different locations within the Bolcana porphyry copper-gold system (Blannin et al., 2019; Ivascanu et al., 2019; Milu et al., 2003; Laura Tusa et al., 2019) were analysed. Hyperspectral images were acquired on the halves cores after which thin sections were prepared from selected regions of interest and analysed by SEM-MLA. Each region is further labelled as a, b and/or c starting from the left-hand side of the drill-core sample as illustrated in Figure 4-1. The ore minerals in the studied system are chalcopyrite, bornite, covellite, chalcocite and gold. Gold is dominantly present as fine inclusions in pyrite and chalcopyrite. The main encountered alteration types are potassic, sodic—calcic, phyllic and argillic. In the studied samples the first three are present, some samples presenting a transitional character and are described in this section. Please see Sillitoe, (2010) for details on the mineralogical characteristics of the alteration styles typically associated with porphyry Cu-Au systems.

While the summary of the results for each sample is presented in the results section, an emphasis is made on DC-1 in order to illustrate all the potential information that can be extracted using the proposed methodology. Therefore, a more detailed description of this sample is available in the current section. Sample DC-1 consists of a diorite porphyry. Hydrothermal alteration in this sample appears transitional between potassic, represented by the presence of biotite and potassic feldspar and sodic-calcic characterized by the plagioclase-chlorite assemblage. Chlorite is more abundant than biotite in the first two thin sections, "a" and "b". The third thin section, though, due to the lower vein density and implicit associated alteration presents significant amounts of biotite disseminated as well as in clusters in the matrix. Plagioclase feldspar is dominant in all three thin sections, near the veins however, an increase in potassic feldspar is observed.

Thin section "a" of sample DC-1 captures three main vein types: an oblique early quartz vein which exhibits a low intensity white mica alteration halo likely associated with a younger cross-cutting gypsum vein that has a sulphide centerline and a wide white mica-chlorite alteration halo (top). The alteration halo here is mica-dominant in the proximity of the vein and chlorite-dominant towards its edges. The third vein present in section "a" consists of quartz with a gypsum centerline and a spotty, low intensity white mica alteration halo (bottom). Thin section "b" captures three main vein types as well: two sub-vertical veins consist of variable ratios of gypsum and quartz and are surrounded by a strong white mica low-chlorite alteration halo. Compositionally, these veins appear to be a mixture between the first and third veins mentioned for thin section "a"; they have, however, a different morphology. In proximity to sub-horizontal veinlets in the lower half of the thin section, an increase in the pyrite and chlorite content is observed. The two sub-horizontal veinlets show strong similarity with the horizontal veins in the first thin section. The alteration intensity surrounding the sub-horizontal veinlets appears to be related to complex interactions with pre-existing veinlets in this area of section

"b". Thin section "c" hosts several fine veinlets, of highest width, the two cross-cutting ones near the top of the thin section. The veinlets consist of variable amounts of quartz, gypsum, pyrite and white mica and present a white mica and chlorite alteration halo. Similar to the subvertical veins in thin section "b" these veins appear to have a composition intermediate between the horizontal veins in thin section "a". Unlike the two veins in thin section "b" however, the extent of the alteration halo is much lower.
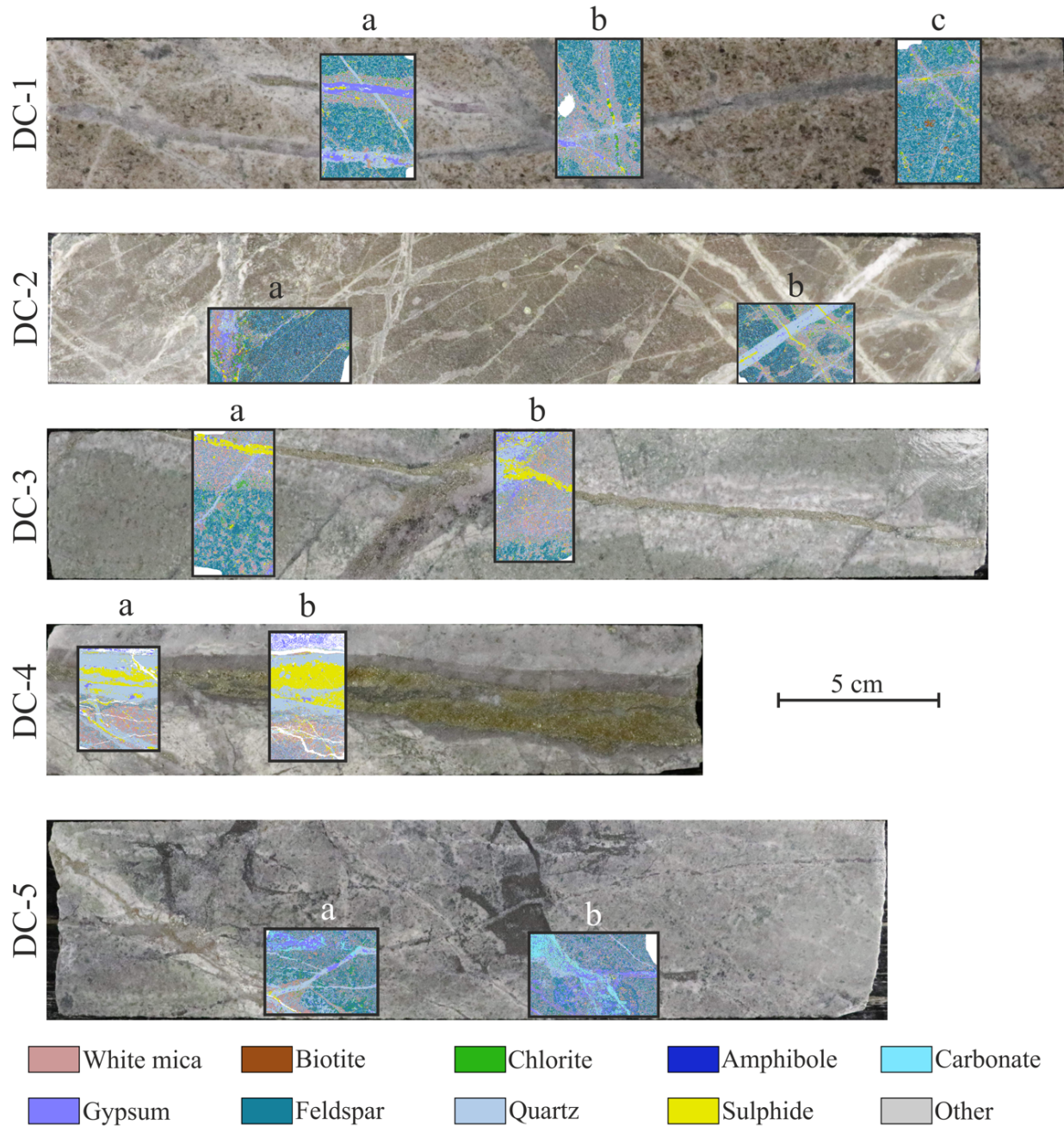
Figure 4-1 RGB photograph of the analysed drill-cores (labelled on the left-hand side from DC-1 to DC-5) with overlain high-resolution mineral maps (labelled a, b and c) obtained by SEM-MLA.

Sample DC-2 is marked by pervasive potassic alteration characterized by the presence of K-feldspar, biotite and minor chlorite. Two main vein types are present in this sample: veins hosting dominantly sulphide which show a strong phyllic alteration halo caused by the late reaction of mineralizing hydrothermal fluids with the host rock. The second vein type comprises dominantly quartz with sulphide or with sulphide-calcium

sulphate (gypsum or anhydrite) centreline. Additional veins of varying composition are present in the sample (left-hand side as illustrated in Figure 4-1). They appear to be the result of complex reopening and cross-cutting of the previously described veins.

A sodic-phyllic rock matrix hosting two main vein-types characterizes sample DC-3. The first vein comprises of sulphide and presents a large white mica alteration halo. The second vein type consists predominantly of quartz, calcium sulphate and sulphide. The changing symmetry and mineral association in these latter veins indicate the reopening of an initially present quartz vein.

Sample DC-4 is characterized by the presence of intense phyllic alteration in the matrix related to the thick pyrite-quartz-gypsum vein cross-cutting the sample. Additional fine veinlets comprising mostly quartz and pyrite are cutting the mica-rich matrix.

The matrix in sample DC-5 consists of dominantly feldspar and subordinately white mica. Three main vein types can be observed in the samples: a sulphide dominant vein with a broad white mica alteration halo, quartz veinlets and carbonate iron-oxide veins which show low or absent alteration halos.

For the understanding of the modal composition of the available thin sections, the abundances of the minerals or mineral groups for all the analysed thin sections are illustrated in the bar charts in Figure 4-2 (left). For most samples, quartz and feldspar represent the main rock-forming minerals. There is, however, a variation in the extent of alteration of feldspar to white mica ranging from low (DC-2a) to high (DC-4). In most of the analysed samples, the amphibole is to a large extent altered to chlorite and/or biotite. Biotite is only present in significant amounts in sample DC-2 and DC-1 "c". The variation of the quartz, carbonate and gypsum contents is related to the surface abundance of the veins and veinlets filled mostly by these three minerals. While quartz and gypsum are present in significant amounts in all thin sections, carbonate is mainly represented in sample DC-5. The class "sulphide" comprises mainly pyrite, chalcopyrite, bornite, chalcocite and covellite but minor amounts of native gold hosted as inclusions in pyrite and chalcopyrite is also considered. While pyrite is not an ore mineral by itself, it frequently represents the host of micron-size native gold inclusions. The sulphide content in the thin sections ranges from around 1 area % in DC-5b to almost 30 area % in DC-4b. The main target being the quantification and understanding of the distribution of sulphide minerals within the presented samples, their mineral association is also analysed and presented in the bar chart in Figure 4-2 (right).

While an influence of the modal mineralogy can be observed on the mineral association, a strong increase in the white mica, chlorite, biotite, carbonate and gypsum can be seen. This is the result of the distribution of these minerals within or surrounding the veins also hosting the bulk of sulphides. The listed gangue minerals, unlike the sulphide, show distinct absorption features in the VNIR-SWIR region of the electromagnetic spectrum and may, therefore, be used as proxies for the distribution of the ore minerals.

While an influence of the modal mineralogy can be observed on the mineral association, a strong increase in the white mica, chlorite, biotite, carbonate and gypsum can be seen. This is the result of the distribution of these minerals within or surrounding the veins also hosting the bulk of sulphides. The listed gangue minerals, unlike the sulphide, show distinct absorption features in the VNIR-SWIR region of the electromagnetic spectrum and may, therefore, be used as proxies for the distribution of the ore minerals.
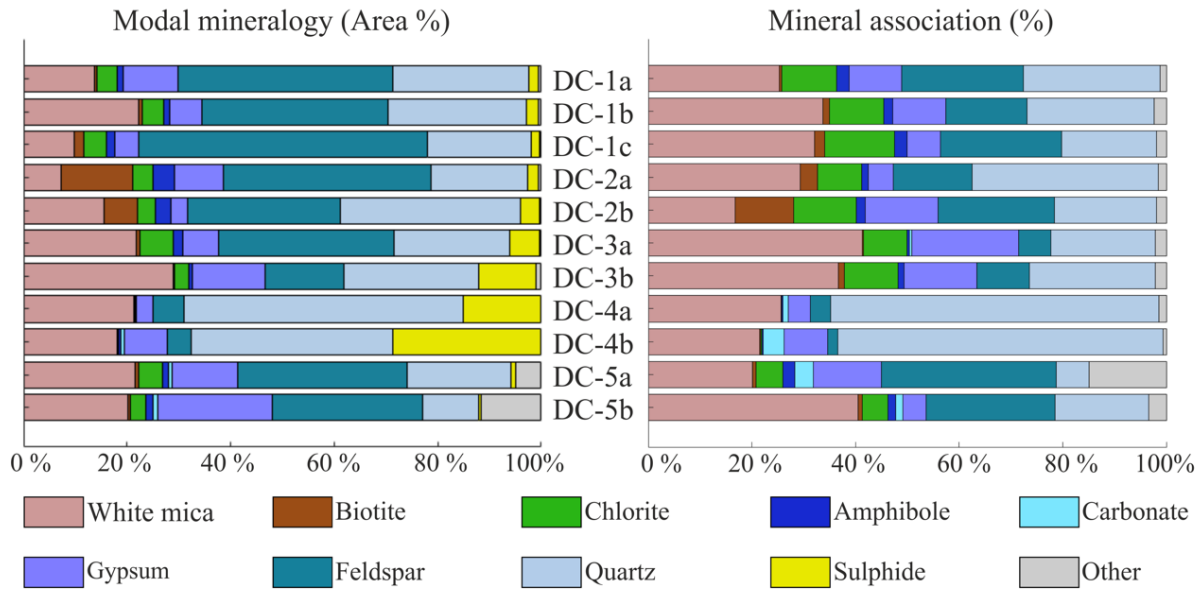
Figure 4-2 Modal mineralogy and mineral association of analysed thin sections illustrated through mineral maps in Figure 4-1. The labels of each sample and thin section are illustrated between the two bar charts.

4.4 Methodological Framework

4.4.1 HSI—SEM-MLA Data Integration

For the proposed approach, the SEM-MLA data is upscaled by adopting a re-sampling procedure. The two-dimensional SEM-MLA mineral map with high spatial resolution is transformed to a three-dimensional mineral abundance map with the lower spatial resolution of the hyperspectral data (Contreras Acosta et al., 2019). The third dimension consists of the relative abundance of each mineral present in each SEM-MLA map re-sampled to the hyperspectral pixel size (Figure 4-3). Note that a co-registration stage is needed after the re-sampling of the SEM-MLA data. Following Acosta et al., 2019, the structural features, such as veins, the mineral composition, and spectral responses are used to find suitable tie points. As a result of the co-registration each pixel where the SEM-MLA data is available is characterised by two vectors: the hyperspectral feature vector Xi of dimension d (i.e., the number of bands in the hyperspectral data) or r (number of extracted features) and a mineral abundance vector Yi containing the corresponding fractional abundances of the minerals identified by SEM-MLA.

Once the hyperspectral and SEM-MLA data are co-registered, they are divided into training and testing. For this procedure the following approach is adopted:

Using 50% randomly selected pixels from all thin section regions within one drill-core sample for training, the remaining drill-core hyperspectral data for testing. The validation is performed using the remaining 50% data points from the MLA regions.

Using 1 thin section for training and the second for testing and validation for all drill-core samples.

For DC-1, where 3 thin sections are available, an additional test is performed using 2 thin sections for training and the last for testing and validation.

As can be seen from the main flowchart, shown in Figure 4-4, the proposed workflow is carried out in three main phases. In the training phase, different regression models (i.e., RF, SVM and FF-ANN) are trained following any of the three approaches mentioned before. In the prediction phase, the learned models are used to predict the mineral abundances on the entire drill-core samples. Finally, in the validation phase, the root mean square error (RMSE) (Draper et al., 2013) is calculated on the remaining SEM-MLA test data to assess the performance of the abundance mapping.

$$Mineral\ Abundances = [5, 20, 0]$$
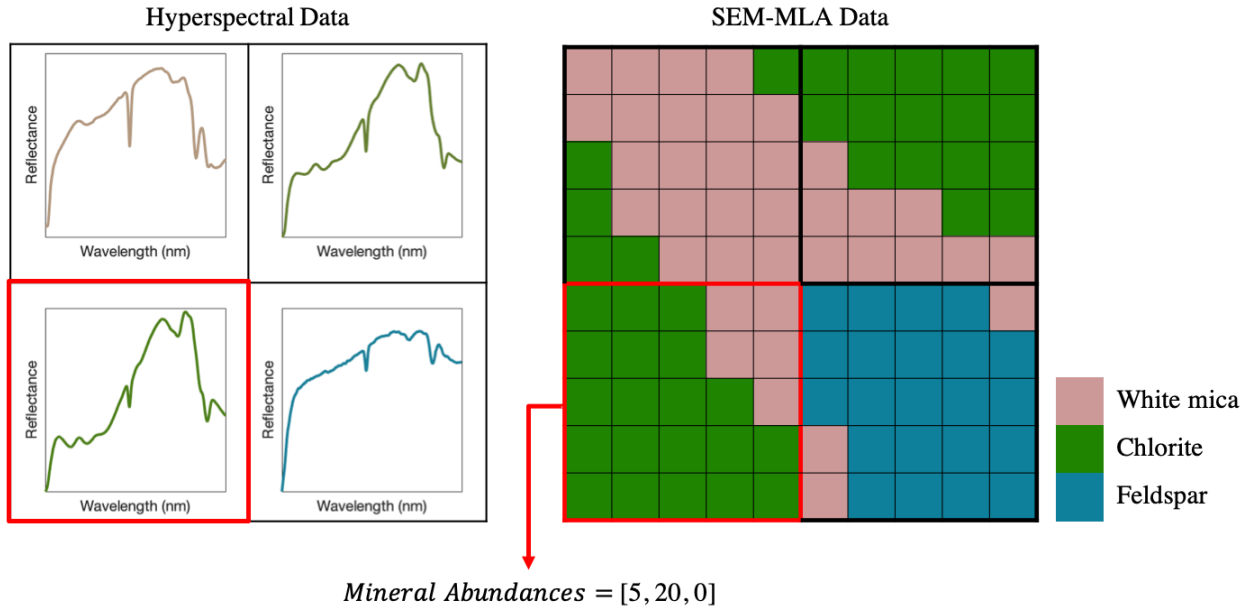
Figure 4-3 Graphical illustration of the co-registration and resampling process for the SEM-MLA to hyperspectral data. In red, the size of a hyperspectral pixel characterized by a mineral mixture in the SEM-MLA data and a spectrum in the hyperspectral data. The colour of the spectra (left) is given by the mixture ratio of the minerals illustrated in the SEM-MLA simplified example (right).
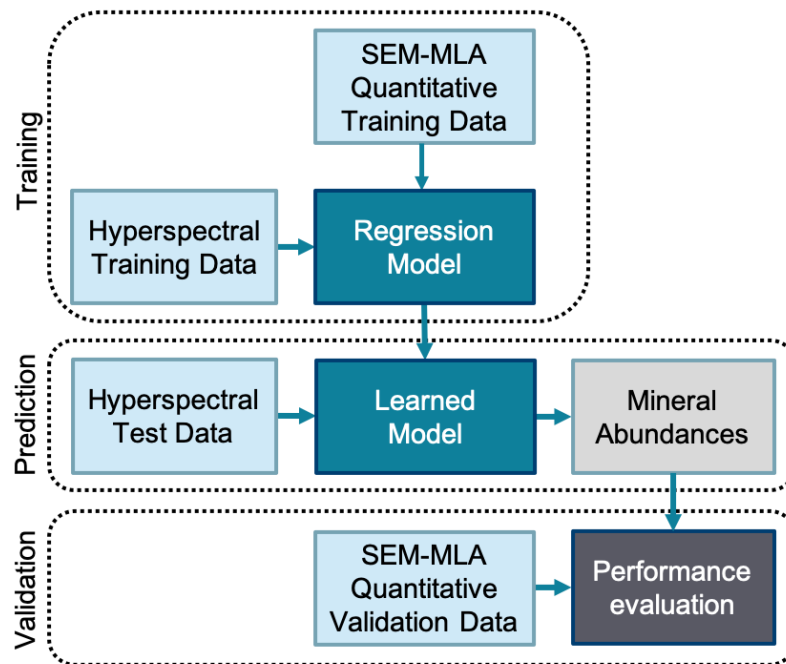
Figure 4-4 Flowchart illustrating the three main stages of the proposed workflow.

Two analysis types are further performed on the resulting mineral abundance data. For each validation set, the modal mineralogy is calculated based on the average abundance of each mineral phase in each pixel and compared to the modal mineralogy data obtained from SEM-MLA. Additionally, the concept of mineral association is adapted from the automated mineralogy field (Figure 4-2). There, the mineral association is calculated by counting the neighbouring pixels to a specific target mineral. Slight changes in the approach have to be made when the spatial resolution of the hyperspectral data is used. The association of the main target group, i.e., sulphide, is a fundamental aspect in the present geological study. For each hyperspectral pixel the estimated mineral abundance of each mineral phase, except of the target, is normalized by the abundance of sulphide in the respective pixel. While this approach does not directly indicate the grain contact between the two minerals (or rather mineral groups) it can be seen as the probability of their association and occurrence at the scale of hyperspectral data resolution. The mineral association is calculated on the ground truth or validation data as well as on the estimated abundances calculated with the three proposed regression models.

4.4.2   Random Forest Regression

Random forests (RFs) are currently one of the most popular supervised learning techniques for classification and regression problems (Ghamisi et al., 2017; Rodriguez-Galiano et al., 2015; Waske et al., 2009). RFs are ensemble-based algorithms in which several models (trees) are running in parallel with randomized sampling. The individual results of these trees are then combined into the final prediction by an averaging process (Breiman, 2001). For regression purposes, the trees are given numerical values as predictors whereas in classification problems they are fed class labels. The RF technique is desirable in cases where only few training samples are available, as is usually the case in drill-core hyperspectral imaging.

4.4.3   Support Vector Regression

The aim of support vector machines (SVMs) is to search for hyperplane decision boundaries to define a linear prediction model (Cortes and Vapnik, 2001; Vapnik, 1999). To locate and orientate the hyperplane, only the samples that are close to the hyperplane, so-called support vectors, have an influence. Therefore, SVMs perform well when a limited number of well-chosen training samples are available (Cortes and Vapnik, 2001; Ghamisi et al., 2017; Vapnik, 1999). This model can be used for classification or regression tasks. SVMs were originally proposed to solve linear problems. However, decision boundaries are often non-linear. To cope with the non-linearity problem, the kernel-based SVMs were introduced to project the data points into a higher dimensional feature space where the samples are linearly separable (Ghamisi et al., 2017).

4.4.4   Artificial Neural Network Regression

Artificial neural networks have become some of the most popular methods in regression and classification because of their success in capturing the non-linearity relation between independent and dependent variables (Specht, 1991). We chose a so-called "feedforward neural network" (FF-ANN) (Rumelhart and Hintont, 1986), as it fits the requirements of the problem at hand. In a feedforward network, each neuron in one layer is directly connected to neurons of the next layer with no cycle between layers. The applied neural network consists of an input layer, one hidden layer, and an output layer. Each neuron of a layer

is computed by the product sum of the neurons of the previous layers plus a bias for the neuron (Ghamisi et al., 2017). A sigmoid function is applied for activation.

4.5 Experimental Results

In order to showcase the suitability of the proposed approach, the first drill-core sample presented in the data section (DC-1) is used. The remaining four samples have been analysed following the same procedure. A summary of the results is presented in this section followed by a complete illustration of the results in Appendix 4A. Additionally, all numerical results are presented in the Electronic Supplementary Materials (Table S1).

From the entire drill-core sample (DC-1), the VNIR-SWIR hyperspectral data of size 33 by 189 pixels. The 420 spectral bands cover wavelengths from 480 nm to 2500 nm. The hyperspectral data is subjected to PCA leading to the reduction in dimensionality to 13 principal components in the third dimension. Moreover, the high-resolution mineralogical data obtained from representative regions (thin sections "a", "b" and "c") were used. In the thin section regions of the drill-core sample, each hyperspectral pixel covers an area of 1.5 by 1.5 mm^2, which is characterized by about 250,000 pixels in the SEM-MLA image. The fractional abundances were computed by considering the frequency of the identified minerals in the corresponding region of the SEM-MLA image for each hyperspectral pixel. To have more consistent results, we considered a threshold of 250,000 pixels (i.e., a hyperspectral pixel size) in each thin section region, for discarding minerals which have a very low frequency in the original SEM-MLA image. Taking this factor into consideration, the following six mineral classes remained: white mica (WM), biotite (Bt), chlorite (Chl), amphibole (Amp), gypsum (Gp), feldspar (Fsp), quartz (Qz), sulphide including sulphosalts and native gold (SP); less abundant minerals were grouped as "other". Because of the low abundance of biotite and accessory minerals in thin sections "a" and "b", the number of mineral classes considered was decreased accordingly. The test setups presented in the methodological framework section are used.

Cross-validation has been used to find the optimal parameters in order to train three models by internally resampling the training data. The main tested parameter ranges for each algorithm are presented in Table 4-3. The setups were chosen according to the lowest associated root-mean-square error (RMSE) based on cross-validation within 30 averaged iterations.

Table 4-3 Parameters and parameter ranges for the choice in optimum setup of the three tested algorithms.

RF	SVM	FF-ANN
Nb. of trees – 500 : 600	*Kernel* – Radial Basis Function *Cost* – 2 : 0.5 : 4 *Sigma* – 5 : 0.5 : 7	*Training function* – Scaled conjugate gradient backpropagation *Nb. of hidden layers* – 1 *Nb. of neurons* – 30 : 10 : 80

4.5.1 Mineral Abundance and Association Mapping

With the first experimental setup, presented in the methodological framework, 50% randomly distributed samples of the available thin section regions were used to train the regression models the mineral abundances estimation in the entire drill-core sample (Figure 4-5).

Based on the visual analysis of the core and results analysis, RF and FF-ANN show better results in estimating the abundance of minerals with local distribution and small concentrations. With respect to matrix

mineralogy, while biotite is well estimated by SVM in comparison with RF and FF-ANN, other major components of the matrix such as feldspar present a rather poor estimation. Similar performances of the algorithms can be observed for vein mineral components such as gypsum and sulphide.
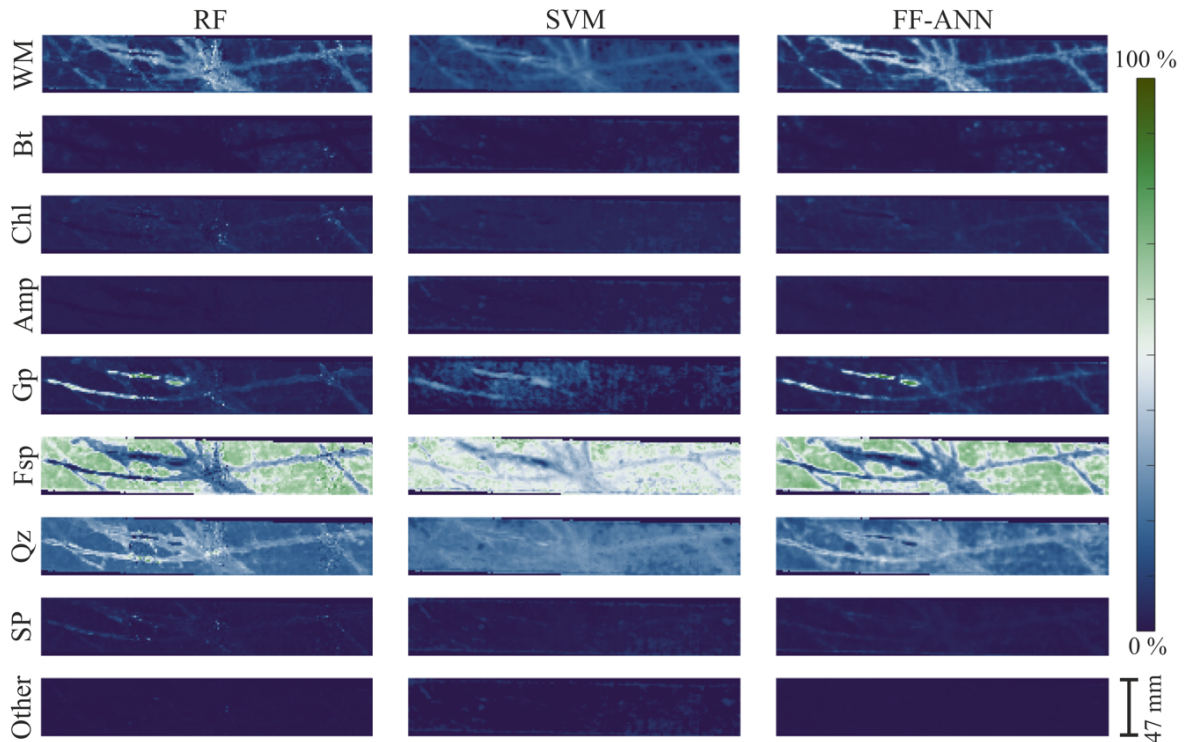
Figure 4-5 Drill-core mineral abundance maps of white mica (WM), biotite (Bt), chlorite (Chl), amphibole (Amp), gypsum (Gp), feldspar (Fsp), quartz (Qz), sulphide (SP) and accessory minerals (Other) using randomly distributed 50% of the available ground truth data for training for random forest (RF), support vector machine (SVM) and feed-forward neural network (FF-ANN) regressions.

With regards to the samples DC-2 (Figure 4-10), DC-3 (Figure 4-12), DC-4 (Figure 4-14) and DC-5 (Figure 4-16), using 50% of the available ground truth data for training, RF and FF-ANN show good, similar performances, while SVM shows limitations specifically in transitional areas between veins and matrix. Among the SWIR-diagnostic minerals, white mica, biotite and carbonate appear well mapped in all the samples, chlorite is slightly underestimated in samples DC-2 and DC-3 and gypsum is overestimated in sample DC-5. Among the SWIR non-diagnostic minerals, quartz shows the highest mapping inconsistencies between vein and matrix, particularly for samples DC-4 and DC-5. Sulphide, however, appears to be well mapped in most areas of the samples.

The quantitative evaluation of the mineral abundance mapping through the calculation of the RMSE supports the visual observations (Table 4-4). All three tested algorithms present low RMSEs and prove suitable to be used for mineral abundance mapping purposes. RF shows the lowest overall RMSE of 0.07, followed by FF-ANN with 0.08 and SVM with 0.1. Regarding the per class RMSE, RF and FF-ANN show similar results with the largest error associated with quartz, which can be the result of the lack of diagnostic absorption features in the VNIR-SWIR regions of the electromagnetic spectrum. SVM on the other hand shows larger per class errors for feldspar together with an increase in the error on white mica distribution. This can be explained by a misclassification between the two mineral groups. The mineral association of the sulphide in each pixel was calculated from the results of the mineral abundance mapping. Based on this calculation an equivalent overall

performance of the methods was obtained (Table 4-5). For each of the methods, the error for the association of sulphide with feldspar is the largest.

Table 4-4 Evaluation of the three tested methods for the mineral abundance mapping of DC-1 through overall RMSE and per class RMSE values.

Method	RMSE	RMSE per Class								
		WM	Bt	Chl	Amp	Gp	Fsp	Qz	SP	Other
RF	0.07	0.06	0.06	0.06	0.06	0.06	0.05	0.08	0.06	0.05
SVM	0.10	0.12	0.03	0.05	0.01	0.12	0.21	0.12	0.04	0.02
NN	0.08	0.06	0.06	0.07	0.06	0.06	0.07	0.09	0.07	0.07

Table 4-5 Evaluation of the three tested methods for the mineral association mapping of DC-1 through overall RMSE and per class RMSE values.

Method	RMSE	RMSE per Class								
		WM	Bt	Chl	Amp	Gp	Fsp	Qz	Other
RF	0.05	0.05	0.00	0.01	0.00	0.02	0.13	0.05	0.00
SVM	0.06	0.06	0.01	0.02	0.00	0.02	0.15	0.06	0.00
NN	0.05	0.05	0.00	0.01	0.00	0.02	0.13	0.05	0.00

To assess the importance of sampling and representativeness of the SEM-MLA regions, thin sections "a", "b" (Figure 4-6) and "a + b" (Figure 4-7) of sample DC-1 were used for training the models in order to estimate the mineral abundance and association in thin section "c".

For the three used methods, strong differences in the estimates of sample "c" mineralogy can be observed when using thin sections "a" and "b" for training (Table 4-6).
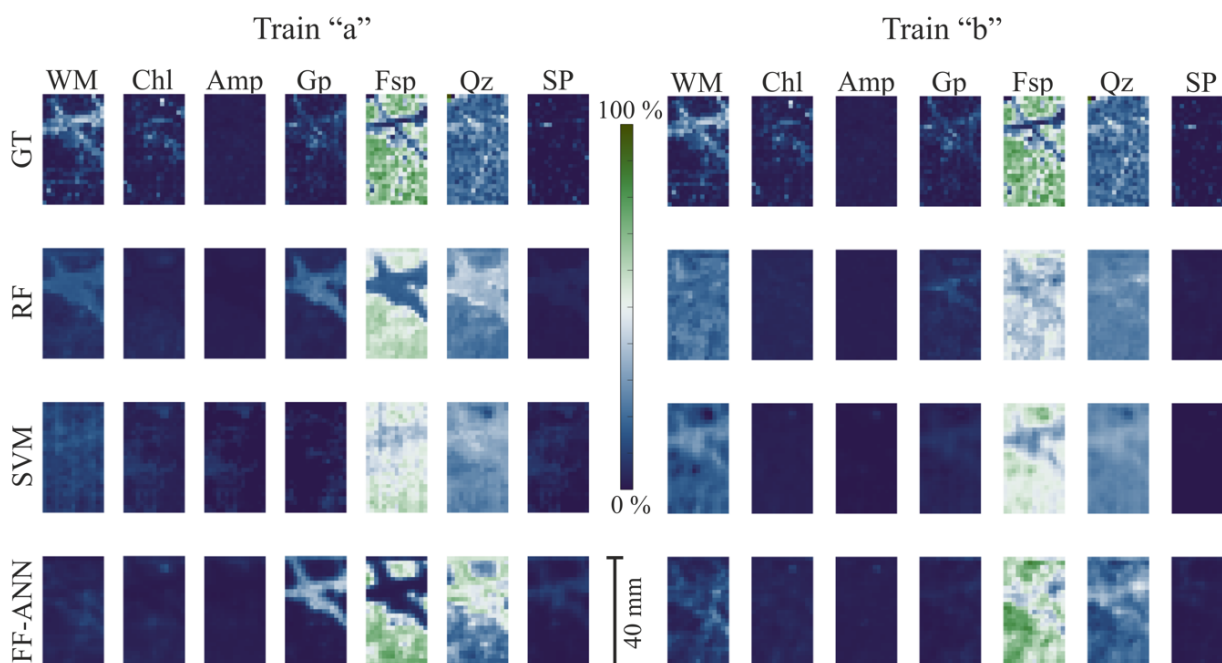
Figure 4-6 White mica (WM), chlorite (Chl), amphibole (Amp), gypsum (Gp), feldspar (Fsp), quartz (Qz) and sulphide (SP) abundance maps of TS-1c using TS-1a and TS-1b, respectively, for the training of random forest (RF), support vector machine (SVM) and feed-forward neural network (FF-ANN) regressions. The ground truth (GT) resized MLA data is presented for comparison.
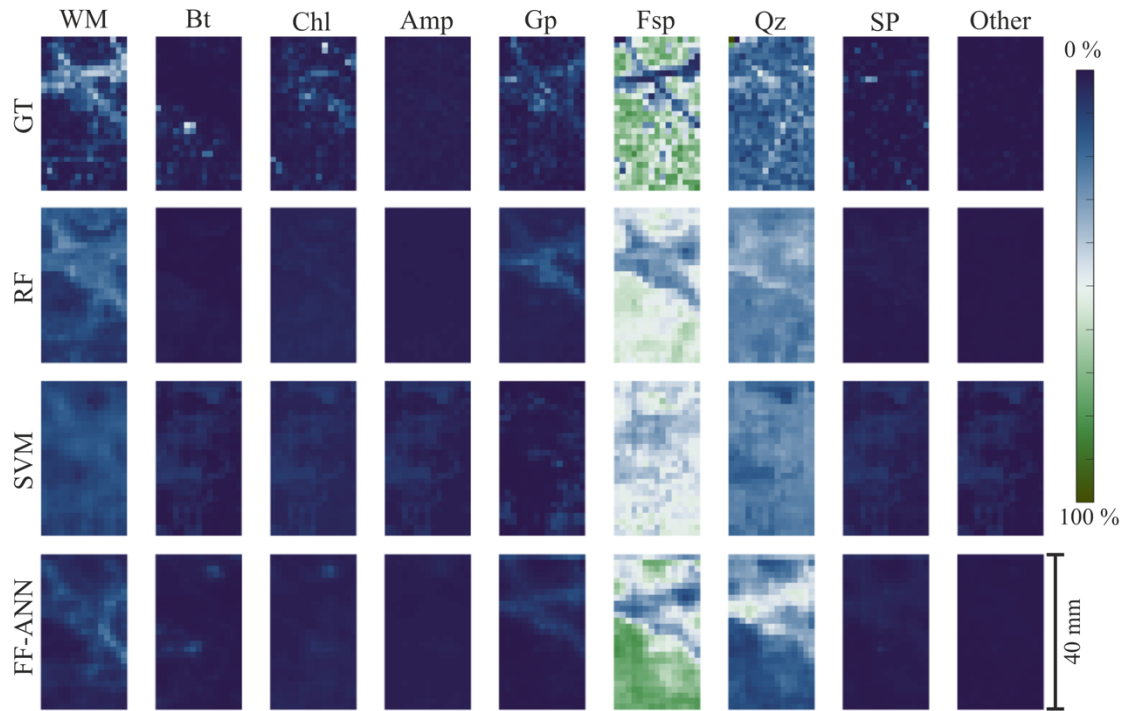
Figure 4-7 White mica (WM), biotite (Bt), chlorite (Chl), amphibole (Amp), gypsum (Gp), feldspar (Fsp), quartz (Qz), sulphide (SP) and accessory minerals (Other) abundance maps of TS-c using TS-a + TS-b for the training of random forest (RF), support vector machine (SVM) and feed-forward neural network (FF-ANN) regressions. The ground truth (GT) MLA data is presented for comparison.

Table 4-6 Evaluation of the three tested methods for the mineral abundance mapping of DC-1 thin section "c" through overall RMSE and per class RMSE values using different samples for training.

	Train and Valid. Data	Overall RMSE	RMSE per Class								
			WM	Bt	Chl	Amp	Gp	Fsp	Qz	SP	Other
RF	50%–50% rand. sel	0.07	0.06	0.06	0.06	0.06	0.06	0.05	0.08	0.06	0.05
	Train a—Test c	0.10	0.08		0.06	0.01	0.06	0.18	0.13	0.03	
	Train b—Test c	0.12	0.15		0.05	0.01	0.05	0.24	0.09	0.03	
	Train a + b—Test c	0.08	0.09	0.04	0.05	0.01	0.04	0.18	0.11	0.03	0.01
SVM	50%–50% rand. sel	0.10	0.12	0.03	0.05	0.01	0.12	0.21	0.12	0.04	0.02
	Train a—Test—c	0.10	0.10		0.06	0.02	0.06	0.20	0.12	0.04	
	Train b—Test—c	0.09	0.11		0.06	0.02	0.04	0.18	0.10	0.04	
	Train a + b—Test c	0.09	0.09	0.05	0.06	0.03	0.07	0.21	0.09	0.05	0.03
FF-ANN	50"–50% rand. sel	0.08	0.06	0.06	0.07	0.06	0.06	0.07	0.09	0.07	0.07
	Train a—Test—c	0.17	0.12		0.07	0.02	0.14	0.28	0.27	0.06	
	Train b—Test—c	0.12	0.12		0.07	0.02	0.06	0.25	0.14	0.04	
	Train a + b—Test c	0.10	0.10	0.05	0.06	0.01	0.05	0.20	0.16	0.04	0.01

The use of thin section "a" provides particularly better results for white mica and feldspar, which are confused using region "b" that hosts distinctly lower amounts of feldspar. On the other hand, using thin section "a" for training leads to an overestimation of the gypsum content. The use of both thin sections ("a" + "b") for training improves the classification leading to lower overall and per class RMSE values. As for the remaining drill-core samples, RF outperforms SVM and FF-ANN for most training scenarios, except when using thin section "b" for training. A similar effect of sampling on the RMSE evaluation can be seen for the mineral association mapping of DC-1 in all the scenarios (**Error! Not a valid bookmark self-reference.**).

Table 4-7 Evaluation of the three tested methods for the mineral association mapping of DC-1 thin section "c" through overall RMSE and per class RMSE values using different samples for training.

	Train and Validation data	Overall RMSE	RMSE per Class							
			WM	Bt	Chl	Amp	Gp	Fsp	Qz	Other
RF	50%–50% rand. sel	0.05	0.05	0.00	0.01	0.00	0.02	0.13	0.05	0.00
	Train a—Test—c	0.06	0.05		0.04	0.01	0.05	0.05	0.10	
	Train b—Test—c	0.03	0.04		0.03	0.00	0.01	0.01	0.02	
	Train a + b—Test c	0.02	0.01	0.01	0.04	0.01	0.00	0.01	0.06	0.00
SVM	50%–50% rand. sel	0.06	0.06	0.01	0.02	0.00	0.02	0.15	0.06	0.00
	Train a—Test—c	0.05	0.05		0.02	0.02	0.07	0.06	0.06	
	Train b—Test—c	0.04	0.05		0.05	0.01	0.01	0.02	0.05	
	Train a + b—Test c	0.03	0.05	0.03	0.01	0.03	0.06	0.03	0.00	0.03
FF-ANN	50%–50% rand. sel	0.05	0.05	0.00	0.01	0.00	0.02	0.13	0.05	0.00
	Train a—Test—c	0.17	0.13		0.05	0.01	0.15	0.24	0.28	
	Train b—Test—c	0.07	0.07		0.04	0.00	0.04	0.15	0.00	
	Train a + b—Test c	0.05	0.09	0.00	0.05	0.01	0.02	0.06	0.10	0.00

For the remaining samples, each having two regions analysed by SEM-MLA, the mineral abundance estimations obtained using the second setup are illustrated in Figure 4-11 (DC-2), Figure 4-13 (DC-3), Figure 4-15 (DC-4) and Figure 4-17 (DC-5).

The tested methods show similar results for mineral abundance and association mapping on the remaining four drill-cores (Table 4-8). Overall, RF performs best, followed by FF-ANN and then SVM. For samples DC-1, DC-2, DC-3 and DC-5 each method results in comparable errors where similar amounts of training data are used. For sample DC-4 the overall RMSE values are higher, exceeding 0.2 depending on training data. For each sample the selection of the training data location plays an important role that is reflected into the RMSE evaluation.

Table 4-8 Methods evaluation for the mineral abundance and association mapping of the remaining four samples through overall RMSE and per class RMSE values using different data for training.

Sample ID	Train and Validation data	Mineral abundance mapping			Mineral association mapping		
		RF	SVM	FF-ANN	RF	SVM	FF-ANN
DC-2	50%–50% rand. sel	0.07	0.09	0.08	0.07	0.07	0.07
	Train a—Test—b	0.11	0.18	0.10	0.09	0.17	0.09
	Train b—Test—a	0.14	0.14	0.19	0.13	0.16	0.13
DC-3	50%–50% rand. sel	0.08	0.11	0.09	0.12	0.12	0.12
	Train a—Test—b	0.14	0.14	0.17	0.09	0.18	0.07
	Train b—Test—a	0.11	0.14	0.14	0.10	0.11	0.09
DC-4	50%–50% rand. sel	0.12	0.20	0.14	0.12	0.12	0.12
	Train a—Test—b	0.24	0.29	0.24	0.08	0.10	0.05
	Train b—Test—a	0.16	0.20	0.19	0.04	0.16	0.07
DC-5	50%–50% rand. sel	0.07	0.10	0.08	0.03	0.03	0.03
	Train a—Test—b	0.11	0.13	0.11	0.05	0.18	0.05
	Train b—Test—a	0.13	0.13	0.15			

4.5.2 Modal Mineralogy

The modal mineralogy in area % is calculated by averaging the mineral abundances over the entire tested sample. To evaluate the modal mineralogy estimates sample DC-1 is used and the estimates are compared to the ground truth, using 50% of the available SEM-MLA data for training and 50% for testing (Table 4-9).

Table 4-9 Ground truth and estimated modal mineralogy of the SEM-MLA test regions of DC-1, using 50% randomly selected data for training.

Method	Modal Mineralogy (Area %)								
	WM	Bt	Chl	Amp	Gp	Fsp	Qz	SP	Other
GT	16.0%	1.1%	4.3%	1.8%	7.3%	42.3%	24.9%	1.8%	0.5%
RF	15.8%	1.1%	4.3%	1.7%	7.4%	42.2%	25.1%	2.0%	0.5%
SVM	14.2%	1.2%	3.8%	1.8%	7.8%	44.3%	24.4%	1.8%	0.6%
NN	15.8%	1.1%	4.3%	1.7%	7.3%	42.6%	24.8%	1.9%	0.5%

The estimates for all methods show good results with the highest RMSE value of 0.01 obtained with SVM. The complete modal mineralogy results are available in Table S1. The results for all the setups and all samples and methods are illustrated in Figure 4-8 by plotting the estimated values from RF (left), SVM (centre) and FF-ANN (right) against the ground truth values known from the re-sampled SEM-MLA data.
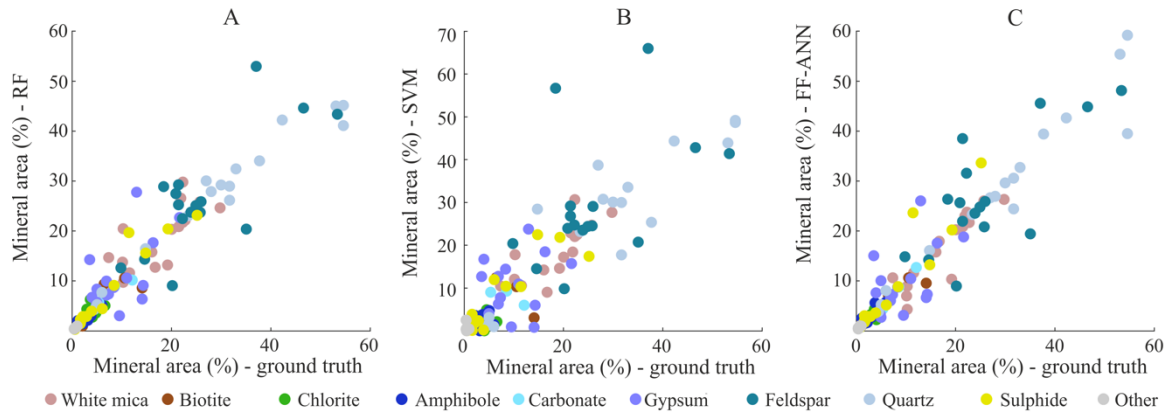
Figure 4-8 Scatter-plots of the ground truth vs. estimated mineral area % in all analysed scenarios and samples using A. RF, B. SVM and C. FF-ANN.

The estimated and true values for RF and FF-ANN show overall a good correlation with local outliers related to mineral groups such as feldspar, as these do not have distinct spectral features in the VNIR-SWIR regions of the electromagnetic spectrum. Outliers can also be observed for white mica where the training and testing classes were unbalanced and confusions between mica and feldspar occurred. SVM, on the other hand, shows higher deviations from a linear correlation. Additionally, an important factor influencing the results is the data used for sampling. All test scenarios results are included in Figure 4-8 and as observed in the mineral abundance mapping results (Table 4-8), sampling plays a critical role in method performance.

4.5.3   *Mineral Association*

The overall mineral association is calculated by averaging the sulphide association in each classified pixel. The results for the setup consisting of 50% of the SEM-MLA regions of DC-1 for training and 50% for testing are presented in Table 4-10. For each regression method, the association of sulphide with white mica, chlorite, gypsum and quartz is underestimated, while the feldspar association is overestimated. The same tendency is observed for the rest of the calculated mineral associations in all samples and setups (Appendix 4A, Figure 4-10 – Figure 4-17). The relationship between ground truth and estimated data is illustrated in the scatter-plots in Figure 4-9. The results of the mineral association are strongly influenced by the estimation of the sulphide abundance as well as of the other mineral groups. Therefore, the highest errors in sulphide abundance mapping are consistent with the largest errors for sulphide association.

Table 4-10 Ground truth and estimated mineral association of the SEM-MLA test regions of DC-1, using 50% randomly selected data for training.

Method	Sulphide Association							
	WM	Bt	Chl	Amp	Gp	Fsp	Qz	Other
GT	21.0%	0.7%	5.6%	1.5%	9.9%	30.1%	30.5%	0.6%
RF	16.2%	1.1%	4.4%	1.8%	7.6%	42.8%	25.7%	0.5%
SVM	14.5%	1.2%	3.9%	1.9%	7.8%	45.1%	24.8%	0.6%
NN	16.2%	1.1%	4.4%	1.8%	7.5%	43.2%	25.3%	0.5%
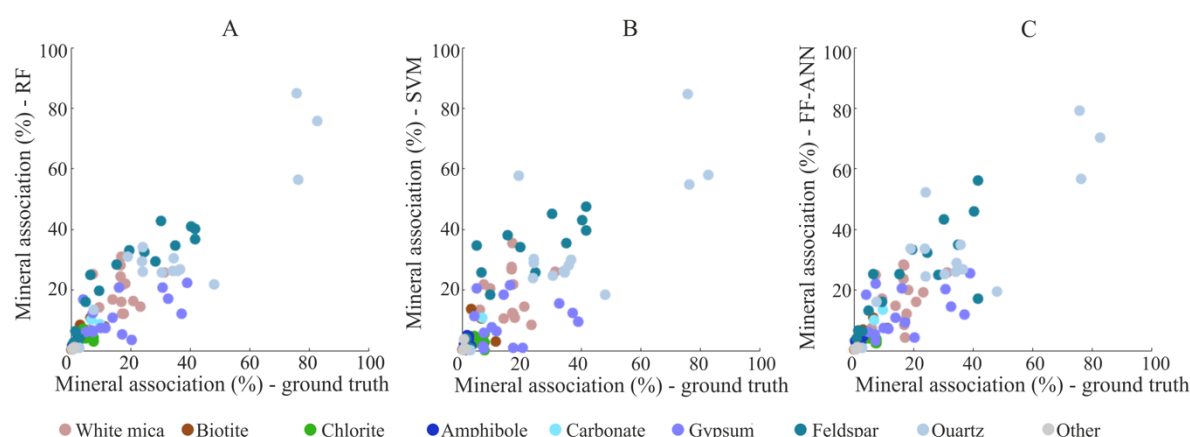
Figure 4-9 Scatter-plots of the ground truth vs. estimated mineral association in all analysed scenarios and samples using A. RF, B. SVM and C. FF-ANN.

4.6   Discussion

The proposed approach for data preparation and analysis illustrates the potential to arrive at robust quantitative mineral abundance estimates from hyperspectral drill-core data—even for those minerals that do not have diagnostic absorption features in the VNIR-SWIR regions of the electromagnetic spectrum (e.g., feldspars, quartz, sulphides). Three regression methods were tested in this paper for mineral abundance estimation: random forest (RF), support vector machines (SVM) and feedforward artificial neural networks (FF-ANN). These methods were applied to quantify mineral abundances—also of minerals devoid of characteristic HS spectral features (here sulphide minerals). In addition, attempts were made to extract mineral association data from HS information at a lateral resolution far below the actual size of mineral grains in the studied ore. For this purpose, the abundance of each gangue mineral in each HS pixel is normalized to the content of ore minerals that are the main target in the currently studied porphyry system, thus constituting a rather simple proxy for the opportunity of two minerals or mineral groups to occur in direct contact with each other.

The abundance estimation of SWIR diagnostic mineral phases and groups is good overall, particularly for white mica, amphibole and chlorite. For the case of gypsum, however, due to its pervasive association with white mica in some training samples, errors in the abundance estimation occurred. Even though it is present in minor amounts in comparison to white mica, the estimation error can reach similar amplitudes as those of white mica. An additional reason for high errors associated with gypsum is related to its composition. The higher the degree of hydration of anhydrite towards gypsum the stronger and more distinct its absorption features. While SEM-MLA methods cannot measure the amount of water in the structure of the hydrated calcium sulphate, hyperspectral sensors are highly sensitive to these changes. Therefore, having training samples hosting mostly calcium sulphate with low amount of water can cause miss-estimation in test samples which may have low

60

amounts of highly hydrated calcium sulphate. The local high errors in the estimation of biotite content can be assigned to the low amount of training samples containing relevant amounts of biotite. Sulphide is the main target in the current case study and this group comprises dominantly of pyrite, chalcopyrite, bornite, covellite, chalcocite, minor sulphosalts and native gold as an inclusion in the sulphides. While locally sulphide can be present as disseminations in the matrix, the highest fraction is present in veins. For all methods, the abundance estimation for SWIR non-diagnostic minerals is highly dependent on their association with the hydrothermal alteration minerals. To be able to estimate their abundance, representative sampling is required to avoid the erroneous estimation of these minerals based on local association with SWIR minerals that are not consistent at drill-core scale. For the analysed samples the highest per-class errors are obtained for feldspar and quartz, both SWIR non-diagnostic minerals. In many cases feldspar was overestimated, particularly in samples where white mica abundance was underestimated. As white mica is present as an alteration product of feldspar in the proximity of veins, it can be assumed that the training samples consisted of lower alteration degrees of the feldspar to white mica while the test samples showed contrasting composition. As a result, feldspar particularly represented a bottleneck for the evaluation of the mineral association where their association with sulphide was in each case overestimated. Besides the fact that this mineral group does not show distinctive absorption features in the VNIR-SWIR regions of the electromagnetic spectrum, the spatial resolution of the used sensor can highly influence the misclassification and the overestimation in its association with sulphide. Feldspar is usually present in the host-rock matrix and is expected to have a low association with sulphide, usually being altered to white mica in the proximity of the sulphide-bearing veins. When the vein alteration halo is thinner than the spatial resolution of the sensor (here 1.5 mm), an increase in the apparent association of sulphide with feldspar is observed.

A potential limitation resides in the removal of the mineral fractions present in low concentrations (lower total surface abundance than the size of a hyperspectral pixel). Additionally, the compositional variation of minerals such as white mica and chlorites is not analysed in the current work, but could be performed by auxiliary methods such and minimum wavelength analysis.

To evaluate the performance of the three regression methods employed in this paper, the RMSE was calculated. In general, for the mineral abundance estimation RF performed well and derived the lowest errors. The errors produced by FF-ANN tend to be higher than by SVMs in all the test scenarios, except in the case when 50% of the ground truth was randomly selected as the training data. This highlights the capabilities of SVM to perform well when a limited number of training samples are available and of FF-ANN to achieve good results when enough training data are available. The random selection of the training data allows for a more representative sampling per class than it is for the other two test scenarios where one thin section is used for training and the other thin section is used for the test. This is because certain minerals can be more abundant in one part of the core than in the other as it was previously stated for DC-1 in the results section. Although larger per class RMSE are obtained by minerals without diagnostic absorption features in the VNIR-SWIR, this is countered by random sampling and errors decrease considerably. From the analysis and evaluation of the results obtained by the utilized regression methods, the RF algorithm is the most suitable for the current dataset.

The proposed framework allows for fast evaluation of the modal mineralogy of analysed samples and it shows potential for further upscaling. It proves that hyperspectral drill-core scanning provides a fast, non-invasive mineral identification and quantification if suitable training samples are available. Domaining of the hyperspectral data before the selection of representative samples for detailed analysis can minimize and focus the effort and amount of invasive measures related to sampling and high-resolution mineralogical analyses. The automated character of the approach can be later used on mine sites provided that hyperspectral drill-core scanning is available to support the geologists in the core-logging procedure, as well as training samples characterized by high resolution methods of mapping mineral distributions, such as SEM-based image analyses. The derived mineralogical parameters such as modal mineralogy and mineral association can additionally prove useful past exploration stages as they are essential in defining geometallurgical domains (van den Boogaart and Tolosana-Delgado, 2018).

4.7   Conclusion and Remarks

Hyperspectral drill-core imaging provides fast, extensive and non-destructive mapping of certain minerals with spectral characteristic features in the VNIR-SWIR regions of the electromagnetic spectrum. SEM-MLA analyses allow a precise and exhaustive mineral mapping of selected small samples. We propose to combine both analytical techniques using machine learning in order to provide mineral abundance and association mapping over entire drill-cores. The proposed methodological framework is illustrated on samples collected from a porphyry type deposit, but the procedure is easily adaptable to other ore types. All tested ML algorithms deliver good results but RF is more robust to unbalanced and sparse training sets and is recommended for further work. As a result, quasi-quantitative maps are also produced and evaluated. The mineral abundance results can be further used to calculate parameters such as modal mineralogy, mineral association and other mineralogical indices. Therefore, this approach can be integrated in the standard core-logging procedure, complementing the on-site geologists, and can serve as background for the geometallurgical analysis of numerous ore types.

Supplementary Materials: The following are available as electronic appendices: Table S1: Compilation of numerical results for mineral abundance and mineral association estimation.

Appendix 4A: The results of mineral abundance mapping for DC-2 to DC-5 are shown in Figure 4-10 – Figure 4-17 using all test scenarios.
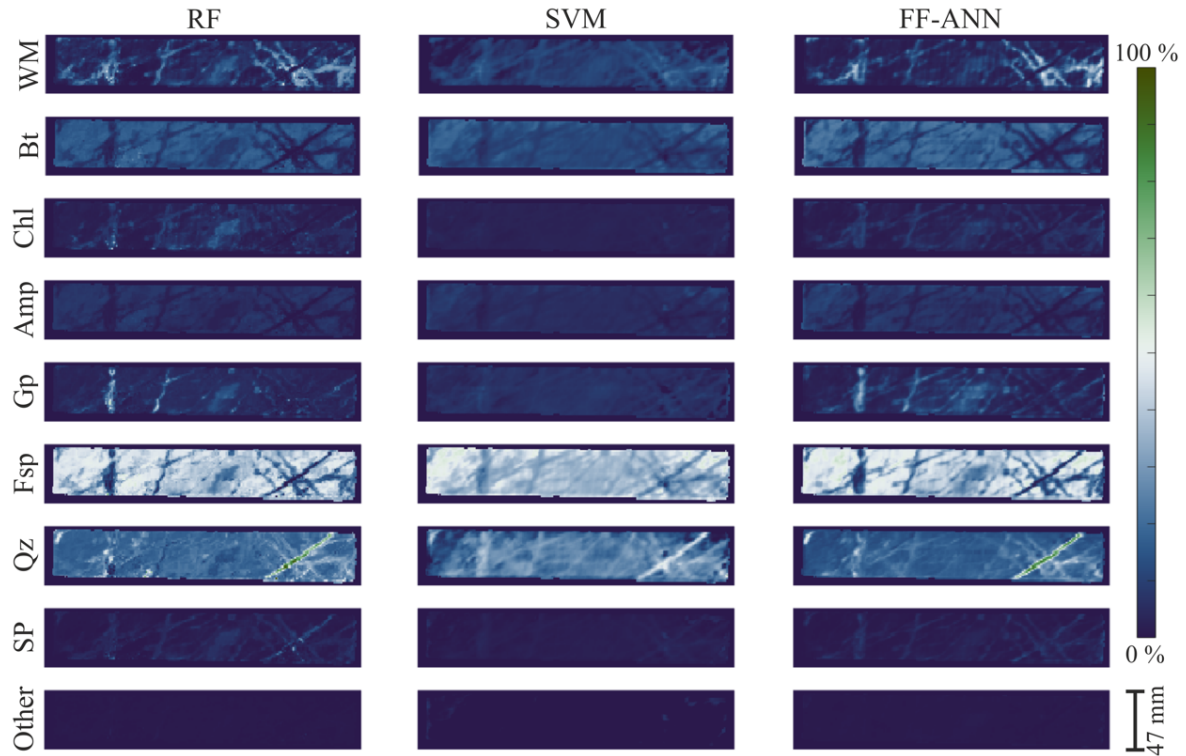
Figure 4-10 Drill-core abundance maps of white mica (WM), biotite (Bt), chlorite (Chl), amphibole (Amp), gypsum (Gp), feldspar (Fsp), quartz (Qz), sulphide (SP) and accessory minerals (Other) for DC-2 using randomly distributed 50% of the available ground truth data for training for random forest (RF), support vector machine (SVM) and feed-forward neural network (FF-ANN) regressions.
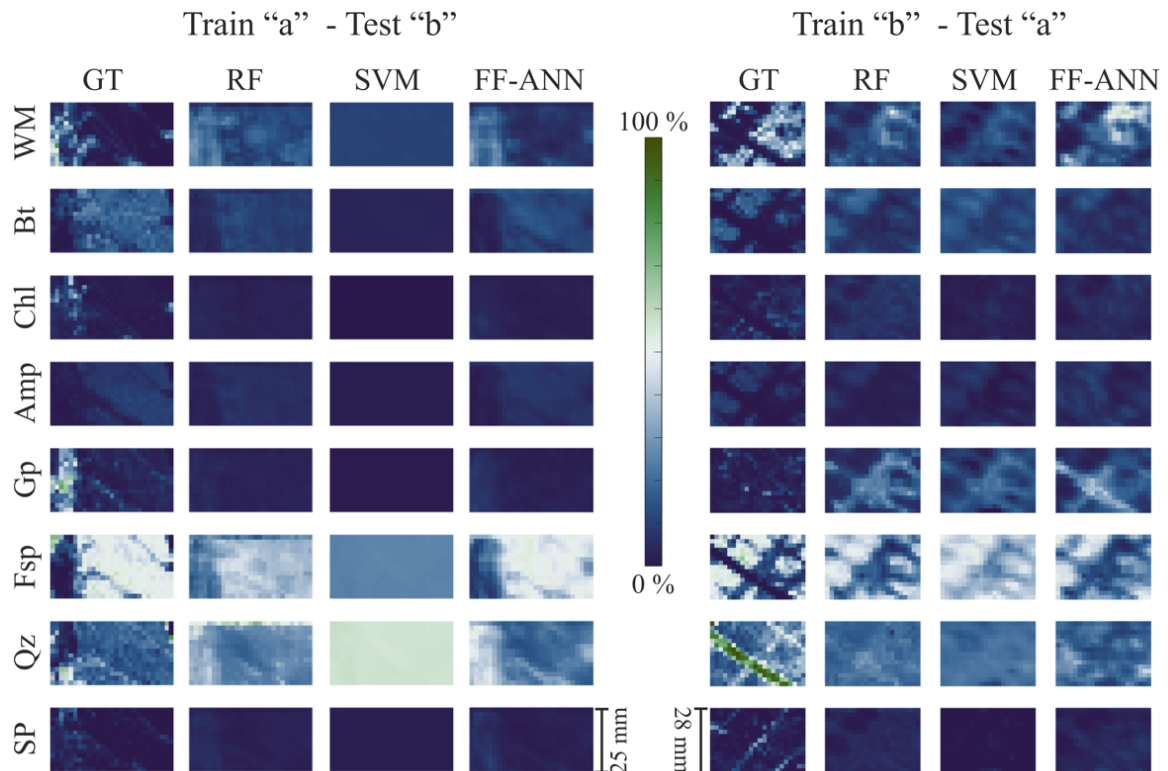
Figure 4-11 White mica (WM), biotite (Bt), chlorite (Chl), amphibole (Amp), gypsum (Gp), feldspar (Fsp), quartz (Qz) and sulphide (SP) abundance maps of TS-2a using TS-2b for training and of TS-2b using TS-2a

respectively for training of random forest (RF), support vector machine (SVM) and feed-forward neural network (FF-ANN) regressions. The ground truth (GT) represented by resized MLA data is presented for comparison.
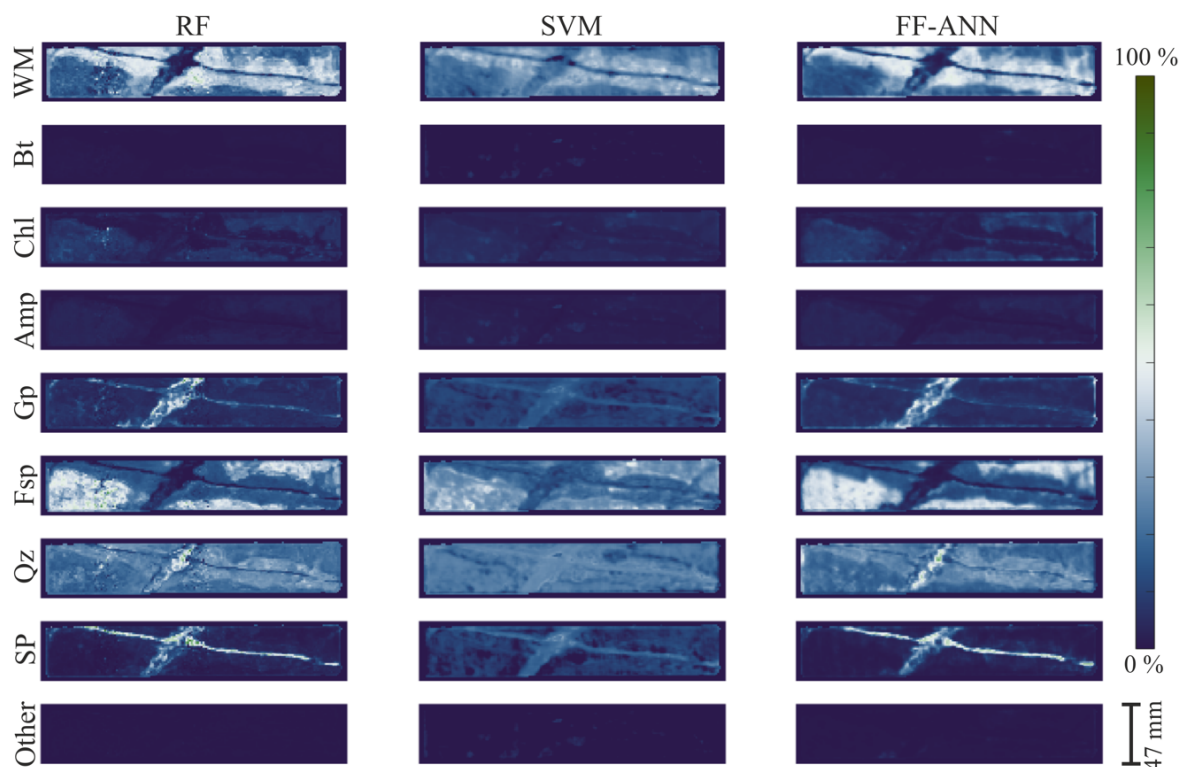
Figure 4-12 Drill-core abundance maps of white mica (WM), biotite (Bt), chlorite (Chl), amphibole (Amp), gypsum (Gp), feldspar (Fsp), quartz (Qz), sulphide (SP) and accessory minerals (Other) for DC-3 using randomly distributed 50% of the available ground truth data for training for random forest (RF), support vector machine (SVM) and feed-forward neural network (FF-ANN) regressions.
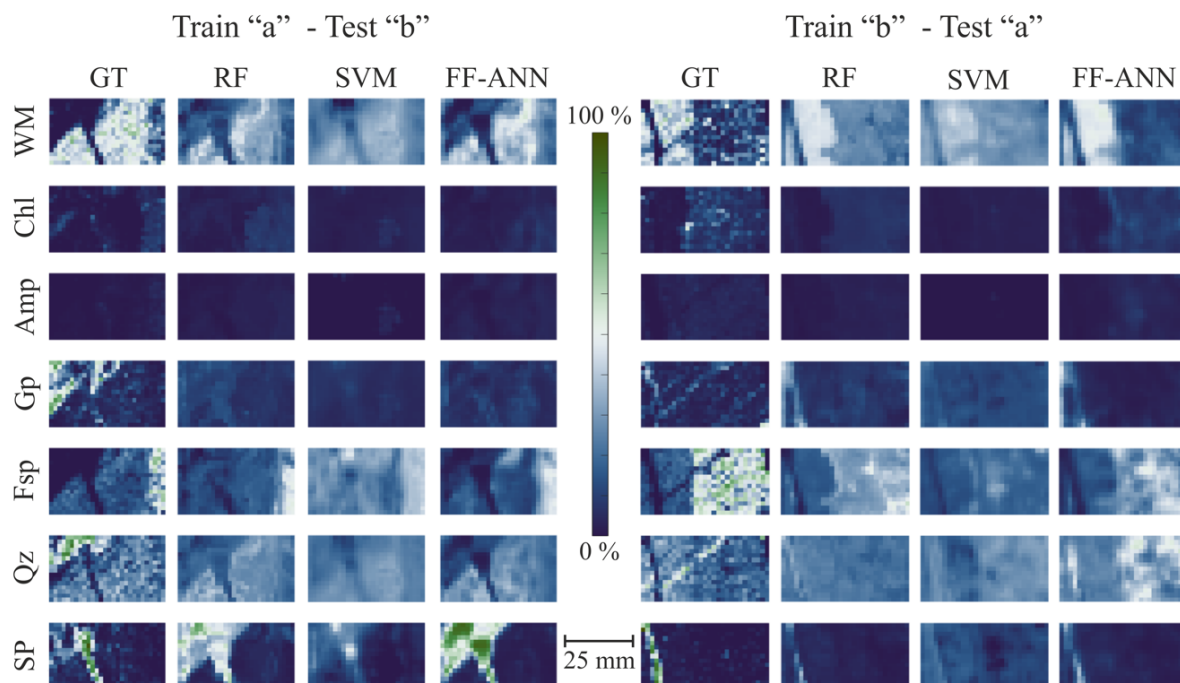
Figure 4-13 White mica (WM), chlorite (Chl), amphibole (Amp), gypsum (Gp), feldspar (Fsp), quartz (Qz) and sulphide (SP) abundance maps of TS-3a using TS-3b for training and of TS-3b using TS-3a respectively for training of random forest (RF), support vector machine (SVM) and feed-forward neural network (FF-ANN) regressions. The ground truth (GT) represented by resized MLA data is presented for comparison.
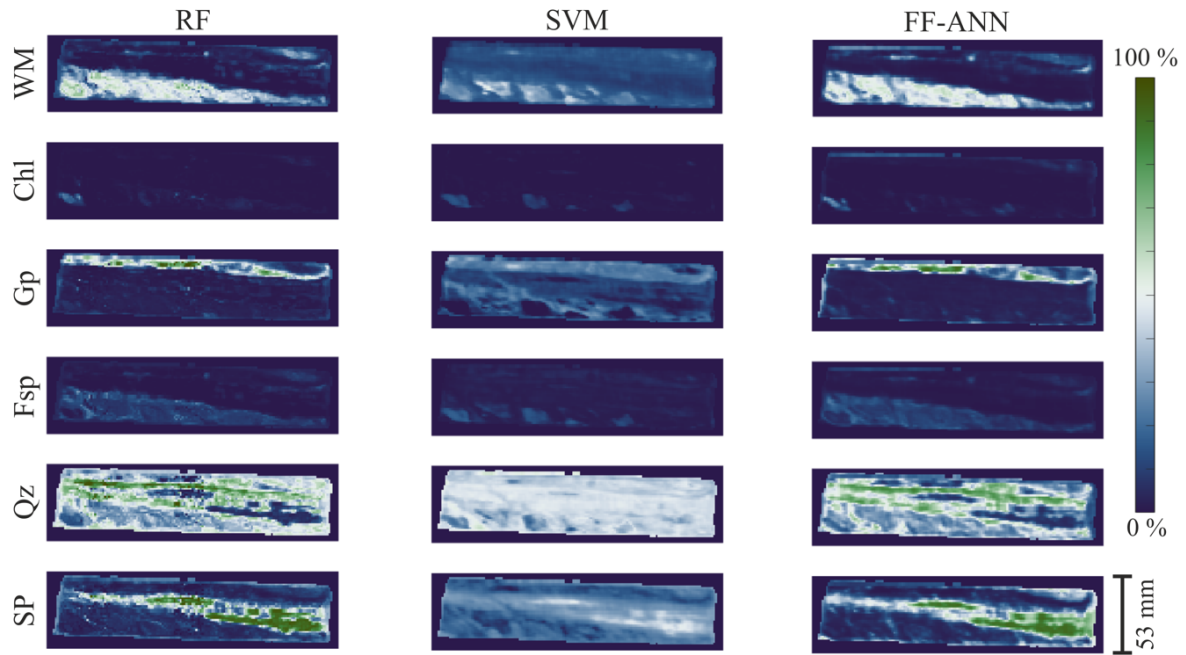
Figure 4-14 Drill-core abundance maps of white mica (WM), chlorite (Chl), gypsum (Gp), feldspar (Fsp), quartz (Qz) and sulphide (SP) for DC-4 using randomly distributed 50% of the available ground truth data for training for random forest (RF), support vector machine (SVM) and feed-forward neural network (FF-ANN) regressions.
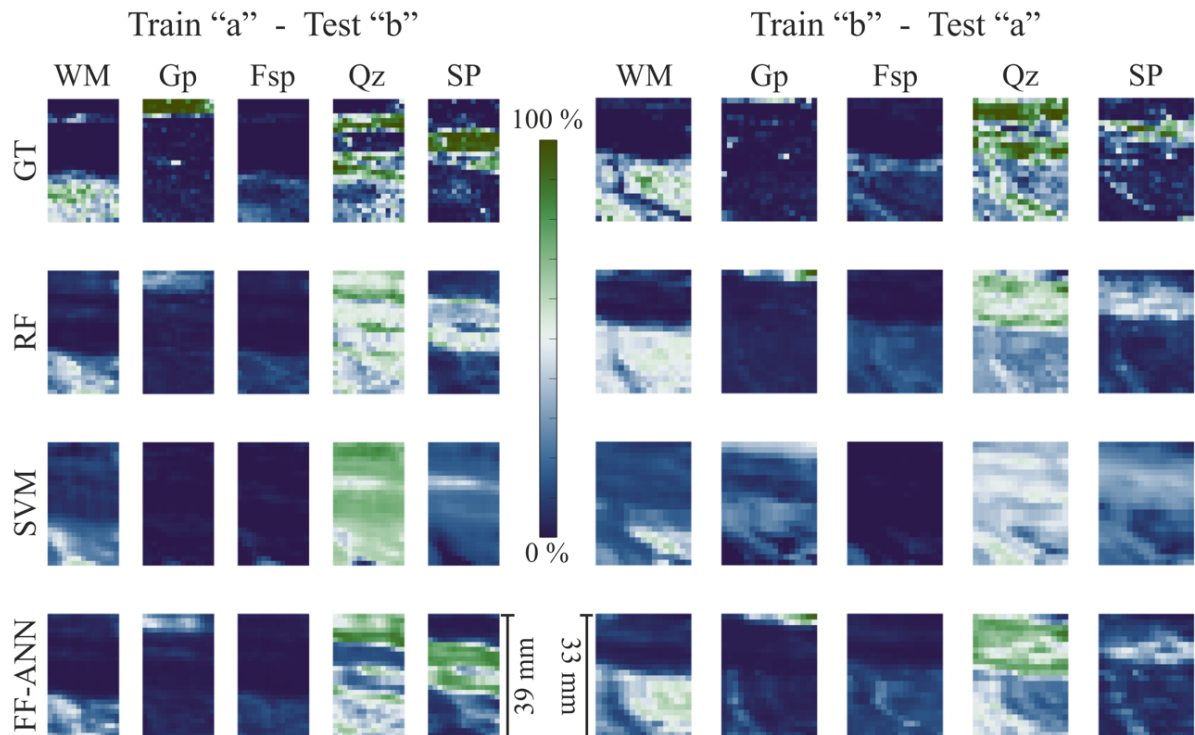
Figure 4-15 White mica (WM), gypsum (Gp), feldspar (Fsp), quartz (Qz) and sulphide (SP) abundance maps of TS-4a using TS-4b for training and of TS-4b using TS-4a respectively for training of random forest (RF), support vector machine (SVM) and feed-forward neural network (FF-ANN) regressions. The ground truth (GT) represented by resized MLA data is presented for comparison.
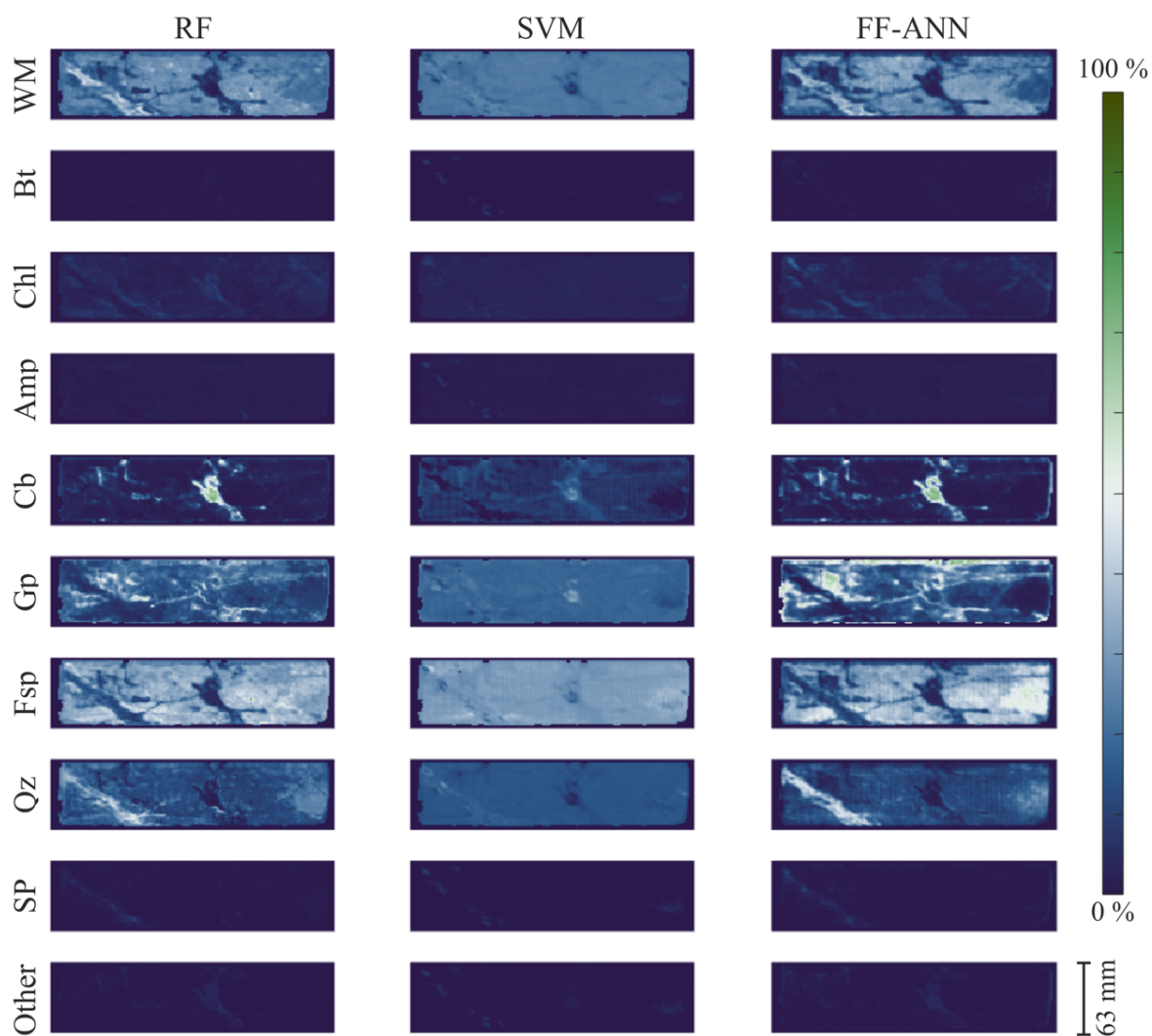
Figure 4-16 Drill-core abundance maps of white mica (WM), biotite (Bt), chlorite (Chl), amphibole (Amp), carbonate (Cb), gypsum (Gp), feldspar (Fsp), quartz (Qz), sulphide (SP) and accessory minerals (Other) for DC-5 using randomly distributed 50% of the available ground truth data for training for random forest (RF), support vector machine (SVM) and feed-forward neural network (FF-ANN) regressions.
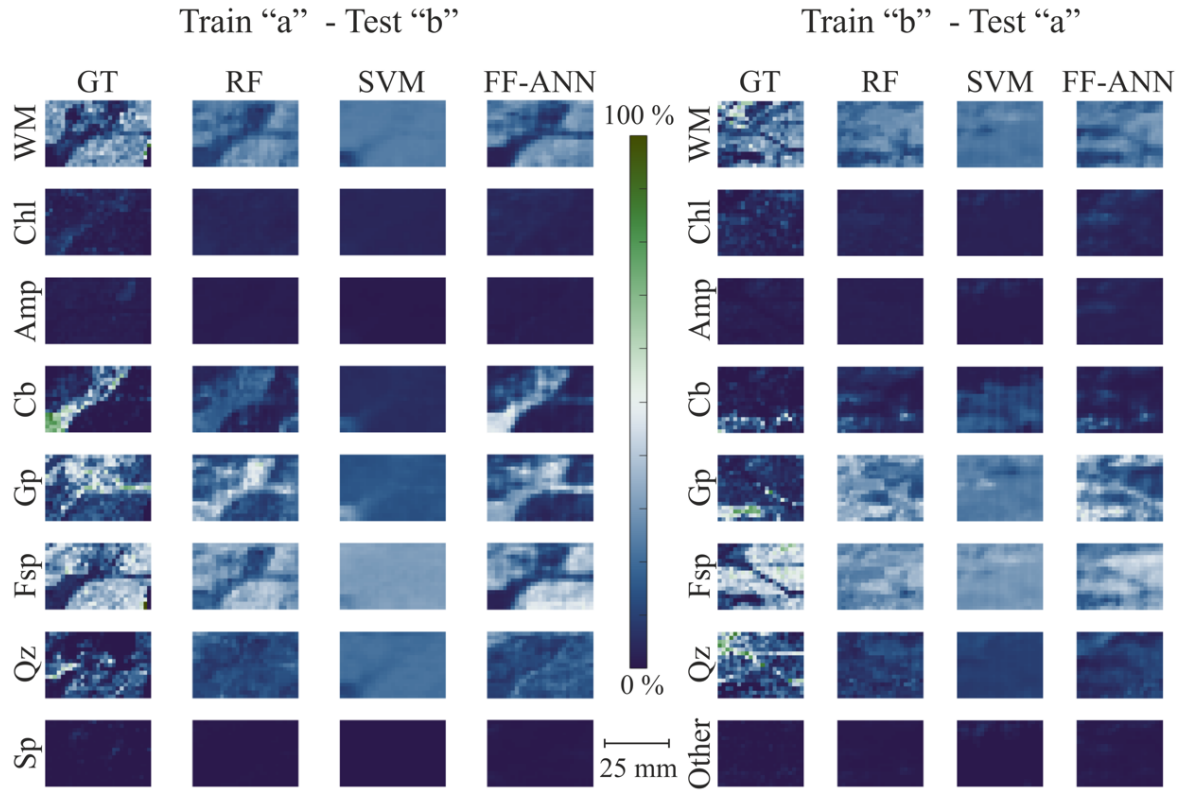
Figure 4-17 White mica (WM), chlorite (Chl), amphibole (Amp), carbonate (Cb), gypsum (Gp), feldspar (Fsp), quartz (Qz) and sulphide (SP) abundance maps of TS-5a using TS-5b for training and of TS-5b using TS-5a respectively for training of random forest (RF), support vector machine (SVM) and feed-forward neural network (FF-ANN) regressions. The ground truth (GT) represented by resized MLA data is presented for comparison.

Chapter 5 Hyperspectral sensors for ore beneficiation

Preface

With the increase of complexity and decrease of grades of mined commodities, sensor sorting technologies are becoming increasingly used for the preconcentration of ores. Most commonly used sensors for this purpose are X-ray fluorescence and X-ray tomography. However, frequently the low grade of the ore and fine grain sizes represent bottlenecks for this purpose, rendering these sensors unsuitable for ore sorting. While frequently hyperspectral sensors can't allow for direct identification of the ore minerals, they can prove suitable for identifying proxies for mineralization. In a previous study we presented the possibility of the use of Short-Wave infrared sensors and basic spectral analysis for the detection of chlorite, a key proxy for the distribution of cassiterite and therefore tin grade. As direct spectral analysis such is not always suitable of the detection of proxies for mineralisation, in this chapter a machine learning approach is tested for the estimation of commodity grade for both the skarn ore presented in the previous study as well as for samples from the Bolcana porphyry system in Romania. The methodology relies, such as in the previous chapter, on the resampling and coregistration of the SEM-MLA data with the hyperspectral data and training different classifiers to predict the ore grade. The results have proved the following:

(1) Improved performance for the skarn ore compared to the basic spectral analysis presented in [1]

(2) Potential to identify subtle proxies for the porphyry mineralization which are not clear by direct spectral and mineralogical analysis

(3) Results include estimated modal mineralogy and mineralogical properties of both the concentrate and tail which have implications for the further processing stages

The original concept and preliminary results of this work were firstly presented in 2019 at the MEI Physical Separation conference [2] and complete content of this chapter was published in the journal Minerals Engineering [3] under the title "Evaluating the performance of hyperspectral short-wave infrared sensors for the pre-sorting of complex ores using machine learning methods".

Authors and contributions

Tuşa L.[1], Kern M.[1], Khodadadzadeh M.[1], Blannin R.[1], Gloaguen R.[1], Gutzmer J.[1]

[1]*Helmholtz-Zentrum Dresden-Rossendorf, Helmholtz Institute Freiberg for Resource Technology*

Conceptualization, L.T., M.Ke.; *methodology*.; *software*, L.T., M.Kh.; *validation*, L.T.; *formal analysis*, L.T., M.Ke., M.Kh.; *investigation*, L.T. and M.Ke.; *data curation*, L.T., R.B. and M.Ke.; *writing—original draft preparation*, L.T. and M.Ke.; *writing—review and editing*, all authors.; *visualization*, L.T.; *supervision*, R.G. and J.G.; *project administration*, L.T., R.G. and J.G.

[1] Kern, M., Tusa, L., Leißner, T., Gerald van den Boogaart, K., Gutzmer, J., 2019. Optimal sensor selection for sensor-based sorting based on automated mineralogy data. J. Clean. Prod. 234, 1144–1152.

[2] Tusa, L., Kern, M., Khodadadzadeh, M., Blannin, R., Gloaguen, R., Gutzmer, J., 2019. Evaluating the performance of hyperspectral short-wave infrared sensors for the pre-sorting of complex ores using machine learning methods. MEI Physical Separation, 13.-14.06.2019, Fallmouth, United Kingdom

[3] Tusa, L., Kern, M., Khodadadzadeh, M., Blannin, R., Gloaguen, R., Gutzmer, J., 2019. Evaluating the performance of hyperspectral short-wave infrared sensors for the pre-sorting of complex ores using machine learning methods. Miner. Eng. 146. https://doi.org/10.1016/j.mineng.2019.106150

Abstract

Sensor-based sorting is increasingly used for the concentration of ores. To assess the sorting performance for a specific ore type, the raw materials industry currently conducts trial-and-error batch tests. In this study, a new methodology to assess the potential of hyperspectral visible to near-infrared (VNIR) and short-wave infrared (SWIR) sensors, combined with machine-learning routines to improve the sorting potential evaluation, is presented. The methodology is tested on two complex ores. The first is a tin ore in which cassiterite—the target mineral—is variable in grain size, heterogeneously distributed and has no diagnostic response in the VNIR-SWIR range of the electromagnetic spectrum. However, cassiterite is intimately associated with SWIR active minerals, such as chlorite and fluorite, which can be used as proxies for its presence. The second case study consists of a copper-gold porphyry, where copper occurs mainly in chalcopyrite, bornite, covellite and chalcocite, while gold is present as inclusions in the copper minerals and in pyrite. Machine-learning techniques such as Random Forest and Support Vector Machine applied to the hyperspectral data predict excellent sorting results in terms of grade and recovery. The approach can be adjusted to optimize sorting for a variety of ore types and thus could increase the attractivity of VNIR-SWIR sensor sorting in the minerals industry.

Graphical abstract
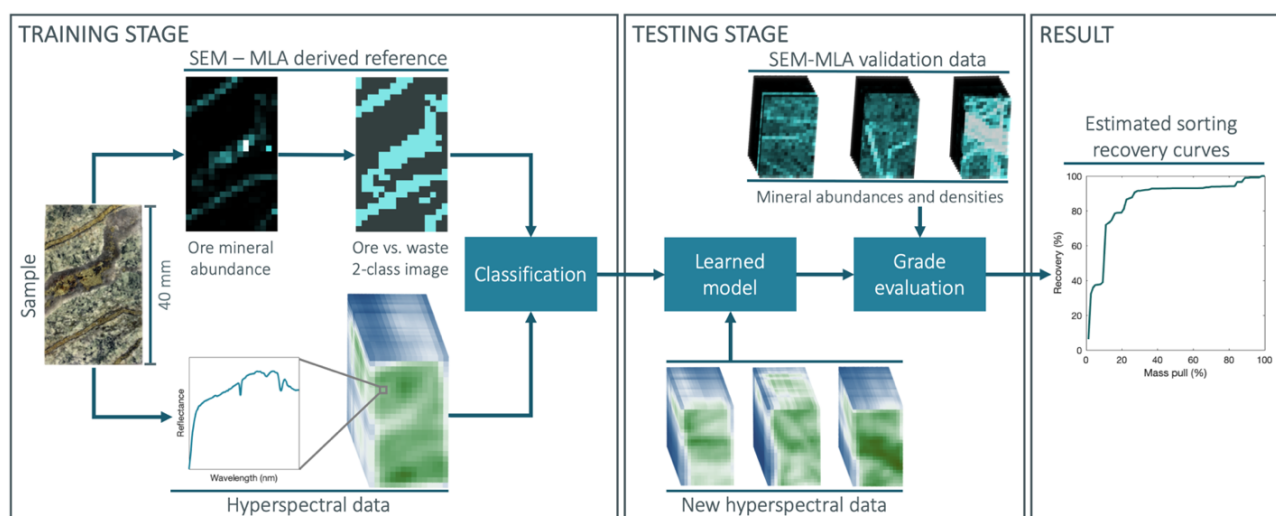
Keywords: Sensor-based sorting, hyperspectral imaging, SWIR, Machine learning, complex ores

5.1 Introduction

Sensor-based sorting technologies are being increasingly used in the mining industry for the pre-concentration of ores usually at particle sizes between 1 and 10 cm (Knapp et al., 2014; Salter and Wyatt, 1991; Wills, 2016). Sensor sorting is applied to remove individual particles from a stream based on their physical-chemical properties identified by a suitable sensor or combination of sensors. As crushing and grinding account for a large portion of the total energy consumption within a mining operation, the implementation of sensor based sorting can be expected to result in a significant reduction in energy consumption and thus also operational expenditure by early removal of barren particles (Lessard et al., 2014). Properties used as proxies and sensor technologies for sorting include colour, fluorescence, visible to near-infrared (VNIR) and short-wave infrared (SWIR) radiation, X-ray fluorescence and luminescence, laser triangulation, laser induced

breakdown spectroscopy or laser induced fluorescence (Dalm et al., 2018; Iyakwari and Glass, 2014; Knapp et al., 2014; Robben and Wotruba, 2010, 2019). In mining operations, however, the most commonly targeted property is atomic density, which is analysed with DE-XRT detectors (Knapp et al., 2014; Neubert and Wotruba, 2017; Robben and Wotruba, 2019). This method is well suited for ores in which the ore minerals have a marked density contrast to the associated gangue. The success of this method can be limited by other minerals besides the target having high atomic densities, the target commodity being present in much finer grain sizes than the voxel size of the sensor system or simply having a highly variable grain size.

The potential of VNIR-SWIR sensors is still not widely exploited in the mining industry due to the lack of diagnostic absorption features of most ore minerals in this range of the electromagnetic spectrum. Successful use of SWIR sensors for pre-sorting of ores has been achieved mostly on industrial minerals such as calcite, dolomite, fluorite, barite and borates (Robben and Wotruba, 2010). There are, however, underlying relationships in most metalliferous mineralized systems between alteration (i.e. gangue) and ore minerals (Kern et al., 2018a). These relationships are widely applied within the context of mineral exploration. Minerals such as chlorites and epidotes, for example, can be used as proximity indicators for certain mineralization styles (Pour and Hashim, 2011; Roache et al., 2011; Wilkinson et al., 2015). Such intimate cogenetic relations between rare ore- and common, rock-forming gangue minerals may, however, also be exploited during eventual exploitation - as shown in some previous studies (Dalm et al., 2018, 2014; Kern et al., 2019). These previous studies also illustrate that the relationship between ore mineralogy and grade, and spectral response of alteration minerals is not always simple.

Machine learning approaches may provide solutions to resolve complex relations between ore and gangue minerals. In the current study, the relationship between the VNIR-SWIR responses of raw material particles and the target commodities for two case studies, one a porphyry deposit, the other from a skarn orebody, are investigated in order to evaluate the sorting potential using two state-of-the-art machine learning algorithms. For this purpose, batches of samples are subjected to high resolution mineralogical analyses and VNIR-SWIR hyperspectral imaging in order to evaluate the sorting potential of the two ores as well as the amount of training samples required for an estimation of the metal grade. Polished thin sections prepared from cut blocks are analysed by scanning-electron microscopy-based image analysis to obtain high resolution mineralogical maps. The remaining blocks are scanned with a hyperspectral sensor. The obtained images are re-sampled and co-registered in order to obtain a direct correspondence between the modal mineralogy and spectral response. A data-driven approach is adopted for the estimation of metal content from VNIR-SWIR spectra. For the classification of the hyperspectral data, random forest (RF) (Breiman, 2001) and support vector machine (SVM) (Vapnik, 1999) are used as binary classifiers.

5.2   Case studies

As two suitable case studies, complex ores from the Hämmerlein Sn-In-Zn skarn deposit located in the Ore Mountains of Germany (Kern et al., 2018a; Schuppan and Hiller, 2012), and the Bolcana Cu-Au porphyry located in the "Gold Quadrilateral" of the South Apuseni Mountains, Romania (Berbeleac et al., 2014; Cioacă et al., 2014; Ivăşcanu et al., 2018), were selected. Both deposits are geologically well-studied, but await industrial exploitation.

5.2.1 *Hämmerlein*

The polymetallic Hämmerlein deposit is currently explored by Saxore Bergbau GmbH. The deposit comprises two lithologically distinct units: a Sn-In-Zn skarn (skarn ore) and greisenized mica schist, known as Schiefererz (Schuppan and Hiller, 2012). In this study, only the mineralogically complex skarn is analysed. The main commodity of economic interest in the skarn is Sn contained in cassiterite (SnO_2). Cassiterite is present in a large variability of grain sizes, ranging from 5 μm to 3 mm. Economically significant tin mineralization in the skarn ore is related to a late metasomatic overprint expressed by the mineral assemblage cassiterite-chlorite-fluorite-sulphides (Kern et al., 2018a). This assemblage occurs in irregular pods, lenses and veins. The preferred association between the minerals of the cassiterite assemblage was quantified in a previous study using the MAMA ratio (Kern et al., 2018a).

5.2.2 *Bolcana*

The Bolcana porphyry copper-gold deposit is explored by Eldorado Gold Corporation through its subsidiary Deva Gold S.A.. It comprises variable chalcopyrite, pyrite, chalcocite, covellite, bornite, magnetite, molybdenite and native gold, occurring as disseminations in the host rock, stockworks and hydrothermal breccias (Ivăşcanu et al., 2018; Milu et al., 2003). The variability of copper and gold throughout the deposit are controlled by key factors including lithology, vein types, alteration, and how these factors vary with depth. Copper occurs mainly in chalcopyrite, with minor contributions from bornite, chalcocite, covellite and sulphosalts. Chalcopyrite is predominantly hosted by thin veinlets cutting across sodic, sodic-calcic, magnetite-albite-chlorite-epidote or potassic altered intermineral porphyries. At shallow depths, bornite, chalcocite and covellite occur as rims around chalcopyrite grains, as a result of supergene and/or epithermal overprints (Blannin et al., 2019). At greater depths, primary bornite occurs, with both chalcopyrite and bornite grains commonly having rims of chalcocite and covellite. Gold typically occurs as <10 μm grains, hosted by copper minerals and to a lesser extent by pyrite and in the host rock in the vein alteration halos. The copper minerals and chalcopyrite- and bornite-hosted gold dominantly occur at higher depths in the magnetite-albite-chlorite-epidote, sodic-calcic and potassic alteration zones. Pyrite-hosted gold is common in the near-surface zones; here it is related to phyllic alteration (Blannin et al., 2019).

5.3 Data acquisition

Observational data for the two case studies was obtained on sets of samples that were deemed representative of the two ore deposits. Yet, given the fact that both deposits are currently in the exploration stage, full representativity cannot be assured due to limited exposure of mineralization in accessible underground mine workings (Hämmerlein) and exploration drill-core (Bolcana), respectively.

5.3.1 *Sample selection and preparation*

The skarn samples were collected from the +590 m level of the Hämmerlein deposit. The hand specimens represent various litho-units, ore types and host rocks encountered in the area of the mine which was accessible for sampling. 68 samples are used for the SWIR sorting simulation. For the porphyry case study, 24 samples were collected from two drill-holes intersecting the top, high-grade, part of the Bolcana porphyry. The samples are considered representative of the main alteration, vein styles and grade observed in this region of the deposit.

The samples were cut into cuboid blocks from which polished thin sections of around 25x40 mm in lateral dimension were prepared. The thin sections were analysed by scanning electron microscopy. The remaining blocks after thin section preparation were scanned using an VNIR-SWIR hyperspectral sensor.

Thin section preparation consisted of milling and polishing of the sample surface. Firstly, one surface of the cuboid block is polished and glued to the glass. Further, part of the sample block is cut leaving only around 0.3-0.4 mm thick sample attached to the glass. The remaining material is then milled in order to reduce the thickness of the thin section to around 30 μm and to obtain a polished surface. This leads to the removal of a small fraction of the material of a thickness up to 0.3 mm. The change in analysed surface causes a small shift in the location of the main features such as veins. However, for the spatial resolution of the chosen sensor (1.5mm/pixel) the shift is considered negligible.

5.3.2 Scanning electron microscopy mineral maps

Quantitative mineralogical data were collected from each polished thin section using the modified approach for automated mineralogy developed by Kern et al. (2018). The analyses were performed using a Mineral Liberation Analyser (MLA) equipped with a FEI Quanta 650 F field emission SEM with two Bruker Quantax X-Flash 5030 energy-dispersive X-ray (EDX) detectors. Backscattered electron (BSE) images are used to define mineral grains. The greyscale level in the BSE images ranges from 26–255 according to the average atomic number (AAN) of the elements comprising a mineral / phase (Fandrich et al., 2007). Lower AAN values correspond to darker grey BSE appearance and correspond to minerals comprising of light elements (in this case, for example, quartz and silicates). Brighter grey shades, in contrast, reflect higher AAN values and indicate that minerals comprise of elements of high atomic number (e.g., cassiterite, gold). Mineral grains were discriminated based on their grayscale level in the BSE images and then identified by performing EDS X-ray measurements on a closely-spaced grid (Fandrich et al., 2007). The operating conditions used for SEM and MLA are listed in Table 5-1. The acquisition parameters may vary somewhat for different samples, depending on the exact set-up of the MLA.

Table 5-1. SEM-MLA data acquisition parameters.

SEM settings		MLA settings	
Acceleration voltage (kV)	25	Pixel size (μm)	2/3
Probe current (nA)	10	Step size (pixels)	6 x 6
Frame width (pixels)	1000/1500	Acquisition time (ms)	5
BSE calibration (Au)	254/243/246	Minimum grain size (pixels)	3/4

Data processing was carried out using the MLA Suite 3.1.4.686 software package. The mineral reference editor was used in online mode in order to complete the mineral list required for the classification of the tested samples. MLA Image Processing software was used for preliminary corrections of data, such as frame edge removal. In the classification script, the spectrum matching threshold was set to 90% and the low counts threshold was set to 2000 counts. Additional pre-processing consists of mineral grouping based on the main occurrence of the targets/commodities.

5.3.3   *Hyperspectral imaging*

Hyperspectral data was acquired using a SisuROCK drill-core scanner equipped with an AisaFENIX VNIR-SWIR hyperspectral sensor. The obtained spatial resolution of the resulting images is 1.5 mm/pixel. A listing of the sensor specification and applied settings is available in Table 5-2

Table 5-2. Specifications and setup parameters of the SisuROCK drill-core scanner and AisaFENIX VNIR-SWIR hyperspectral sensor.

Wavelength range	VNIR 380-970 nm SWIR 970-2500 nm	Integration time	VNIR 15 ms SWIR 4 ms
Sampling distance	VNIR 1.7 nm SWIR 5.7 nm	Spatial binning	VNIR 2 SWIR 1
Number of bands	450	Frame rate	15 Hz
Samples	384	Scanning speed	25.06 mm/s
Field of view (FOV)	32.3°	Spectral binning	VNIR 4 SWIR 1

The conversion of raw digital number over radiance to reflectance was performed with the acquisition software (LUMO Scanner version 2018-5, Spectral Imaging Ltd., Oulu, Finland) using PTFE reference panels (>99% VNIR and >95% SWIR) and closed shutter scans for dark current subtraction. For the pre-processing, the hyperspectral images were corrected using the MEPHySTo toolbox (Jakob et al., 2017). A correction was applied to compensate the spatial shift between the VNIR and SWIR sensors and a geometric correction for the lens effect. The corrected hyperspectral data were smoothed using the Savitzky-Golay (SavGol) filter (Ruffin and King, 1999), with a radius of 5 and a 3rd degree polynomial. Additionally, the first 20 bands were removed from further processing steps in order to avoid the impact of noise on the classifier. The hyperspectral dataset contains 430 bands between 446 and 2503 nm. Additionally, dimensionality reduction is achieved using principal component analysis (PCA) (Rodarmel and Shan, 2002).

5.4   Proposed methodology

Several steps are taken for the integration and processing of hyperspectral and SEM-MLA data (Figure 5-1). The MLA data is resized to the spatial resolution of the hyperspectral images. Cut-off thresholds have to be selected for each ore type in order to convert the SEM-MLA data into a binary map. Selected training samples are then used in order to train two classifiers to predict the belonging of test samples to either concentrate or tailing. For each sample the probability of belonging to the class concentrate is analysed based on the classification scores. This probability also provides a proxy for the metal content of the sample. Based on the metal grade estimates and probability curves a target grade or metal recovery can be chosen for defining optimal metal grade classes. Once the samples are assigned to either concentrate or waste the modal mineralogy of each class can be calculated from the surface abundances and density of each mineral. The performance of the classifiers is assessed based on confusion matrices, average and overall accuracies.
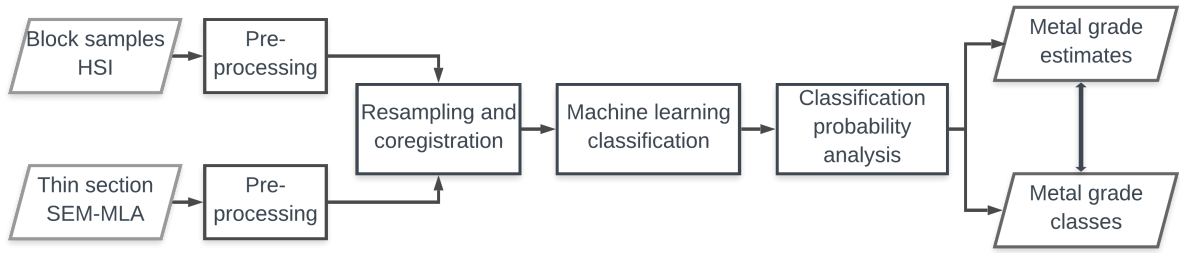
Figure 5-1. Flowchart presenting the main data processing steps in the proposed methodology.

5.4.1 *SEM - HSI data integration*

In order to integrate the two types of measurements, the SEM-MLA mineral maps have to be resampled to the HSI resolution. To achieve this, the high-resolution labelled images are converted into low resolution multiband images, each band consisting of the abundance of a specific mineral. Once the data are at the same resolution, they are co-registered in order to have the mineral abundance, in area and weight percentage, and the spectral response of the analysed surface in the VNIR-SWIR region of the electromagnetic spectrum, for each pixel. The co-registration is performed manually using the false-colour RGB image of the blocks and the abundance resized abundance MLA image. Specific mineral phases are chosen for the SEM-MLA data, which have heterogeneous distribution in the thin section. This facilitates the selection of representative tie-points to be used in the co-registration. Once the SEM-MLA data is resized and co-registered, only the abundances of the target commodities are further considered. Thresholds are then selected for the cut-off grade of each commodity and the MLA data is transformed to a binary image where each pixel is labelled as either waste or concentrate. Note that a co-registration stage is needed after the re-sampling of the SEM-MLA data. The structural features, such as veins, mineral abundances, and spectral responses, are used to find tie points to perform the co-registration of the two images. As a result of the co-registration, each pixel will be characterised by two vectors: the hyperspectral feature vector X of dimension d (i.e., the number of spectral bands) and a Y vector containing the corresponding fractional abundances, summing up to 1, of the minerals identified by SEM-MLA. Figure 5-2 shows a simple example of the resampling procedure (Contreras Acosta et al., 2019).

The main commodity in the skarn ore is tin contained in cassiterite, SnO_2 (78.77 wt% Sn content) and therefore cassiterite is used in this case as a target. Two target commodities are present in the studied porphyry ore: copper and gold. Copper is dominantly present in chalcopyrite and subordinately in bornite, chalcocite and covellite. Electron probe microanalyses were performed on the four copper-bearing sulphides in order to quantify the copper content (Table 5-3). Gold is mostly present in native form as fine inclusions in sulphides and disseminations in the proximity of veins. To estimate the sorting potential of the ore, both copper and gold-bearing minerals have to be considered. As a result, the equivalent copper grade (eq. Cu) is calculated (Osanloo and Ataei, 2003).

Cut-off grades are defined for both ores. The cut-off grade considered for the skarn ore is 0.1 wt% Sn. The value is lower than the usual cut-off grade for mining but is considered appropriate at the sorting stage (Kern et al., 2019). For the porphyry ore on the other hand a high cut-off grade of 1 wt% eq. Cu for the purpose of testing the proposed methodology. While lower cut-off grades may be used in industrial operations, the available samples were collected from high grade areas of the mineralized system and therefore a higher

threshold is required to obtain enough training samples in each class. The training data is then split into class tailing (below cut-off) and class concentrate (above cut-off).
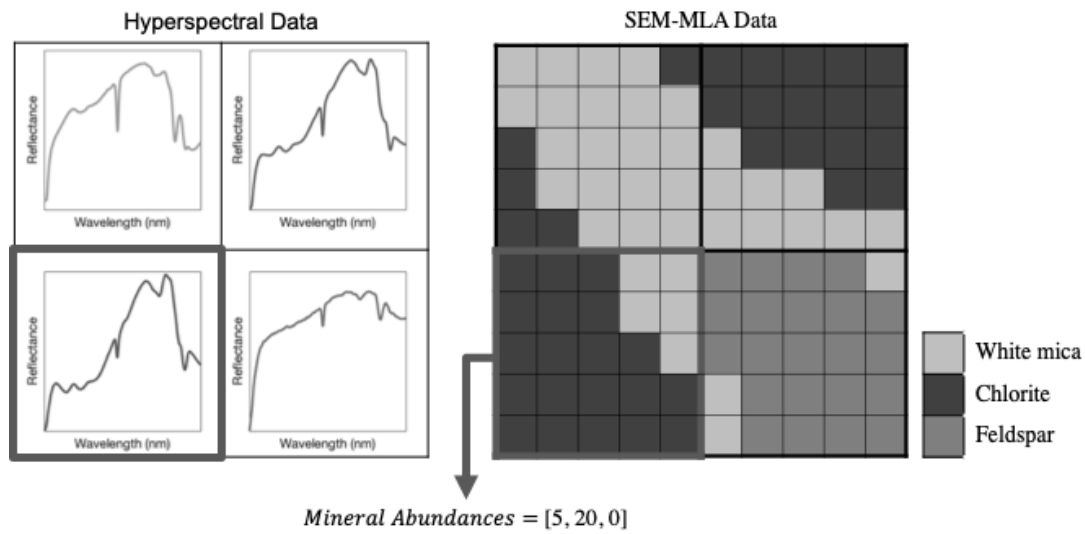
Figure 5-2. Graphical illustration of the co-registration and resampling process for the SEM-MLA image (foreground) to the hyperspectral image (background).

Table 5-3. Empirical formulae of the main copper-bearing minerals in the porphyry ore and the considered copper grades obtained by electron probe microanalyses.

Mineral	Empirical formula	Used copper content
Chalcopyrite	$CuFeS_2$	36%
Bornite	Cu_5FeS_4	65%
Chalcocite	Cu_2S	78%
Covellite	CuS	61%

5.4.2 Hyperspectral data classification

Two well-known classifiers are used to evaluate the potential of the proposed methodology: Random Forest (RF) and Support Vector Machine (SVM). These two were selection due to their robustness when there is no balance between data dimensionality and number of available training samples (Ghamisi et al., 2017). Additionally, SVM has the advantage of being specifically designed for binary classification problems. For the evaluation of the belonging of each sample to class concentrate or class tailings the scores are calculated in Matlab release 2019a as posterior probabilities for each algorithm.

5.4.3 Random Forest (RF)

RF is an ensemble learning method used for both classification and regression. For classification problems, a set of decision tree classifiers is trained. Further, their individual results are combined through a voting process. A classification label is allocated to the input vector (X) through a majority vote: $y_{RF}^B = $ *majority vote* $\{y_b(X)\}_1^B$, where X is the input vector, $y_b(X)$ is the class prediction of the *b*th tree, and B shows the total number of trees (Breiman, 2001).

The training algorithm for RFs applies the general technique of bootstrap aggregating, or bagging, to tree learners. Bootstrap aggregating is used for training data creation by resampling the original data set in a random fashion with replacement. This leads to more efficient model performance. While the predictions of a single tree are highly sensitive to noise in its training set, the average of many trees is not that sensitive as long as the trees are not correlated (Ghamisi et al., 2017).

5.4.4 *Support Vector Machine (SVM)*

The goal of an SVM classifier is to identify the separating hyperplane, defined as a class boundary that separates the feature space in two classes with the largest margin for each class. The hyperplane is identified using an optimization problem solved by structural risk minimization. To train the classifier, only the samples located closest to the hyperplane, and therefore to the class boundaries are needed (Cortes and Vapnik, 2001; Ghamisi et al., 2017; Vapnik, 1999). As only these samples are influential, SVM can classify the input data efficiently even if only a limited number of training samples is available. In addition, SVMs can efficiently handle the classification of noisy patterns and multimodal feature spaces (Ghamisi et al., 2017; Vapnik, 1999).

5.5 Results

The results of the classification are analysed based on the scores that indicate the probability of a pixel reporting to the concentrate class. In each recovery vs. mass pull plot, the commodity (cassiterite or equivalent copper) recovery is illustrated as a function of three proxies: the first one consists of the true commodity recovery in each block known from SEM-MLA analyses, labelled as mineralogical barrier, followed by the second and third, which represent estimated commodity recovery from hyperspectral data by random forest and support vector machine, respectively. By selecting a target commodity recovery or mass pull, the mineral composition and metal content in each of the products can be analysed. For the current study, two target recoveries are considered for each analysis, 90 % and 95 %. At these target values the products are analysed in terms of metal content and mineral composition. The following subchapters present the results of the two tested ore types.

5.5.1 *Skarn ore*

The skarn ore samples show a high variability in modal mineralogy, textures, mode of occurrence of cassiterite and cassiterite content (in this context representing the ore grade). The analysed samples can vary from feldspar-epidote-dominated lithologies to iron oxide-dominated lithologies (Figure 5-3). The skarn ore is sorted based on cassiterite content. Its association with SWIR active minerals such as chlorite and fluorite, has a strong impact on the performance of the grade estimation and recovery at low mass pull values using both RF and SVM as classifiers (Figure 5-4). RF shows better results for sorting high grade blocks in the first stages. However, a shift in the performance can be observed for the low-grade blocks, where SVM shows a better grade estimation.

At a chosen target recovery of 90%, both classifiers show a good separation curves for sorting the high-grade ore at a mass pull of 27 wt% (Figure 5-4). However, when sorting the low grade ore, SVM is able to sort the skarn ore with 95 % recovery at a mass pull of 53 wt% while RF reaches the same recovery at a mass pull of 83 wt%, illustrating poor selectivity. This leads to a high difference in the concentrate tin grades; using RF

a strong dilution of the tin grade occurs in the concentrate (Table 5-4). By selecting recovery thresholds, the performance of the methods in terms of accuracy and the modal mineralogy of the expected sorting products can be estimated from SEM-MLA data.
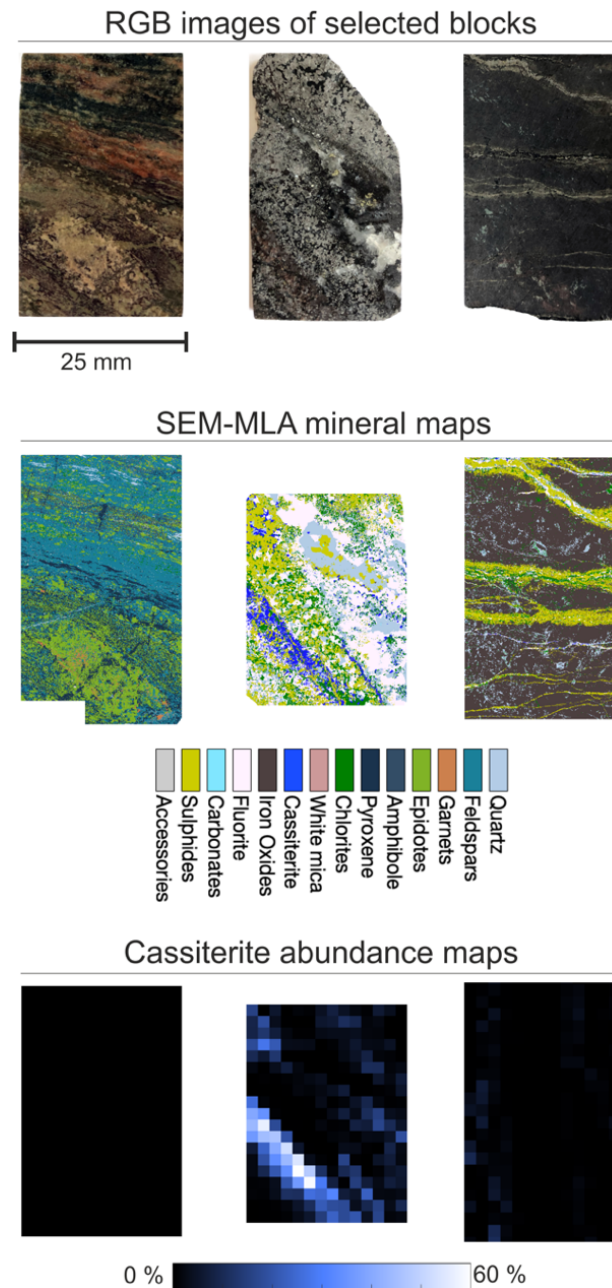
Figure 5-3. Skarn ore samples: RGB images of the analysed blocks, SEM-MLA high resolution mineral maps and resized cassiterite abundance from SEM-MLA to hyperspectral data spatial resolution. Three examples illustrate three lithotypes, including feldspar-epidote skarn (left), cassiterite-chlorite-fluorite-sulphide-quartz (central) and iron oxide-rich skarn (right).

The evaluation of the performance of the classifier can be assessed for each of the target recoveries and respective mass pull. This is achieved by comparing the labelled samples that lead to a selected recovery target at the respective mass pull to the ideal samples. These ideal samples would give the same mass pull in the ideal scenario (mineralogical barrier), which can be obtained from SEM-MLA data (Figure 5-5). With a recovery target of 90 %, 5 samples are misclassified by RF in both products, leading to an overall accuracy of 85 %, and 6 samples are misclassified by SVM, resulting in an overall accuracy of 82 %. An increase in misclassified

78

samples for both algorithms can be observed for a target recovery of 95 %. The average and overall accuracies are listed in Table 5-5.

By achieving 90% recovery, mostly the high grade ore is being sorted out. In this case, a preferential recovery of specific minerals such as chlorite and fluorite, together with cassiterite, can be observed (Figure 5-6). Other abundant minerals in the deposit, such as quartz, amphiboles, iron oxides and sulphides, are also recovered but do not show a preferential distribution into concentrate or waste. Another group of minerals such as feldspars, garnets and epidotes are markedly enriched in the waste stream. Increasing the target recovery to 95 % results in a change in the mineralogy of the concentrates, as the iron oxide content in the concentrate shows a marked increase. Additional mineralogical parameters such as grain sizes and mineral association can also be calculated for both products and will provide valuable information for the subsequent beneficiation stages.
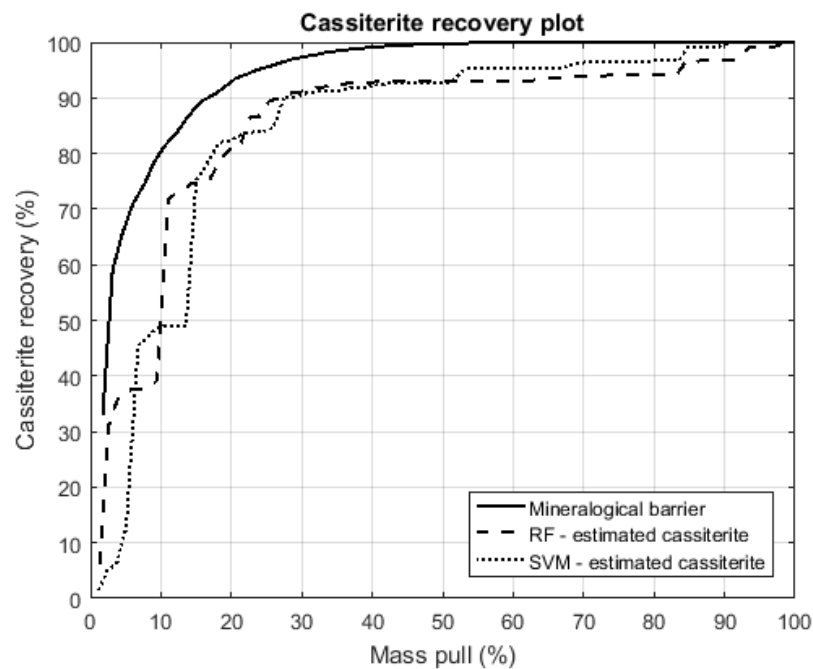
Figure 5-4. Mass pull vs. recovery plots for cassiterite (true grade – mineralogical barrier, estimated grade by RF and estimated grade by SVM)

Table 5-4. Sorting performance in terms of mass pull and products tin grade at selected recoveries for the two tested algorithms (RF and SVM).

	Recovery (%)	Mass pull (%)	Sn grade (%)	
			Conc.	Tail.
RF	90	27	1.46	0.05
	95	83	0.49	0.02
SVM	90	27	1.46	0.05
	95	53	0.82	0.03
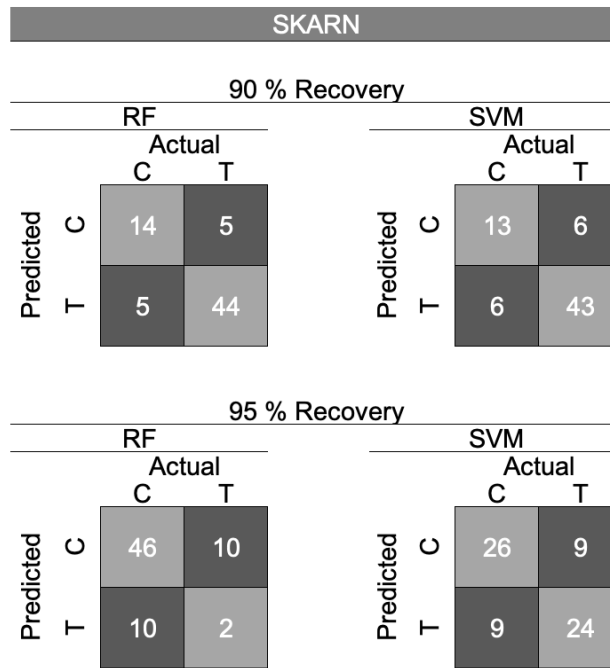
Figure 5-5. Confusion matrices for the evaluation of the two classifiers (RF and SVM) at a target of 90% cassiterite recovery in the skarn ore.

Table 5-5. Evaluation of average and overall accuracies of the two classifiers (RF and SVM) at a target of 90% cassiterite recovery in the skarn ore.

Accuracies	90 % Recovery		95 % Recovery	
	RF	*SVM*	*RF*	*SVM*
AA	82%	78%	49%	74%
OA	85%	82%	71%	74%
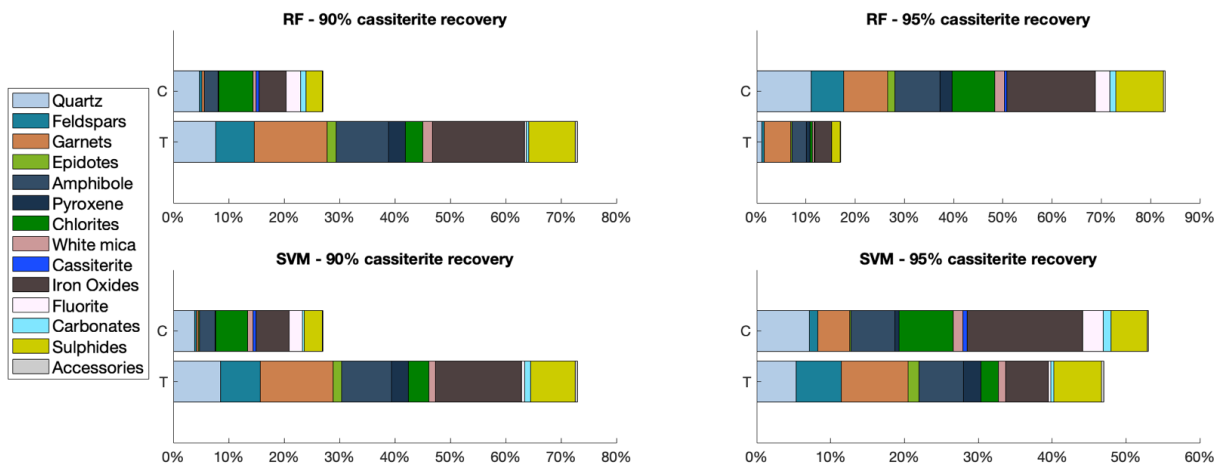
Figure 5-6. Modal mineralogy of skarn pre-sorting products at 90 % and 95 % cassiterite recoveries by RF and SVM.

80

5.5.2 *Porphyry ore*

In comparison to the skarn samples, the host lithology in the porphyry is more simple and homogeneous in composition. Major rock-forming minerals are plagioclase feldspars, quartz and amphiboles. The feldspars and amphiboles show different degrees of alteration to white micas and chlorite and biotite, respectively, depending on vein abundance and vein types. The variability in vein types and their associated alteration halos can be seen in three examples of samples illustrated in Figure 5-7.
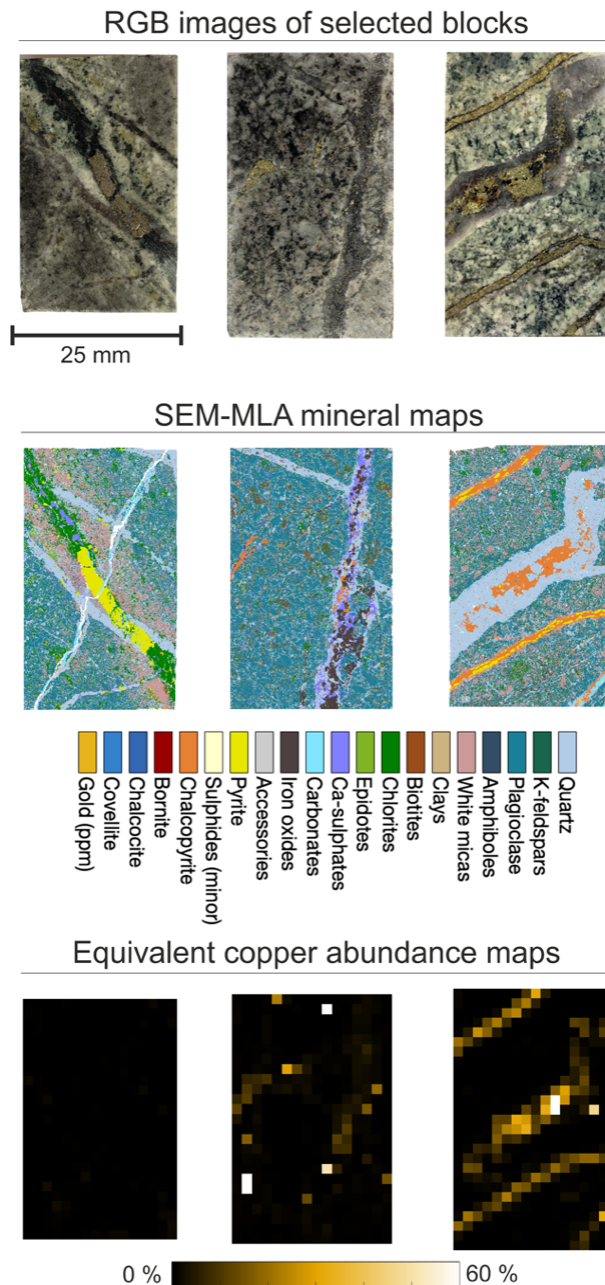
Figure 5-7. Porphyry ore samples: RGB images of the analysed blocks, SEM-MLA high resolution mineral maps and resized equivalent copper abundance from SEM-MLA to hyperspectral data spatial resolution. Several vein types are present in the illustrated samples: late pyrite-chlorite vein with a strong phyllic alteration halo (left), quartz-gypsum-magnetite-chalcopyrite vein (centre), pyrite-chalcopyrite veins and quartz vein with a distinct chalcopyrite centreline (right);

81

The equivalent copper grades on the porphyry samples are greatly influenced by the highly variable distribution of Au. Unlike the skarn ore, a higher fraction of the selected porphyry samples hosts considerable amounts of the target commodities. This aspect is supported by the shape of the mass pull vs recovery curves (Figure 5-8). Here, the equivalent copper recovery, calculated based on the metal concentrations estimated by SEM-MLA, is presented as the mineralogical barrier and it represents the best sorting scenario that can be achieved. The following curves consist of the RF and SVM sorting results and closely follow the mineralogical barrier.

At a chosen recovery target of 90 % equivalent copper, the mass pull estimated by RF is 43 wt%, and 50 wt% by SVM. As with the skarn ore, the SVM performs better for lower grade ore, at 95 % equivalent copper recovery the mass pull obtained is 67 wt%, while for RF the mass pull is 71 wt% (Table 5-6). However, the discrepancy between the two methods is lower for the porphyry ore compared to the skarn ore.
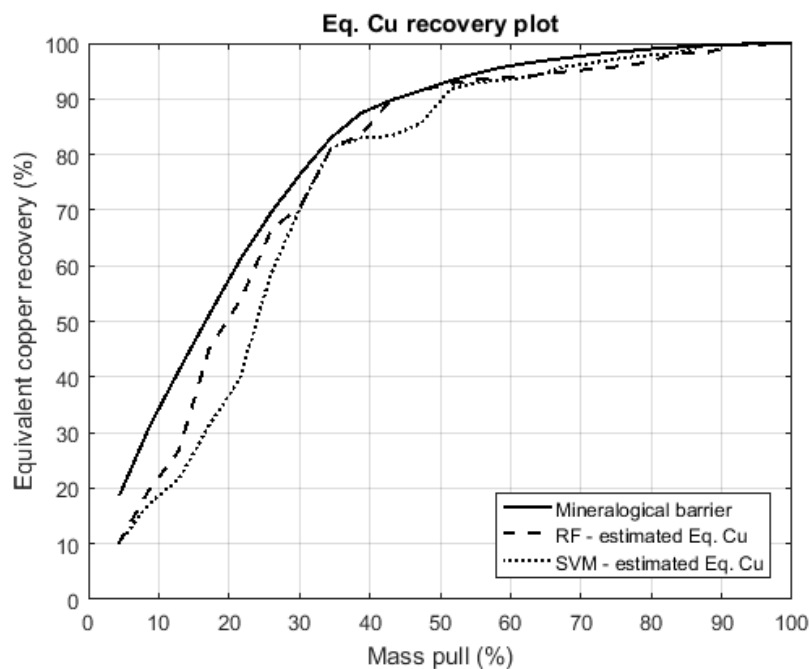
Figure 5-8. Mass pull vs. recovery plots for equivalent copper (true grade – mineralogical barrier, estimated grade by RF and estimated grade by SVM).

Table 5-6. Sorting performance in terms of mass pull and products equivalent copper, copper and gold grades at selected recoveries for the two tested algorithms (RF and SVM).

	Recovery (%)	Mass pull (%)	eq. Cu grade (%)		Cu grade (%)		Au grade (ppm)	
			Conc.	*Tail.*	*Conc.*	*Tail.*	*Conc.*	*Tail.*
RF	90	43	8.47	0.6	2.08	0.24	8.63	0.49
	95	71	5.35	0.61	1.38	0.16	5.36	0.61
SVM	90	50	7.32	0.55	1.8	0.24	7.45	0.43
	95	67	5.7	0.35	1.42	0.22	5.83	0.17

The confusion matrices for the classification of the porphyry samples at a target equivalent copper recovery of 90 % (Figure 5-9) show that no samples are misclassified for RF and only one sample for SVM (of 24 samples classified). At a 95 % target recovery an increase in the number of misclassified samples to 3 for

RF and 2 to SVM occurs. The classification accuracies are higher for the porphyry ore in comparison to the skarn ore, particularly at a target recovery of 90 % (Table 5-7).

The modal mineralogy of the expected products can be calculated from SEM-MLA data for both selected recovery thresholds (90 and 95 % respectively) (Figure 5-10). Unlike for the skarn, preferential relationships between the ore minerals and gangue are not as clear. At a targeted recovery of 90 %, it can be seen that the mineralogy of the products appears relatively similar for both of the estimation methods. However, a reduction in the white micas and clay minerals contents in the concentrate is observed, both of which could have a strong impact on the subsequent separation stages. Additionally, a large fraction of the pyrite is not recovered to the concentrate, leaving the copper minerals as the main sulphides in the concentrate. With an increase in the equivalent copper recovery to 95 %, a decrease in electivity can be observed as larger fractions of the white micas and pyrite are now present in the concentrates.

Figure 5-9. Confusion matrices for the evaluation of the two classifiers (RF and SVM) at a target recovery of 90 % and 95 % equivalent copper in the porphyry ore.

Table 5-7. Evaluation of average and overall accuracies of the two classifiers (RF and SVM) at a target recovery of 90 % at 95 % equivalent copper in the porphyry ore.

Accuracies	90 % Recovery		95 % Recovery	
	RF	*SVM*	*RF*	*SVM*
AA	100%	92%	72%	82%
OA	100%	92%	75%	83%
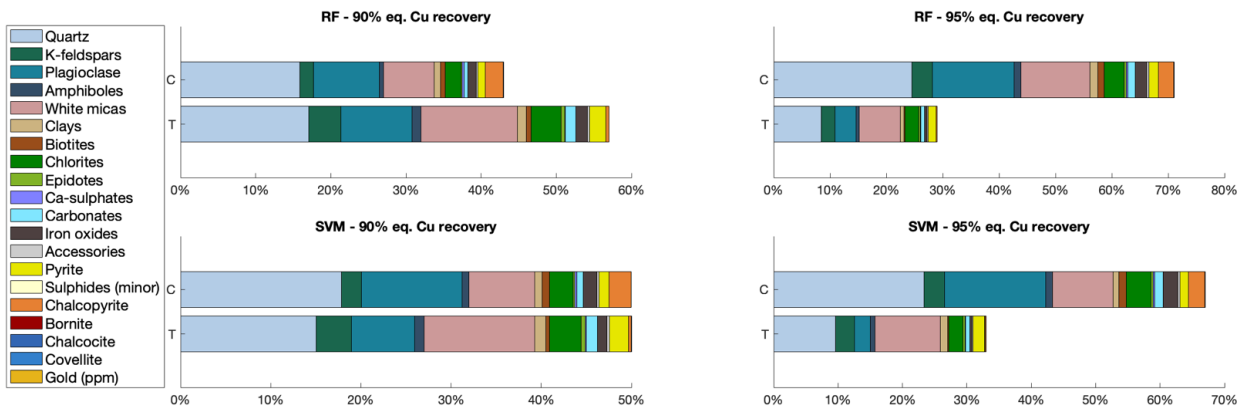
Figure 5-10. Modal mineralogy of porphyry pre-sorting products at 90 % and 95 % cassiterite recoveries by RF and SVM.

5.6   Discussion

The two case studies presented in this contribution illustrate a new methodology for the estimation of metal grade from hyperspectral data that can be used to predict the pre-sorting potential of two complex ores using VNIR-SWIR sensors. Co-registration of the hyperspectral and SEM-MLA data allows for direct evaluation of spectral response of complex mineral assemblages and associations in each pixel whilst machine learning approaches are applied to detect complex relations between mineralogy and grade. For both case studies, the removal of large fractions of rock-forming minerals such as quartz, feldspars, garnets and also iron oxides during pre-sorting is apparent. This leads to an important reduction of the material flow to further grinding stages, leading therefore to a significant decrease in energy consumption.

The results for the skarn case study indicate a particularly promising potential for ore sorting using SWIR sensors, with cassiterite recoveries reaching 90 % at only 27 wt% mass pull. Even though cassiterite does not show a diagnostic response, its association with VNIR-SWIR active minerals, such as chlorite and fluorite, is characteristic. The effect of the presence of these minerals is also shown in the estimated composition of the concentrates. Most of the fluorite will report to concentrate together with a large fraction of the chlorite. In each case, minerals such as epidote and garnet dominantly report to waste, showing a negative correlation with cassiterite. A large fraction of the iron oxides is also found in the waste fraction. This represents an added value since iron oxides have a negative impact on the flotation of cassiterite (Buchmann et al. 2017). Tests have also documented that magnetic separation applied to the skarn ore resulted in a disproportional loss of cassiterite (Buchmann et al., 2018). Reducing the iron oxide content in pre-sorting stages will therefore improve subsequent recovery of cassiterite.

The porphyry case study yields a somewhat lower potential for ore sorting based on the mineralogical barrier represented by the equivalent copper grade. This is explained by systematic variations in the distribution of the commodities in the Bolcana deposit. In the near-surface environment, gold is predominantly associated with pyrite, while copper-bearing minerals are present in low amounts. With depth, the copper content increases, as well as its association with gold. By considering the equivalent copper grade (rather than Au and

Cu grade separately), the best scenario achieved is 90 % recovery at 43% mass pull. An important upgrading of the concentrate is achieved by redirecting of a large fraction of the pyrite to tailings. This will strongly facilitate the recovery of copper-bearing minerals from the sulphide fraction in the late flotation stages (Chen et al., 2014). A second achievement is the removal of a large fraction of white micas and clay minerals, which can strongly impact flotation performance.

Overall, the two tested hyperspectral data classification algorithms show similar results. Slight differences include the better performance of RF with the high grade ore and better SVM performance with the low grade ore. The better performance of RF with high grade ore and outliers can be assigned to its design as a decision tree with bagging, which tend to be robust to noisy data (Hastie et al., 2008). With increase in number of samples per class and implicitly training samples, SVM shows a better performance due to a better definition of the support vectors, i.e. a better class separability. It can, however, be stated that both methods present a high potential for further use for discriminating ore and waste from hyperspectral data in the framework of sensor-based sorting operations. A particular advantage of using machine learning is apparent for the skarn case study. Kern et al. (2019) processed the same SWIR data set for the skarn samples by traditional methods such as band ratios and minimum wavelength analysis (Van Ruitenbeek et al., 2014). By doing so, Kern et al. (2019) were able to achieve a target recovery of 90 % with a mass pull of 70 wt %. By implementing machine learning algorithms, we have been able in this study to reduce mass pull to 27% - achieving the same target recovery.

The general applicability and performance of the proposed framework shows a strong dependence on sample representativeness.

Another fundamental assumption made is that the mineral content within the volume of each particle is similar to that exposed at the analysed surface. For the skarn ore, the material loss on average consisting of up to 0.3 mm can be considered negligible based on the knowledge of textures and mineral distribution in the different domains. For the porphyry ore, the copper mineral content is considered to also be consistent throughout the veins and the material loss will likely not show a strong impact. Gold, however, is present in very fine grains only (<20 μm) mostly as inclusions in chalcopyrite and pyrite. In this case, the nugget effect may show a strong influence on the calculated equivalent copper grade. To compensate for the potential bottlenecks related to the gold distribution, the addition of high-resolution XRT data slices is recommended in order to calculate the average gold grade at selected voxel/pixel sizes.

5.7 Conclusions

The use of reflectance spectroscopy for sorting of ores is increasingly becoming a focus of research as it holds great promise to reduce energy consumption and operational costs in industrial mining operations. Genetic and spatial relationships between ore minerals and associated gangue minerals may be utilized to develop of new methodologies for sensor-based sorting. Two case studies are used to illustrate the inherent potential not only of VNIR-SWIR sensors, but also the predictive assessment of the success of ore sorting by applying a combination of quantitative mineralogical and reflectance data with well-established machine learning approaches. Machine learning algorithms, such as Random Forest or Support Vector Machine thus

become valuable tools for unravelling complex but nevertheless systematic patterns between ore grade, ore mineralogy and spectral response.

Acknowledgements

Chapter 6 3D integration of hyperspectral data for deposit modelling

Preface

The increased geological complexity and decreasing grades of currently mined ores are associated with increased risks of mining operations related to engineering, environmental and economic factors. To tackle these risks geometallurgy is becoming an increasingly adapted concept in exploration and mining operations. The development of a geometallurgical model, combining geological, engineering, economic and environmental information relies on the availability of continuous mineralogical data acquired through exploration drilling. These data are then used for the definition of homogeneous domain which would present constant behaviour throughout the mine cycle. Hyperspectral imaging is probably the only technology which can deliver these extensive datasets with a short turn-around time and at high resolution and provided suitable data processing techniques are available it can become a pillar in geometallurgical programmes. Based on the data processing methods developed and described in chapters 3-5, an integrated workflow is illustrated in this chapter with the following main outcomes:

(1) Development of broad alteration domains based on point spectral data to be used for the selection of representative samples

(2) Quantitative mineral abundance estimation based on the fusion of automated mineralogy and hyperspectral data

(3) Extraction of structural parameters (sulphide vein density) and definition of mineralogical domains based on the estimated mineral abundance. These domains present homogeneous mineralogical, textural and structural properties and can serve as geometallurgical domains

Additional to the above points preliminary 3D modelling based on the point spectral data available over all analysed boreholes was attempted, illustrating the transferability of the spectral data domains to geological bodies.

Authors and contributions

Tusa L. [1,2], Khodadadzadeh M.[1], Fuchs M.[1], Zimmermann R.[1], Gilbricht S.[3], Ivascanu P.[4], Gloaguen R.[1], Gutzmer J.[1]

[1] *Helmholtz-Zentrum Dresden-Rossendorf, Helmholtz Institute Freiberg for Resource Technology*
[2] *THEIA X – Spectral exploration, HZDR Innovation GmbH*
[3] *Technische Universität Bergakademie Freiberg*
[4] *Eldorado Gold Corporation*

Abstract

There are numerous ore deposits discovered worldwide which have not been mined due to various reasons, including low grades, tonnages, high mineralogical complexity or environmental impact rendering them uneconomical. To reduce the related technical and financial risks associated to these projects, the use of a geometallurgical programme can support the resource characterisation and mining process.

One of the pillars in the development of a geometallurgical model is the acquisition of compositional data through systematic sampling and analysis. This sampling is usually achieved during exploration campaigns in which thousands of kilometres of diamond drill-cores are extracted to test subsurface regions with high mineral resource potential.

This research is motivated by the strong need for continuous data over large drill-core intervals that can be used to define mineralogical and textural (geometallurgical) domains. Hyperspectral imaging of drill-cores is identified in this study as a key technology to deliver such data, provided that suitable processing tools are made available. In this regard, a processing and analysis methodology is developed for the available hyperspectral data, allowing for a broad domain definition based on spectral point analysis which can be further used for strategic sampling for higher resolution analyses (for example by SEM-based image analysis at micrometer-scale). These local high-resolution data can be co-registered to the hyperspectral data. The mineralogical and textural information is further upscaled to entire drill-core samples for mineral abundance estimation, using random forest, the algorithm identified in previous works (Tuşa et al., 2020) as best suited for the analysed dataset. The mineral abundances obtained can in a next step be used for extraction of structural or morphological features as well as for defining domains of known average mineralogical composition. This mineralogical knowledge can further support decision making for metallurgical testing and can be incorporated into a 3D model for predicted metallurgical performance in the subsequent mining stages.

6.1 Introduction

Decreasing grades and increasing geological complexity of mineral deposits challenge exploration and mining operations. As a consequence, a strong need arises for both resource and energy efficiency to increase dramatically in the mining industry through the implementation of integrated, multidisciplinary approaches within exploration and mining operations. To satisfy this need the concept of geometallurgy was introduced and is increasingly adopted by exploration and mining companies (Michaux and O'Connor, 2020). It relies on the strategic integration of geological, mining, metallurgical, economical and geoenvironmental parameters to maximize the project value and reduce risk through responsible resource management (Dominy et al., 2018b).

One of the first steps in the development of a geometallurgical program is the acquisition of continuous compositional data through systematic sampling and analysis. Based on the obtained data, spatial models are constructed and geometallurgical domains identified that are marked by limited mineralogical and textural variability. For each domain, laboratory and/or pilot test analyses are performed in order to evaluate the different engineering, metallurgical, environmental and economic parameters characteristic of the specific ore type. However, in order to achieve a representative sampling, extensive data is required for ore characterization (Dominy et al., 2018a). The characterization of ore deposits is currently based on extensive drilling combined

with chemical assays and a visual evaluation of the mineralogical properties of the cores (Dominy et al., 2018a). However, the mineralogy and microfabric of an ore determine its properties and have an important bearing on all mining and beneficiation processes. Therefore, the acquisition of unbiased and consistent data on mineralogy and texture over large drill-core intervals is thus essential.

Hyperspectral drill core imaging provides a valuable tool for efficient and unbiased acquisition of mineralogical and textural data needed to define the geometallurgical domains and respective parameters. First applications of hyperspectral imaging had a clear focus on exploration and concerned with the mapping of alteration mineralogy or structures of mineralized systems in satellite and airborne-based remote sensing approaches (Bedini et al., 2009; Bishop et al., 2011; Kratt et al., 2010; Ngcofe et al., 2013; Pour and Hashim, 2011; Rodriguez-Galiano et al., 2015; Wu et al., 2019) as well as structures related to mineral systems (Jakob et al., 2016). In addition, the monitoring of mines and their environmental impacts is possible (Imagery et al., 2011; Jackisch et al., 2018; Rauhala et al., 2017; Riaza and Mu, 2010). Mapping the more subtle mineralogical changes in outcrops and mines requires a greater spatial resolution. For this purpose, drone and tripod-based systems are increasingly used (Boubanga-Tombet et al., 2018; Kirsch et al., 2018; Krupnik and Khan, 2019; Lorenz et al., 2018; Murphy et al., 2015, 2014, 2012). Through the use of near-field sensing platforms such as laboratory setups, drill-core scanners or conveyor-mounted systems, hyperspectral imaging is today well established in mineral exploration, especially for mapping spectrally distinct, (alteration) minerals that can be used as vectors towards mineralization (Arne et al., 2016; Calvin and Pace, 2016; Contreras Acosta et al., 2019; Huntington et al., 2006; Kruse, 1996; Laukamp et al., 2018; Lypaczewski et al., 2020; Mathieu et al., 2017; Mauger et al., 2007; Tappert et al., 2011; Taylor, 2000; Laura Tusa et al., 2019).

While hyperspectral data has been increasingly used in the last decade for exploration targeting, it has received less attention for ore characterization and pre-concentration. Some recent developments in hyperspectral imaging allow a potential use past the exploration stage and into beneficiation for the pre-concentration of ores (Dalm et al., 2018, 2014; Gallie et al., 2010; Tusa et al., 2019). Little work has been done so far in establishing the role of hyperspectral imaging (HSI) in a geometallurgical context. Johnson et al., (2019)were among the first to present the use of HSI of blast hole cuttings to predict metal recovery and throughput in a processing plant. The study has highlighted the high potential of linking hyperspectral analyses to the performance of mineral beneficiation processes. Integrating the information from spectral analysis gained during the exploration stage into the definition of geometallurgical domains is an obvious opportunity that has, however, received little attention. Yet, such an integrated approach can lead to a better understanding of ore types, both in terms of ore mineralogy and the presence of deleterious minerals and thus allows for ore-waste discrimination and stock-pile and processing route assignment during exploitation and beneficiation.

In this study, a unified methodology integrating point spectral measurements on 2-meter intervals of crushed material, hyperspectral imaging of drill-core samples and Scanning Electron Microscopy Mineral Liberation analysis (SEM-MLA) data on thin sections is presented. The scope of the study is to tackle limitations related to the scale and continuity of the mineralogical information available in exploration and mining campaigns through the use of the full power of hyperspectral imaging combined with local high resolution mineralogical data. Through the proposed methodology, this study aims to tackle the limitations

related to the collection of samples for thorough mineralogical analyses which can provide valuable information related to the microfabric attributes of the ore, through the use of clustering of point spectral measurements to define mineralogically homogeneous domains at large scales. Once a suite of samples has been selected for SEM-MLA analyses the resulting high resolution mineral maps are co-registered with the hyperspectral data in order to estimate mineral abundances in drill-cores subjected to hyperspectral drill-core scanning. By adopting this approach, the usual limitations in obtaining continuous mineralogical information over large drill-core intervals is addressed. The obtained mineral abundance maps can serve as a basis for the extraction of other parameters such as vein density, which are essential to the characterization of some deposits as well as to the definition of geometallurgical domains. Furthermore, the estimated compositional maps are clustered into domains of known mineralogical composition. The knowledge of the modal mineralogy of each domain can support decision making for further sampling and engineering testing that would add further valuable information to these drill-core domains. The final drill-core data can then be modelled and integrated into a geometallurgical domain containing geochemical and mineralogical information as well as predictions of how each domain will behave in the future mining and beneficiation stages and also in mine closure and remediation.

We illustrate the potential of the proposed methodological framework with the Bolcana gold-copper porphyry system. The Bolcana system is marked by high variability of mineralogical composition over short drill-core intervals. This makes it an ideal case study for the use of hyperspectral imaging.

6.2   Geological setting

The Bolcana porphyry system is located in the Western Tethyan magmatic belt, spanning across Slovakia, Hungary, Romania, Serbia, Bulgaria, Kosovo, Macedonia, Greece and Turkey (Baker, 2019). The Bolcana system is currently explored by Eldorado Gold through their Romanian subsidiary, Deva Gold S.A. It is located in the Golden Quadrilateral in the southern part of the Apuseni Mountains, Romania. This region is considered one of Europe's most significant porphyry Cu-Au and epithermal provinces (Berbeleac et al., 2014; Cioacă et al., 2014). The geodynamic evolution of the magmatic belt commences with Cretaceous magmatism related to subduction-rollback in the Carpathian arc, transitioning from convergence and collision to post-orogenic extension from the late Eocene to early Oligocene, followed by widespread post-collisional extension-related magmatism during the Miocene (Baker, 2019; Richards, 2005). The metallogenic endowment in the region is related to a Miocene post-collision back-arc extension-related magmatic event, mainly between 14.9 and 9 Ma (Pécskay et al., 2006; Roşu et al., 1997). Bolcana is located in the southern part of the Brad-Sacaramb extensional basin (Figure 6-1), where the main direction of the distribution of the ore deposits follows a ESE-trending dextral, strike-slip fault system (Neubauer et al., 2005). The basement in the area consists of Middle Jurassic-Lower Cretaceous basaltic andesites, lava flows and pyroclastics, as well as Lower Cretaceous rhyolites, overlain by Paleocene and Miocene sediments. Neogene subvolcanic bodies, of dioritic composition, intrude the basement and the older sedimentary units (Rhys, 2014). These intrusions are associated with magmatic-hydrothermal mineralization.
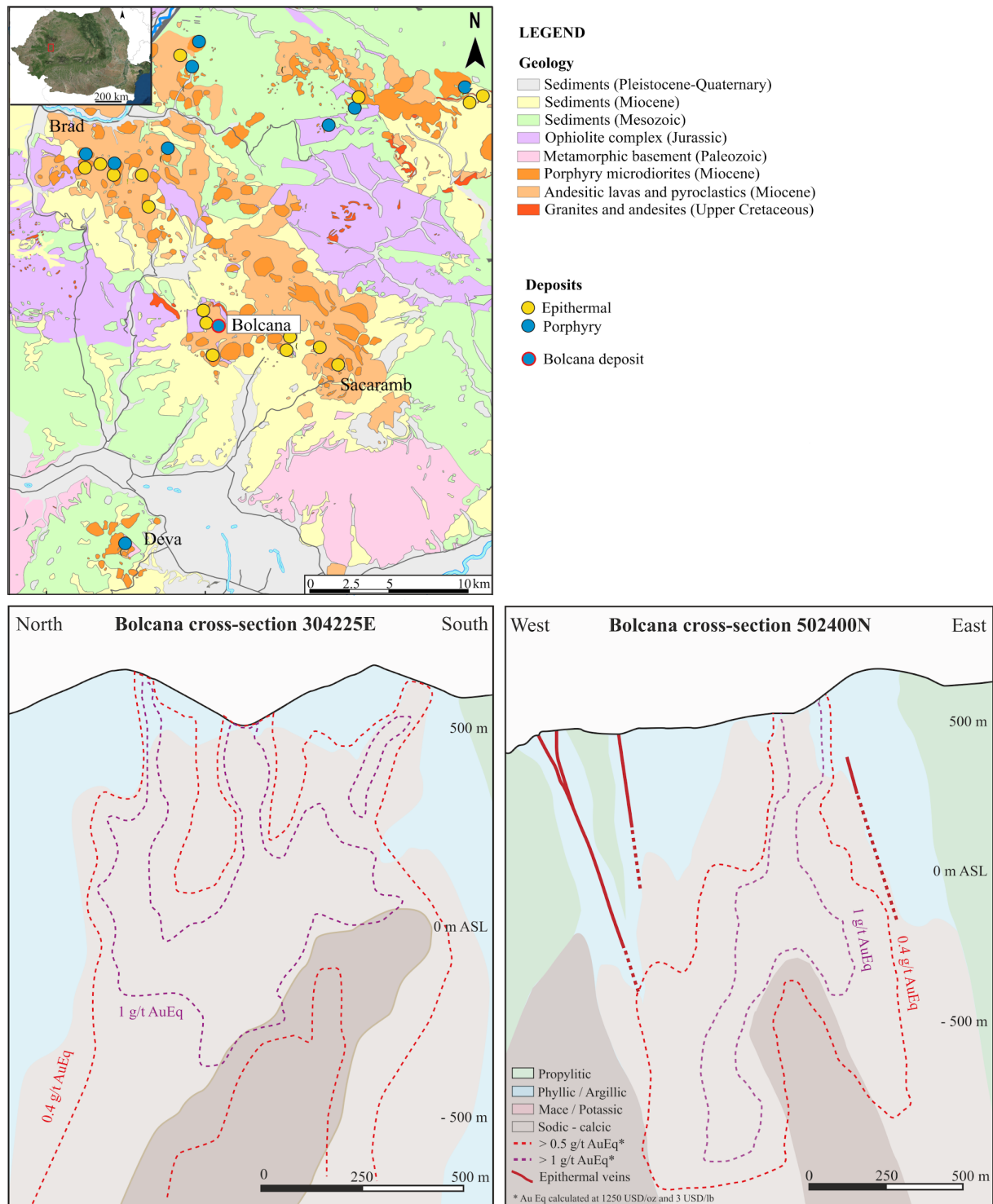
Figure 6-1 Left: simplified geological map of the Brad-Sacaramb extensional basin with marked locations of the epithermal and porphyry deposits, Centre: N-S cross-section of the hydrothermal alteration styles in the Bolcana porphyry system and equivalent gold grade contours, Right: W-E cross-section of the hydrothermal alteration styles in the Bolcana porphyry system and equivalent gold schematic outline (modified after Ivascanu et al., 2019).

At the surface, the Bolcana system has a broad 2 km by 1 km North-South elongated argillic footprint, controlled by faults that host late epithermal veins which flank the mineralised system (Ivascanu et al., 2019).

The Bolcana system consists of a series of polyphase intrusions and has a mapped depth extent of approximately 1.5 km. The main alteration types encountered in the system follow roughly the standard zonation characteristic of porphyry deposits (Sillitoe, 2010). The phyllic-argillic assemblages are observed on the flanks of the system and in near-surface zones, transitioning to a magnetite-chlorite dominant assemblage and further to a potassic character towards the centre of the system (Blannin et al., 2019; Ivascanu et al., 2019). Additionally, a sodic-calcic core was described by Ivascanu et al., (2019) (Figure 6-1). The ore minerals are represented by chalcopyrite, bornite, chalcocite, covellite and native gold and occur mainly as stockworks, hydrothermal breccias and subordinately as fine disseminations. The gold association varies with the location in the system. At shallow levels, in the phyllic and argillic zones gold is mostly present as fine inclusions in pyrite, while with the extension to depth it is dominantly associated with the copper sulphides (Blannin et al., 2019).

6.3 Sampling and data acquisition

Between 2017 and 2019 several sampling campaigns were conducted targeting exploration drill-cores in the Bolcana system. Point VNIR-SWIR measurements were collected from crushed assay rejects over 2 m intervals from around 20 km of core using a field-portable spectrometer. During two sampling campaigns, conducted in 2017 and 2019, around 200 drill-core intervals ranging in length from 15 to 40 cm were collected. These intervals were considered representative of the respective lithologies and major alteration and mineralization styles encountered in the system. 54 polished thin sections were prepared from regions of interest in the selected core intervals, representing the main vein and alteration types encountered in the system, and analysed by Scanning Electron Microscopy-based Mineral Liberation Analysis (SEM-MLA). The location of all samples and a schematic illustration of sample and measurement types is shown in Figure 6-2. The size of the collected drill-core and SEM-MLA samples was increased here for visualization purposes. The available samples and data thus consist of around 200 drill-core samples collected from three boreholes together with point spectral measurements over 2 m intervals from around 20 km of core.

6.3.1 Hyperspectral point measurements on pulps

Point measurements were acquired on the crushed material remaining from geochemical analyses. Samples represent 2-meter core intervals that were crushed to a particle size passing the 2 mm sieve. The collected spectra covers the VNIR (350-970 nm) and SWIR (970-2500 nm) regions of the electromagnetic spectrum. The probe contact surface covers a circular area of a diameter of 2 cm.

6.3.2 Hyperspectral drill-core scanning

The collected drill-core samples consist of half cores and the flat surface was analysed by hyperspectral imaging using a SisuROCK drill-core scanner equipped with an AisaFENIX hyperspectral sensor (Spectral Imaging Ltd., Oulu, Finland). The AisaFENIX camera implements two sensors to cover the VNIR (380-970 nm) and SWIR (970-2500 nm) regions of the electromagnetic spectrum. The acquisition setup follows the framework outlined in Tușa et al., (2020). The resulting spatial sampling of the hyperspectral images is 1.5 mm/pixel and the spectral resolution in the VNIR is 1.7 nm and in the SWIR 5.7 nm. The conversion from radiance to reflectance was

performed within the acquisition software for the hyperspectral data (LUMO Scanner version 2018-5, Spectral Imaging Ltd., Oulu, Finland) using a PTFE reference panel (>99% VNIR and >95% SWIR). The MEPHySTo toolbox (Jakob et al., 2017) was used for the correction of the spatial shift between the VNIR and SWIR sensors and for the sensor specific optical distortions. A Savitzky–Golay filter was applied to decrease noise while preserving spectral features with a window of 5 bands and a second degree polynomial (Ruffin and King, 1999; Savitzky and Golay, 1964). Principal component analysis (PCA) (Rodarmel and Shan, 2002) was performed on the hyperspectral dataset for data dimensionality reduction while preserving 99.9% of the information.
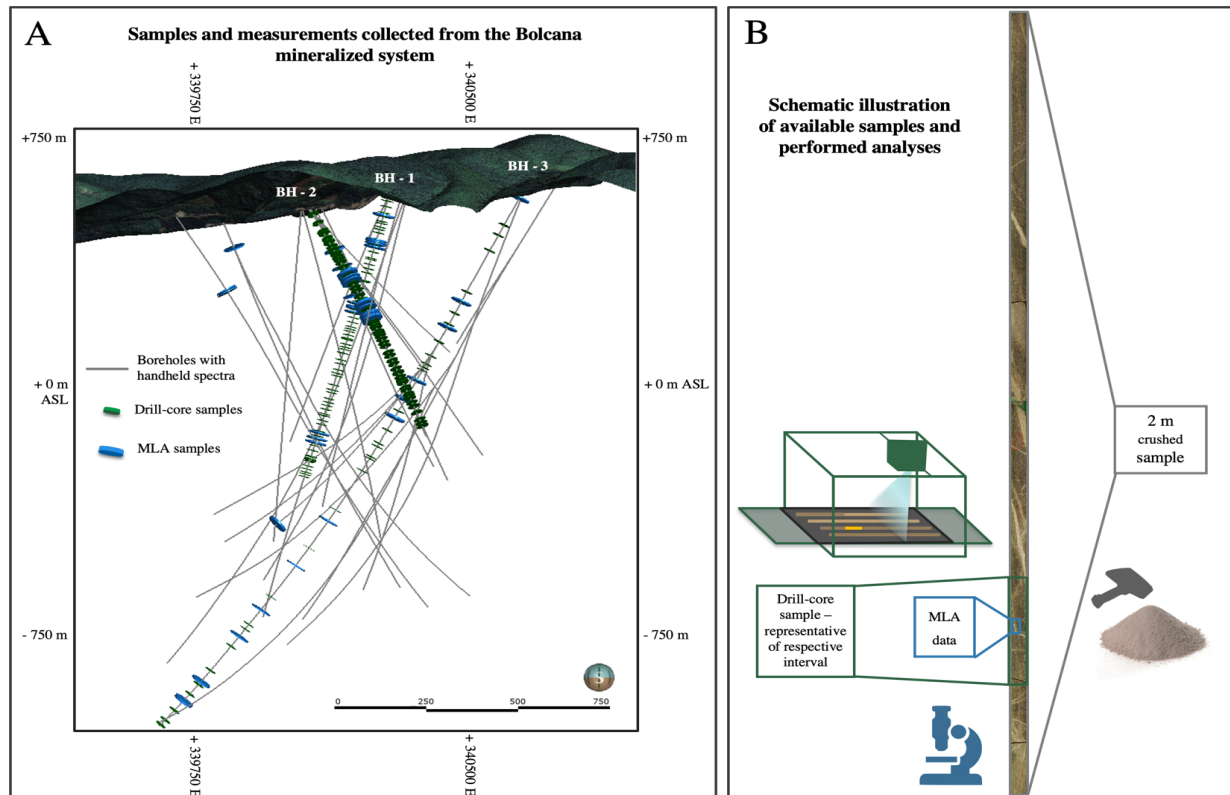
Figure 6-2 A - Cross-section view, looking North, of the analysed boreholes through the Bolcana deposit by point VNIR-SWIR spectroscopy. Clearly marked are drill-core samples collected for VNIR-SWIR hyperspectral imaging and SEM-MLA analyses, respectively. B - schematic illustration of sample and analyses types.

6.3.3 *Scanning Electron Microscopy-Based Mineral Liberation Analysis*

The 54 selected samples were prepared into polished thin sections and analysed with Scanning Electron Microscope (SEM)-based Mineral Liberation Analysis (MLA) using the grain-based X-ray mapping (GXMAP) mode (Kern et al., 2018b). For this purpose, a FEI Quanta 650F field emission SEM (FEI, Hillsboro, OR, USA), equipped with two Bruker Quantax X-Flash 5030 energy dispersive X-ray (EDX) detectors (Bruker, Billerica, MA, USA) ae) was used. The measurements followed the experimental setup presented in (Tuşa et al., 2020). The resulting spatial sampling of the mineral maps is 3 μm/pixel.

For the classification of the obtained EDX data, a mineral list was developed using the mineral reference editor in online mode resulting in a total of 59 entries. As the MLA data are meant to serve as training/validation

for a procedure using VNIR and SWIR HSI data, some classes need concatenation. To ensure the relevance of the products, minerals with extremely low abundances will not be imaged by the HSI data that have a coarser spatial resolution. Some minerals such as metal sulphides, quartz and feldspars are not identified by the HSI sensor. Finally, in order to improve the performance and the usability of the procedure for the geometallurgical modelling, we identified geologically relevant mineral groups. As a result, thirteen main mineral groups are considered: white mica (WM), clay, biotite (Bt), chlorite (Chl), epidote (Ep), amphibole (Amp), carbonate (Cb), gypsum (Gp), iron oxides (IO) feldspar (Fsp), quartz (Qz), sulphides (Sp) and other minerals (other). In order to allow data comparison, MLA data were resized to fit the HSI spatial sampling as proposed by Tusa et al. (2020). The resulting data is a data cube with the spatial sampling of the HSI data containing the dominant mineral abundances of the respective MLA data.

As a final step, the SEM-MLA mineral maps were resized to the spatial resolution of the hyperspectral images by converting the 2D labelled high-resolution image to a 3D image where each pixel contains 13 bands carrying the abundance information for each mineral or mineral group. This resampling is performed using the methodology presented in (Tuşa et al., 2020).

6.4   Methodology

The proposed methodology relies on the integration of three datasets; (a) hyperspectral point measurements on crushed material (pulp samples) over 2m intervals, (b) hyperspectral drill-core scans of selected drill core intervals and (c) SEM-MLA data resized to the spatial resolution of the hyperspectral drill-core scans. A schematic summary of the workflow is illustrated in Figure 6-3.

To delineate alteration domains and ensure the representativity of the available core samples to the alteration styles encountered in the Bolcana porphyry system, the point spectral measurements collected on the crushed drill-core material every 2 m were clustered into seven clusters or domains. This was achieved using sparse subspace clustering (SSC) (Elhamifar and Vidal, 2013). The SSC algorithm was chosen upon testing its performance in comparison with other hyperspectral data clustering algorithms on a selection of samples from the Bolcana deposit (Khodadadzadeh et al., 2018). Seven domains were considered suitable for the current dataset based on the knowledge on the alteration domain distribution within the deposit (Blannin et al., 2019; Ivascanu et al., 2019). To confirm the estimation of the virtual dimensionality of the data leading to the choice in the number of clusters, the elbow method was additionally used (Ketchen and Shook, 1996).

Then the obtained domains were applied to evaluate the representativity of the available SEM-MLA samples and measurements. Ensuring that a minimum of two samples is available for each domain, the 54 MLA samples were divided into 36 training and 18 validation samples. Further, the borehole domaining results are used for the development of a 3D model of the alteration in the Leapfrog Geo software package (version 5.0.4, Seequent Limited). The MLA samples continue to be used for the supervised multivariate regression for the estimation of modal mineralogy and development of mineral maps for the selected drill-core samples.
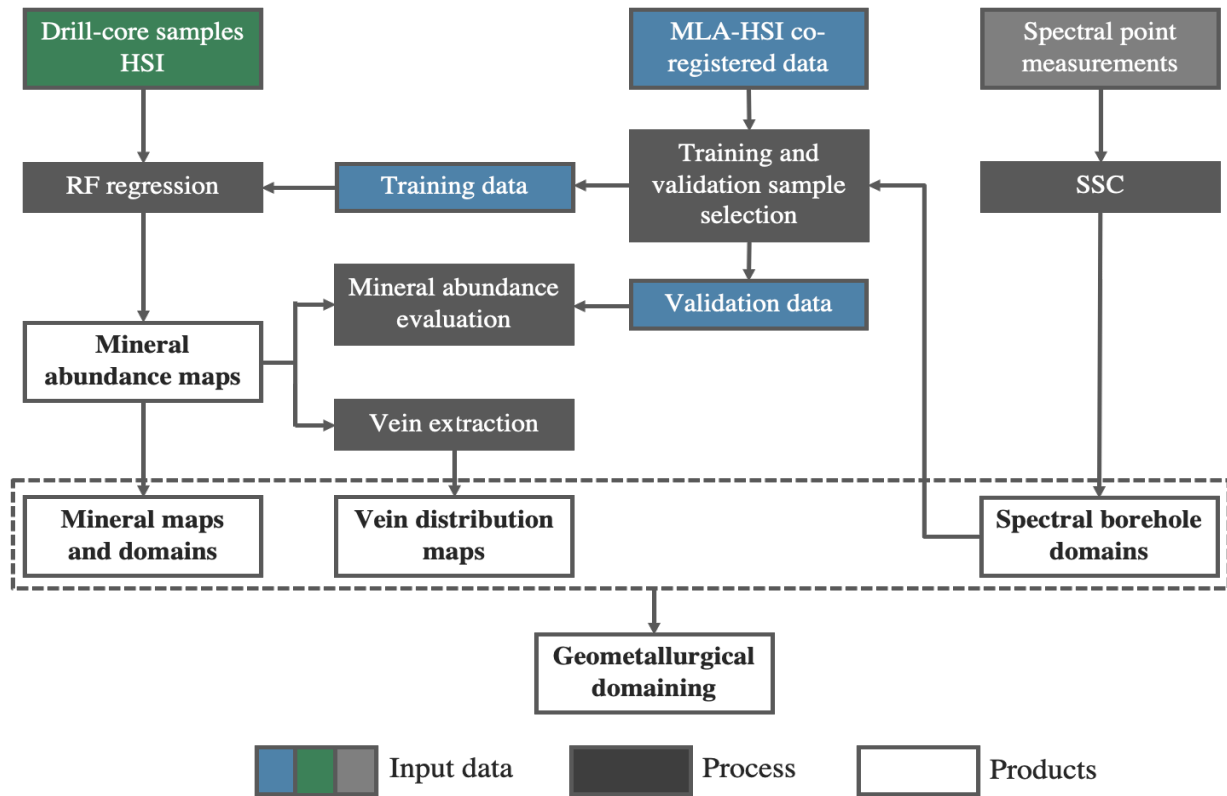
Figure 6-3 Flowchart illustrating the proposed methodology (HSI: hyperspectral images, RF: random forest, MLA: Mineral Liberation Analysis, SSC: sub-space clustering).

6.4.1 Mineral domaining based on pulp point measurements

For the purpose of dividing the hyperspectral data points into mineralogically relevant domains a subspace clustering algorithm (i.e., SSC) was used. Given that the point spectral measurements have been collected from crushed materials of 2 m drill-core samples, the obtained hyperspectral data is expected to contain a large number of data points containing mixed spectral information. We have demonstrated in our previous studies (Khodadadzadeh et al., 2018; Shahi et al., 2020) that subspace-based machine learning algorithms are powerful tools to handle mineral mapping in highly mixed hyperspectral data. Particularly, the SSC algorithm that performs subspace clustering using techniques from sparse representation theory, has shown improved performance in hyperspectral data clustering. This algorithm applies spectral clustering to a similarity graph, which is formed by representing each data point as a linear combination of all the other data points (Elhamifar and Vidal, 2013; Khodadadzadeh et al., 2018).

6.4.2 Mineral abundance estimation, mapping and vein detection

Following the resampling process, the resulting SEM-MLA mineral maps were manually co-registered with the hyperspectral scans of the corresponding blocks and drill cores. The training set as defined from the SSC results was used to train a multivariate Random Forest (RF) (Breiman, 2001) regression for the estimation of the abundance of each mineral group. This technique was chosen due to its good performance when only few training samples are available (Ghamisi et al., 2017). Additionally, RF was tested in comparison with other

methods for a smaller subset of the current dataset in (Tușa et al., 2020); here RF was proven most adequate for the current regression problem. To ensure the validity of the model within 100 iterations the training data was subsampled between training (66%) and cross-validation (33 %).

As a next step and because of the compositional character of the data, k-means clustering (Ranjan et al., 2017) was applied on the estimated mineral abundances. Mineral abundance data are subjected to collinearity removal and logarithmic transformation, prior to clustering. These transformations are necessary prior to using machine learning algorithms, such as clustering, when variables are considered collinear, meaning that two variables lie almost on the same line and therefore the angle between the data vectors is small (Belsley, 1991). In this investigation, the data are transformed using a centred log-ratio (CLR) algorithm. Within CLR, the data is scaled by its geometric mean (Egozcue et al., 2003). Further, the transformed mineral abundance data is clustered into domains using k-means. Within the k-means algorithm the Euclidean distance is used to measure the similarity between different data points, the points with the lowest Euclidean distances between them being grouped into clusters and treated in this study as spectral domains.

Furthermore, the estimated average composition of each domain was evaluated. The mineral abundance maps of the sulphide class, consisting of pyrite, chalcopyrite, bornite, chalcocite, covellite and sulfosalts, are further used to highlight and quantify the abundances of veinlets containing the bulk of the sulphide minerals. For this purpose, vessel enhancement filtering (Frangi et al., 1998) was used following the methodology presented in Tusa et al. (2019).

6.5   Results

This section is divided into (1) the domaining results obtained from the analysis of the point measurements over 2 m bulk samples and their implications on the choice of training and validation samples for (2) drill-core mineral abundance estimation, mineral mapping and vein extraction and (3) numerical and visual validation of the results. The second section presents the results at sample scale as well as at drill core scale where the implications of the results on the understanding of alteration at deposit scale can be highlighted.

6.5.1   *Domaining results*

The clustering of the handheld spectrometer data using SSC was performed to define spectral domain characteristics of the main alteration zones in the Bolcana system. The centre spectra and the interquartile range for each domain are illustrated in Figure 6-4. Seven domains were considered suitable for the current dataset and the domaining results highlight the distribution and variation of SWIR-active assemblages throughout the deposit.

A general zonation in the spatial distribution of the spectral domains can be observed in the analysed drill cores (Figure 6-5), ranging from the presence of domain (1) - argillic and (2) – phyllic-argillic in the near surface zone, followed by (3) and (4) as transitional domains to what is expected to comprise the chlorite-magnetite alteration assemblage described by Ivascanu et al., (2019) as "MACE", (3) being present more towards the fringes of the porphyry while (4) towards the centre. Domain (5) constitutes large intervals in the near-surface zone and short intervals in the core of the Bolcana system. Based on its distribution and spectral characteristics described below, it is expected that it represents a transition between the phyllic (chlorite-

sericite) and the propylitic alteration. The sixth spectral domain is distributed as a shell around the potassic core of the system (domain (7)).
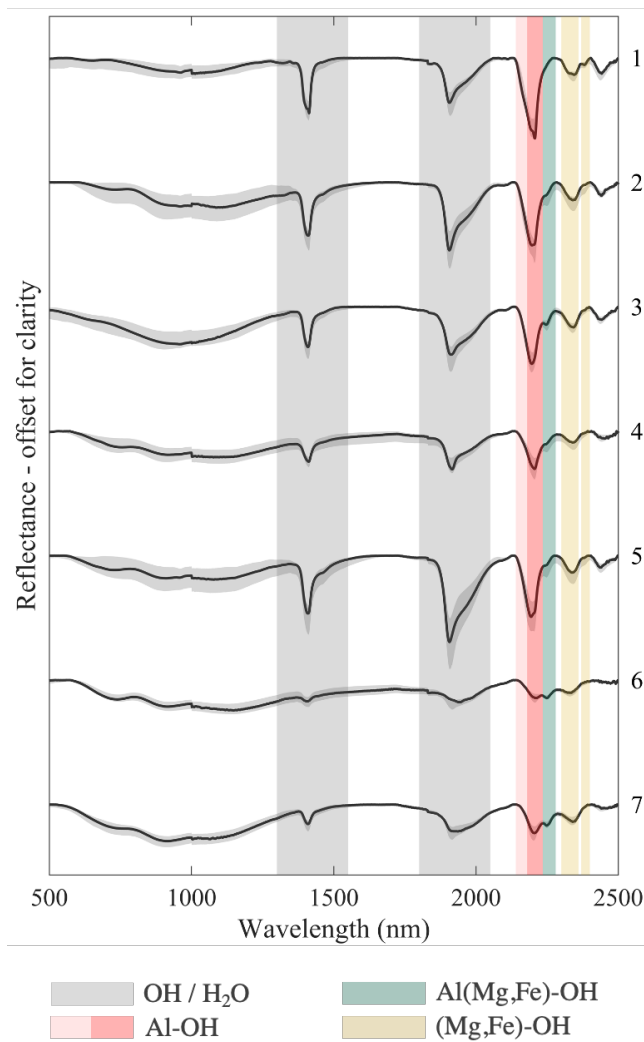
Figure 6-4 Spectral plot presenting the centre spectra and the associated interquartile range for each of the spectral domains obtained by subspace clustering of the point spectral measurements.

The spectral features of the first domain (Figure 6-4) indicate the presence of both kaolinite and muscovite based on the Al-OH absorption with a small doublet at 2200 nm and the doublet in the range of the water feature at 1400 nm. By comparison, the second domain does not preserve the doublet in the Al-OH feature characteristic of kaolinite in most of the spectra but an individual feature at 2208 nm characteristic of mica of intermediate composition between muscovite and phengite and medium crystallinity based on the ratio of this feature and the water feature around 1900 nm. It additionally exhibits a shoulder in the Al(Mg,Fe)-OH range indicating the presence of small amounts of chlorite. The presence of a Fe-rich silicate is supported by the increase in the iron features in the VNIR range. The third domain shows similar spectral features to the second domain with an increase in intensity of the chlorite feature and an increase in the crystallinity of the mica. Spectra of the fourth domain are marked by shallower absorption features compared to domains (1)-(3). This may indicate a lower alteration intensity or simply a different mineral matrix for these drill-core intervals.

The fifth domains has once again a similar spectral response to the second domain, but with reduced crystallinity of the mica, which is expected as most of the extensive intervals of this domain are located either on the fringes of the system or in the near-surface zones. The two last domains, (6) and (7) are characterized by the dominance of chlorite in domain (6) and of biotite in (7). These minerals are distinguished based on the ratio of the Al(Mg,Fe)-OH and (Mg,Fe)-OH features and the shape of the spectra in the VNIR range. A significant amount of muscovite is present in (7), as identified by the presence of the typical AlOH feature. This is likely due to the presence of muscovite in the alteration halo of the veins present in the potassic zone. The composition of mica-group minerals in the different domains varies from paragonitic in domain (2) to muscovitic in domain (7) based on the location of the minima of the AlOH absorption feature. A slightly phengitic composition of the mica is observed in some of the spectra of domain (6). However, due to the high abundance of chlorite in this domain the shift in the position of the minima of the Al-OH feature can be assigned to the mixture. Slight variations are present in the location of the minima for the Al(Mg,Fe)-OH feature among these domains, 2252-2255 nm in (3), 2248-2253 nm in (4) and 2250-2253 nm in (5). The lower wavelengths indicate a more magnesian composition of the chlorite while the higher ones indicate an increase in iron content.
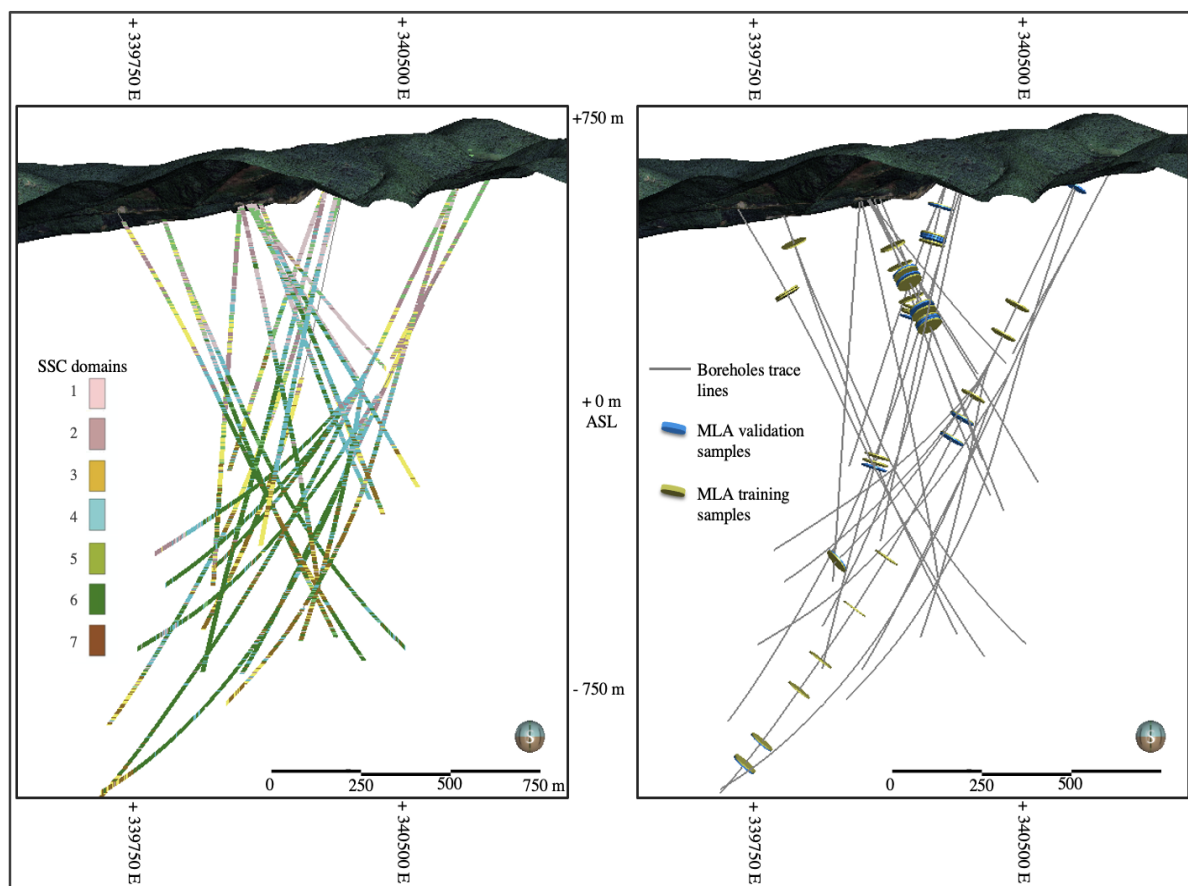
Figure 6-5 Left: N view of the spectral clustering of point spectra over the boreholes, Right: N view of the location of the selected training and validation MLA samples based on the spectral clustering.

Following the interpretation of the spectral response of each domain, based on the location of each SEM-MLA sample and their belonging to a specific domain, the samples are divided into training and validation

datasets, making sure that each domain is well represented in each set. These samples are later used for the mineral abundance mapping. The location of these samples within the Bolcana mineralized system is illustrated in Figure 6-5.

6.5.2 *Drill-core mineral mapping and vein extraction*

In the case of the drill-core scans, the domain definition is performed through the clustering of the mineral abundances obtained from the upscaling of the SEM-MLA data by RF regression. Following a similar approach as for the point measurements for the estimation of the number of clusters, seven domains were delineated. In Figure 6-6, five samples are selected to exemplify the mineral abundance, vein distribution and mineral mapping / domaining results. The mineral composition of each domain is calculated from the estimated mineral abundance in each domain as an average for all the samples from the three analysed drill cores. The spectral signatures of each domain are analysed based on the center spectra and interquartile range (Figure 6-7). Further, the dominant label in the mineral maps is considered as the dominant mineralogical domain in the sample and respective sampling interval. The spatial distribution of the domains in the analysed samples from the three drill cores (Figure 6-8, Appendix 6A: Figure 6-11, Figure 6-12) are also discussed in this section.

Based on the modal mineralogy of each drill-core domain calculated from the mineral abundance estimates (Figure 6-6) the following interpretations can be made for the alteration labelling of these domains:

- Domain (1) – dominated by white mica and clay, cumulatively over 40 % - assemblage indicative of the phyllic alteration transitioning to argillic
- Domain (2) – a decrease in both white mica and clay, cumulatively around 30 % - assemblage defined as mica dominant phyllic alteration with an increase in gypsum likely related to veins
- Domain (3) – is marked by an increase in the chlorite : white mica ratio compared to domain (2) and is considered to be characteristic of chlorite-rich phyllic alteration
- Domains (4) and (5) – presents similar chlorite : white mica ratios characteristic to the chlorite-dominant alteration. The iron oxide and gypsum increase in domain (4) indicate the alteration domain defined by Ivascanu et al., (2019) "MACE"
- Domains (6) marks the transition to the potassic core (7), presenting increased amounts of biotite and magnetite and decreased white mica contents

Throughout the domains, the sulphide and quartz contents appear to be proportional. The highest sulphide contents are present in the two transitional domains (3) and (5) between the potassic and the phyllic zones. The highest sulphide contents are not only related to the highest amounts of sulphide present in veinlets but also to the present of disseminated pyrite in the matrix.

The mineral maps presented in Figure 6-6, together with the vein intensity maps indicate that different vein halo compositions are characteristic to different pervasive alteration domains. The modal mineralogy and more specifically the abundances of clay, white mica, chlorite, biotite and gypsum are reflected in the spectral response of the domains illustrated in Figure 6-7. For domain 1 the main absorption features are characteristic of water and Al-OH characteristic of white mica. The Al-OH feature at 2200 nm presents a shoulder towards 2165 nm indicative of clay as supported by the estimated modal mineralogy. In the second domain spectra the shoulder for clays is no longer identified due to the low clay concentrations in this domain. Additionally, the features characteristic of gypsum are observed here through the fine water features between 1450 and 1550 nm

as well as the feature at 1750 nm. The water feature around 1900 nm presents two absorption minima given by the mixture of white mica and gypsum. The increase in chlorite content is marked in the spectra of domain 3 through the appearance of a fine Al(Mg,Fe)-OH feature.
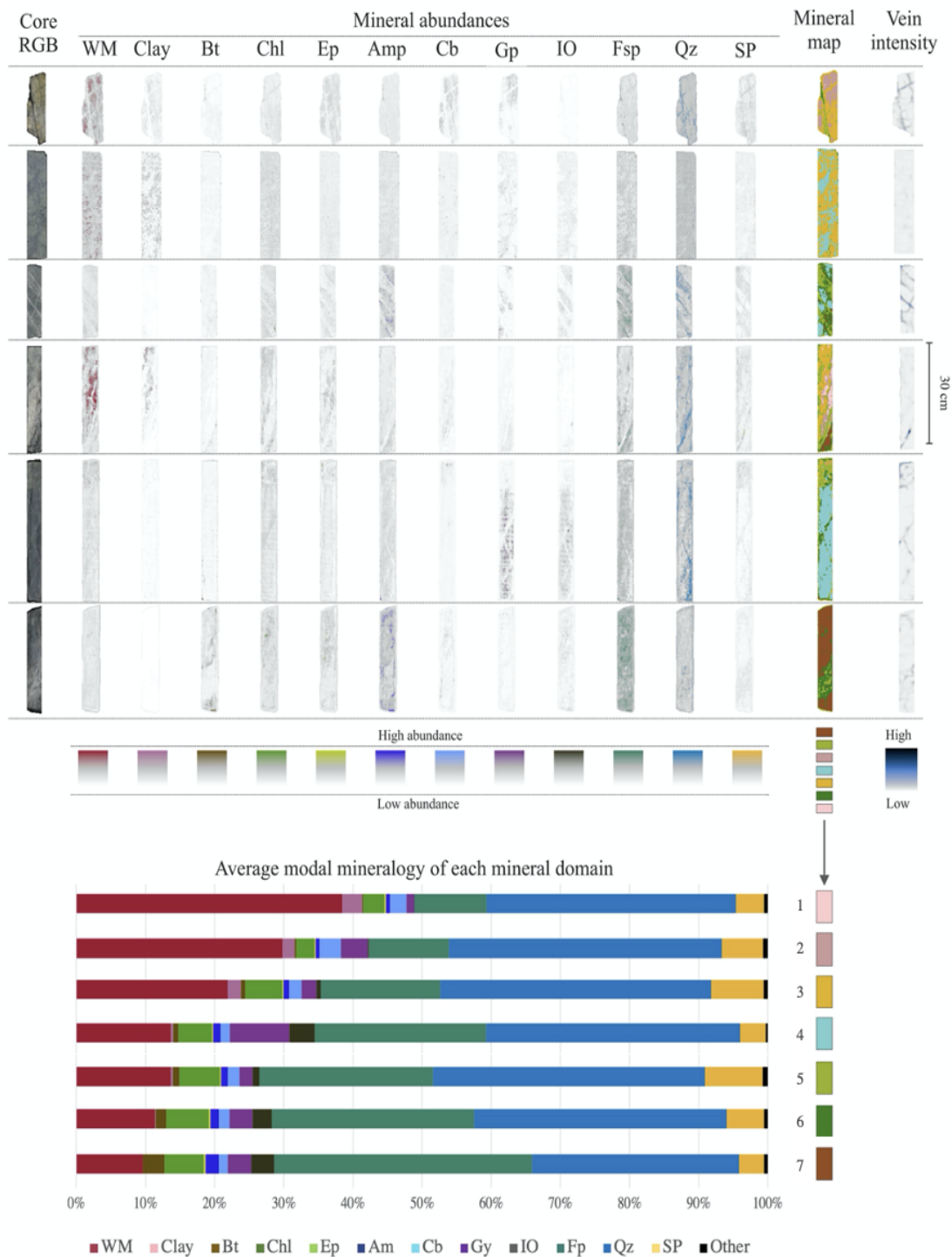
Figure 6-6 Examples of drill-core abundance estimation, vein extraction and clustering into classes or domains of known mineral composition (white mica (WM), biotite (Bt), chlorite (Chl), epidote (Ep), amphibole (Amp), carbonate (Cb), gypsum (Gp), iron oxides (IO) feldspar (Fsp), quartz (Qz), sulphide (Sp)).

While clay is present in this domain in similar amounts as in domain 2, the shoulder at 2165 nm is more prominent. The spectra of domain (4) supports the estimated modal mineralogy, particularly the increase in

chlorite and biotite concentrations given by the Al(Mg,Fe)-OH feature and of gypsum marked by the water feature between 1450 and 1550 nm. The intensity of the absorption features in this domain is relatively low for all SWIR diagnostic minerals, and can be assigned to the dark appearance of the samples likely due to the high content of disseminated magnetite. By comparison to the former domain, the following, (5), presents a strong decrease in gypsum abundance and an increase in the chlorite, biotite (Al(Mg,Fe)-OH) and white mica (Al-OH). The two last domains are characterised by further increase in biotite content and decrease in white mica clearly observed in the change in ratio between the Al-OH and Al(Mg,Fe)-OH features (Figure 6-7).
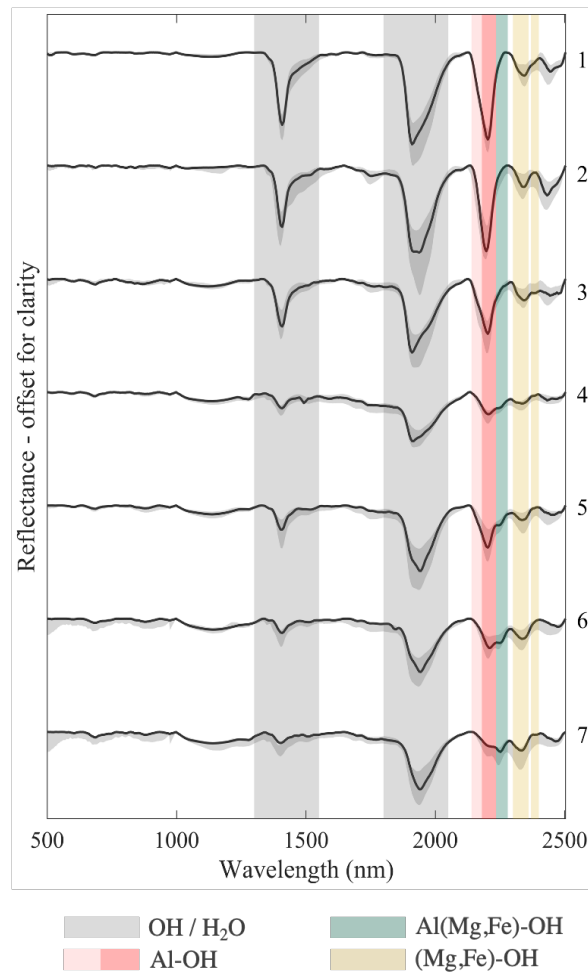
Figure 6-7 Spectral plot presenting the centre spectra and the associated interquartile range for each of the mineralogical domains obtained by the clustering of estimated drill-core mineral abundances by RF.

With regards to the spatial distribution of these domains in the analysed cores, a general transition with depth and proximity to the core of the system from mica-rich domains to chlorite and biotite-rich domains can be observed in all three boreholes. However, variations occur depending on the location of each borehole within the system (Figure 6-2), documenting spatial complexity and successive overprinting of alteration and mineralization styles in a telescoped magmatic-hydrothermal system (Paul – 2019).

Due to its location, BH-1 (Figure 6-8) crosses all the main alteration styles encountered in the Bolcana system. This borehole crosses part of the system starting from the central zone and bearing towards WSW with a dip of roughly 74 degrees. The mineral abundance, domain and vein intensity logs are presented in Figure

6-8. A transition is recognized from argillic and phyllic assemblages in the near-surface zone to a chlorite-rich zone and further a biotite-rich zone at depth. Intervals with white mica-dominant alteration as well as increased clay abundance are observed at greater depths. These intervals are frequently related to fracture zones and epithermal overprints.
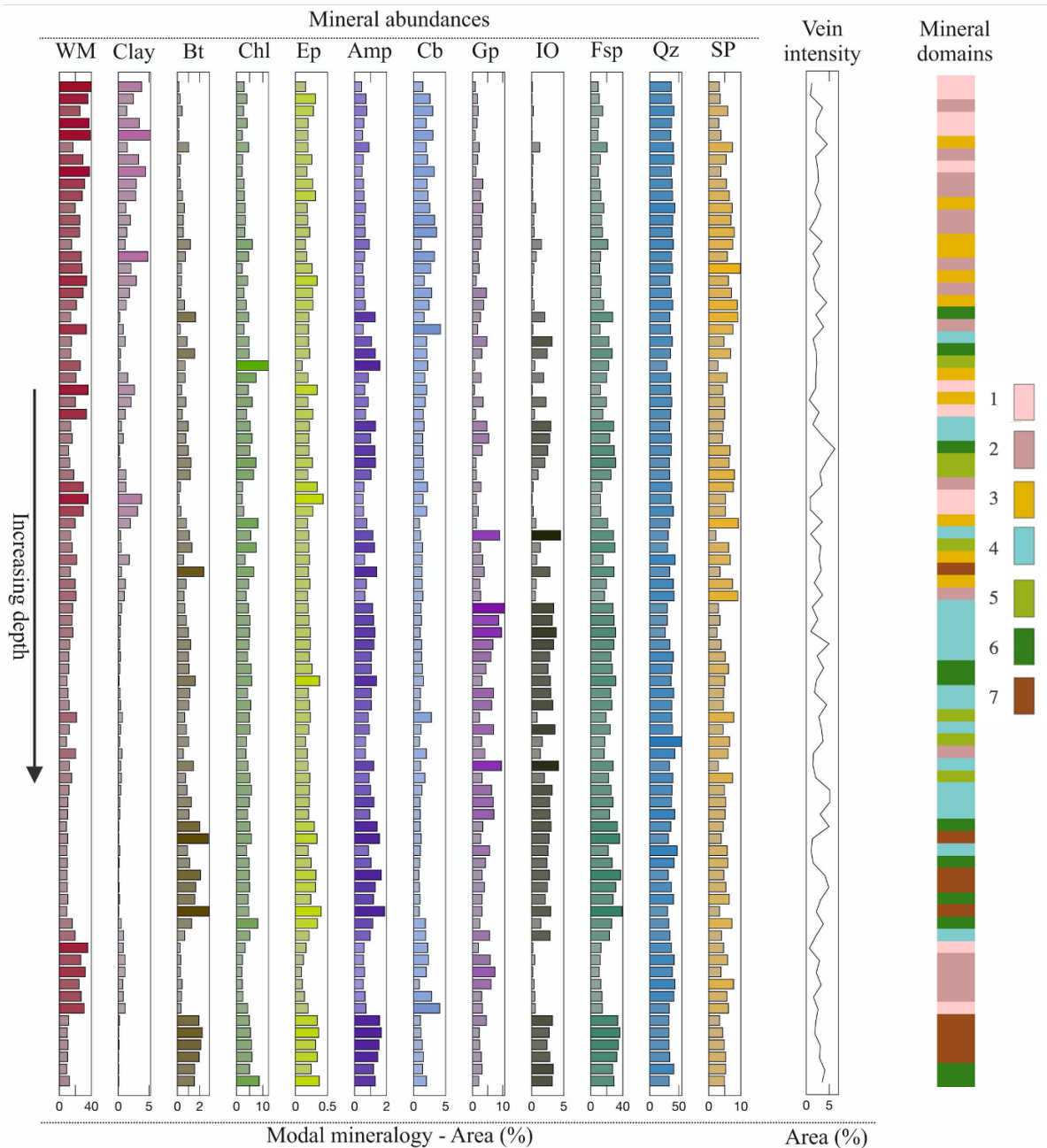
Figure 6-8 BH-1: Borehole mineral abundance, vein extraction and domaining based on drill-core hyperspectral data analysis (white mica (WM), biotite (Bt), chlorite (Chl), epidote (Ep), amphibole (Amp), carbonate (Cb), gypsum (Gp), iron oxides (IO) feldspar (Fsp), quartz (Qz), sulphide (SP)).

The second borehole, BH-2, starts from the Central-West side of the system towards ESE, with a dip of roughly 56 degrees. A lower variability of the alteration is encountered in this borehole (Appendix 6A: Figure 6-11), the transitional domain (domain 5) comprising white mica and chlorite being dominant. Three chlorite- and chlorite-biotite-rich domains are crossed, likely related to the fringes of the cores of one or several porphyry

102

bodies. Towards the end of the sampled interval a white mica and clay rich zone is present. This is interpreted to be related to an epithermal overprint, similar to BH-1.

BH-3 was sampled over a 2000 m depth extent; data was collected more widely spaced than in the two other holes. BH-3 starts from the Eastern fringe of the exploration license and outside of the porphyry mineralization. The first two samples in the borehole are chlorite and chlorite-biotite enriched. This can, in this case, not be attributed to the proximity to the core of the Bolcana hydrothermal system, but is rather characteristic of propylitic alteration distal to the magmatic-hydrothermal system. Epidote is not present in relevant amounts in the samples, its absence can be however assigned to the lack of training data from this domain. Other than that, the zonation appears similar to that encountered in BH-1, ranging from a white mica and clay-dominant alteration assemblage towards an enrichment in chlorite and biotite with depth and proximity to the core of the Bolcana porphyry system (Appendix 6A: Figure 6-12). The observed white mica-dominant intervals represent again areas marked by an epithermal overprint.

6.6   Validation of results

The evaluation of the mineral abundance estimation was performed using 18 thin section blocks with available MLA data from polished thin section surfaces through RMSE (Root Mean Square Error) calculation. The overall and per class (mineral group) RMSE values are listed in Table 6-1. The highest errors are associated with quartz and feldspar abundances. These minerals do not have diagnostic SWIR features and are the most abundant in the analysed samples. It is likely that these errors are related to the distribution of these minerals in the matrix of the samples and that overestimation of feldspar leads to the underestimation of quartz and vice-versa. Among the SWIR diagnostic minerals, the highest RMSE values are obtained for white mica, which is present in large concentrations. Additionally, gypsum, which is only present in low amounts, has a high error associated with its abundance estimation. It is, however, important to mention that this class comprises both gypsum as a hydrated endmember and anhydrite. The abundance estimation results in comparison with the ground truth MLA validation data for a selection of samples from the set used for numerical validation from different alteration zones within the system is presented in Figure 6-9.

Table 6-1 Overall and per mineral group Root Mean Square Error (RMSE) values for the mineral abundance validation dataset consisting of 18 thin section blocks (white mica (WM), biotite (Bt), chlorite (Chl), epidote (Ep), amphibole (Amp), carbonate (Cb), gypsum (Gp), iron oxides (IO) feldspar (Fsp), quartz (Qz), sulphide (SP)).

Overall RMSE	Per class RMSE											
	WM	Clay	Bt	Chl	Ep	Amp	Cb	Gp	IO	Fsp	Qz	SP
0.10	0.13	0.04	0.03	0.05	0.02	0.01	0.03	0.10	0.05	0.19	0.24	0.11
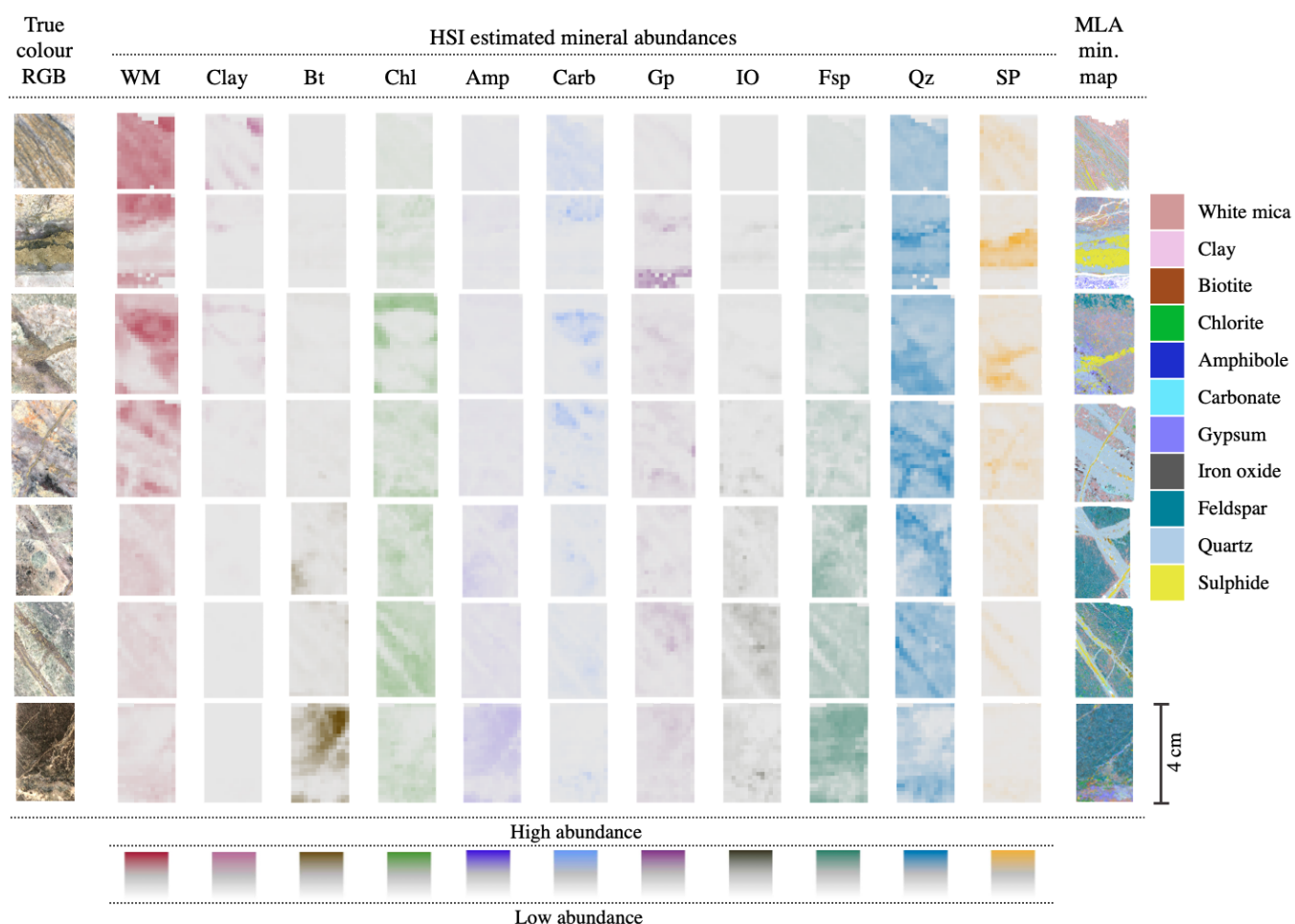
Figure 6-9 Comparison of mineral abundance estimation and ground truth SEM-MLA data for a selection of 7 from the 18 validation samples collected from different alteration domains and hosting various vein types (white mica (WM), biotite (Bt), chlorite (Chl), epidote (Ep), amphibole (Amp), carbonate (Cb), gypsum (Gp), iron oxides (IO) feldspar (Fsp), quartz (Qz), sulphide (SP)).

Discussion

The collection and analysis of representative samples is a crucial step in drill core analysis for exploration as well as for the employment of machine learning routines for upscaling mineralogical data. In the current study, hand-held spectra collected from pulps representing two-meter intervals of around 20 km of drill core were used to develop preliminary spectral domains. This allowed representative sampling of each spectral domain characteristic of a distinct alteration assemblage. Although the point spectral measurements provide indications on the location within the system, related to the different porphyry bodies, this information is not suitable to provide spatially resolved information such as on the distribution of the different spectrally active minerals in matrix or on different vein types. To provide such information, hyperspectral drill core scanning is an essential tool.

Using the large-scale domains obtained through the clustering of the point spectra by SSC, the 54 available thin section blocks were divided into a training and a validation set to be further used for upscaling of the mineralogical data obtained by SEM-MLA to drill-core scale. The domaining data was further imported

into Leapfrog Geo and, using its intuitive 3D modelling tools, a preliminary spectral model was developed (Figure 6-10). The observed spatial coherence of the model with the porphyry-type zonation of the Bolcana system represents an important argument that hyperspectral data can be used effectively to provide insight into the architecture of a porphyry system (Sillitoe, 2010) – and may thus also be used to provide guidance for the development of a geometallurgical model (Kern et al., 2018a). Additionally, even with only spectral point measurements it provides more information on the zonation of the main alteration assemblages compared to traditional logging (Figure 6-1).
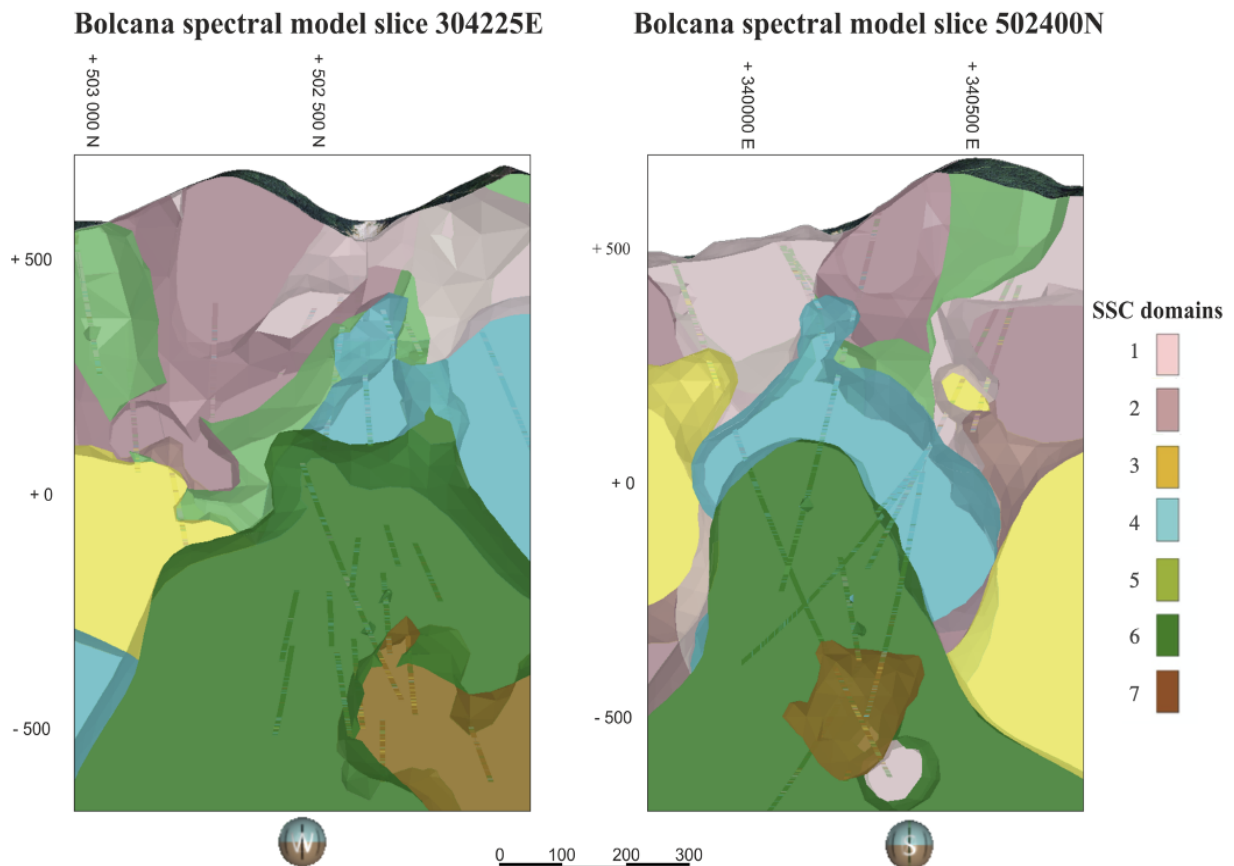
Figure 6-10 N-S and W-E cross-section views through the spectral domain model obtained from the clustering of handheld spectra.

On the other hand, the use of point measurements only allows for the discrimination of the main alteration zones in the system, while the use of hyperspectral imaging of the drill core provides valuable information on the spatial and compositional variability at high resolution. The selected samples subjected to SEM-MLA analyses were thus used for training a regression model to upscale relevant mineral abundances to drill core scale.

Drill core scale analysis, through the upscaling of the SEM-MLA mineral maps, has rendered mineral abundance maps over entire drill cores for twelve important mineral groups: white mica, clay, biotite, chlorite, epidote, amphibole, carbonate, gypsum group (calcium sulphate), iron oxide, feldspar, quartz and sulphide. The quality of the mineral abundance estimation through upscaling was evaluated through the calculation of

the RMSE using 18 thin section blocks analysed by SEM-MLA. Among the SWIR active minerals, white mica has the highest associated error. This can be assigned to its high abundance in the samples, together with its strong association with quartz around veins and feldspars in the matrix, leading to local misclassifications. A similar effect can be observed for calcium sulphate, e.g. anhydrite (SWIR non-diagnostic) or gypsum (SWIR-diagnostic), which, due to the different intensity of the absorption features, together with its frequent association with white micas tends to be in some areas overestimated where white mica is dominant and gypsum only present in small amounts. Epidote is only present in minor amounts in the analysed samples but had a relatively high error by comparison due to the low number of training samples containing epidote and its similar spectral response to chlorite. Clay, chlorite, biotite, amphibole, carbonate and iron oxide, key minerals for the understanding of the system and all having diagnostic features in the spectral range of the used sensor, present low estimation errors. Sulphide, the key ore mineral group in the system, comprising the copper bearing minerals together with pyrite, which locally hosts native gold inclusions (Blannin et al., 2021), shows a relatively good estimation accuracy, particularly in veins. Sometimes the sulphide abundance tends to be overestimated in the matrix. For this reason, vein extraction was performed on the sulphide abundance maps in order to significantly improve the identification and quantification of sulphide and therefore ore-bearing veins. Frangi filters proved successful in enhancing the veins. The resulting mineral abundance can be used to segment the vein abundance maps into labels indicating areas with and without veins. However, for the purpose of vein quantification the intensity of the veins after the Frangi filter was used as some of the veins have thicknesses under the spatial resolution of the hyperspectral sensor (1.5 mm/pixel). This way, the fine veins, while they are mapped show a lower intensity which appears to be proportional to their thickness as well as to the abundance of sulphide inside the vein.

Following up the abundance estimation, the mineral abundances were clustered into domains. The vein distribution is also highly variable between domains. In BH-1 the highest vein densities are present in domains (4) and (6), while in the second borehole, where domain (4) is only locally present, the highest vein abundance is observed in domains (2) and (6). In this work, the vein estimation is focused on the sulphide abundance maps, sulphide being the main copper and gold bearing mineral group (Blannin et al., 2019). Further work on estimating the vein density on other mineral abundances related to veins, such as gypsum and quartz are recommended.

The understanding of the modal mineralogy of each domain already provides valuable information for the estimation of engineering parameters past the exploration stage. When it comes to slope regulation, the quantification of the abundance of clay and gypsum in the drill cores can indicate the requirements for slope adjustment: clays increase volume in the presence of water and reduce volume in dry seasons, gypsum can be dissolved leading to the creation of voids inside the walls. Both minerals can therefore increase the risk of slope failure if not well handled. These indications combined with the estimation of weathering degree and quantification of joints following the same methodology as for vein extraction. Additionally, when it comes to the beneficiation stages, minerals such as clay and white mica can inhibit sulphide flotation through slime coating and entrainment (Chen et al., 2014).

6.7   Conclusion

In the current work a methodology for drill-core mineral abundance estimation, mineral mapping and domaining is presented. The obtained results show high potential for their use in understanding the architecture of the Bolcana deposit and the use of this data for geometallurgical modelling. Additionally, the clustering of the mineral abundances and their segmentation into domains support the development of homogeneous mineralogical domains that are inherently linked to different ore types in terms of composition, vein abundance and grade. For the Bolcana system, seven main mineral domains were identified, presenting a clear spatial zonation from white mica dominant assemblages in the near-surface zones to chlorite and chlorite-biotite dominant assemblages at depth. Additional transitional domains are distinguished based on increased abundance of other key minerals such as clays, gypsum and iron oxide. The mineral composition in each domain can give preliminary information on the engineering behaviour of each ore type in different mining and beneficiation processes.

Besides the understanding of the mineralogical composition within the domains, the current approach allows for strategic sampling in homogeneous domains for further testing. Domains of homogeneous composition are expected to illustrate a similar behaviour in different processes such as comminution and flotation. [JG1] By collecting samples for testing from each domain and the creation of a digital twin of each process, the obtained information can be further extrapolated to deposit scale leading to the ultimate development of a predictive geometallurgical model (van den Boogaart and Tolosana-Delgado, 2018). The automated character of the proposed methodology could be easily transferred to other deposit types as well as other data acquisition setups and other sensors.

Appendix 6A. Mineral abundance, vein intensity and mineral domain logs for BH-2 and BH-3

Figure 6-11 BH-2: Borehole mineral abundance, vein extraction and domaining based on drill-core hyperspectral data analysis (white mica (WM), biotite (Bt), chlorite (Chl), epidote (Ep), amphibole (Amp), carbonate (Cb), gypsum (Gp), iron oxides (IO) feldspar (Fsp), quartz (Qz), sulphide (SP)).
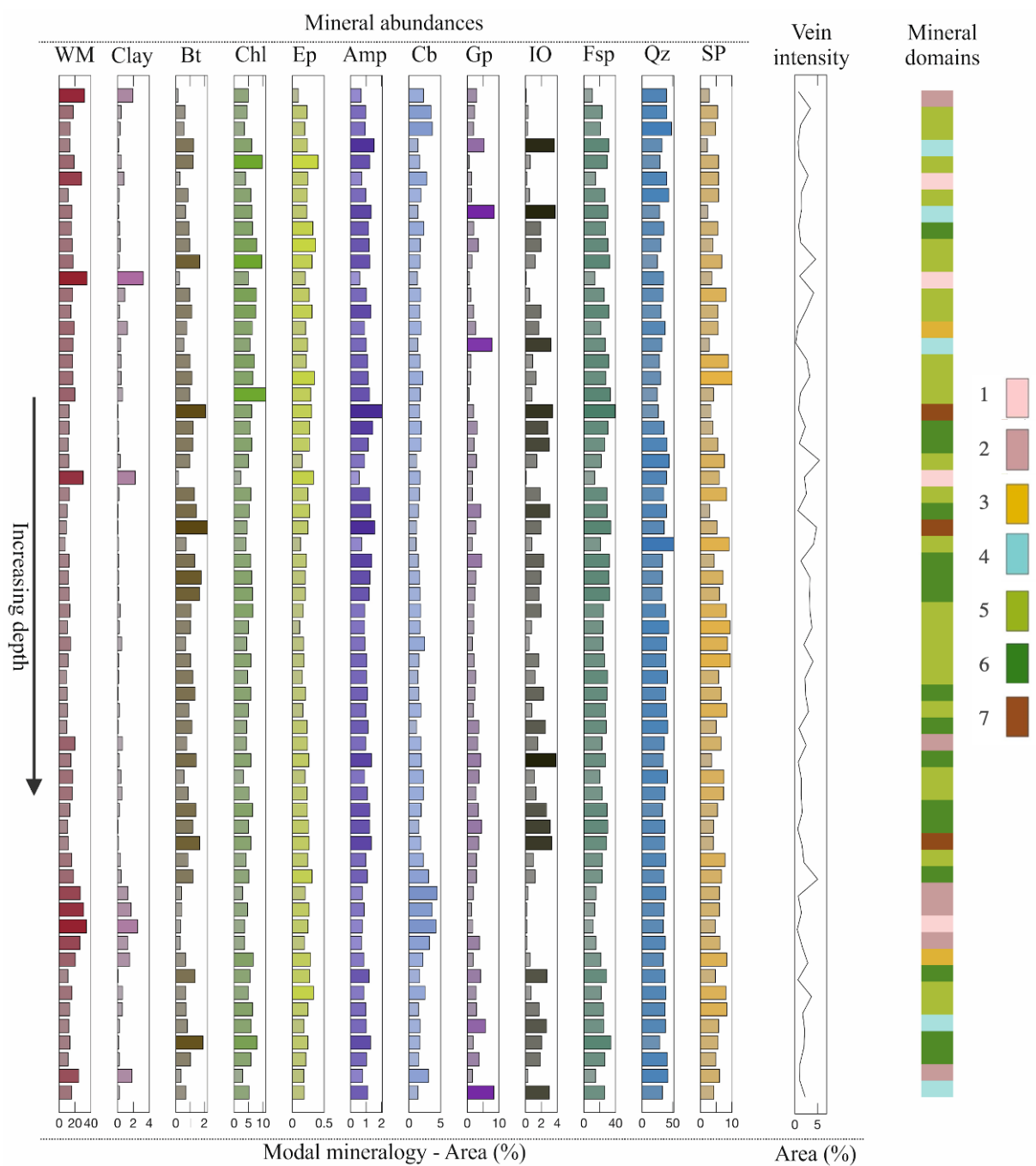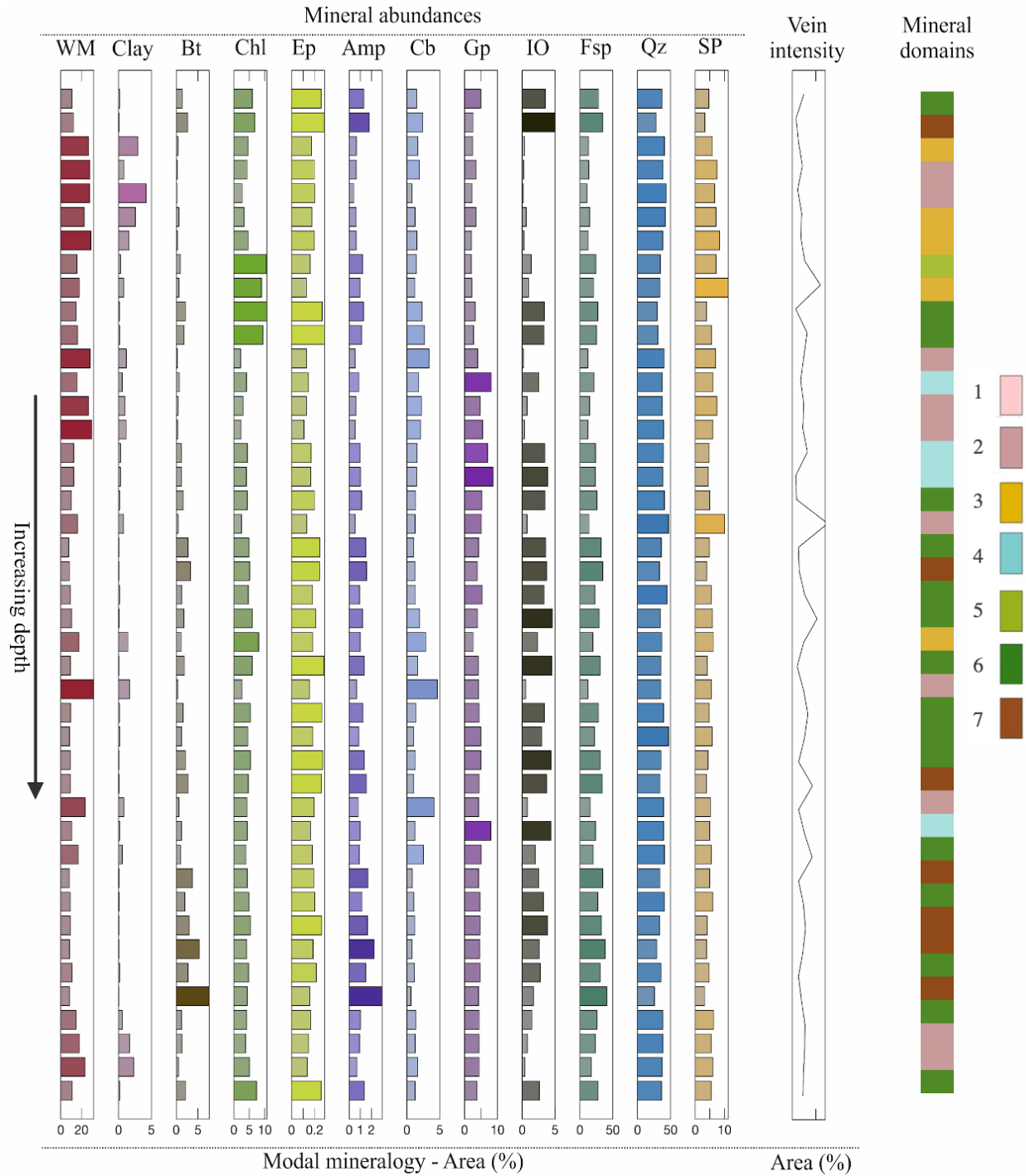
Figure 6-12 BH-3: Borehole mineral abundance, vein extraction and domaining based on drill-core hyperspectral data analysis (white mica (WM), biotite (Bt), chlorite (Chl), epidote (Ep), amphibole (Amp), carbonate (Cb), gypsum (Gp), iron oxides (IO) feldspar (Fsp), quartz (Qz), sulphide (SP)).

Chapter 7   Concluding remarks

This thesis develops a comprehensive framework for the use of hyperspectral drill-core scanning for the acquisition and delivery of continuous mineralogical and textural data for mineral exploration and early establishment of a geometallurgical model.

The Bolcana porphyry copper-gold system in Romania is used as a case study as it shows variable and complex mineralogy and mineralization styles, representing therefore a challenge for most established methods for ore characterisation and geometallurgical models. Additionally, the variable copper grades represent a strong motivation for the understanding of the different ore types and their composition as well as for the pre-concentration of the ore after crushing, prior to further beneficiation.

Different methodological approaches are used relying on different levels of understanding of a deposit and available ground-truth mineralogical and textural data. As a result, a variety of tools were developed to provide the following outcomes or deliverables:

1. Identifying and mapping of the main alteration minerals in the system based on unsupervised mineral mapping techniques and spectral analysis

2. Discriminating mineral abundances related to both veins and pervasive alteration from the aforementioned maps through morphological analysis.

3. With the availability of ground truth mineralogical data, the estimation the modal mineralogy related to different grade domains through supervised machine learning methods

4. Support in metallurgical design by providing extensive modal mineralogy and mineral association data

5. Estimation of vein abundance and orientation (azimuth) based on either vein halo mineralogy or composition of the veins.

6. A framework for the simulation of sensor sorting potential using hyperspectral sensors based on machine learning approaches which allow for the identification of subtle proxies for mineralization which are not clear by direct spectral and mineralogical analyses

7. Prediction of the mineralogical and textural composition of different beneficiation products for different sorting scenarios using hyperspectral sensors.

These products can be used in the different stages of an exploration and mining project (Figure 7-1). In the case of regional exploration, where samples are collected from outcrops and preliminary drilling is performed, the methodology presented in the third chapter (Tusa et al., 2019) can be used to identify the different spectrally diagnostic minerals, map different alteration domains that can help target and delineate mineralized bodies. Additionally, in this chapter morphological analyses are performed on relative mineral abundance maps in order to extract and quantify the vein distribution. These analyses can be additionally performed on other types of maps such as those described in chapters four and five.

With increased availability of mineralogical and textural data, mineral abundances derived from the hyperspectral data using machine learning techniques can support resource definition and later grade control,

through not only estimating the metal content in the analysed samples but also the main associated gangue mineral groups. The presence of specific minerals as well as the overall modal mineralogy derived from the hyperspectral data using the methodology proposed in the fourth chapter (Tuşa et al., 2020) can complement local geotechnical tests into defining mine slope design and blasting strategy. Additionally, the modal mineralogy and mineral association estimates can guide the design for further beneficiation. With regards to direct impact on mineral beneficiation, in Chapter 5 a machine learning framework for the testing of the suitability of SWIR sensors was presented. In the case of the Bolcana it was shown that provided that representative samples are made available for training, a machine learning model can be trained to predict the grade of the ore (Tusa et al., 2019a). Using this methodology, information on the modal mineralogy of the products can be delivered which will, as in the previous stage support decision making in the further beneficiation stages.
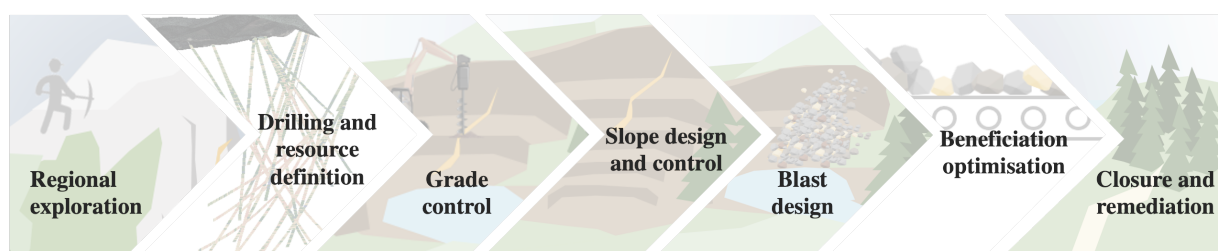
Figure 7-1. Flowchart illustrating the main stages of an exploration and mining project where near-field hyperspectral imaging and more specifically the methodologies presented in this thesis present relevant contributions.

The workflows presented in chapters three, four and five can be upscaled to large drill-core intervals providing continuous mineralogical data which are key in the development of geometallurgical models. Based on the available drill-core samples, mineralogical and textural data and point spectral measurements, Chapter 6 illustrates a methodology for the integration and use of these datasets to produce 3D models based on the hyperspectral data. Additionally, this chapter illustrates the level of detail that different datasets provide. While only the point measurements were available over all the drilled boreholes in the Bolcana system, they can be used to model the main alteration domains in the system. However, on the three boreholes where drill-core samples were available the quality and detail of the obtained mineralogical information were highly increased. While the broad domaining can still be used in geometallurgical modelling, the use of drill-core scanning on all the boreholes in the system would have provided a better understanding of the mineralization styles and related alteration assemblages.

Based on the results presented in the previous chapters, conclusions can be drawn on the most suitable way to plan the use of hyperspectral imaging in the geometallurgical context. In Figure 7-2 a flowchart is presented for this purpose, the stages where hyperspectral data, more precisely the methods described in detail in the papers included in Chapters 3-6 can be used, are highlighted in green. The proposed workflow starts with the scanning of exploration cores and the use of these data to identify spectral (and therefore mineralogical) domains. The domaining results will support representative sampling for laboratory analyses, such as Scanning Electron Microscopy-based image analyses. The laboratory analyses results are then upscaled using the hyperspectral data to entire borehole intervals for the developments of mineral abundance maps.

These maps are then subjected to the calculation of mineralogical parameters (e.g., mineral association) and extraction of textural and structural features (e.g., veins). Through supervised classification, these results are the basis of the definition of mineralogical and textural domains and will support the sampling strategy for engineering tests, process simulation and digital twin creation. If such a strategy is strictly applied, then the engineering test results can be used in conjunction with the available hyperspectral data to develop a three-dimensional predictive geometallurgical model. With the progress of the mine, the geometallurgical model can be updated through online characterisation of particles on a conveyor belt or mine face mapping before and after blasting using the same or similar sensor to that used for the mapping of drill-cores.
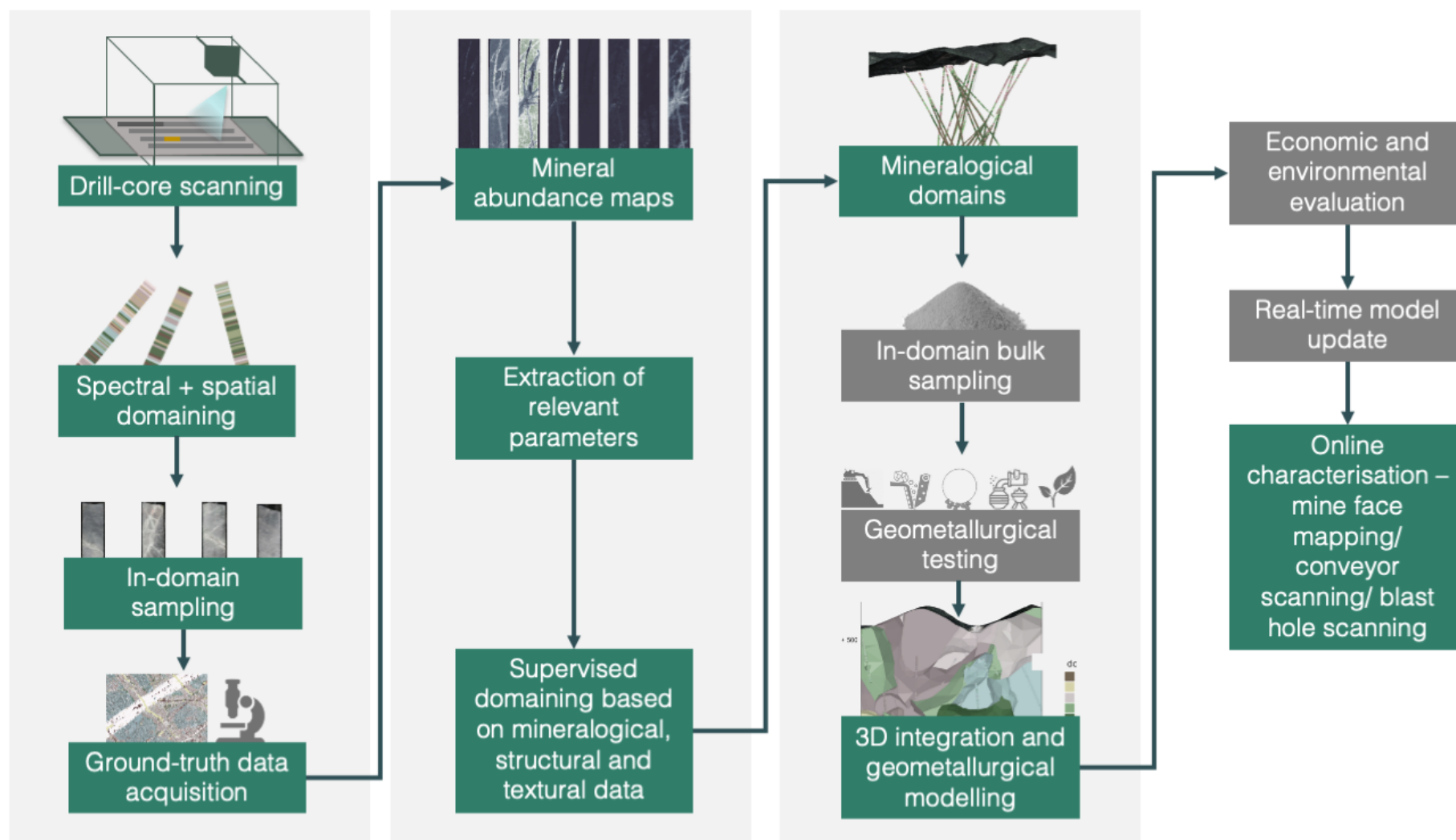
Figure 7-2 Proposed workflow for the integration of hyperspectral imaging in geometallurgical modelling from early exploration through mining.

Chapter 8 References

Apopei, A.I., Damian, G., Buzgar, N., Milovska, S., Buzatu, A., 2014. New occurrences of hessite, petzite and stützite at coranda-hondol open pit (certej gold-silver deposit, Romania). Carpathian J. Earth Environ. Sci. 9, 71–78.

Arne, D., House, E., Pontual, S., Huntington, J., 2016. Hyperspectral interpretation of selected drill cores from orogenic gold deposits in central Victoria, Australia. Aust. J. Earth Sci. 63, 1003–1025. https://doi.org/10.1080/08120099.2016.1223171

Asadzadeh, S., De Souza Filho, C.R., 2016. Iterative Curve Fitting: A Robust Technique to Estimate the Wavelength Position and Depth of Absorption Features from Spectral Data. IEEE Trans. Geosci. Remote Sens. 54. https://doi.org/10.1109/TGRS.2016.2577621

Ayling, B., Huntington, J., Smith, B., Edwards, D., 2016. Hyperspectral logging of middle Cambrian marine sediments with hydrocarbon prospectivity: a case study from the southern Georgina Basin, northern Australia. Aust. J. Earth Sci. 63, 1069–1085. https://doi.org/10.1080/08120099.2016.1204625

Baker, T., 2019. Gold ± copper endowment and deposit diversity in the western Tethyan Magmatic Belt, Southeast Europe: Implications for exploration. Econ. Geol. 114, 1237–1250. https://doi.org/10.5382/econgeo.4643

Barton, I.F., Gabriel, M.J., Lyons-Baral, J., Barton, M.D., Duplessis, L., Roberts, C., 2021. Extending geometallurgy to the mine scale with hyperspectral imaging: a pilot study using drone- and ground-based scanning. Mining, Metall. Explor. 38, 799–818. https://doi.org/10.1007/s42461-021-00404-z

Bedini, E., van der Meer, F., van Ruitenbeek, F., 2009. Use of HyMap imaging spectrometer data to map mineralogy in the Rodalquilar caldera, southeast Spain. Int. J. Remote Sens. 30, 327–348. https://doi.org/10.1080/01431160802282854

Belsley, D.A., 1991. A Guide to using the collinearity diagnostics. Comput. Sci. Econ. Manag. 4, 33–50. https://doi.org/10.1007/BF00426854

Berbeleac, I., Udubaşa, S.S., Iatan, E.-L., Vişan, M., 2014. Geological and Structural Constraints on the Localization of Neogene Porphyry– Epithermal Related Cu-Au (Mo), and Epigenetic Hydrothermal Deposits/Prospects from South Apuseni Mts., Romania. Rom. J. Miner. Depos. 87, 47–52.

Bierwirth, P.N., 2008. Laboratory and imaging spectroscopy of tourmaline - a tool for mineral exploration. 14th Australas. Remote Sens. Photogramm. Conf.

Bishop, C.A., Liu, J.G., Mason, P.J., 2011. Hyperspectral remote sensing for mineral exploration in Pulang, Yunnan province, China. Int. J. Remote Sens. 32, 2409–2426. https://doi.org/10.1080/01431161003698336

Blannin, R., Frenzel, M., Tuşa, L., Birtel, S., Ivăşcanu, P., Baker, T., Gutzmer, J., 2021. Uncertainties in quantitative mineralogical studies using scanning electron microscope-based image analysis. Miner. Eng. 167. https://doi.org/10.1016/j.mineng.2021.106836

Blannin, R., Tusa, L., Birtel, S., Gutzmer, J., Gilbricht, S., Ivascanu, P., 2019. Metal deportment and ore variability of the Bolcana porphyry Au-Cu system (Apuseni Mts, Romania) - Implications for ore processing. 15th SGA Biennial Meeting 2019 Proceedings.

Booysen, R., Gloaguen, R., Lorenz, S., Zimmermann, R., Nex, P.A.M., 2020. Geological Remote Sensing, 2nd ed,

References

Reference Module in Earth Systems and Environmental Sciences. Elsevier Inc. https://doi.org/10.1016/b978-0-12-409548-9.12127-x

Bostinescu, S., 1984. Porphyry copper systems in the South Apuseni Mountains, Romania. An. Inst. Geol. Geophys. LXIV, 163–175.

Boubanga-Tombet, S., Huot, A., Vitins, I., Heuberger, S., Veuve, C., Eisele, A., Hewson, R., Guyot, E., Marcotte, F., Chamberland, M., 2018. Thermal infrared hyperspectral imaging for mineralogy mapping of a mine face. Remote Sens. 10, 1–15. https://doi.org/10.3390/rs10101518

Breiman, L., 2001. Random forests. Mach. Learn. 45, 5–32. https://doi.org/10.1007/9781441993267_5

Buchmann, M., Schach, E., Tolosana-Delgado, R., Leißner, T., Astoveza, J., Kern, M., Möckel, R., Ebert, D., Rudolph, M., van den Boogaart, K., Peuker, U., 2018. Evaluation of Magnetic Separation Efficiency on a Cassiterite-Bearing Skarn Ore by Means of Integrative SEM-Based Image and XRF–XRD Data Analysis. Minerals 8, 390. https://doi.org/10.3390/min8090390

Calvin, W.M., Pace, E.L., 2016. Mapping alteration in geothermal drill core using a field portable spectroradiometer. Geothermics 61, 12–23. https://doi.org/10.1016/j.geothermics.2016.01.005

Cardon, O., Reisberg, L., Andre-Mayer, A., Leroy, J., Milu, V., Zimmermann, C., 2008. Re-Os systematics of pyrite from the bolcana porphyry copper deposit, Apuseni Mountains. Econ. Geol. 1695–1702.

Chen, X., Peng, Y., Bradshaw, D., 2014. The separation of chalcopyrite and chalcocite from pyrite in cleaner flotation after regrinding. Miner. Eng. 58, 64–72. https://doi.org/10.1016/j.mineng.2014.01.010

Cioacă, M.E., Munteanu, M., Qi, L., Costin, G., 2014. Trace element concentrations in porphyry copper deposits from Metaliferi Mountains, Romania: A reconnaissance study. Ore Geol. Rev. 63, 22–39. https://doi.org/10.1016/j.oregeorev.2014.04.016

Clark, R.N., 1999. Spectroscopy of Rocks and Minerals and Principles of Spectroscopy. Manual of Remote Sensing, Remote Sensing for the Earth Sciences: Manual of Remote Sensing.

Clark, R.N., Boardman, J., Mustard, J., Kruse, F., Ong, C., Pieters, C., Swayze, G.A., 2006. Mineral mapping and applications of imaging spectroscopy. Int. Geosci. Remote Sens. Symp. 1986–1989. https://doi.org/10.1109/IGARSS.2006.514

Contreras Acosta, C.I., Khodadadzadeh, M., Tusa, L., Ghamisi, P., Gloaguen, R., 2019. A Machine Learning Framework for Drill-Core Mineral Mapping Using Hyperspectral and High-Resolution Mineralogical Data Fusion. IEEE J. Sel. Top. Appl. Earth Obs. Remote Sens. 1–14. https://doi.org/10.1109/jstars.2019.2924292

Copper International Study Group, 2021. The World Copper Factbook 2021.

Corbett, G.J., Leach, T.M., 1998. Southwest Pacific rim gold–copper systems: structure, alteration and mineralization. Soc. Econ. Geol. Special Pu, 236.

Cortes, C., Vapnik, V., 2001. Dispensing system boosts throughput 50 percent. Assembly 44, 97.

Crósta, A.P., De Souza Filho, C.R., Azevedo, F., Brodie, C., 2003. Targeting key alteration minerals in epithermal deposits in Patagonia, Argentina, using ASTER imagery and principal component analysis. Int. J. Remote Sens. 24, 4233–4240. https://doi.org/10.1080/0143116031000152291

Dalm, M., Buxton, M.W.N., van Ruitenbeek, F.J.A., 2018. Ore–Waste Discrimination in Epithermal Deposits Using Near-Infrared to Short-Wavelength Infrared (NIR-SWIR) Hyperspectral Imagery. Math. Geosci. 1–27.

https://doi.org/10.1007/s11004-018-9758-6

Dalm, M., Buxton, M.W.N., Van Ruitenbeek, F.J.A., Voncken, J.H.L., 2014. Application of near-infrared spectroscopy to sensor based sorting of a porphyry copper ore. Miner. Eng. 58, 7–16. https://doi.org/10.1016/j.mineng.2013.12.016

Di Tommaso, I., Rubinstein, N., 2007. Hydrothermal alteration mapping using ASTER data in the Infiernillo porphyry deposit, Argentina. Ore Geol. Rev. 32, 275–290. https://doi.org/https://doi.org/10.1016/j.oregeorev.2006.05.004

Dominy, S.C., O'Connor, L., Glass, H.J., Purevgerel, S., Xie, Y., 2018a. Towards representative metallurgical sampling and gold recovery testwork programmes. Minerals 8. https://doi.org/10.3390/min8050193

Dominy, S.C., O'connor, L., Parbhakar-Fox, A., Glass, H.J., Purevgerel, S., 2018b. Geometallurgy—A route to more resilient mine operations. Minerals 8, 1–33. https://doi.org/10.3390/min8120560

Draper, C., Reichle, R., de Jeu, R., Naeimi, V., Parinussa, R., Wagner, W., 2013. Estimating root mean square errors in remotely sensed soil moisture over continental scale domains. Remote Sens. Environ. 137, 288–298. https://doi.org/10.1016/j.rse.2013.06.013

Egozcue, J.J., Pawlowsky-Glahn, V., Mateu-Figueras, G., Barceló-Vidal, C., 2003. Isometric Logratio Transformations for Compositional Data Analysis. Math. Geol. 35, 279–300. https://doi.org/10.1023/A:1023818214614

Elhamifar, E., Vidal, R., 2013. Sparse subspace clustering: Algorithm, theory, and applications. IEEE Trans. Pattern Anal. Mach. Intell. 35, 2765–2781. https://doi.org/10.1109/TPAMI.2013.57

Fandrich, R., Gu, Y., Burrows, D., Moeller, K., 2007. Modern SEM-based mineral liberation analysis. Int. J. Miner. Process. 84, 310–320. https://doi.org/10.1016/j.minpro.2006.07.018

Farooq, A., Qurat-ul-ain, F., 2012. Pixel Purity Index Algorithm and n-Dimensional Visualization for ETM+ Image Analysis: A Case of District Vehari. Glob. J. Hum. Soc. Sci. Arts Humanit. 12, 23–32.

Frangi, A.., Niessen, W.., Vincken, K.., Viergever, M.., 1998. Multiscale Vessel Enhancement Filtering, in: International Conference on Medical Image Computing and Computer-Assisted Intervention. Springer Berlin Heidelberg, pp. 130–137.

Gallie, E.A., Mcardle, S., Rivard, B., Francis, H., 2010. International Journal of Estimating sulphide ore grade in broken rock using visible / infrared hyperspectral reflectance spectra 37–41. https://doi.org/10.1080/01431160110075604

Gandhi, S.M., Sarkar, B.C., Gandhi, S.M., Sarkar, B.C., 2016. Chapter 8 – Drilling, Essentials of Mineral Exploration and Evaluation. https://doi.org/10.1016/B978-0-12-805329-4.00015-6

Ghamisi, P., Plaza, J., Chen, Y., Li, J., Plaza, A.J., 2017. Advanced Spectral Classifiers for Hyperspectral Images: A review. IEEE Geosci. Remote Sens. Mag. 5, 8–32. https://doi.org/10.1109/MGRS.2016.2616418

Ghitulescu, T., Socolescu, M., 1941. Étude géologique et minière des Monts Métallifères (Quadrilatère aurifère et régions environnantes). Ann. Inst. Geol. Roum XXI, 181–464.

Gisbert, G., Tornos, F., Losantos, E., Pons, J.M., Videira, J.C., 2021. Vectors to ore in replacive volcanogenic massive sulfide (VMS) deposits of the northern Iberian Pyrite Belt: Mineral zoning, whole rock geochemistry, and application of portable X-ray fluorescence. Solid Earth 12, 1931–1966. https://doi.org/10.5194/se-12-

References

1931-2021

Gomez, C., Lagacherie, P., Coulouma, G., 2008. Continuum removal versus PLSR method for clay and calcium carbonate content estimation from laboratory and airborne hyperspectral measurements. Geoderma 148, 141–148. https://doi.org/10.1016/j.geoderma.2008.09.016

Gordon, G., McAvaney, S., Wade, C., 2016. Spectral characteristics of the Gawler Range Volcanics in drill core Myall Creek RC1. Aust. J. Earth Sci. 63, 973–986. https://doi.org/10.1080/08120099.2016.1264475

Graedel, T.E., Allwood, J., Birat, J.-P., Buchert, M., Hagelüken, C., Reck, B., Sibley, S., Sonnemann, G., 2011. Recycling Rates of Metals, A Status Report. United Nations Environment Programme.

Gu, Y., 2003. Automated scanning electron microscope based mineral liberation analysis. J. Miner. Mater. Charact. Eng. 2, 33–41. https://doi.org/10.4236/jmmce.2003.21003

Gustafson, L.B., Hunt, J.P., 1975. The Porphyry Copper Deposit at El Salvador, Chile. Econ. Geol. 70, 857–912.

Hastie, T., Tibshirani, R., Friedman, J., 2008. The Elements of Statistical Learning, 2nd ed. ed. Springer.

Herrington, R., 2021. Mining our green future. Nat. Rev. Mater. 6, 456–458. https://doi.org/10.1038/s41578-021-00325-9

Herrmann, W., Blake, M., Doyle, M., Huston, D., Kamprad, J., Merry, N., Pontual, S., 2001. Short Wavelength Infrared (SWIR) spectral analysis of hydrothermal alteration zones associated with base metal sulfide deposits at Rosebery and Western Tharsis, Tasmania, and Highway-Reward, Queensland. Econ. Geol. 96, 939–955. https://doi.org/10.2113/gsecongeo.96.5.939

Hollas, J.M., 2004. Modern spectroscopy. John Wiley & Sons, Inc.

Hunt, G.R., 1977. Spectral signatures of particulate minerals in the Visible and Near Infrared. Geophysics 42, 501–511. https://doi.org/10.1190/1.1440721

Huntington, J.F., Mauger, A.J., Skirrow, R.G., Bastrakov, E.N., Connor, P., Mason, P., Keeling, J.L., Coward, D. a, Berman, M., Phillips, R., Whitbourn, L.B., Heithersay, P.S., 2006. Automated mineralogical core logging at the Emmie Bluff iron oxide- copper- gold Prospect. Mesa J. 41, 38–44.

Imagery, H., Riaza, A., Buzzi, J., García-meléndez, E., Carrère, V., 2011. Monitoring the Extent of Contamination from Acid Mine Drainage in the Iberian Pyrite Belt (SW Spain) Using 2166–2186. https://doi.org/10.3390/rs3102166

Ivascanu, P., Baker, T., Lewis, P., Kulcsar, Z., Denes, R., Tamas, C., 2019. Bolcana, Romania: Geology and discovery history of a gold rich porphyry deposit, in: NewGenGold.

Ivăşcanu, P., Kulcsar, Z., Dénes, R., Baker, T., Lewis, P., 2018. Bolcana Porphyry Au-Cu Deposit, Apuseni Mountains, Romania. AME Roundup 2018 Core Shack Abstr. Guid. 31.

Iyakwari, S., Glass, H.J., 2014. Influence of mineral particle size and choice of suitable parameters for ore sorting using near infrared sensors. Miner. Eng. 69, 102–106. https://doi.org/10.1016/j.mineng.2014.07.014

Jackisch, R., Lorenz, S., Zimmermann, R., Möckel, R., Gloaguen, R., 2018. Drone-borne hyperspectral monitoring of acid mine drainage: An example from the Sokolov lignite district. Remote Sens. 10. https://doi.org/10.3390/rs10030385

Jakob, S., Gloaguen, R., Laukamp, C., 2016. Remote sensing-based exploration of structurally-related

mineralizations around Mount Isa, Queensland, Australia. Remote Sens. 8. https://doi.org/10.3390/rs8050358

Jakob, S., Zimmermann, R., Gloaguen, R., 2017. The Need for Accurate Geometric and Radiometric Corrections of Drone-Borne Hyperspectral Data for Mineral Exploration: MEPHySTo-A Toolbox for Pre-Processing Drone-Borne Hyperspectral Data. Remote Sens. 9. https://doi.org/10.3390/rs9010088

Jin, J., Yang, L., Shang, X., Ding, M., 2013. Vascular Tree Segmentation in Medical Images Using Hessian-Based Multiscale Filtering and Level Set Method. Comput. Math. Methods Med. 9.

Johnson, C.L., Browning, D.A., Pendock, N.E., 2019. Hyperspectral imaging applications to geometallurgy: Utilizing blast hole mineralogy to predict Au-Cu recovery and throughput at the Phoenix mine, Nevada. Econ. Geol. 114, 1481–1494. https://doi.org/10.5382/econgeo.4684

Kern, M., Kästner, J., Tolosana-Delgado, R., Jeske, T., Gutzmer, J., 2018a. The inherent link between ore formation and geometallurgy as documented by complex tin mineralization at the Hämmerlein deposit. Miner. Depos. 683–698. https://doi.org/10.1007/s00126-019-00874-8

Kern, M., Möckel, R., Krause, J., Teichmann, J., Gutzmer, J., 2018b. Calculating the deportment of a fine-grained and compositionally complex Sn skarn with a modified approach for automated mineralogy. Miner. Eng. 116, 213–225. https://doi.org/10.1016/j.mineng.2017.06.006

Kern, M., Tusa, L., Leißner, T., Gerald van den Boogaart, K., Gutzmer, J., 2019. Optimal sensor selection for sensor-based sorting based on automated mineralogy data. J. Clean. Prod. 234, 1144–1152. https://doi.org/10.1016/j.jclepro.2019.06.259

Ketchen, D.J., Shook, C.L., 1996. The Application Of Cluster Analysis In Ecnomics Science. Strateg. Manag. J. 17, 441–458. https://doi.org/10.2991/icessms-16.2017.104

Khodadadzadeh, M., Tusa, L., Contreras Acosta, I.C., Gloaguen, R., 2018. Subspace clustering algorithms for mineral mapping 71. https://doi.org/10.1117/12.2500080

Kirbas, C., Quek, F., 2004. A review of vessel extraction techniques and algorithms. ACM Comput. Surv. 36, 81–121. https://doi.org/10.1145/1031120.1031121

Kirsch, M., Lorenz, S., Zimmermann, R., Tusa, L., Möckel, R., Hödl, P., Booysen, R., Khodadadzadeh, M., Gloaguen, R., 2018. Integration of Terrestrial and Drone-Borne Hyperspectral and Photogrammetric Sensing Methods for Exploration Mapping and Mining Monitoring. Remote Sens. 10, 1366. https://doi.org/10.3390/rs10091366

Knapp, H., Neubert, K., Schropp, C., Wotruba, H., 2014. Viable Applications of Sensor-Based Sorting for the Processing of Mineral Resources. ChemBioEng Rev. 1, 86–95. https://doi.org/10.1002/cben.201400011

Kokaly, R.F., Clark, R.N., Swayze, G.A., Livo, K.E., Hoefen, T.M., Pearson, N.C., Wise, R.A., Benzel, W.M., Lowers, H.A., Driscoll, R.L., Klein, A.J., 2017. USGS Spectral Library Version 7, Data Series. Reston, VA. https://doi.org/10.3133/ds1035

Kopăcková, V., Koucká, L., 2017. Integration of absorption feature information from visible to longwave infrared spectral ranges for mineral mapping. Remote Sens. 9, 8–13. https://doi.org/10.3390/rs9101006

Kratt, C., Calvin, W.M., Coolbaugh, M.F., 2010. Mineral mapping in the Pyramid Lake basin: Hydrothermal alteration, chemical precipitates and geothermal energy potential. Remote Sens. Environ. 114, 2297–2304. https://doi.org/10.1016/j.rse.2010.05.006

References

Krohn, M.D., Altaner, S.P., 1987. Near infrared detection of ammonium minerals. Geophysics 52, 924–930. https://doi.org/10.1190/1.1442362

Krupnik, D., Khan, S., 2019. Close-range, ground-based hyperspectral imaging for mining applications at various scales: Review and case studies. Earth-Science Rev. 198, 102952. https://doi.org/10.1016/j.earscirev.2019.102952

Kruse, F. a., Weatherbee, O., Peppin, W., Bedell, R., Calvin, W., Taranik, J. V., 2010. HSI mineral mapping from airborne, outcrop, and drill-core perspectives. Proc. SPIE Symp. Def. Secur. SPIE Symp. Def. Secur. 7687, 76870K-76870K–15. https://doi.org/10.1117/12.855445

Kruse, F.A., 1996. Identification and mapping of minerals in drill core using hyperspectral image analysis of infrared reflectance spectra. Int. J. Remote Sens. 17, 1623–1632. https://doi.org/10.1080/01431169608948728

Kruse, F.A., Bedell, R.L., Taranik, J. V., Peppin, W.A., Weatherbee, O., Calvin, W.M., 2012. Mapping alteration minerals at prospect, outcrop and drill core scales using imaging spectrometry. Int. J. Remote Sens. 33, 1780–1798. https://doi.org/10.1080/01431161.2011.600350

Laukamp, C., Rodger, A., Legras, M., Lampinen, H., Lau, I.C., Pejcic, B., Stromberg, J., Francis, N., Ramanaidou, E., 2021. Mineral physicochemistry underlying feature-based extraction of mineral abundance and composition from shortwave, mid and thermal infrared reflectance spectra. Minerals 11. https://doi.org/10.3390/min11040347

Laukamp, C., White, A., Rodger, A., Gum, J., Metelka, V., Lau, I.C., Gordon, G., Fonteneau, L.C., 2018. Mapping mineral footprints through cover using surface and subsurface mineralogy and geochemistry. Int. Geosci. Remote Sens. Symp. 2018-July, 8352–8355. https://doi.org/10.1109/IGARSS.2018.8517522

Lessard, J., De Bakker, J., McHugh, L., 2014. Development of ore sorting and its impact on mineral processing economics. Miner. Eng. 65, 88–97. https://doi.org/10.1016/j.mineng.2014.05.019

Li, H.., Chang, C.I., 2015. Linear spectral unmixing using least squares error, orthogonal projection and simplex volume for hyperspectral images. 7th Work. Hyperspectral Image Signal Process. Evol. Remote Sens. (WHISPERS), Tokyo 1–4.

Lindholm, R.C., 1987. Mineral identification using X-ray diffraction, in: A Practical Approach to Sedimentology. Springer Netherlands, Dordrecht, pp. 124–153. https://doi.org/10.1007/978-94-011-7683-5_6

Littlefield, E., Calvin, W., Stelling, P., Kent, T., 2012. Reflectance spectroscopy as a drill core logging technique: An example using core from the Akutan. Geotherm. Resour. Counc. Annu. Meet. 2012 - Geotherm. Reliab. Renewable, Glob. GRC 2012 36 2, 1281–1283.

Lorenz, S., 2019. The Need for Accurate Pre-processing and Data Integration for the Application of Hyperspectral Imaging in Mineral Exploration. Technischen Universität Bergakademie Freiberg.

Lorenz, S., Salehi, S., Kirsch, M., Zimmermann, R., Unger, G., Sørensen, E.V., Gloaguen, R., 2018. Radiometric correction and 3D integration of long-range ground-based hyperspectral imagery for mineral exploration of vertical outcrops. Remote Sens. 10. https://doi.org/10.3390/rs10020176

Lowell, J.D., Guilbert, J.M., 1970. Lateral and vertical alteration-mineralization zoning in porphyry ore deposits. Econ. Geol. 65, 373–408.

Lypaczewski, P., Rivard, B., 2018. Estimating the Mg# and Al VI content of biotite and chlorite from shortwave

infrared reflectance spectroscopy: Predictive equations and recommendations for their use. Int. J. Appl. Earth Obs. Geoinf. 68, 116–126. https://doi.org/10.1016/j.jag.2018.02.003

Lypaczewski, P., Rivard, B., Lesage, G., Byrne, K., D'angelo, M., Lee, R.G., 2020. Characterization of mineralogy in the highland valley porphyry cu district using hyperspectral imaging, and potential applications. Minerals 10, 1–31. https://doi.org/10.3390/min10050473

Marcoux, E., Grancea, L., Lupulescu, M., Milési, J., 2002. Lead isotope signatures of epithermal and porphyry-type ore deposits from the Romanian Carpathian Mountains. Miner. Depos. 37, 173–184. https://doi.org/10.1007/s00126-001-0223-x

Markard, J., 2018. The next phase of the energy transition and its implications for research and policy. Nat. Energy 3, 628–633. https://doi.org/10.1038/s41560-018-0171-7

Markowski, A., Vallance, J., Chiaradia, M., Fontboté, L., 2006. Mineral zoning and gold occurrence in the Fortuna skarn mine, Nambija district, Ecuador. Miner. Depos. 41, 301–321. https://doi.org/10.1007/s00126-006-0062-x

Mars, J.C., Rowan, L.C., 2011. ASTER spectral analysis and lithologic mapping of the Khanneshin carbonatite volcano, Afghanistan. Geosphere 7, 276–289. https://doi.org/10.1130/GES00630.1

Mason P., H.J., 2012. Technical Note 2012-002 HyLogger 3 components and pre-processing: An overview.pdf. North. Territ. Geol. Surv.

Mathieu, M., Roy, R., Launeau, P., Cathelineau, M., Quirt, D., 2017. Alteration Mapping on drill cores using HySpex SWIR-320m hyperspectral camera: application to the exploration of an unconformity-related uranium deposit (Saskatchewan, Canada). J. Geochemical Explor. 172, 71–88. https://doi.org/https://doi.org/10.1016/j.gexplo.2016.09.008

Mauger, A.J., Keeling, J.L., Huntington, J.F., 2007. Alteration mapping of the Tarcoola Goldfield (South Australia) using a suite of hyperspectral methods. Appl. Earth Sci. 116, 2–12. https://doi.org/10.1179/174327507X167028

Maydagán, L., Franchini, M., Impiccini, A., Lentz, D., Patrier, P., Beaufort, D., 2018. Chlorite, white mica and clay minerals as proximity indicators to ore in the shallow porphyry environment of Quebrada de la Mina deposit, Argentina. Ore Geol. Rev. 92, 297–317. https://doi.org/10.1016/j.oregeorev.2017.11.028

Michaux, S., O'Connor, L., 2020. How to Set Up and Develop a Geometallurgical Program - GTK Open Work File Report 72/2019.

Milu, V., Leroy, J.L., Piantone, P., 2003. Le gisement de cuivre-or de Bolcana (monts Métallifères Roumanie) : Premières données sur les altérations et minéralisations associées. Comptes Rendus - Geosci. 335, 671–680. https://doi.org/10.1016/S1631-0713(03)00120-2

Mitchell, C., 2016. Momentum is increasing towards a flexible electricity system based on renewables. Nat. Energy 1, 15030. https://doi.org/10.1038/nenergy.2015.30

Mudd, G.M., Jowitt, S.M., 2018. Growing Global Copper Resources, Reserves and Production: Discovery Is Not the Only Control on Supply. Econ. Geol. 113, 1235–1267. https://doi.org/10.5382/econgeo.2018.4590

Murphy, R.J., Monteiro, S.T., Schneider, S., 2012. Evaluating classification techniques for mapping vertical geology using field-based hyperspectral sensors. IEEE Trans. Geosci. Remote Sens. 50, 3066–3080.

References

_____

https://doi.org/10.1109/TGRS.2011.2178419

Murphy, R.J., Schneider, S., Monteiro, S.T., 2014. Mapping layers of clay in a vertical geological surface using hyperspectral imagery: Variability in parameters of SWIR absorption features under different conditions of illumination. Remote Sens. 6, 9104–9129. https://doi.org/10.3390/rs6099104

Murphy, R.J., Taylor, Z., Schneider, S., Nieto, J., 2015. Mapping clay minerals in an open-pit mine using hyperspectral and LiDAR data. Eur. J. Remote Sens. 48, 511–526. https://doi.org/10.5721/EuJRS20154829

Murray, H.H., Lyons, S.C., 1955. Correlation of Paper-Coating Quality with Degree of Crystal Perfection of Kaolinite. Clays Clay Miner. 4, 31–40. https://doi.org/10.1346/CCMN.1955.0040105

Neubauer, F., Lips, A., Kouzmanov, K., Lexa, J., Ivăşcanu, P., 2005. 1: Subduction, slab detachment and mineralization: The Neogene in the Apuseni Mountains and Carpathians. Ore Geol. Rev. 27, 13–44. https://doi.org/10.1016/j.oregeorev.2005.07.002

Neubert, K., Wotruba, H., 2017. Investigations on the Detectability of Rare-Earth Minerals Using Dual-Energy X-ray Transmission Sorting. J. Sustain. Metall. 3, 3–12. https://doi.org/10.1007/s40831-016-0069-1

Ngcofe, L., Minnaar, H., Halenyane, K., Chevallier, L., 2013. MULTISPECTRAL AND HYPERSPECTRAL REMOTE SENSING: TARGET AREA GENERATION FOR PORPHYRY COPPER EXPLORATION IN THE NAMAQUA METAMORPHIC PROVINCE, SOUTH AFRICA. SOUTH AFRICAN J. Geol. 116, 259–272. https://doi.org/10.2113/gssajg.116.2

Osanloo, M., Ataei, M., 2003. Using equivalent grade factors to find the optimum cut-off grades of multiple metal deposits. Miner. Eng. 16, 771–776. https://doi.org/10.1016/S0892-6875(03)00163-8Get

Papari, G., Petkov, N., 2011. Edge and line oriented contour detection: State of the art. Image Vis. Comput. 29, 79–103. https://doi.org/10.1016/j.imavis.2010.08.009

Pécskay, Z., Lexa, J., Szakács, A., Seghedi, I., Balogh, K., Konečný, V., Zelenka, T., Kovacs, M., Póka, T., Fülöp, A., Márton, E.M.Ő., Panaiotu, C., Cvetković, V., 2006. Geochronology of Neogene magmatism in the Carpathian arc and intra-Carpathian area. Geol. Carpathica 57, 6, 511–530.

Plaza, A., Chang, C.-I., 2005. An improved N-FINDR algorithm in implementation 298. https://doi.org/10.1117/12.602373

Pontual, S., Merrry, N., Gamson, .P, 1997. Spectral Interpretation Field Manual - Volume 1. AusSpec International Ltd.

Post, J.L., Noble, P.N., 1993. The Near-Infrared Combination Band Frequencies of Dioctahedral Smectites, Micas, and Illites. Clays Clay Miner. 41, 639–644. https://doi.org/10.1346/CCMN.1993.0410601

Pour, A.B., Hashim, M., 2011. Identification of hydrothermal alteration minerals for exploring of porphyry copper deposit using ASTER data, SE Iran. J. Asian Earth Sci. 42, 1309–1323. https://doi.org/10.1016/j.jseaes.2011.07.017

Ranjan, S., Nayak, D.R., Kumar, K.S., Dash, R., Majhi, B., 2017. Hyperspectral image classification: A k-means clustering based approach. 2017 4th Int. Conf. Adv. Comput. Commun. Syst. ICACCS 2017 0–6. https://doi.org/10.1109/ICACCS.2017.8014707

Rauhala, A., Tupmela, A., Davids, C., Rossi, P.M., 2017. UAV Remote Sensing Surveillance of a Mine Tailings Impoundment in Sub-Arctic Conditions 1–14. https://doi.org/10.3390/rs9121318

Rhys, D., 2014. Certej Gold Deposit, Romania: geological observations and interpretations.

Riaza, A., Mu, A., 2010. Hyperspectral remote sensing monitoring of pyrite mine wastes : a record of climate variability (Pyrite Belt , Spain) 575–594. https://doi.org/10.1007/s12665-009-0368-y

Richards, J.P., 2005. Porphyry-Epithermal Deposits — Short : Sofia 2005 Tectonomagmatic controls on porphyry and epithermal mineralization Primary melts : Partial melting of hydrated mantle wedge above subducting slab Porphyry-Epithermal Deposits — Short : Sofia 2005 Magma 1–11.

Roache, T.J., Walshe, J.L., Huntington, J.F., Quigley, M.A., Yang, K., Bil, B.W., Blake, K.L., Hyvärinen, T., 2011. Epidote-clinozoisite as a hyperspectral tool in exploration for Archean gold. Aust. J. Earth Sci. 58, 813–822. https://doi.org/10.1080/08120099.2011.608170

Robben, M., Wotruba, H., 2010. Near-infrared Sorting for Minerals. Proc. Sensorgestützte Sortierung 1–12.

Robben, Wotruba, 2019. Sensor-Based Ore Sorting Technology in Mining—Past, Present and Future. Minerals 9, 523. https://doi.org/10.3390/min9090523

Rodarmel, C., Shan, J., 2002. Principal Component Analysis for Hyperspectral Image Classification. Surv. L. Inf. Syst. 62, 115–122.

Rodriguez-Galiano, V., Sanchez-Castillo, M., Chica-Olmo, M., Chica-Rivas, M., 2015. Machine learning predictive models for mineral prospectivity: An evaluation of neural networks, random forest, regression trees and support vector machines. Ore Geol. Rev. 71, 804–818. https://doi.org/10.1016/j.oregeorev.2015.01.001

Roşu, E., Pécskay, Z., Stefan, A., Popescu, G.C., Panaiotu, C., Panaiotu, C.E., 1997. The Evolution Of the Neogene Volcanism In the Apuseni Mountains (Rumania) - Constraints From New K-Ar Data. Geol. Carpathica 48, 353–359.

Roşu, E., Seghedi, I., Downes, H., Alderton, D.H.M., Szakács, A., Pécskay, Z., Panaiotu, Cristian, Panaiotu, Ce, Nedelcu, L., 2004. Extension-related Miocene calc-alkaline magmatism in the Apuseni Mountains, Romania: Origin of magmas. Schweizerische Mineral. Petrogr. Mitteilungen 84, 153–172. https://doi.org/10.1007/s00464-010-0917-1

Ruffin, C., King, R.L., 1999. The analysis of hyperspectral data using Savitzky-Golay filtering-theoretical basis. 1. IEEE 1999 Int. Geosci. Remote Sens. Symp. IGARSS'99 (Cat. No.99CH36293) 2, 756–758. https://doi.org/10.1109/IGARSS.1999.774430

Rumelhart, D.E., Hintont, G.E., 1986. Learning representations by back-propagating errors. Nature 323, 533–536.

Salter, J.D., Wyatt, N.P.G., 1991. Sorting in the minerals industry: Past, present and future. Miner. Eng. 4, 779–796. https://doi.org/10.1016/0892-6875(91)90065-4

Savitzky, A., Golay, M., 1964. Smoothing and differentiation of data by simplified least squares procedures. Anal. Chem. 36, 1627–1639.

Schlesinger, M.E., King, M.J., Sole, K.C., Davenport, W.G., 2011. Overview, Extractive Metallurgy of Copper. https://doi.org/10.1016/b978-0-08-096789-9.10001-0

Schodlok, M.C., Whitbourn, L., Huntington, J., Mason, P., Green, A., Berman, M., Coward, D., Connor, P., Wright, W., Jolivet, M., Martinez, R., 2016. HyLogger-3, a visible to shortwave and thermal infrared reflectance spectrometer system for drill core logging: functional description. Aust. J. Earth Sci. 63, 929–940. https://doi.org/10.1080/08120099.2016.1231133

References

Schuppan, W., Hiller, A., 2012. Die Komplexlagerstätten Tellerhäuser, Uranbergbau und Zinnerkundung in der Grube Pöhla der SDAG Wismut. Bergbau in Sachsen.

Schwartz, G.M., 1959. Hydrothermal alteration. Econ. Geol. 54, 161–183.

Scott, K.M., Yang, K., 1997. Spectral Reflectance Studies of White Micas. Australian Mineral Industries Research Association, Ltd.: Parkville, Australia, 1997; 35p.

Shahi, K.R., Khodadadzadeh, M., Tusa, L., Ghamisi, P., Tolosana-Delgado, R., Gloaguen, R., 2020. Hierarchical Sparse Subspace Clustering (HESSC): An automatic approach for hyperspectral image analysis. Remote Sens. 12, 8–13. https://doi.org/10.3390/RS12152421

Sillitoe, R.H., 2010. Porphyry Copper Systems. Econ. Geol. 105, 3–41. https://doi.org/10.2113/gsecongeo.105.1.3

Silván-Cárdenas, J.L., Wang, L., 2010. Fully constrained linear spectral unmixing: Analytic solution using fuzzy sets. IEEE Trans. Geosci. Remote Sens. 48, 3992–4002. https://doi.org/10.1109/TGRS.2010.2072931

Simpson, M.P., 2015. Reflectance spectrometry [SWIR] of alteration minerals surrounding the Favona epithermal vein. Waihi vein system, Hauraki Goldfield. AusIMM New Zeal. Branch Annu. Conf. 2015 490–499.

Specht, D.F., 1991. A General Regression Neural Network. IEEE Trans. Neural Networks 2.

Steger, C., 1998. An unbiased detector of curvilinear structures. IEEE Trans. Pattern Anal. Mach. Intell. 20(2), 113–125.

Sun, W.D., Liang, H.Y., Ling, M.X., Zhan, M.Z., Ding, X., Zhang, H., Yang, X.Y., Li, Y.L., Ireland, T.R., Wei, Q.R., Fan, W.M., 2013. The link between reduced porphyry copper deposits and oxidized magmas. Geochim. Cosmochim. Acta 103, 263–275. https://doi.org/10.1016/j.gca.2012.10.054

Sutton, A., 2021. Copper. Gordon Brother.

Tappert, M., Rivard, B., Giles, D., Tappert, R., Mauger, A., 2011. Automated drill core logging using visible and near-infrared reflectance spectroscopy: A case study from the Olympic Dam Iocg deposit, South Australia. Econ. Geol. 106, 289–296. https://doi.org/10.2113/econgeo.106.2.289

Taylor, G.S., 2000. Mineral and lithology mapping of drill core pulps using visible and infrared spectrometry. Nat. Resour. Res. 9, 257–268.

Thompson, A.J.B., 2020. Innovation in mineral exploration.

Turner, D., Rivard, B., Groat, L., 2014. Rare earth element ore grade estimation of mineralized drill-core from hyperspectral imaging spectroscopy. IEEE Int. Geosci. Remote Sens. Symp. Proc. 4612–4615.

Tusa, Laura, Andreani, L., Khodadadzadeh, M., Contreras, C., Ivascanu, P., Gloaguen, R., Gutzmer, J., 2019. Mineral Mapping and Vein Detection in Hyperspectral Drill-Core Scans: Application to Porphyry-Type Mineralization. Minerals 9, 122. https://doi.org/10.3390/min9020122

Tusa, L, Kern, M., Khodadadzadeh, M., Blannin, R., Gloaguen, R., Gutzmer, J., 2019a. Evaluating the performance of hyperspectral short-wave infrared sensors for the pre-sorting of complex ores using machine learning methods. Miner. Eng. 146. https://doi.org/10.1016/j.mineng.2019.106150

Tuşa, L., Khodadadzadeh, M., Contreras, C., Rafiezadeh Shahi, K., Fuchs, M., Gloaguen, R., Gutzmer, J., 2020. Drill-Core Mineral Abundance Estimation Using Hyperspectral and High-Resolution Mineralogical Data. Remote Sens. 12, 1218. https://doi.org/10.3390/rs12071218

Udubaşa, S.S., Roşu, E., Seghedi, I., Ivăşcanu, P.M., 2001. The "Golden Quadrangle" in the Metaliferi Mts ., Romania : What Does This Really Mean?, in: ABCD-GEODE 2001 Workshop Vata Bai, Romania: Bucharest, Romania, Geological Institute of Romania, Romanian Journal of Mineral Deposits: Abstracts. pp. 24–34.

van den Boogaart, K.G., Tolosana-Delgado, R., 2018. Predictive Geometallurgy: An Interdisciplinary Key Challenge for Mathematical Geosciences, in: Daya Sagar, B.S., Cheng, Q., Agterberg, F. (Eds.), Handbook of Mathematical Geosciences: Fifty Years of IAMG. Springer International Publishing, Cham, pp. 673–686. https://doi.org/10.1007/978-3-319-78999-6_33

van der Meer, F.D., van der Werff, H.M.A., van Ruitenbeek, F.J.A., Hecker, C.A., Bakker, W.H., Noomen, M.F., van der Meijde, M., Carranza, E.J.M., de Smeth, J.B., Woldai, T., 2012. Multi- and hyperspectral geologic remote sensing: A review. Int. J. Appl. Earth Obs. Geoinf. 14, 112–128. https://doi.org/10.1016/j.jag.2011.08.002

Van Ruitenbeek, F.J.A., Bakker, W.H., Van Der Werff, H.M.A., Zegers, T.E., Oosthoek, J.H.P., Omer, Z.A., Marsh, S.H., Van Der Meer, F.D., 2014. Mapping the wavelength position of deepest absorption features to explore mineral diversity in hyperspectral images. Planet. Space Sci. 101, 108–117. https://doi.org/10.1016/j.pss.2014.06.009

Vapnik, V.N., 1999. An overview of statistical learning theory. IEEE Trans. Neural Networks 10, 988–999. https://doi.org/10.1109/72.788640

Wang, D., Lagerstrom, R., Sun, C., Laukamp, C., Quigley, M., Whitbourn, L., Mason, P., Connor, P., Fisher, L., 2017. Automated vein detection for drill core analysis by fusion of hyperspectral and visible image data. M2VIP 2016 - Proc. 23rd Int. Conf. Mechatronics Mach. Vis. Pract. https://doi.org/10.1109/M2VIP.2016.7827317

Wang, R., Cudahy, T., Laukamp, C., Walshe, J.L., Bath, A., Mei, Y., Young, C., Roache, T.J., Jenkins, A., Roberts, M., Barker, A., Laird, J., 2017. White mica as a hyperspectral tool in exploration for the sunrise dam and Kanowna belle gold deposits, Western Australia. Econ. Geol. 112, 1153–1176. https://doi.org/10.5382/econgeo.2017.4505

Waske, B., Benediktsson, J.A., Arnason, K., Sveinsson, J.R., 2009. Mapping of hyperspectral AVIRIS data using machine-learning algorithms. Can. J. Remote Sens. 35, S106–S116. https://doi.org/10.5589/m09-018

Wilkinson, J.J., Chang, Z., Cooke, D.R., Baker, M.J., Wilkinson, C.C., Inglis, S., Chen, H., Bruce Gemmell, J., 2015. The chlorite proximitor: A new tool for detecting porphyry ore deposits. J. Geochemical Explor. 152, 10–26. https://doi.org/10.1016/j.gexplo.2015.01.005

Wills, B.A., 2016. An Introduction to the Practical Aspects of Ore Treatment and Mineral Recovery, Wills' Mineral Processing Technology. https://doi.org/10.1016/B978-0-08-097053-0.00018-2

Winter, M.E., 1999. N-FINDR: an algorithm for fast autonomous spectral end-member determination in hyperspectral data, in: Proc.SPIE. https://doi.org/10.1117/12.366289

Wu, M., Zhou, K., Wang, Q., Wang, J., 2019. Mapping hydrothermal zoning pattern of porphyry Cu deposit using absorption feature parameters calculated from ASTER data. Remote Sens. 11. https://doi.org/10.3390/rs11141729

Yang, K., Huntington, J.F., Browne, P.R.L., Ma, C., 2000. An infrared spectral reflectance study of hydrothermal

alteration minerals from the Te Mihi sector of the Wairakei geothermal system, New Zealand. Geothermics 29, 377–392. https://doi.org/10.1016/S0375-6505(00)00004-3

Yang, K., Huntington, J.F., Gemmell, J.B., Scott, K.M., 2011. Variations in composition and abundance of white mica in the hydrothermal alteration system at Hellyer, Tasmania, as revealed by infrared reflectance spectroscopy. J. Geochemical Explor. 108, 143–156. https://doi.org/10.1016/j.gexplo.2011.01.001